Doctoral Dissertation

Jingyi Han

Mass transfer characteristics of CO2 absorption into liquid droplets

Telemark University College
Faculty of Technology

Mass transfer characteristics of CO_2 absorption into liquid droplets

Jingyi Han

Jingyi Han

Mass transfer characteristics of CO_2 absorption into liquid droplets

Thesis for the Degree of Doctor of Philosophy

Porsgrunn, Norway

January, 2014

Tel–Tek
Telemark University College

Tel–Tek
Telemark University College

Thesis for the degree of doctor of philosophy

ISBN 978-82-7206-377-0

Doctoral Thesis at TUC, 2014

Acknowledge

This work is completed under the guidance of my supervisor Prof. Morten C. Melaaen. In the past four years, Prof. Morten C. Melaaen gave me very selfless help and support in both work and life. He gave good guidance in the elaboration of my degree courses, the implementation of the research project and my thesis writing which I benefited a lot. He set a good example for me because of his professional dedication and rigorous scholarship. I would like to take this opportunity to express my heartfelt thank to Prof. Morten C. Melaaen.

I especially want to thank my family for many years of support and encouragement on my study and life. During my hard time, they gave me the confidence and strength to overcome the difficulties. They will always be my solid backing. I wish them healthy and happy.

Also sincerely thank my co-supervisor Prof. Dag A. Eimer who gave me a lot of help to make me successfully complete the Ph.D study. His optimistic spirit and profound knowledge deeply inspired me. I would also like to thank Sigbjørn Wiersdalen, who is a very kind friend and gave me a lot of help in the experimental work. I won't get those results without his help.

I would like to express my gratitude to Marit Larsen and Hans Aksel Haugen for giving me this opportunity to take a Ph.D in Norway. I had a great time here. This experience will be one of the most important parts of my life. I would like to express my sincere gratitude to Prof. Klaus. J. Jens for his enthusiastic help and guidance. I would like to thank Marit Kleven because she worked together with me on the CFD simulation and helped a lot. I would also like to thank other colleagues in Tel-Tek and Telemark University College, Liv Axelsen, Marit Kleven, Trond Risberg, Joachim Lundberg, Talleiv Skredtveit, Eivind Fjelddalen, Per Morten Hansen, and Chameera Jayarathna, who helped me very much.

I would like to thank Wang Tielin and Ying Jiru. We started the Ph.D work together, share the same office, take the same courses and work in the same lab. They helped me like an elder brother and I learned a lot from them. I would also like to thank my best friends in China and in Norway. It is a great happiness to have your company.

Thanks again to my family, teachers and friends sincerely. Wish you all the best!

Abstract

CO_2 capture from exhaust gases has been paid more and more attention in order to avoid global warming. One of the methods for removing CO_2 from the flue gas streams is the use of absorption and aqueous alkanolamine solutions as absorbents. Alkanolamines such as monoethanolamine (MEA), diethanolamine (DEA) and N-methyldiethanolamine (MDEA) are widely used in CO_2 capture because of their high CO_2 absorbing capacity and lower energy consumption. Physical properties such as density and surface tension of the pure compounds of amines, the mixtures with water and CO_2 loaded aqueous amine solutions are important for optimal designing of absorption-desorption processes and the related engineering calculations. The absorption of CO_2 into aqueous amine solutions by the spray method is a possible process for bulk removal of CO_2 from a gaseous stream. A deep understanding of the mass transfer characteristics in the spray column is very important for the optimization design of the column and the selection of absorbent. The study of mass transfer between CO_2 and the unit part of a spray - individual droplets is crucial for better understanding the mass transfer characteristics in the spray column.

In this work, densities in liquid solutions of water + monoethanolamine (MEA), water + diethanolamine (DEA) and water + N-methyldiethanolamine (MDEA) have been measured at temperatures from (298.15 to 423.15) K by Anton Paar density meters DMA 4500 and DMA HP. The mass fraction of amine ranged from 0.3 to 1.0. Excess molar volumes of the binary system were derived and correlated by a Redlich-Kister equation. The model uses a third order Redlich-Kister equation and a linear relationship with the temperature for unloaded aqueous MEA solutions, while a fourth order Redlich-Kister equation and a second polynomial function with respect to the temperature for unloaded aqueous DEA and MDEA solutions. Densities of CO_2 loaded aqueous MEA solutions (water + MEA + CO_2) were measured at temperatures from (298.15 to 413.15) K by Anton Paar density meters DMA 4500 and DMA HP. The mass fraction of MEA in water was 0.3, 0.4, 0.5 and 0.6. Densities in liquid solutions of water + DEA + CO_2 and water + MDEA + CO_2 were measured at temperatures from (298.15 to 423.15) K by Anton Paar density meters DMA 4500 and DMA HP. The mass fraction of DEA and MDEA in water was 0.3 and 0.4. The CO_2 loading ranged from 0.1 to 0.5. Molar volumes of the ternary system were derived and correlated by the equation from Weiland et al. at each temperature. The parameters were in turn fitted by a

polynomial function of the temperature. The agreement between the measured density results and the correlated data is good. The uncertainties of density measurements were analyzed.

Surface tensions of aqueous MEA solutions were measured at temperatures from (303.15 to 333.15) K by the sessile drop method. A Rame-Hart Model 500 Advanced Goniometer with DROPimage Advanced v2.4 was employed. The mass fraction of MEA ranged from 0 to 1.0. Measured surface tensions of aqueous MEA solutions in this work were compared with Vázquez et al.'s data. The experimental surface tensions were correlated with temperature by a linear relationship. The correlated surface tensions by the linear equation and the experimental data have very good agreement. The surface tensions of aqueous MEA solutions were correlated with mole fraction of MEA by both an empirical model and the chemical model. The chemical model shows better agreement with the experimental surface tension data than the empirical model. The uncertainties of surface tension measurements were analyzed.

In order to study the mass transfer characteristics between CO_2 and liquid droplets, a novel experimental set-up was constructed. This system produces individual droplets by pushing the liquid through a needle with the help of pressurized nitrogen. The droplets fall through a gas chamber one by one and finally deposit under kerosene. Pure CO_2 is filled in the gas chamber to eliminate the gas side mass transfer resistance. A temperature control box was built outside the chamber in order to perform the absorption experiments under controlled temperatures. The pressure inside the chamber keeps constant and the same as the atmosphere by an overflow section. The experiments can be performed at different droplet falling heights by adjusting the length of the overflow tube. The volume flow rate of CO_2 was measured by a soap film flow meter to calculate the absorption rate. A high speed camera system was used to determine the size of droplet, droplet formation time and droplet formation rate. The absorption of CO_2 into the kerosene can be measured before the droplets start dripping. The results from this blank experiment will be subtracted to determine the concentration of CO_2 that is absorbed by liquid droplets. Because the density of kerosene is much smaller than the solvent, the droplets deposit under kerosene very fast. Hence, the coalescence effect can be eliminated.

The liquid phase mass transfer coefficients of CO_2 absorption by liquid droplets were measured at different temperatures, droplet formation times and droplet falling heights.

Physical absorption (CO_2 + water droplets) and chemical absorption (CO_2 + droplets of 30% MEA solutions) were both investigated.

The liquid phase mass transfer coefficients of CO_2 absorption into water droplets during droplet life-time (formation and fall together) were measured at temperatures T = 303.65 K and 323.15 K, droplet falling heights h = 0.41 m and 0.59 m, and droplet formation times t_1 = (0.352 to 2.315) s. It was found that there exists convection inside the water droplets which significantly enhances the mass transfer between CO_2 and water droplets. The convection increases as the droplet formation time decreases. The absorption rates of CO_2 into water droplets during droplet formation were measured at different droplet formation times and temperatures T = 297.15 K and 323.15 K. The measured absorption rates of CO_2 absorption into water droplets during formation at 297.15 K agree well with Dixon and Russell's data. The correlation of the absorption rate of CO_2 into water droplets during formation with droplet formation time at 323.15 K was determined. The correlation between the Sherwood number and the Reynolds number of CO_2 absorption by water droplets during droplet fall at 323.15 K was obtained.

The absorption rates of CO_2 into droplets of 30% MEA solutions during droplet formation were measured at 323.15 K and different droplet formation times. It was found that the mass transfer between CO_2 and droplets of 30% MEA solutions was not affected by the droplet formation time, which is probably because the convection inside droplets of 30% MEA solutions is small and the intensity of convection does not change very much over the range that these measurements covered. The liquid phase mass transfer coefficients of CO_2 absorption into droplets of 30% MEA solutions during droplet life-time (formation and fall together) were measured at temperatures T = 303.65 K and 323.15 K, and droplet falling heights h = (0.07 to 0.53) m. The correlation between the Sherwood number and the Reynolds number of CO_2 absorption by droplets of 30% MEA solutions during droplet fall at 323.15 K was obtained. The enhancement factors of CO_2 absorption by droplets of 30% MEA solutions are estimated. The liquid phase mass transfer coefficients without chemical reaction for CO_2 into water droplets and that for CO_2 into droplets of 30% MEA solution are compared.

Contents

1. Introduction

1.1 Background

Global warming has been paid more and more attention nowadays because it causes a series of environmental and ecological problems. It is generally agreed that CO_2 released by human activity is the main reason that caused the global warming. The carbon dioxide produced by the combustion of fossil fuels is the main source of human-caused CO_2 emissions. Although renewable energy and nuclear energy were vigorously developed in the recent years, fossil fuel will still account for the majority of global energy demand (about 85%) in the next decades.[1] According to the report from the Intergovernmental Panel on Climate Change (IPCC), the annual CO_2 emissions due to human activities have increased by about 80%, from 21 to 38 gigatonnes (Gt) between 1970 and 2004 as shown in Figure 1.[2] Reducing CO_2 emissions is crucial and significant to the future sustainable development of the whole world.

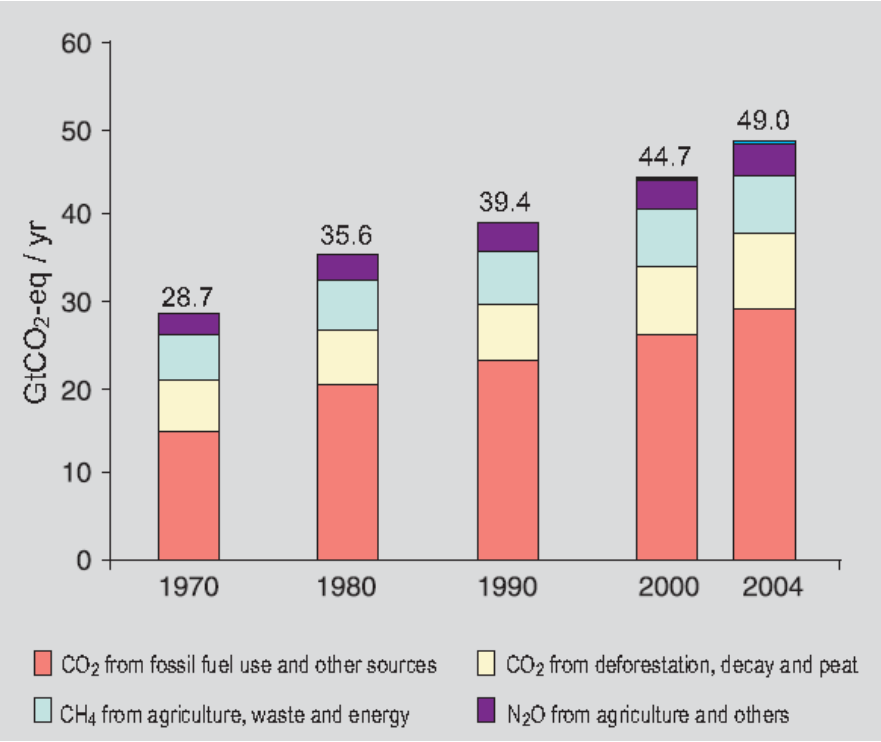

Figure 1-1. Global annual emissions of anthropogenic GHGs from 1970 to 2004.[2]

Carbon capture and storage (CCS) refer to the process of capturing CO_2 from industrial sources, transporting the compressed CO_2 to a storage site and then isolating it from the

atmosphere in the long term. CCS has caused widespread concern and become a key technology to mitigate the climate change in recent years because of its huge potential for CO_2 emission reduction. According to the prediction from the International Energy Agency (IEA), CO_2 emissions reduced by CCS technology will account for 19% of the whole CO_2 emission reduction by 2050.[3]

There are three main approaches for CO_2 capture; pre-combustion decarbonization, decarbonization during combustion and post combustion decarbonization.

Pre-combustion decarbonization, i.e. Integrated Gasification Combined Cycle (IGCC), uses a gasifier to convert coal into synthesis gas and then remove the impurities (sulfur, particulates, and mercury) to produce clean syngas which mainly consists of CO and H_2. Carbon monoxide is shifted to carbon dioxide through the reaction with steam. As a result, the fuel does not contain carbon. CO_2 produced by the shift reaction can be captured before combustion.

Decarbonization during combustion includes O_2/CO_2 recycle combustion and chemical-looping combustion (CLC). O_2/CO_2 recycle combustion technology uses a mixture of oxygen and recycled fuel gas instead of air to burn with fuel; hence the concentration of CO_2 in the dry flue gas is as high as 95%. Chemical-looping combustion technology decomposes the traditional combustion that fuels directly contact with air into two gas-solid reactions by means of an oxygen carrier. A metal oxide as the oxygen carrier transfers oxygen from the air to the fuel so that there is no direct contact between fuel and air. The produced outlet gas (CO_2 and H_2O) will be effectively separated after the combustion. Both O_2/CO_2 recycle combustion and chemical-looping combustion produce high concentrated CO_2 in the flue gas and eliminate the emissions of NO_x, so that the cost of separation and recovery of CO_2 will be greatly reduced.

Post combustion decarbonization captures CO_2 from the flue gas after the combustion process. Depending on the different principles, post combustion capture technology can be mainly divided into physical adsorption, chemical absorption and membrane method.

Chemical absorption technology is namely the use of some absorbents reacting with CO_2. The nature of capturing CO_2 by chemical absorption is a comprehensive process of mass

transfer and reaction. The selection of absorbent needs comprehensive consideration of its absorption capacity, absorption rate, regeneration, corrosivity and cost. Since CO_2 is an acidic gas, the available chemical absorbents include inorganic absorbents (aqueous ammonia, potassium carbonate solutions, etc.), organic absorbents (amine solutions, etc.) and mixed absorbents. Aqueous amine solution is the most common absorbent for CO_2 removal in industry because it has the advantages of high absorption efficiency, fast absorption rate, easy to regenerate and low cost.[4] The commonly used amines as chemical absorbent are monoethanolamine (MEA), diethanolamine (DEA), and methyldiethanolamine (MDEA).

1.2 Objectives

The objective of the work is twofold: to obtain the physical properties (density and surface tension) of amine solutions over a wide range of temperature and concentration, and to investigate mass transfer characteristics between CO_2 and individual liquid droplets. The main targets are:

1. Measure densities of amine solutions by Anton Paar density meters DMA 4500 and DMA HP at different temperatures and concentrations. Correlate the measured data and analyse the uncertainties of the density measurements.
2. Measure surface tensions of amine solutions by Rame-Hart Model 500 Advanced Goniometer at different temperatures and concentrations. Correlate the measured data and analyse the uncertainties of the surface tension measurements.
3. Establish a new experimental set-up to study mass transfer characteristics between CO_2 and liquid droplets. Measure liquid phase mass transfer coefficients of CO_2 absorption by water droplets and droplets of 30% MEA solutions at different temperatures, droplet formation times, droplet falling heights, and stages of droplet life-time. Develop correlations for liquid phase mass transfer coefficients of CO_2 absorption into liquid droplets.

1.3 Main contributions

The main contributions of this study are:

1. Densities of unloaded and CO_2 loaded aqueous MEA, DEA, and MDEA solutions were measured at different concentrations and a full temperature range (298.15 K to

423.15K). Surface tensions of unloaded aqueous MEA solutions were measured at different temperatures and a full concentration range (mass fraction of MEA 0 to 1.0).

2. Measured density and surface tension data were correlated with different models. The agreement between the measured results and the correlated data is good. The uncertainties of density and surface tension measurements were analyzed.
3. A new experimental set-up called "droplet chamber" was built to investigate mass transfer between CO_2 and liquid droplets. It was achieved to generate monosized droplets with the size known and perform the experiments at different temperatures and droplet falling heights.
4. Physical absorption (CO_2 + water droplets) and chemical absorption (CO_2 + droplets of 30% MEA solutions) were both investigated by the droplet chamber. Mass transfer characteristics of CO_2 absorption into liquid droplets during droplet formation, during droplet fall, and during droplet life time (formation and fall together) were studied. The influences of temperature, droplet formation time and droplet falling height were discussed. The correlations between the Sherwood number and the Reynolds number of CO_2 absorption by liquid droplets during droplet fall were obtained.
5. Based on the PhD work, two journal papers and one conference paper have been published already. The third journal paper is submitted.

1.4 Outline of the thesis

This thesis is composed of six chapters. Chapter 2 introduces the background knowledge of CO_2 capture technology by chemical absorption. The technical process, types of absorption columns and reaction mechanism of amine solutions with CO_2 were discussed. The literature review of mass transfer between gas-liquid phases were also presented in Chapter 2, including three fundamental mass transfer theories, mass transfer models between liquid droplets and continuous phase, and the correlation for the mass transfer coefficient in the spray column. In addition, the measuring methods and the correlation equations of physical properties (density, viscosity, surface tension, solubility and diffusivity) of amine solutions were summarized in Chapter 2.

Chapter 3 presents the measured results for densities of unloaded and CO_2 loaded aqueous MEA, DEA, and MDEA solutions at different temperatures and compositions. Excess molar

volumes of the unloaded aqueous amine solutions were derived and correlated by a Redlich-Kister equation.[5] The parameters from the Redlich-Kister equation were then fitted by a polynomial function of temperature. Molar volumes of CO_2 loaded aqueous amine solutions were derived and correlated by the equation from Weiland et al.[6] at each temperature. The parameters were in turn fitted by a polynomial function of the temperature. The uncertainties of density measurements were calculated.

Chapter 4 presents the measured results for surface tensions of aqueous MEA solutions at temperatures from (303.15 to 333.15) K and mass fraction of MEA from 0 to 1.0. The theory of the sessile drop method was interpreted. The effects of temperature and mole fraction of MEA on surface tension and the explanations were discussed. The surface tensions of aqueous MEA solutions were correlated with temperature by a linear relationship. The surface tensions of aqueous MEA solutions were correlated with mole fraction of MEA by both an empirical model and the chemical model. The uncertainties of surface tension measurements were calculated.

Chapter 5 presents the mass transfer study of CO_2 absorption into liquid droplets. A novel experimental set-up was constructed. The experimental system produces individual droplets by pushing the liquid through a needle with the help of pressurized nitrogen. The droplets fall through a gas chamber one by one and finally deposit under kerosene. The liquid phase mass transfer coefficients of CO_2 absorption into water droplets during droplet life-time (formation and fall together) were measured at temperatures T = 303.65 K and 323.15 K, droplet falling heights h = 0.41 m and 0.59 m, and droplet formation times t_1 = (0.352 to 2.315) s. The liquid phase mass transfer coefficient of CO_2 absorption into water droplets decreases as the droplet formation time increases, first very quickly and then only gradually. Moreover, it increases as the temperature and droplet falling height rises. The absorption rates of CO_2 absorption into water droplets during only droplet formation were measured and compared to the literature. The correlation of the absorption rate of CO_2 into water droplets during droplet formation with droplet formation time at 323.15 K was obtained. The liquid phase mass transfer coefficients of CO_2 absorption into water droplets during only droplet fall were derived at different droplet falling heights and droplet formation times. The correlation between the Sherwood number and the Reynolds number of CO_2 absorption by water droplets during droplet fall at 323.15 K was obtained.

The absorption rates of CO_2 absorption by droplets of 30% MEA solutions during only droplet formation were measured at 323.15 K and different droplet formation times. The absorption rate of CO_2 into droplets of 30% MEA solution almost does not vary as the droplet formation time changes. The liquid phase mass transfer coefficients of CO_2 absorption into droplets of 30% MEA solutions during droplet life-time (formation and fall together) were measured at temperatures T = 303.65 K and 323.15 K, and droplet falling heights h = (0.07 to 0.53) m. The liquid phase mass transfer coefficient of CO_2 into droplets of 30% MEA solution increases as the temperature and droplet falling height rises. The liquid phase mass transfer coefficients of CO_2 absorption by droplets of 30% MEA solutions during only droplet fall were derived at different droplet falling heights and droplet formation times. The correlation between the Sherwood number and the Reynolds number of CO_2 absorption by droplets of 30% MEA solutions during droplet fall at 323.15 K was obtained.

The conclusions of this work are summarized in Chapter 6. Moreover, the suggestions for the future work, mainly on the droplet chamber experiments, are also listed in Chapter 6.

References

(1) Tanaka, N. World Energy Outlook [R]. Cancun: International Energy Agency, 2010.

(2) Pachauri et al. Climate Change 2007: Synthesis Report [R]. Geneva: Intergovernmental Panel on Climate Change, 2007.

(3) Han, J. H.; Lee, I. B. Development of a Scalable and Comprehensive Infrastructure Model for Carbon Dioxide Utilization and Disposal. *Ind. Eng. Chem. Res.* **2012**, *50*, 6297-6315.

(4) Kohl, A.; Riesenfeld, F. *Gas Purification*; Houston: Gulf Pub Co, 1985.

(5) Redlich, O.; Kister, A. T. Algebraic representation of thermodynamic properties and the classification of solutions. *Ind. Eng. Chem.* **1948**, *40*, 345-348.

(6) Weiland, R. H.; Dingman, J. C.; Cronin, D. B.; Browning, G. J. Density and Viscosity of Some Partially Carbonated Aqueous Alkanolamine Solutions and Their Blends. *J. Chem. Eng. Data* **1998**, *43*, 378-382.

2. Literature Review

In this chapter, the existing literature on CO_2 capture by chemical absorption is reviewed in the context of the present study. Since the mass transfer of CO_2 absorption by liquid droplets which are the unit parts of the absorbent in the spray column is our main concern, the literature which covers the fundamental gas-liquid mass transfer models, the mechanisms for the specific situation of mass transfer between dispersed droplets and surrounding continuous phases, as well as the mass transfer in the spray column are investigated. In addition, the measuring and correlation methods of physical properties of the most commonly used chemical absorbents — amine solutions in the literature are summarized.

2.1 CO_2 capture — chemical absorption by amine solutions

CO_2 capture by the chemical absorption method is one of the most mature and economically feasible capture technologies because it has the advantages of high removal efficiency, large capture capacity and easy to operate. Aqueous amine solution is the most popular absorbent for CO_2 removal in industry because it has the advantages of high absorption efficiency, fast absorption rate, easy regeneration and low cost.[1] The technological process of CO_2 capture by chemical absorption, various types of absorption columns and reaction mechanism of amine solutions with CO_2 are introduced in this section.

2.1.1 Chemical absorption process

The flow diagram of CO_2 capture process by the chemical absorption method is shown in Figure 2-1. This process mainly consists of two parts — absorption and desorption. Precooled flue gas enters the absorption column from the bottom and reacts with lean aqueous amine solution countercurrently. The operating temperature in the absorption column is normally (30 to 40) °C. The water wash loop at the top of the absorber is used to minimize amine losses and make up water. The cleaned gas enters through the water wash seat and then is vented to the atmosphere from the top of the column. The produced rich aqueous amine solution with high CO_2 loading is heated by lean solution in the heat exchanger and then enters the desorption column (stripper). The operating temperature in the desorption column is about (100 to 120) °C, while the steam in a reboiler provides the heat required for the desorption reaction. The regenerated lean aqueous amine solution is recycled into the absorption column

after passing through the heat exchanger and a cooler. CO_2 produced by the desorption process passes through a condenser and a separator. The volatilized water and absorbent are condensed in the overhead condenser and then sent back to the stripper for reuse, therefore CO_2 with a high purity is obtained. Pure CO_2 is then compressed and transported to a certain storage site.

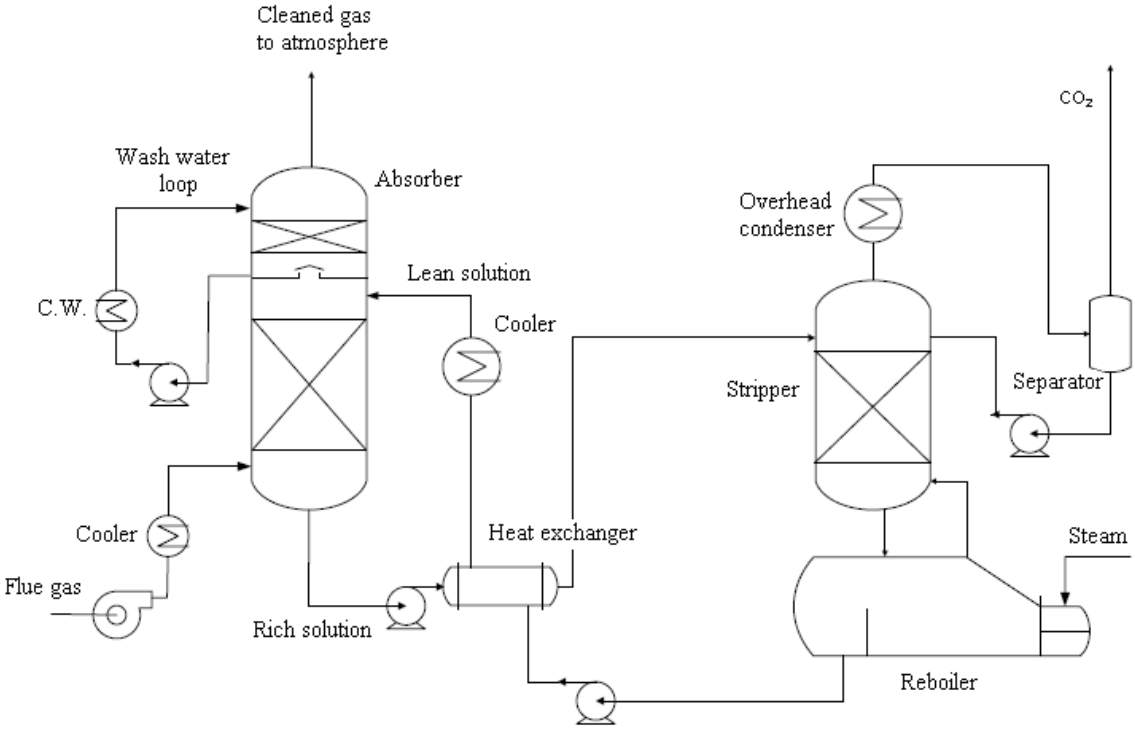

Figure 2-1. The flowsheet of chemical absorption and desorption process for capturing CO_2.

2.1.2 Different kinds of absorption columns

The absorption column is the gas-liquid mass transfer equipment. The contact method between gas and liquid phases differs for various types of absorption columns. The common absorption columns were listed in Table 2-1.

Table 2-1. The Common Absorption Columns.

Name	Gas-Liquid Contact Way	Gas-Liquid Flow
Packed column	Moving liquid films contact with gas	Countercurrent, cocurrent
Plate column	Gas bubbles disperse in the liquid	Countercurrent
Spray column	Liquid droplets disperse in the gas	Countercurrent, cocurrent
Wetted-wall column	Moving liquid films contact with gas	Countercurrent, cocurrent
Bubble column	Gas bubbles disperse in the liquid	Countercurrent, cocurrent
Stirred bubble column	Gas bubbles disperse in the liquid	-

The packed column is the most widely used absorption column in which packing materials are placed on the support plate in random dumped or structured way. Liquid is sprayed onto the packings by the liquid distributor and flows down along the surface of the packings. Gas passes through the gas distribution device and then contacts with the liquid on the surface of the packings to perform mass transfer. The composition of the two phases changes along the column continuously. The packed column has the advantages of large capacity, high separation efficiency, less corrosion problem and small liquid holdup. The disadvantages are that it is easy to clog, sensitive to the change of liquid load and smaller operating range.[2]

Another widely used absorption column is the plate column. Several trays are horizontally placed in the plate column according to certain spacing. Liquid flows through each tray in turn under gravity and discharges from the bottom of the column. Gas passes through each tray from the bottom up in the differential pressure driven and contacts with the liquid layer on the tray to perform mass transfer. Compared to the packed column, the plate column does not have serious clogging problem, therefore it is easier to clean up. In addition, the plate column is more suitable for the situation which has a large operating range or heat transfer in the process. However, the plate column has a higher pressure drop, larger liquid holdup, and more expensive when the column diameter is not large.

In the absorption process, except the commonly used packed column and plate column, the other types of absorption devices such as the spray column, the wetted-wall column, the bubble column and the stirred bubble column are also used in industry. In the spray column, liquid is sprayed into small droplets by the nozzle and then contacts the gas. The spray column has the advantages of simple structure, low cost, small pressure drop and less scaling problem. However, it has a high requirement for the material and structure of the nozzle. In

the wetted-wall column, liquid film which flows along the inner wall of the vertical tube contacts with the gas which flows in the center of the tube to perform mass transfer. The characteristics of the wetted-wall column are small pressure drop, large gas load and more suitable for the high thermal effect absorption process. In the bubbling reactor, including the bubble column and the stirred bubble column, gas enters the column from the bottom continuously and forms gas bubbles through a sieve plate and a gas distributor to contact with the liquid. The bubbling reactor is suitable for the absorption process in which the reaction is slow and controlled by the liquid phase.

For flue gas treating, the packed column is preferred for CO_2 absorption since there is little available pressure drop, and the spray column is the most widely used type for desulfurization.

2.1.3 Reaction mechanism of amine solutions with CO_2

The commonly used amines as chemical absorbent are monoethanolamine (MEA), methyldiethanolamine (MDEA), and diethanolamine (DEA). The fundamental physical properties of these three amines were shown in Table 2-2. Reaction mechanisms of MEA, DEA and MDEA with CO_2 were introduced below.

Table 2-2. The Fundamental Physical Properties of Commonly Used Amine Absorbents.

Amine	Molecular Formula	Molar Mass [g/mol]	Melting Point [°C]	Boiling Point [°C]	Vapor Pressure
MEA	$HO(CH_2)_2NH_2$	61.08	10.3	170	25 Pa (20 °C)
DEA	$NH(C_2H_4OH)_2$	105.14	28.0	217	<0.01 hPa (20 °C)
MDEA	$CH_3N(C_2H_4OH)_2$	119.20	-21.0	247	-

a) Reaction mechanism between primary amine (MEA) and CO_2, as well as secondary amine (DEA) and CO_2

MEA has been widely used as absorbent in gas purification industry as early as 1930s. The technology of using aqueous MEA solution to absorb CO_2 was developed maturely due to its high chemical reactivity, fast absorption rate with CO_2 and low solvent cost.[3, 4] The shortcomings of MEA are that it is easily degraded, more corrosive compared to other amines, and more heat energy consumed to regenerate.[5] Mass fraction of MEA was generally increased from 0.15 to 0.30 by 1970, and this has been standard since then.

DEA has been developed as an absorbent since 1950s. It has a lower vapor pressure, lower heat of reaction, less corrosive, but lower reaction rate compared to MEA.[6] Mass fraction of DEA used in industry can be increased to 0.55 so that acid gas load was increased and the circulation amount of absorbent was reduced.

Both primary and secondary alkanolamines will react with CO_2 and produce stable carbamate. Caplow[7] and Danckwerts[8] proposed the zwitterion mechanism for the reaction of primary and secondary alkanolamines with CO_2 which had been adopted by most of the researchers and proved to reconcile with their kinetics data. For this mechanism, CO_2 reacts with primary or secondary amine to form an unstable zwitterion. The proton in the zwitterion will be neutralized by a base B immediately. B can be H_2O, OH^- or amine. The reactions are given by:

$$CO_2 + R_1R_2NH \underset{k_{-1}}{\overset{k_2}{\rightleftharpoons}} R_1R_2NH^+COO^- \tag{2-1}$$

$$R_1R_2NH^+COO^- + B \underset{k_{-b}}{\overset{k_b}{\rightleftharpoons}} R_1R_2NCOO^- + BH^+ \tag{2-2}$$

Here R_1 is CH_2CH_2OH and R_2 is H for MEA, R_1 and R_2 are both CH_2CH_2OH for DEA.

The general reaction rate of CO_2 with primary or secondary amine based on the zwitterion mechanism were derived by:[9-11]

$$r = \frac{k_2[CO_2][R_1R_2NH] - k_{-1}[R_1R_2NCOO^-](\sum k_{-b}[BH^+]/\sum k_b[B])}{1 + k_{-1}/\sum k_b[B]} \tag{2-3}$$

A simple second order kinetics for MEA-CO_2 reaction was proposed:[8]

$$r_{CO_2-MEA} = k_2[CO_2][R_1R_2NH] \tag{2-4}$$

While for DEA-CO_2 reaction, the reaction rate was simplified as:[12]

$$r_{CO_2-DEA} = k_2[CO_2][R_1R_2NH](\sum k_b[B])/k_{-1} \tag{2-5}$$

b) Reaction mechanism between tertiary amine MDEA and CO_2

Aqueous MDEA solution has good thermal stability, large absorption capacity and lower regeneration energy consumption.[13] Furthermore, it is not easy to degrade and almost non-

corrosive to equipment.[14] Hence, MDEA has been widely used to capture CO_2 after 1980s. The disadvantages of MDEA as an absorbent are that it has relatively low absorption rate with CO_2 and high solvent cost.

CO_2 is absorbed by aqueous MDEA solution both physically and chemically. Due to the fact that there is no active hydrogen atom attached to the nitrogen bond, MDEA cannot directly react with CO_2. MDEA has played a catalytic role of CO_2 hydrolysis. The reactions are as follows:

$$CO_2 + H_2O \rightarrow H^+ + HCO_3^- \quad (2\text{-}6)$$

$$H^+ + (C_2H_4OH)_2NCH_3 \rightarrow (C_2H_4OH)_2NCH_4^+ \quad (2\text{-}7)$$

The MDEA-CO_2 reaction was assumed to be a pseudo-first-order reaction in most literature as follows:[9, 15, 19]

$$r_{CO_2-MDEA} = k_2[CO_2][MDEA] \quad (2\text{-}8)$$

c) Kinetics data

Some representative kinetics data on the reaction between CO_2 and aqueous MEA, DEA and MDEA solutions in the literature were summarized in Table 2-3.

Table 2-3. Literature Kinetics Data on the Reaction between CO_2 and Amine Solution.

Reference	Amine	[amine] ($mol \cdot l^{-1}$)	T (K)	k_2 ($l \cdot mol^{-1} \cdot s^{-1}$)	Experimental method
Danckwert and Sharma[16] (1966)	MEA	1.0	291	5100	Laminar jet absorber
	MEA	1.0	298	7600	Laminar jet absorber
	MEA	1.0	308	13000	Laminar jet absorber
Leder[17] (1971)	MEA	-	353	90400	Stirred cell reactor
Hikita et al.[18] (1977)	MEA	0.02-0.18	278.6-308.4	$9.77\times10^{10}\cdot\exp(-4955/T)$	Rapid mixing method
Donaldson and Nguyen[19] (1980)	MEA	0.03-0.08	298	6000	Membranes method
Penny and Ritter[2] (1983)	MEA	0-0.06	278-303	$1.23\times10^{11}\cdot\exp(-5078/T)$	Stopped flow method
Horng and Li[21] (2002)	MEA	0.1-0.5	303-313	$3.014\times10^{11}\cdot\exp(-5376.2/T)$	Wetted wall column
Versteeg and van Swaaij[12] (1988)	DEA	-	293-303	$\ln k_2 = pK_a + 23.17 - (7188/T)$	Stirred cell reactor
Littel et al.[22] (1990)	MDEA	0.1-3	293-333	$1.34\times10^{9}\cdot\exp(-5771/T)$	Stirred cell reactor
Ko and Li[23] (2000)	MDEA	1.0-2.5	303-313	$4.01\times10^{11}\cdot\exp(-5400/T)$	Wetted wall column

2.2 Mass transfer between gas-liquid phases

One target of this work is to understand the mass transfer behavior between CO_2 and liquid droplets in order to provide the foundation for the optimization design of the spray column. Hence as the background knowledge, the fundamental mass transfer theories, mass transfer mechanisms between liquid droplets and continuous phase, as well as the mass transfer coefficient correlation in the spray column are introduced in this section.

2.2.1 Three fundamental mass transfer theories

CO_2 absorption by amine solutions is the gas-liquid mass transfer process. Three common gas-liquid mass transfer models were introduced below.

a) Two film theory

Lewis and Whitman had put forward the two film theory in 1924.[24] The key points of the two film theory are as follows:

(1) There exist stagnant gas film and liquid film on both sides of the gas-liquid two-phase interface. The solute can only pass through these two films by molecular diffusion.

(2) The mass transfer resistance of each phase is concentrated in this imaginary film. The resistance in the turbulent zone outside the film can be ignored.

(3) The gas-liquid phases reach equilibrium at the interface. The total mass transfer resistance is the sum of the resistance in the two films.

According to the two film theory, the mass transfer coefficient can be presented as:

$$k = \frac{D}{l} \tag{2-9}$$

Here k is the mass transfer coefficient, D is the diffusion coefficient and l is the thickness of the film. Because l is unknown, k cannot be derived from the model itself. This model is suitable for the mass transfer without any obvious disturbance at the interface. However the correlation that k is proportional to D does not comply with the experimental results.

b) Solute penetration theory

Higbie proposed the solute penetration model in 1935 which considers the transition time for forming the concentration gradient.[25] The solute permeates from the interface to depth direction in the liquid film gradually during this transition time. At the initial stage, the gas-

liquid contact time is very short, the penetration of the solute is also shallow, and therefore the instantaneous concentration gradient at the interface is very large. As the contact time increases, the penetration depth of the solute increases, the concentration gradient and the mass transfer rate decrease.

In the penetration theory, the time average mass transfer coefficient can be presented as:

$$k = 2\sqrt{D v_{max} / \pi L} \tag{2-10}$$

Here v_{max} is the interfacial velocity of the liquid. L is the length of the exposed film. The quantity L/v_{max} is the contact time of gas-liquid phases which is also not known a priori.

c) Surface renewal theory

Danckwerts proposed the surface renewal theory in 1951 which considers that some swirl in a turbulent fluid can directly move between the interface and the turbulent bulk.[26] Therefore the surface of the liquid can be renewed continually by a liquid unit that moved from the turbulent zone. The replacement of the liquid units at the surface is random. These liquid units absorb solutes from the gas by the the non-steady state diffusion.

The mass transfer coefficient in the surface renewal theory can be deduced as:

$$k = \sqrt{D/\tau} \tag{2-11}$$

Here τ is a characteristic constant which means an average residence time for an element in the interfacial region.[27]

The graphic descriptions of these three mass transfer theories were given in Figure 2-2. The two film theory was used in the mass transfer characteristic study of CO_2 absorption by liquid droplets in this work.

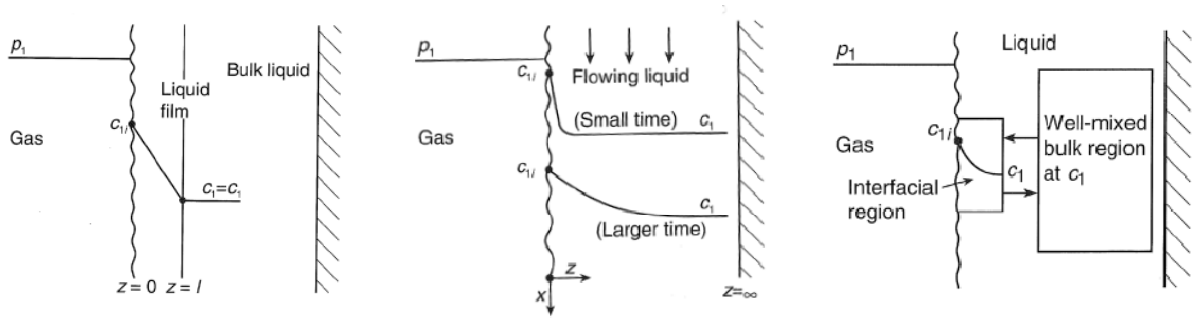

(a) Two film theory (b) Solute penetration theory (c) Surface renewal theory

Figure 2-2. The graphic descriptions of gas-liquid mass transfer theories.[27]

2.2.2 Mass transfer mechanisms between liquid droplets and continuous phase

Mass transfer into liquid droplets has been widely used in industrial processes, such as absorption and extraction, because it increases the contact area and improves the mass transfer efficiency. In the absorption process, the dispersed phase is liquid droplets and the continuous phase is gas. While in the extraction process, the dispersed phase is liquid droplets and the continuous phase is also liquid. Previous authors proposed the mass transfer mechanisms of liquid droplets for both absorption and extraction. The logarithm fraction unabsorbed or unextracted as a function of time during drop movement corresponding to different mass transfer mechanisms were summarized below.

a) Mass transfer mechanism of gas absorption by a falling droplet

Hatta and Baba[28] proposed the theoretical formulas for gas absorption by a falling drop in accordance with three different assumptions. The formulas were summarized in Table 2-4.

Table 2-4. Mass Transfer Mechanisms of Gas Absorption by a Falling Drop Proposed by Hatta and Baba[28].

Case	Assumption	Formula
1	No damping of turbulence in the drop during fall	$-\ln(1-C/C_s)=6k_Lt/d$
2	Gradual damping of turbulence during drop fall	$k_L=\alpha e^{-\beta t}$ * $-\ln(1-C/C_s)=6\alpha(1-e^{-\beta t})/(d\beta)$
3	Perfect damping at the start of drop fall, i.e., no turbulence during drop fall	$q=4Dt/d^2$ $C/C_s=6\sqrt{q}/\sqrt{\pi}-3q$

*: α, β are constants

Since other researchers found out that there exists turbulence during the drop formation, they made these assumptions under the consideration of whether the turbulence is damping during drop fall. In the formulas, C is the concentration of gas in the liquid bulk, C_s is the saturated concentration, k_L is the liquid phase mass transfer coefficient, t is the absorption time, d is the diameter of droplet and D is the diffusion coefficient.

b) Mass transfer mechanism for drop movement in liquid-liquid extraction

Licht and Pansing[29] summarized the mechanisms of solute transfer for drop movement in liquid-liquid extraction as shown in Table 2-5.

Table 2-5. Mass Transfer Mechanisms for Drop Movement in Liquid-liquid Extraction[29].

Case	Mechanisms	Slope log(1-*E*) vs. *t*
1	Two-film	$-2.61\frac{K_d}{d}$
2	Diffusion within drop	$-17.15\frac{D_d}{d^2}$
3	Diffusion within drop plus film resistance	$-\frac{\alpha^2 D_d}{2.303}$
4	Streamline convection within drop	$-46.8\frac{D_d}{d^2}$
5	Transient films	$-2.95\sqrt{\frac{D_c u_d}{d^3}}\frac{f_c}{(\sqrt{\frac{D_c}{D_d}}+\frac{C_d}{C_c})}$
6	Interfacial resistance	$-\frac{0.83}{Rd^3}$

Here E is the solute extracted fraction, log(1-E) is the logarithm fraction unextracted, t is the extraction time, K is the over-all mass transfer coefficient, D is the diffusion coefficient, d is the diameter of drop, α is constant, v is the velocity of drop, f_c is a factor relating the lifetime of transient film, C is the concentration and R is the interfacial resistance. The subscripts d and c mean dispersed phase and continuous phase, respectively. The first mechanism assumes that the mass transfer resistance exists in the liquid film and gas film. The slope of log(1-E) versus t is proportional to 1/d for case 1. The second mechanism

assumes that the mass transfer resistance is caused by pure diffusion within the drop and negligible in the continuous phase. The slope of log(1-E) versus t is proportional to $1/d^2$ for case 2. The third mechanism supposes that the mass transfer resistance exists in both two films and the diffusion within drop. The slope of log(1-E) versus t is constant for case 3. The fourth mechanism assumes that there exists streamline currents within the drop which results from the drag by the continuous phase.[30] Mass transfer among streamline currents is caused by molecular diffusion. The slope of log(1-E) versus t is proportional to $1/d^2$ for case 4. The fifth mechanism is proposed by applying Higbie's solute penetration theory for gas absorption to liquid-liquid extraction. It assumes that there exists a transient film which forms on the surface of the drop and then moves through the surface into the drop bulk with solute depleted or enriched.[31] The slope of log(1-E) versus t is proportional to $\sqrt{v/d^3}$ for case 5. The sixth mechanism assumes that there exists an undefined interfacial resistance between the dispersed and continuous phase. In addition, the concentrations of the drop bulk and the continuous phase are both uniform. The slope of log(1-E) versus t is proportional to $1/d^3$ for case 6. Noteworthily, the formula for the first assumption in the gas absorption that no damping of turbulence in the drop during fall has the same form as the two films mass transfer mechanism in liquid-liquid extraction.

2.2.3 Mass transfer coefficient in the spray column

Hong et al.[32] deduced the correlation for volumetric mass transfer coefficient of droplet swarm in the spray column on the basis of a single droplet mass transfer equation combined with the movement features of droplet swarm:

$$K_y a = 2.320\times10^{-4} H_L d_s^{-1.2152} z^{-0.778} \times \left(\frac{u_d}{H_L} - \frac{u_c}{1-H_L}\right)^{0.7848} \quad (2\text{-}12)$$

Here $K_y a$ is the gas phase volumetric mass transfer coefficient, H_L is the liquid holdup, d_s is the Sauter mean diameter of droplet swarm, z is the column height, u_d is the apparent velocity of the droplet phase and u_c is the apparent velocity of the continuous phase.

2.3 Physical properties of amine solutions

Physical properties, such as density, viscosity, surface tension, solubility, and diffusivity, are very important for simulating and designing the absorption-desorption process. An

overview of these properties is presented in this section. The measuring methods and the correlation models are summarized. In our group, the density and surface tension of amine solutions were measured by me. While, the other two Ph.D candidates measured the viscosity, solubility and diffusivity of amine solutions.

2.3.1 Density, viscosity and surface tension

The density, viscosity and surface tension of unloaded aqueous amine solutions and CO_2 loaded aqueous amine solutions are needed for engineering calculations. The density, viscosity and surface tension of these solutions are affected by temperature, concentration and CO_2 loading. The density can be measured by various methods such as hydrometer, pycnometer and Anton Paar densimeter. Anton Paar densimeter which uses the oscillating U-tube technique has been most widely applied to measure densities of amine solutions by the researchers because it has a high accuracy and a large measuring range of temperature and viscosity. The viscosity can be measured by various types of viscometer and rheometer using the capillary method, falling sphere method, the rotating method and the oscillating method. The surface tension can be measured by various types of stalagmometer, tensiometer and goniometer using the capillary-rise technique, Du Noüy ring method, Wilhelmy plate principle and pendant/sessile drop method.

Densities of binary systems of amine + water can be correlated by a Redlich-Kister equation.[33] Excess molar volumes of the binary systems are derived to be used in the fitting equation as follows:

$$V_m{}^E = x_2(1-x_2)\sum_{j=0}^{i} A_j(1-2x_2)^j \tag{2-13}$$

Here A_j are adjustable parameters, and i represents an integer varying from 1 to how big a number can be justified by the data.

Molar volumes of the mixture need to be calculated to analyse the density of CO_2 loaded aqueous amine solutions. Densities of ternary systems of amine + water + CO_2 can be correlated by eqs 2-14 and 2-15 as suggested by Weiland et al.[34]:

$$V_m = x_1V_1 + x_2V_2 + x_3V_{CO_2} + x_1x_2V^* + x_2x_3V^{**} \tag{2-14}$$

$$V^{**} = c + dx_2 \tag{2-15}$$

Here V_{CO2}, V^*, c and d are free parameters.

The correlated parameters in eqs 2-13 to 2-15 A_j, V_{CO2}, V^*, c and d can in turn be fitted to the polynomial function of temperature.

Viscosities of binary systems of amine + water can be correlated by eq 2-16 as proposed by Teng et al.[35]:

$$\ln \mu_m = \ln \mu_1 + \sum_{j=0}^{i} a_j w_2^{\ j} \tag{2-16}$$

Here a_j are adjustable parameters which depend on the suitable order of the polynomial. The correlated parameters a_j can be in turn fitted to the polynomial function of temperature.

In addition, the Redlich-Kister equation[33] for thermodynamic property correlation can also be used to fit the viscosity of unloaded aqueous amine solutions. Excess kinematic viscosity can be calculated by:

$$\delta \nu_m^{\ E} = \ln \nu_m - (x_1 \ln \nu_1 + x_2 \ln \nu_2) \tag{2-17}$$

Here v_m is the measured kinetics viscosity of the mixture. Then the derived excess kinematic viscosity can be used in the fitting equation as follows:

$$\delta \nu_m^{\ E} = x_2(1-x_2)\sum_{j=0}^{i} A_j (1-2x_2)^j \tag{2-18}$$

The adjustable parameters A_j may have the following temperature-dependence:

$$A_j = a_j + \frac{b_j}{T + c_j} \tag{2-19}$$

Viscosities of ternary systems of amine + water + CO_2 can be correlated by eq 2-20 as suggested by Weiland et al.[34]:

$$\frac{\mu}{\mu_1} = \exp\left(\frac{[(aw_2 + b)T + (cw_2 + d)][\alpha(ew_2 + fT + g) + 1]w_2}{T^2}\right) \tag{2-20}$$

Here a, b, c, d, e, f and g are the fitting parameters.

An empirical correlation model for estimating the surface tension of unloaded and CO_2 loaded aqueous amine solutions is suggested by Norbert Asprion[36]:

$$\gamma_m = \gamma_1 + \sum_{i\geq 2} \frac{S_i x_i}{1+\sum_{j\geq 2}^{i} (S_j\text{-}1)x_j} (\gamma_i - \gamma_1) \tag{2-21}$$

The prediction of chemical model of Connors and Wright[37] also shows good agreement with surface tensions of amine solutions:

$$\gamma_m = \gamma_1 + \sum_{i\geq 2}(1 + \frac{a_i x_1}{(1-b_i)(1+\sum_{j\geq 2}^{i}\frac{b_j}{(1-b_j)}x_j)})x_i(\gamma_i - \gamma_1) \quad (2\text{-}22)$$

The correlated parameters are S_i, a_i and b_i in eqs 2-21 and 2-22.

2.3.2 Solubility and diffusivity

The solubility and diffusivity of CO_2 in aqueous amine solutions at various temperatures and amine concentrations are very important for reaction kinetics study and engineering calculations. The physical solubility of gas phase in liquid phase can be presented by Henry's law:

$$H = \frac{P}{C_e} \quad (2\text{-}23)$$

Here H is the Henry's coefficient, P is the partial pressure of gas, and C_e is the equilibrium concentration of gas in liquid.

Because CO_2 will react with amine solutions, the solubility and diffusivity of CO_2 in aqueous amine solutions cannot be directly measured. An N_2O analogy method is generally used to measure the solubility and diffusivity of CO_2 in amine solutions since N_2O has the similar molecular structure and the same molecular weight as CO_2, while it does not react with amine solutions.[12, 38] The N_2O analogy equations are as follows:

$$H_{CO_2} = H_{N_2O}(H_{CO_2}/H_{N_2O})_{water} \quad (2\text{-}24)$$

$$D_{CO_2} = D_{N_2O}(D_{CO_2}/D_{N_2O})_{water} \quad (2\text{-}25)$$

Here H_{CO_2} and H_{N_2O} are Henry's coefficient of CO_2 and N_2O in amine solutions, D_{CO_2} and D_{N_2O} are the diffusivity of CO_2 and N_2O in amine solutions respectively. The solubility and diffusivity of N_2O in amine solutions at different temperatures and concentrations will be directly measured. $(H_{CO_2}/H_{N_2O})_{water}$ and $(D_{CO_2}/D_{N_2O})_{water}$ can be got by experiments or using the previous authors' correlation results as shown in eqs 2-26 to 2-29. Therefore, the solubility and diffusivity of CO_2 in amine solutions can be calculated by eqs 2-24 and 2-25.

The dependence of solubility and diffusivity of CO_2 and N_2O in water with temperature were developed by Versteeg and van Swaaij[39]:

$$(H_{CO_2})_{water} = 2.82\times10^{6}\exp(\frac{-2044}{T}) \tag{2-26}$$

$$(H_{N_2O})_{water} = 8.55\times10^{6}\exp(\frac{-2284}{T}) \tag{2-27}$$

$$(D_{CO_2})_{water} = 2.35\times10^{-6}\exp(\frac{-2119}{T}) \tag{2-28}$$

$$(D_{N_2O})_{water} = 5.07\times10^{-6}\exp(\frac{-2371}{T}) \tag{2-29}$$

The physical solubility of N_2O in amine solutions can be measured by either the volumetric method or the pressure drop method. The fitting equations of the solubility of N_2O in amine solutions are as follows:[40]

$$\delta H_m{}^{E} = \ln H_{N_2O} - (w_1 \ln H_1 + w_2 \ln H_2) = w_1 w_2 A_i \tag{2-30}$$

$$A_i = \sum_{j=0}^{i} a_j (T - 273.15)^j + b w_2 \tag{2-31}$$

Here i represents an integer varying from 1 to how big a number that can be justified by the measured data.

The diffusivity of N_2O in amine solutions can be measured by laminar jet absorber, stirred cell reactor and wetted wall column, etc. The fitting equation of the diffusivity of N_2O in amine solutions is:[41]

$$D_{N_2O} = (a_0 + a_1 C + a_2 C^2)\times\exp(\frac{a_3 + a_4 C}{T}) \tag{2-32}$$

Here a_0, a_1, a_2, a_3 and a_4 are the fitting parameters.

Notation

α	constant in serious solution
C	concentration, mol/m^3
d	droplet diameter, m
d_s	sauter mean diameter of droplet swarm, m
D	diffusion coefficient, m^2/s
E	fraction solute extracted
f_c	correlation factor for transient film mechanism

H	Henry's coefficient, Pa·m^3/mol
H_L	liquid holdup, m^3/m^3
k	mass transfer coefficient, m/s
k_2	forward second order reaction rate constant, l/(mol·s)
k_{-1}	backward first order reaction rate constant, l/(mol·s)
k_b	forward second order reaction rate constant for base B, l/(mol·s)
k_{-b}	reverse second order reaction rate constant for base B, l/(mol·s)
K	over-all mass transfer coefficient, m/s
$K_y a$	gas phase volumetric mass transfer coefficient, mol/(m^3·s)
l	thickness of the film, m
L	length of the exposed film, m
P	pressure, Pa
r	rate of reaction, mol/(l·s)
R	undefined interfacial resistance
t	time, s
T	temperature, K
u_d	apparent velocity of the droplets, m/s
u_c	apparent velocity of the continuous phase, m/s
v	kinematic viscosity, m^2/s
v_{max}	interfacial velocity of the liquid, m/s
V	molar volume, m^3/mol
V_m^E	excess molar volume of the mixture, m^3/mol
w	mass fraction
x	mole fraction
z	column height, m
[ ]	concentration, mol/l

Greek letters

α	CO_2 loading, moles of CO_2/moles of amine
γ	surface tension, N/m
δH_m^E	excess Henry's coefficient, Pa·m^3/mol
δv_m^E	excess kinematic viscosity, m^2/s
μ	dynamic viscosity, kg/(m·s)
τ	characteristic constant in surface renewal theory, s

Subscripts

1	water
2	amine
3	CO_2
c	continuous phase
d	dispersed phase (droplet)
e	equilibrium
L	liquid phase
m	mixture
s	saturation

References

(1) Kohl, A.; Riesenfeld, F. *Gas Purification*; Gulf Pub Co: Houston, 1985.

(2) Tan, L. S.; Shariff, A. M.; Lau, K. K.; Bustam, M. A. Factors Affecting CO_2 Absorption Efficiency in Packed Column: A Review. *J. Ind. Eng. Chem.* **2012**, *18*, 1874-1883.

(3) Mandal, B. P.; Kundu, M.; Bandyopadhyay, S. S. Density and Viscosity of Aqueous Solutions of (N-Methyldiethanolamine + Monoethanolamine), (N-Methyldiethanolamine + Diethanolamine), (2-Amino-2-methyl-1-propanol + Monoethanolamine), (2-Amino-2-methyl-1-propanol + Diethanolamine). *J. Chem. Eng. Data* **2003**, *48*, 703-707.

(4) Pellegrini, G.; Strube, R.; Manfrida, G. Comparative Study of Chemical Absorbents in Post combustion CO_2 Capture. *Energy* **2010**, *35*, 851-857.

(5) Bai, H. Comparison of Ammonia and Monoethanolamine Solvents to Reduce CO_2 Greenhouse Gas Emissions. *Sci. Total Environ.* **1999**, *228*, 121-133.

(6) Mokhatab, S.; Poe, W. A. *Handbook of Natural Gas Transmission and Processing*; Gulf Pub Co: Waltham, 2012.

(7) Caplow, M. Kinetics of Carbamate Formation and Breakdown. *J. Am. Chem. Soc.* **1968**, *90*, 6795-6803.

(8) Danckwerts, P. V. The Reaction of CO_2 with Ethanolamines. *Chem. Eng. Sci.* **1979**, *34*, 443-446.

(9) Blauwhoff, P. M. M.; Versteeg, G. F.; Van Swaaij, W. P. M. A Study on the Reaction between CO_2 and Alkanolamines in Aqueous Solutions. *Chem. Eng. Sci.* **1984**, *39*, 207-225.

(10) Glasscock, D. A.; Critchfield, J. E.; Rochelle, G. T. CO_2 Absorption/Desorption in Mixtures of Methyldiethanolamine with Monoethanolamine or Diethanolamine. *Chem. Eng. Sci.* **1991**, *46*, 2829-2845.

(11) Versteeg, G. F.; Van Dijck, L. A. J.; Van Swaaij, W. P. M. On the Kinetics between CO_2 and Alkanolamines Both in Aqueous and Non-Aqueous Solutions, an Overview. *Chem. Eng. Comm.* **1996**, *144*, 133-158.

(12) Versteeg, G. F.; Van Swaaij, W. P. M. On the Kinetics between CO_2 and Alkanolamines both in Aqueous and Non-aqueous Solutions - I. Primary and Secondary Amines. *Chem. Eng. Sci.* **1988**, *43*, 573-585.

(13) Jou, F. Y.; Mather, A. E.; Otto, F. D. Solubility of Hydrogen Sulfide and Carbon Dioxide in Aqueous Methyldiethanolamine Solutions. *Ind. Eng. Chem. Process Des. Dev.* **1982**, *21*, 539-544.

(14) Shen, K.; Li, M. Solubility of Carbon Dioxide in Aqueous Mixtures of Monoethanolamine with Methyldiethanolamine. *J. Chem. Eng. Data* **1992**, *37*, 96-100.
(15) Versteeg, G. F.; Van Swaaij, W. P. M. On the Kinetics between CO_2 and Alkanolamines both in Aqueous and Non-aqueous Solutions – II. Tertiary Amines. *Chem. Eng. Sci.* **1988**, *43*, 587-591.
(16) Danckwerts, P. V.; Sharma, M. M. The Absorption of Carbon Dioxide into Solutions of Alkalis and Amines. *Chem. Eng.* **1966**, *10*, CE244-CE280.
(17) Leder, F. The Absorption of CO_2 into Chemically Reactive Solutions at High Temperature. *Chem. Eng. Sci.* **1971**, *26*, 1381-1390.
(18) Hikita, H.; Asai, S.; Ishikawa, H.; Honda, M. The Kinetics of Reaction of Carbon Dioxide with Monoethanolamine, Diethanolamine and Triethanolamine by a Rapid Mixing Method. *Chem. Eng. J.* **1977**, *13*, 7-12.
(19) Donaldson, T. L.; Nguyen, Y. N. Carbon Dioxide Reaction Kinetics and Transport in Aqueous Amine Membranes. *Ind. Eng. Chem. Fund.* **1980**, *19*, 260-266.
(20) Penny, D.; Ritter, T. Kinetics Study of Reaction between Carbon Dioxide and Primary Amines. *J. Chem. Soc., Faraday Trans.* **1983**, *79*, 2103-2109.
(21) Horng, S.; Li, M. Kinetics of Absorption of Carbon Dioxide into Aqueous Solutions Monoethanolamine + Triethanolamine. *Ind. Eng. Chem. Res.* **2002**, *41*, 257-266.
(22) Littel, R. J.; Van Swaaij, W. P. M.; Versteeg, G. F. Kinetics of Carbon Dioxide with Tertiary Amines in Aqueous Solution. *A.I.C.h.E. J.* **1990**, *36*, 1633-1640.
(23) Ko, J.; Li, M. Kinetics of Absorption of Carbon Dioxide into Solutions of N-methyldiethanolamine + water. *Chem. Eng. Sci.* **2000**, *55*, 4139-4147.
(24) Lewis, W. K.; Whitman, W. G. Principles of Gas Absorption. *Ind. Eng. Chem. Res.* **1924**, *16*, 1215-1220.
(25) Higbie, R. The Rate of Absorption of a Pure Gas into a Still Liquid during Short Periods of Exposure. *Trans. A. Inst. Chem. Eng.* **1935**, *31*, 365-383.
(26) Danckwerts, P. V. Significance of Liquid-film Coefficient in Gas Absorption. *Ind. Eng. Chem. Res.* **1951**, *43*, 1460-1467.
(27) Cussler, E. L. *Diffusion — Mass Transfer in Fluid Systems*; Cambridge University Press: New York, 2009.
(28) Hatta, S.; Baba, A. A Theoretical Study on the Liquid-Side Resistance against the Gas Absorption by a Liquid Drop. *J. Soc. Chem. Ind.* **1935**, *38*, 544-546.
(29) Licht, W.; Pansing, W. F. Solute Transfer from Single Drops in Liquid-Liquid Extraction. *Ind. Eng. Chem.* **1953**, *45*, 1885-1896.

(30) Kronig, R.; Brink, J. C. On the Theory of Extraction from Falling Droplets. *Appl. Sci. Research* **1950**, *2*, 142-154.

(31) West, F. B.; Robinson, P. A.; Morganthaler, A. C.; Beck, T. R.; Mcgregor, D. K. Liquid-Liquid Extraction from Single Drops. *Ind. Eng. Chem.* **1951**, *43*, 234-238.

(32) Hong, D.; Long, J.; Jiang, S.; Zhou, X. Mass Transfer in the Spray Column. *J. Chem. Eng.* (*China*) **1989**, *17*, 26-32.

(33) Redlich, O.; Kister, A. T. Algebraic representation of thermodynamic properties and the classification of solutions. *Ind. Eng. Chem.* **1948**, *40*, 345-348.

(34) Weiland, R. H.; Dingman, J. C.; Cronin, D. B.; Browning, G. J. Density and Viscosity of Some Partially Carbonated Aqueous Alkanolamine Solutions and Their Blends. *J. Chem. Eng. Data* **1998**, *43*, 378-382.

(35) Teng, T. T.; Maham, Y.; Helper, L. G.; Mather, A. E. Viscosity of Aqueous Solutions of N- Methyldiethanolamine and Diethanolamine. *J. Chem. Eng. Data* **1994**, *39*, 290-293.

(36) Asprion, N. Surface Tension Models for Aqueous Amine Blends. *Ind. Eng. Chem. Res.* **2005**, *44*, 7270-7278.

(37) Connors, K. A.; Wright, J. L. Dependence of Surface Tension on Composition of Binary Aqueous-Organic Solutions. *Anal. Chem.* **1989**, *61*, 194-198.

(38) Saha, A. K.; Bandyopadhyay, S. S.; Biswas, A. K. Solubility and Diffusivity of N_2O and CO_2 in Aqueous Solutions of 2-Amino-2-methyl-1-propanol. *J. Chem. Eng. Data* **1993**, *38*, 78-82.

(39) Versteeg, G. F.; van Swaaij, W. P. M. Solubility and Diffusivity of Acid Gases (CO_2, N_2O) in Aqueous Alkanolamine Solutions. *J. Chem. Eng. Data* **1988**, *33*, 29-34.

(40) Jiru, Y.; Eimer, D. A.; Wenjuan, Y. Measurements and Correlation of Physical Solubility of Carbon Dioxide in (Monoethanolamine + water) by a Modified Technique. *Ind. Eng. Chem. Res.* **2012**, *51*, 6958-6966.

(41) Ko, J.; Tsai, T.; Lin, C.; Wang, H.; Li, M. Diffusivity of Nitrous Oxide in Aqueous Alkanolamine Solutions. *J. Chem. Eng. Data* **2001**, *46*, 160-165.

3. Density measurements of amine solutions

Abstract

Densities in liquid solutions of water + monoethanolamine (MEA), water + diethanolamine (DEA) and water + N-methyldiethanolamine (MDEA) have been measured at temperatures from (298.15 to 423.15) K. The mass fraction of amine ranged from 0.3 to 1.0. Excess molar volumes of the binary system were derived and correlated by a Redlich-Kister equation. The model uses a third order Redlich-Kister equation and a linear relationship with the temperature for unloaded aqueous MEA solutions, while a fourth order Redlich-Kister equation and a second polynomial function with respect to the temperature for unloaded aqueous DEA and MDEA solutions.

Densities of CO_2 loaded aqueous MEA solutions (water + MEA + CO_2) were measured at temperatures from (298.15 to 413.15) K. The mass fraction of MEA in water was 0.3, 0.4, 0.5 and 0.6. Densities in liquid solutions of water + DEA + CO_2 and water + MDEA + CO_2 were measured at temperatures from (298.15 to 423.15) K. The mass fraction of DEA and MDEA in water was 0.3 and 0.4. The CO_2 loading ranged from 0.1 to 0.5. Molar volumes of the ternary system were derived and correlated by the equation from Weiland et al. at each temperature. The parameters were in turn fitted by a polynomial function of the temperature.

3.1 Introduction

One of the methods for removing CO_2 from the flue gas streams is the use of absorption and aqueous alkanolamine solutions as absorbents. Alkanolamines such as monoethanolamine (MEA), diethanolamine (DEA) and N-methyldiethanolamine (MDEA) are widely used in CO_2 capture. Physical properties such as density of the pure compounds of amines, the mixtures with water and CO_2 loaded aqueous amine solutions are important for designing absorption-desorption processes. Density (ρ) is defined as mass per unit volume; the unit is kg/m^3.

Density data for unloaded aqueous MEA solutions have previously been reported by a number of authors. These are summarized in Table 3-1 where ranges of concentrations and temperatures investigated are given for each source. There is also information on the number

of points measured and the method used by all authors. Apart from those works summarised in Table 3-1, it is known that Weiland et al.[11] refer to unpublished data transmitted to the Gas Processors Association in 1993. These data have not been accessed here. Literature values cover all the composition range up to 353.15 K.

Table 3-1. Reported Liquid Density Measurements of Water (1) + MEA (2).

Source	w_2		T/K		Number of measurements	Method*
	Low	High	Low	High		
Leibush et al.[1] (1947)	0.2	1.0	283.15	353.15	40	Pyc
Touhara et al.[2] (1982)	0	1.0	298.15	298.15	14	Pyc
Murrieta-Guevara et al.[3] (1984)	1.0	1.0	298.15	333.15	8	Sod
Wang et al.[4] (1984)	1.0	1.0	293.15	361.15	5	Pyc
Li et al.[5] (1992)	0.3	1.0	303.15	353.15	16	Pyc
DiGullio et al.[6] (1992)	1.0	1.0	294.15	431.15	8	Pyc
Pagé et al.[7] (1993)	0	1.0	283.15	313.15	69	Sod
Maham et al.[8] (1994)	0	1.0	298.15	353.15	110	AP
Li et al.[9] (1994)	0.2	1.0	303.15	353.15	12	Pyc
Lee et al.[10] (1995)	0.27	1.0	303.15	323.15	30	Pyc
Weiland et al.[11] (1998)	0.1	0.4	298.15	298.15	4	Hyd
Mandal et al.[12] (2003)	0.3	0.3	293.15	323.15	7	Pyc
Pouryosefi and Idem[13] (2008)	0	1.0	295.15	333.15	88	AP
Amundsen et al.[14] (2009)	0.2	1.0	298.15	353.15	35	AP
Present work	0.3	1.0	298.15	423.15	160	AP

*AP: Anton Paar (Oscillating) / Hyd: Hydrometer / Pyc: Pycnometer / Sod: Sodev (Oscillating)

Maham et al.[8] measured densities of unloaded aqueous DEA solutions at temperatures from (298.15 to 353.15) K and mole fractions of DEA from 0 to 1 by the Anton Paar DMA 45 densimeter. Their tabulated value of pure DEA density at 298.15 K had been estimated by extrapolation of the densities of pure liquid DEA at high temperatures. Rinker et al.[15] measured densities of unloaded aqueous DEA solutions at temperatures from (293.15 to 373.15) K and mole fractions of DEA from 0.1 to 0.3 by 25 cm^3 (at 20 °C) pycnometers of the Gay-Lussac type. Spasojević et al.[16] measured densities of unloaded aqueous DEA solutions at temperatures from (298.15 to 343.15) K and mole fractions of DEA from 0.05 to 0.25 by the Anton Paar DMA 5000 densimeter. Murrleta-Guevara et al.[3] measured densities of pure DEA at temperatures from (298.15 to 333.15) K.

Rinker et al.[15] measured densities of unloaded aqueous MDEA solutions at temperatures from (333.15 to 373.15) K and mole fractions of MDEA from 0.1 to 0.5 by pycnometers. Pouryousefi and Idem[13] presented densities of unloaded aqueous MDEA solutions at temperatures from (295.15 to 333.15) K and mole fractions of MDEA from 0 to 1 by the Anton Paar densitometer DMA 4500/5000. Muhammad et al.[17] measured densities of unloaded aqueous MDEA solutions at temperatures from (298.15 to 338.15) K and mole fractions of MDEA from 0 to 1 by the Anton Paar density meter DMA 5000.

Densities of CO_2 loaded aqueous amine solutions are also important. However, few literatures were found as can be seen summarised in Table 3-2.

Table 3-2. Reported Liquid Density Measurements of Water (1) + Amine (2) + CO_2 (3).

Source	**Amine Type**	w_2		α		T/K		**Method***
		Low	High	Low	High	Low	High	
Weiland et al.[11] (1998)	MEA	0.1	0.4	0.05	0.5	298.15	298.15	Hyd
Weiland et al.[11] (1998)	DEA	0.1	0.4	0.05	0.5	298.15	298.15	Hyd
Weiland et al.[11] (1998)	MDEA	0.3	0.6	0.05	0.5	298.15	298.15	Hyd
Amundsen et al.[14] (2009)	MEA	0.2	0.4	0.1	0.5	298.15	353.15	AP
Present work	MEA	0.3	0.6	0.10	0.56	298.15	413.15	AP
Present work	DEA	0.3	0.4	0.1	0.5	298.15	423.15	AP
Present work	MDEA	0.3	0.4	0.1	0.5	298.15	423.15	AP

*AP: Anton Paar (Oscillating) / Hyd: Hydrometer

Densities of unloaded and CO_2 loaded aqueous amine solutions from the literature both cover the temperature range up to 353.15 K. Density data of unloaded and CO_2 loaded aqueous amine solutions at higher temperatures are required for designing the CO_2 desorption process and associated engineering calculations.

In the present work densities of unloaded aqueous MEA, DEA, and MDEA solutions with mass fractions of amine from 0.3 to 1.0 were measured from (298.15 to 423.15) K. Densities of CO_2 loaded aqueous MEA solutions were measured with mass fractions of MEA in water from 0.3 to 0.6 at (298.15 to 413.15) K. Densities of CO_2 loaded aqueous DEA and MDEA

solutions were measured at temperatures from (298.15 to 423.15) K, mass fractions of DEA or MDEA in water equal to 0.3 and 0.4. The temperature range that we measured covers data needed for engineering estimates related to the desorption part of the CO_2 capture process which previous investigations did not include. These measurements also represent an effort to cover densities for the full range of temperatures and compositions normally met when performing process engineering design estimates.

3.2 Experimental Section

3.2.1 Preparing amine solutions

Sample descriptions of pure amines and CO_2 are given in Table 3-3. Water was produced by a Milli-Q integral water purification system (18.2 MΩ-cm) which uses resin filters and deionization to purify the water.

Table 3-3. Chemical Sample Descriptions.

Chemical Name	Source	Initial Mole Fraction Purity	Purification Method	Final Mole Fraction Purity	Analysis Method
MEA[a]	Merck	0.995	none	-	GC[b]
DEA[c]	Sigma	0.98	none	-	GC
MDEA[d]	Sigma	0.98	none	-	GC
Carbon dioxide	AGA	0.9999	none	-	-

[a] Monoethanolamine [b] Gas-liquid chromatography
[c] Diethanolamine [d] N-methyldiethanolamine

3.2.1.1 Preparing unloaded aqueous amine solutions

Pure amine and Milli-Q water were degassed by a rotary evaporator before mixing. Rotavapor R-210/215 which consists of vacuum pump, cooling system, rotary glass flask and water bath was used in this experiment and shown in Figure 3-1. The specific number of mass of all the components was calculated based on the purity of different amines and given in Table 3-4. All samples (of approximately 100 g) were prepared using an analytical balance with an accuracy of ± 0.1 mg. The protective nitrogen gas was blown to the conical flask after the mixed solution was made to prevent the solution from absorbing CO_2 from the air.

Table 3-4. The Ideal Mass of Each Component in Different Mass Fraction of the Mixture.

	w_2						
	0.3	**0.4**	**0.5**	**0.6**	**0.7**	**0.8**	**0.9**
m_{MEA} [g]	30.1508	40.2010	50.2513	60.3015	70.3518	80.4020	90.4523
m_{DEA} [g]	30.6122	40.8163	51.0204	61.2245	71.4286	81.6327	91.8267
m_{MDEA} [g]	30.6122	40.8163	51.0204	61.2245	71.4286	81.6327	91.8267
mixture [g]	100	100	100	100	100	100	100

Figure 3-1. The rotary evaporator for degassing distilled water and pure amines.

3.2.1.2 Preparing CO_2 loaded aqueous amine solutions

a) Loading aqueous amine solutions with CO_2

A long glass column with 2 μm pore size sinter inside was used to make the CO_2 loaded aqueous amine solutions as shown in Figure 3-2. First the CO_2 gas valve was opened and the mass flow rate was set to 0.150 NL/min. Then unloaded aqueous amine solution was filled into the column through the top. When CO_2 is absorbed by the amine solution, bubbling is observed in the flask. A phase difference can be seen in the solution in the process of loading as shown in Figure 3-3. Since CO_2 diffuses slowly in the solution from bottom to top, the lower part of the solution is boiling because of the strong reaction and the upper part of the solution is calm. Therefore, the phase difference appears in the solution. The phase difference moves up very slowly, large bubbles are observed below and small bubbles above. The

reaction is much stronger below the phase difference because CO_2 comes from the bottom and most of it was absorbed by the solution below. There is also a temperature difference in the solution, higher temperature below the phase difference and lower temperature above because the reaction between amine solutions and CO_2 is exothermic. The process of loading aqueous amine solution with CO_2 is completed when the phase difference moves up to the top of the solution and disappears.

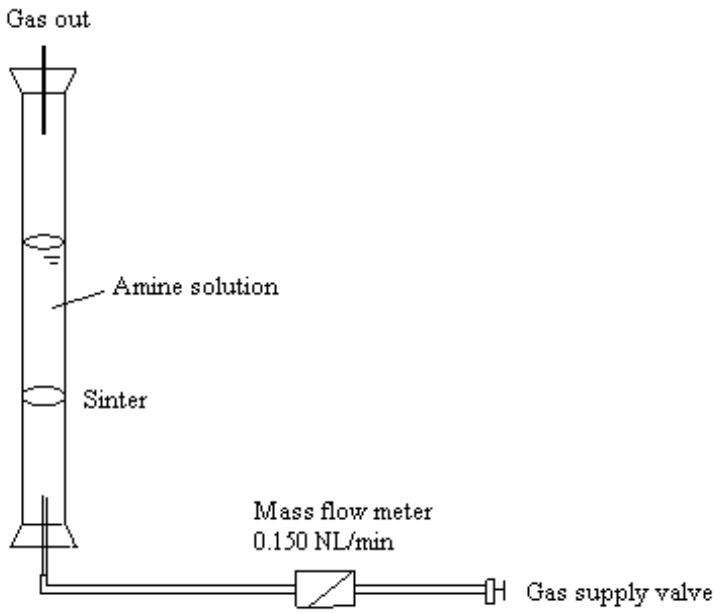

Figure 3-2. Equipment used to load amine solutions with CO_2.

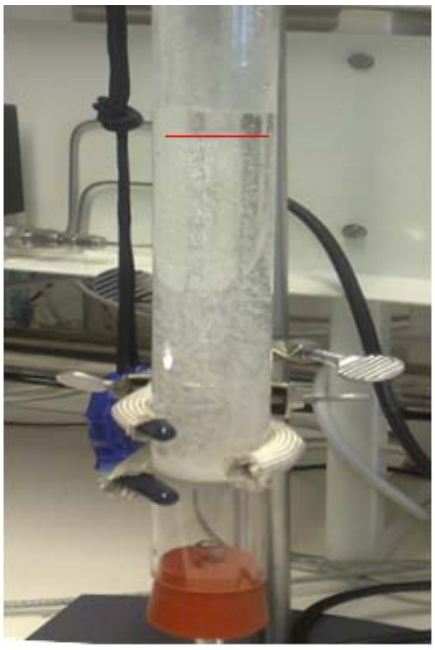

Figure 3-3. The phase difference in the amine solutions in the gas column.

b) Analyzing the mole number of CO_2 in the loaded amine solutions

The high loaded amine solutions were then analyzed by a method based on precipitation of $BaCO_3$ and titration. Titrator T50 (from Metler Toledo) is used in this experiment and shown in Figure 3-4. A sample of (0.05 to 0.1) g was mixed together with 41.7 mL 0.3 M $BaCl_2$ solution and 50 mL 0.1 M NaOH solution. This mixture was boiled for 4 to 5 minutes, cooled down in a bath and then filtered. The filter cake was added to 50 mL degassed, distilled water and then titrated with 0.1 M HCl solution to pH 2. The mixture was finally titrated with NaOH to pH 7 to calculate the amount of excess HCl.

Figure 3-4. Titrator T50 used for analyzing the amount of CO_2 in the loaded amine solutions.

Reactions 3-1 to 3-3 present the chemistry of the analysis.

$$Ba^{2+} + CO_2 + 2OH^- \rightarrow BaCO_3 + H_2O \quad (3\text{-}1)$$

$$BaCO_3 + 2HCl \rightarrow BaCl_3 + CO_2 + H_2O \quad (3\text{-}2)$$

$$HCl + NaOH \rightarrow NaCl + H_2O \quad (3\text{-}3)$$

The mole number of CO_2 absorbed by the sample can be calculated as follows:

$$n_{CO_2} = \left(\frac{c_{HCl} \cdot V_{HCl} - c_{NaOH} \cdot V_{NaOH}}{2}\right)_{sample} - \left(\frac{c_{HCl} \cdot V_{HCl} - c_{NaOH} \cdot V_{NaOH}}{2}\right)_{blank} \quad (3\text{-}4)$$

Here c_{HCl} and c_{NaOH} are the concentration of HCl solution and NaOH solution, V_{HCl} is the volume of HCl solution which reacts with $BaCO_3$, V_{NaOH} is the volume of NaOH solution which is used to neutralize the excess HCl. Therefore, $\left(\frac{c_{HCl} \cdot V_{HCl} - c_{NaOH} \cdot V_{NaOH}}{2}\right)_{sample}$ is the

mole number of CO_2 which is obtained by titrating the sample. Because the NaOH solution which is used to precipitate CO_2 in the sample will absorb a certain amount of CO_2 in the atmosphere, the blank experiment is needed. The procedure of the blank experiment is the same as described above except that the sample is not added. $(\frac{c_{HCl} \cdot V_{HCl} - c_{NaOH} \cdot V_{NaOH}}{2})_{blank}$ is the mole number of CO_2 which is obtained from the blank experiment. Hence, the mole number of CO_2 absorbed by the sample can be calculated by eq 3-4.

The mole number of amine in the sample can be calculated by:

$$n_{amine} = \frac{w_2(m_{sample} - n_{CO_2} M_{CO_2})}{M_{amine}} \tag{3-5}$$

Here w_2 is the mass fraction of amine in water, m_{sample} is the mass of the sample, M_{CO_2} is the molar mass of CO_2, $n_{CO_2} M_{CO_2}$ is the mass of CO_2 in the sample, $w_2(m_{sample} - n_{CO_2} M_{CO_2})$ is the mass of amine in the sample, M_{amine} is the molar mass of amine.

Hence, CO_2 loading of the high loaded amine solution can be calculated by:

$$\alpha = \frac{n_{CO_2}}{n_{amine}} \tag{3-6}$$

c) Preparation of specific loaded amine solutions

Unloaded and high loaded aqueous amine solutions were then mixed to produce a set of samples with a range of CO_2-loadings. The spreadsheets of calculation examples to the titration process and dilution process are enclosed in Appendix 3-2 and 3-3.

3.2.2 Measuring instrument and procedure

A combination of Anton Paar density meters DMA 4500 (with the LCD) and DMA HP were used for the density measurements and shown in Figure 3-5. The measuring temperature range of DMA 4500 is from (273.15 to 363.15) K and it only works at normal atmosphere, while the measuring temperature range of DMA HP is from (263.15 to 473.15) K and it can work at the pressures from (0 to 70) MPa. Each sample is injected into a measurement cell by a syringe. Instrument accuracy for DMA 4500 is given as ± 0.05 $kg \cdot m^{-3}$ by the manufacturer,

while for DMA HP the accuracy is given as ± 0.1 kg·m^{-3}. Both densimeters are based on an oscillating U-tube technique to determine densities.

Figure 3-5. The combination of densimeter: DMA 4500 + DMA HP.

Densities of unloaded and CO_2 loaded aqueous amine solutions were measured using an Anton Paar Density Meter (DMA 4500) in the temperature range (298.15 to 363.15) K. Density check by distilled degassed water at 20 °C is necessary to check the validity and accuracy of DMA 4500 from time to time. It will show "density check: OK" on the screen if the deviation between the density check displayed value and the reference value is within the permitted range. Otherwise calibration by air and water is needed. The calibration procedure is accomplished if the deviation between the new adjustment and the last adjustment is smaller than 0.05 kg·m^{-3}. Then the measurements can be performed.

The measurements should shift to Anton Paar Density Meter DMA HP when the bubble appears during the experiments. DMA HP can be used at higher temperature because the pressure in U-tube is high which can restrain the evaporation of amine and CO_2 through desorption. The pressure here is the pressure in our gas supply system which is limited to 8 bar. The flow sheet of DMA HP is shown in Figure 3-6. DMA HP must be calibrated every time before it is used while the calibration of the 4500 model may be done a little less frequently. Nitrogen and degassed distilled water were used for calibration. Densities of nitrogen and degassed distilled water under high pressure were enclosed in Appendix 3-4.

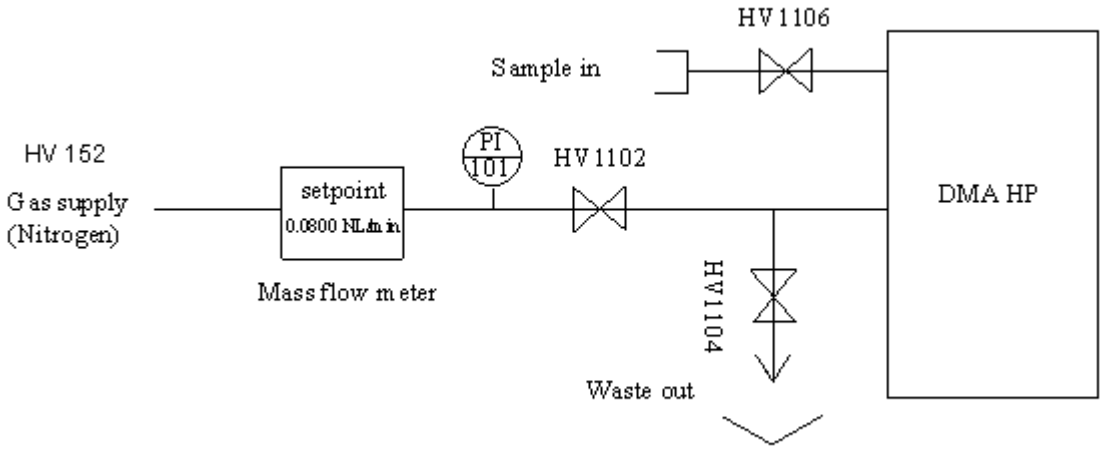

Figure 3-6. The flow sheet of DMA HP.

3.3 Results and Discussion

3.3.1 Density results of unloaded aqueous amine solutions

All the density measurements and the deduced excess volumes of water (1) + MEA (2) solutions are given in Table 3-5. Densities of pure water are from the International Association for the Properties of Water and Steam (IAPWS). The temperature ranges from (298.15 to 423.15) K, and the composition ranges from w_2 = 0 to 1.0. The pressure was atmospheric below 373.15 K and 0.7 MPa from 373.15 K and higher.

Figure 3-7 displays the densities of aqueous MEA solutions for selected temperatures as a function of composition. The maximum value on each curve always occurs at w_2 = 0.5 to 0.7. The densities become lower when the temperature increases for all the compositions. Pure MEA densities may be higher or lower than that of water depending on the temperature.

Figure 3-8 shows the excess molar volume trends of aqueous MEA solutions for selected temperatures. The behaviour with respect to composition is the same over the whole temperature range. It may be noted that the excess molar volumes of water (1) + MEA (2) solutions were less negative when the temperature was increased, and that this trend is the same at the higher pressure used in the range (373.15 to 423.15) K.

Table 3-5. Mass Fraction w, Liquid Densities ρ/kg·m^{-3}, and Deduced Excess Molar Volume V_m^E/m^3·mol^{-1} for [Water (1) + MEA (2)] Mixture.[a, b, c]

		298.15 K		303.15 K		308.15 K		313.15 K		318.15 K		323.15 K		328.15 K	
w_2	x_2	ρ	$10^6 V_m^E$	ρ	$10^6 V_m^E$	ρ	$10^6 V_m^E$	ρ	$10^6 V_m^E$	ρ	$10^6 V_m^E$	ρ	$10^6 V_m^E$	ρ	$10^6 V_m^E$
0	0	997.0	0	995.6	0	994.0	0	992.2	0	990.2	0	988.0	0	985.7	0
0.3	0.1122	1010.9	-0.213	1008.4	-0.205	1006.2	-0.210	1003.5	-0.205	1001.1	-0.211	998.1	-0.206	995.5	-0.213
0.4	0.1643	1016.3	-0.330	1013.8	-0.328	1011.0	-0.323	1008.3	-0.324	1005.3	-0.321	1002.3	-0.322	999.2	-0.320
0.5	0.2278	1021.3	-0.457	1018.2	-0.445	1015.2	-0.446	1012.1	-0.442	1009.0	-0.441	1005.6	-0.437	1002.4	-0.437
0.6	0.3067	1024.8	-0.572	1021.4	-0.562	1018.2	-0.559	1014.7	-0.552	1011.4	-0.550	1007.8	-0.545	1004.4	-0.545
0.7	0.4077	1026.3	-0.651	1022.8	-0.644	1019.3	-0.638	1015.7	-0.633	1012.0	-0.629	1008.3	-0.624	1004.6	-0.622
0.8	0.5412	1024.7	-0.632	1021.0	-0.626	1017.3	-0.622	1013.5	-0.617	1009.7	-0.612	1005.9	-0.610	1002.0	-0.606
0.9	0.7264	1020.0	-0.461	1016.2	-0.459	1012.3	-0.454	1008.5	-0.454	1004.5	-0.449	1000.6	-0.450	996.7	-0.447
1.0	1	1011.9	0	1008.0	0	1004.0	0	1000.0	0	996.0	0	992.0	0	988.0	0
		333.15 K		338.15 K		343.15 K		348.15 K		353.15 K		358.15 K		363.15 K	
w_2	x_2	ρ	$10^6 V_m^E$	ρ	$10^6 V_m^E$	ρ	$10^6 V_m^E$	ρ	$10^6 V_m^E$	ρ	$10^6 V_m^E$	ρ	$10^6 V_m^E$	ρ	$10^6 V_m^E$
0	0	983.2	0	980.5	0	977.7	0	974.8	0	971.8	0	968.6	0	965.3	0
0.3	0.1122	992.3	-0.208	989.5	-0.215	986.1	-0.211	983.0	-0.218	979.4	-0.214	976.1	-0.220	972.5	-0.221
0.4	0.1643	996.1	-0.322	992.7	-0.321	989.4	-0.323	985.9	-0.323	982.4	-0.324	978.7	-0.325	975.0	-0.326
0.5	0.2278	999.0	-0.437	995.4	-0.435	991.9	-0.435	988.3	-0.435	984.5	-0.434	980.8	-0.435	976.9	-0.435
0.6	0.3067	1000.7	-0.540	997.1	-0.541	993.2	-0.537	989.5	-0.538	985.6	-0.535	981.8	-0.537	977.7	-0.533
0.7	0.4077	1000.8	-0.619	997.0	-0.618	993.1	-0.614	989.2	-0.614	985.2	-0.610	981.2	-0.610	977.1	-0.609
0.8	0.5412	998.2	-0.605	994.2	-0.602	990.2	-0.602	986.2	-0.599	982.1	-0.598	978.0	-0.595	973.9	-0.595
0.9	0.7264	992.7	-0.447	988.7	-0.445	984.6	-0.445	980.6	-0.446	976.5	-0.445	972.3	-0.442	968.1	-0.444
1.0	1	983.9	0	979.8	0	975.8	0	971.6	0	967.5	0	963.4	0	959.2	0
		373.15 K		383.15 K		393.15 K		403.15 K		413.15 K		423.15 K			
w_2	x_2	ρ	$10^6 V_m^E$	ρ	$10^6 V_m^E$	ρ	$10^6 V_m^E$	ρ	$10^6 V_m^E$	ρ	$10^6 V_m^E$	ρ	$10^6 V_m^E$		
0	0	958.6	0	951.2	0	943.4	0	935.1	0	926.3	0	917.1	0		
0.3	0.1122	965.3	-0.224	957.4	-0.223	949.1	-0.224	940.6	-0.227	931.7	-0.229	922.3	-0.227		
0.4	0.1643	967.2	-0.319	959.1	-0.317	950.7	-0.316	941.9	-0.317	932.9	-0.317	923.3	-0.311		
0.5	0.2278	969.0	-0.428	960.6	-0.424	952.0	-0.422	943.1	-0.421	934.0	-0.420	924.3	-0.416		
0.6	0.3067	969.4	-0.522	960.8	-0.516	952.1	-0.513	943.1	-0.509	933.8	-0.506	924.1	-0.497		
0.7	0.4077	968.5	-0.592	959.8	-0.583	950.9	-0.578	941.9	-0.574	932.6	-0.570	922.8	-0.559		
0.8	0.5412	965.3	-0.579	956.5	-0.572	947.6	-0.567	938.6	-0.562	929.3	-0.557	919.5	-0.546		
0.9	0.7264	959.3	-0.413	950.6	-0.409	941.7	-0.405	932.7	-0.403	923.6	-0.401	914.1	-0.393		
1.0	1	950.9	0	942.3	0	933.5	0	924.7	0	915.7	0	906.4	0		

[a]: The data were measured under 0.1 MPa from (298.15 to 363.15) K and under 0.7 MPa from (373.15 to 423.15) K.
[b]: Pure water data are from IAPWS.[16]
[c]: Excess molar volumes of aqueous MEA solutions here are derived data.

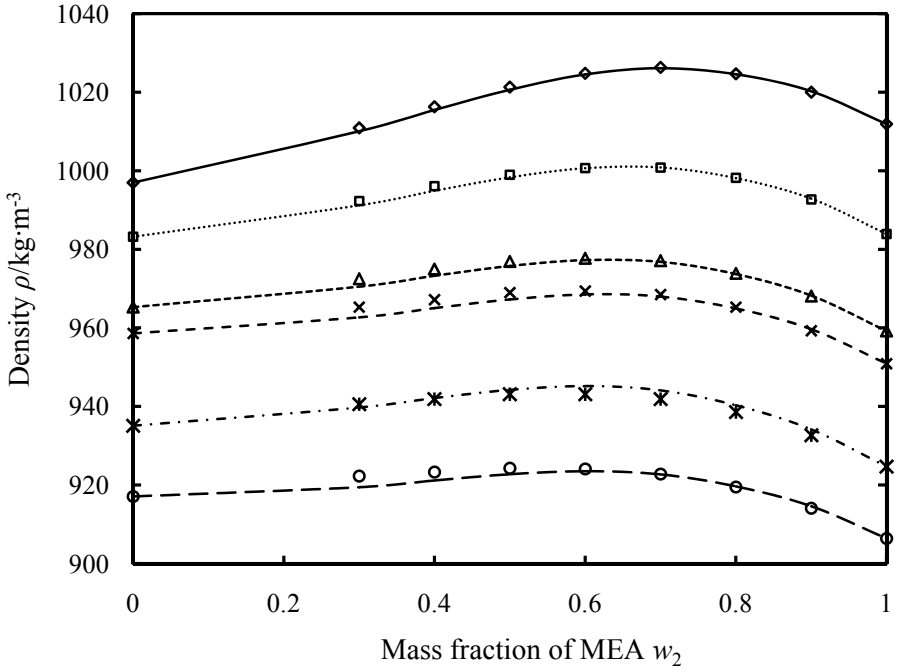

Figure 3-7. Densities of the H_2O (1) + MEA (2) solutions at selected temperatures. Symbols refer to experimental data: ◊, 298.15 K; □, 333.15 K; △, 363.15 K; ×, 373.15 K; *, 403.15 K; ○, 423.15 K. Lines are correlated data by the Redlich-Kister equation with parameters from Table 3-16: —, 298.15 K; ·····, 333.15 K; ---, 363.15 K; – –, 373.15 K; – · –, 403.15 K; ——, 423.15 K.

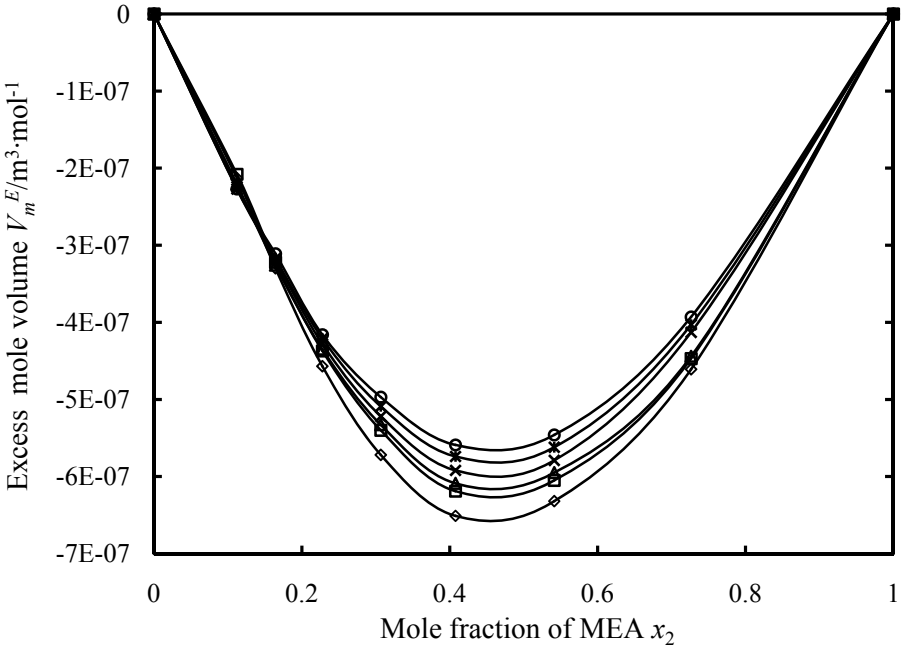

Figure 3-8. Excess molar volumes of H_2O (1) + MEA (2) solutions at selected temperatures: ◊, 298.15 K; □, 333.15 K; △, 363.15 K; ×, 373.15 K; *, 403.15 K; ○, 423.15 K.

Figure 3-9 indicates densities of unloaded aqueous MEA solutions in various concentrations as a function of temperature. It can be seen that there is no marked discontinuity when the measurements are shifted from one densimeter to the other. The reason for anomalous behavior of densities of mass fraction 0.4 MEA solutions is that the tendency of density changes with mass fraction of MEA is parabolic. The maximum density of aqueous MEA solutions for a given temperature always occurs at w_2 = 0.5 to 0.7. This peak value decreases as temperature increases. The maximum density occurs at w_2 = 0.7 at 298.15 K, and w_2 = 0.5 at 423.15 K. So densities of mass fraction 0.4 MEA solutions are lower than mass fraction 0.7 MEA solutions, and more and more close to mass fraction 0.7 MEA solutions as temperature increases.

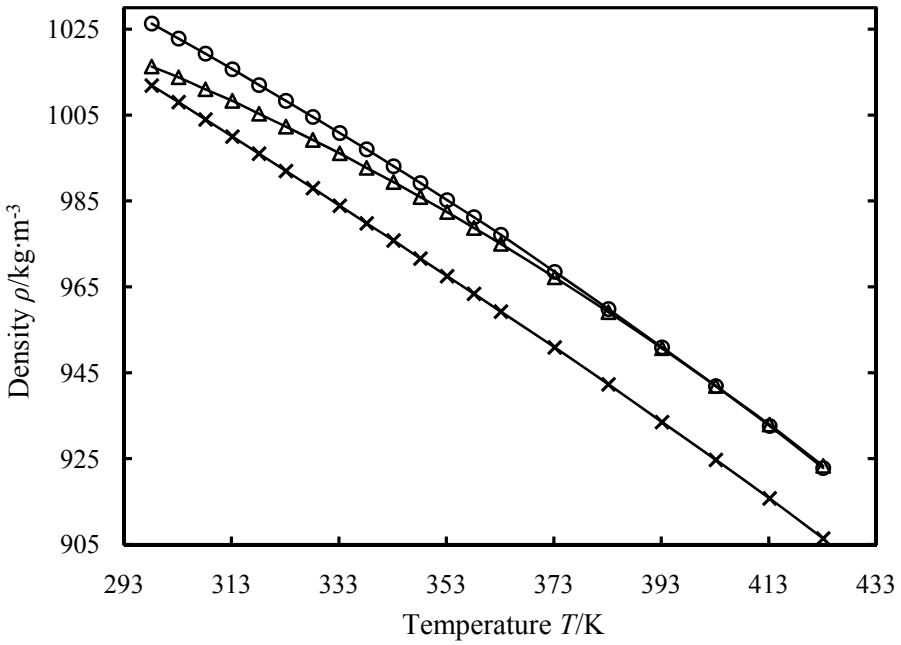

Figure 3-9. Densities of H_2O (1) + MEA (2) solutions at selected mass fractions of MEA: △, 0.4; ○, 0.7; ×, 1.0.

A comparison of measured densities for w_2 = 0.3, 0.4 and 0.5 unloaded aqueous MEA solutions between this work and the values of Pouryosefi and Idem [13] is shown in Figure 3-10. Measurements from this work were on average 0.19 kg·m^{-3} higher for w_2 = 0.3, 0.33 kg·m^{-3} higher for w_2 = 0.4, and 0.30 kg·m^{-3} higher for w_2 = 0.5 respectively when compared to the values from Pouryosefi and Idem. These deviations in results are less than the experimental error and therefore acceptable.

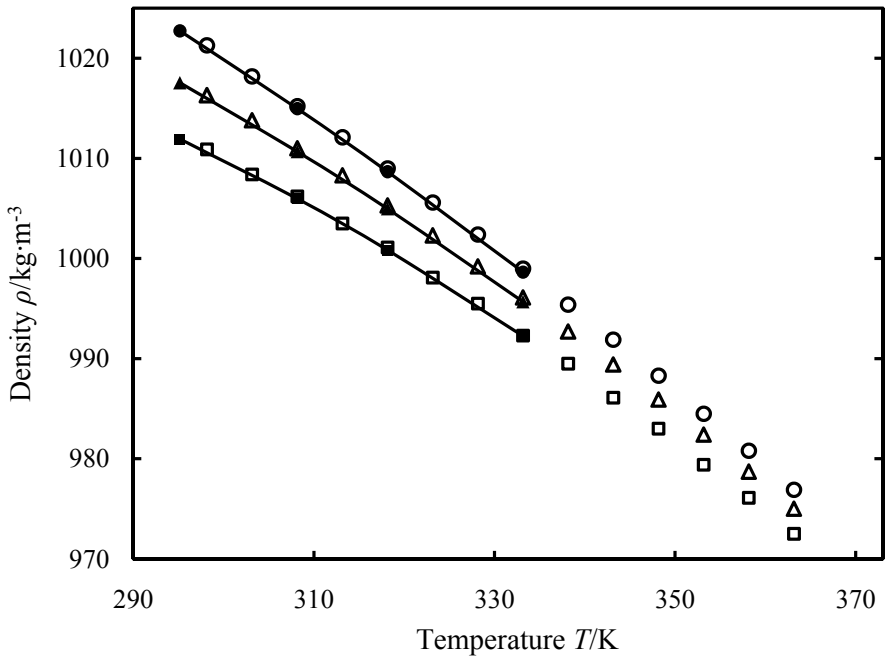

Figure 3-10. Comparison of measured and literature densities of H_2O (1) + MEA (2) solutions for three mass fractions of MEA: This work □, 0.3; △, 0.4; ○, 0.5; and values from Pouryousefi and Idem[13] ■, 0.3; ▲, 0.4; ●, 0.5.

All the density measurements and the deduced excess molar volumes of water (1) + DEA (2) solutions at temperatures from (298.15 to 423.15) K and mass fractions of DEA from 0 to 1 are given in Table 3-6.

Figure 3-11 displays densities of unloaded aqueous DEA solutions as a function of concentration for selected temperatures. It can be seen from Figure 3-11 that densities of unloaded aqueous DEA solutions decrease with the temperature increasing, and increase with the DEA concentration becoming greater. Figure 3-12 indicates densities of unloaded aqueous DEA solutions in various concentrations as a function of temperature. It can be seen that densities of unloaded aqueous DEA solutions have the approximate linear relationship with the temperature. Unlike the trend in Figure 3-9, the curves in Figure 3-12 are parallel. The reason is that densities of unloaded aqueous DEA solutions increase monotonically with the rising mass fraction of DEA, and the rate of increase is the same for different temperatures.

Table 3-6. Mass Fraction w, Liquid Densities ρ/kg·m^{-3}, and Deduced Excess Molar Volume V_m^E/m^3·mol^{-1} for [Water (1) + DEA (2)] Mixture.[a, b, c]

		298.15 K		303.15 K		308.15 K		313.15 K		318.15 K		323.15 K		328.15 K	
w_2	x_2	ρ	$10^6 V_m^E$	ρ	$10^6 V_m^E$	ρ	$10^6 V_m^E$	ρ	$10^6 V_m^E$	ρ	$10^6 V_m^E$	ρ	$10^6 V_m^E$	ρ	$10^6 V_m^E$
0	0	997.0	0	995.6	0	994.0	0	992.2	0	990.2	0	988.0	0	985.7	0
0.3	0.0684	1034.0	-0.222	1031.8	-0.216	1029.7	-0.216	1027.2	-0.211	1024.9	-0.211	1022.2	-0.206	1019.5	-0.207
0.4	0.1025	1047.2	-0.340	1044.8	-0.332	1042.4	-0.329	1039.6	-0.320	1037.0	-0.318	1034.2	-0.312	1031.4	-0.311
0.5	0.1463	1059.5	-0.457	1056.9	-0.447	1054.2	-0.441	1051.3	-0.432	1048.4	-0.426	1045.4	-0.417	1042.4	-0.412
0.6	0.2045	1071.4	-0.590	1068.5	-0.578	1065.6	-0.568	1062.6	-0.559	1059.5	-0.551	1056.6	-0.547	1053.2	-0.534
0.7	0.2856	1081.0	-0.680	1077.9	-0.668	1074.9	-0.659	1071.7	-0.650	1068.6	-0.640	1065.3	-0.630	1062.1	-0.622
0.8	0.4067	1088.0	-0.693	1085.0	-0.687	1081.8	-0.679	1078.7	-0.674	1075.5	-0.668	1072.2	-0.658	1068.9	-0.653
0.9	0.6066	1092.2	-0.541	1088.9	-0.531	1085.8	-0.530	1082.7	-0.532	1079.5	-0.530	1076.2	-0.524	1073.0	-0.523
1.0	1	1093.6	0	1090.4	0	1087.1	0	1083.8	0	1080.6	0	1077.4	0	1074.1	0
		333.15 K		338.15 K		343.15 K		348.15 K		353.15 K		358.15 K		363.15 K	
w_2	x_2	ρ	$10^6 V_m^E$	ρ	$10^6 V_m^E$	ρ	$10^6 V_m^E$	ρ	$10^6 V_m^E$	ρ	$10^6 V_m^E$	ρ	$10^6 V_m^E$	ρ	$10^6 V_m^E$
0	0	983.2	0	980.5	0	977.7	0	974.8	0	971.8	0	968.6	0	965.3	0
0.3	0.0684	1016.6	-0.202	1013.8	-0.205	1010.6	-0.200	1007.5	-0.199	1004.2	-0.197	1000.8	-0.196	997.3	-0.195
0.4	0.1025	1028.3	-0.304	1025.2	-0.303	1022.0	-0.298	1018.8	-0.298	1015.3	-0.293	1011.9	-0.291	1008.3	-0.288
0.5	0.1463	1039.2	-0.405	1036.0	-0.401	1032.6	-0.396	1029.3	-0.393	1025.8	-0.387	1022.3	-0.385	1018.6	-0.379
0.6	0.2045	1049.9	-0.525	1046.5	-0.519	1043.1	-0.514	1039.7	-0.509	1036.0	-0.500	1032.5	-0.496	1028.7	-0.489
0.7	0.2856	1058.8	-0.615	1055.3	-0.607	1051.8	-0.599	1048.3	-0.594	1044.8	-0.589	1041.1	-0.581	1037.2	-0.569
0.8	0.4067	1065.6	-0.644	1062.2	-0.642	1058.8	-0.635	1055.3	-0.631	1051.7	-0.625	1048.0	-0.619	1044.4	-0.616
0.9	0.6066	1069.6	-0.518	1066.3	-0.516	1062.9	-0.513	1059.4	-0.512	1055.9	-0.509	1052.4	-0.509	1048.8	-0.504
1.0	1	1070.8	0	1067.4	0	1064.0	0	1060.6	0	1057.2	0	1053.7	0	1050.1	0
		373.15 K		383.15 K		393.15 K		403.15 K		413.15 K		423.15 K			
w_2	x_2	ρ	$10^6 V_m^E$	ρ	$10^6 V_m^E$	ρ	$10^6 V_m^E$	ρ	$10^6 V_m^E$	ρ	$10^6 V_m^E$	ρ	$10^6 V_m^E$		
0	0	958.6	0	951.2	0	943.4	0	935.1	0	926.3	0	917.1	0		
0.3	0.0684	990.2	-0.187	982.3	-0.181	974.2	-0.176	965.8	-0.172	957.1	-0.169	947.9	-0.163		
0.4	0.1025	1000.9	-0.275	992.9	-0.266	984.7	-0.259	976.3	-0.252	967.5	-0.245	958.1	-0.232		
0.5	0.1463	1011.5	-0.375	1003.3	-0.363	995.1	-0.352	986.7	-0.343	977.9	-0.334	969.0	-0.332		
0.6	0.2045	1021.2	-0.468	1012.9	-0.454	1004.7	-0.440	996.2	-0.428	987.5	-0.413	978.2	-0.395		
0.7	0.2856	1029.9	-0.555	1021.7	-0.539	1013.5	-0.523	1005.1	-0.509	996.5	-0.492	987.2	-0.465		
0.8	0.4067	1037.2	-0.601	1028.9	-0.584	1020.9	-0.570	1012.8	-0.557	1004.5	-0.544	995.4	-0.515		
0.9	0.6066	1041.8	-0.498	1033.8	-0.489	1026.0	-0.482	1018.2	-0.475	1010.2	-0.467	1001.7	-0.454		
1.0	1	1043.3	0	1035.5	0	1028.1	0	1020.5	0	1012.9	0	1004.8	0		

[a]: The data were measured under 0.1 MPa from (298.15 to 363.15) K and under 0.7 MPa from (373.15 to 423.15) K.
[b]: Pure water data are from IAPWS.[16]
[c]: Excess molar volumes of aqueous DEA solutions here are derived data.

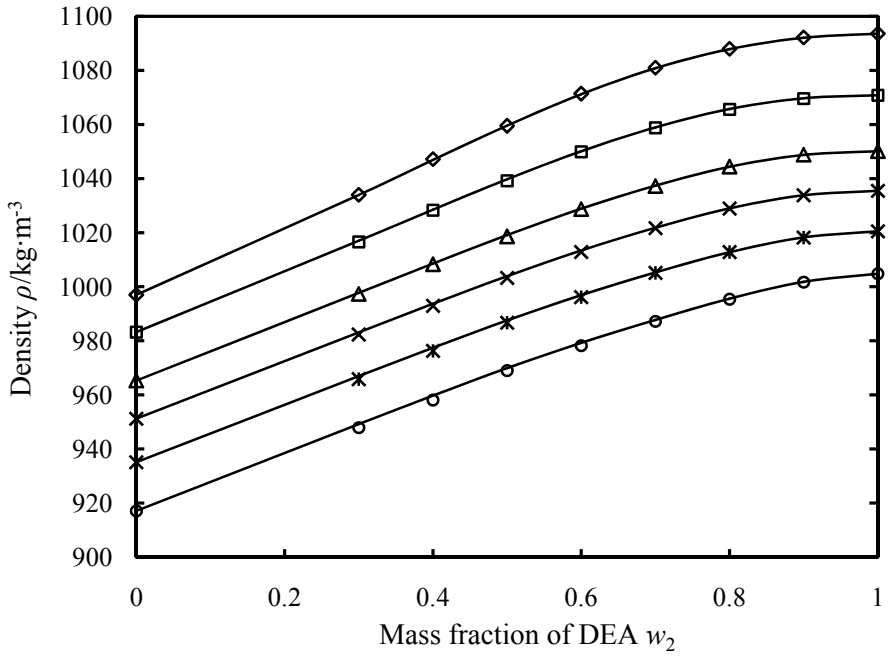

Figure 3-11. Densities of the H_2O (1) + DEA (2) solutions as a function of mass fraction of DEA at selected temperatures. Symbols refer to the experimental data: ◇, 298.15 K; □, 333.15 K; △, 363.15 K; ×, 383.15 K; *, 403.15 K; ○, 423.15 K. Lines are calculated by the Redlich-Kister equation with parameters from Table 3-17.

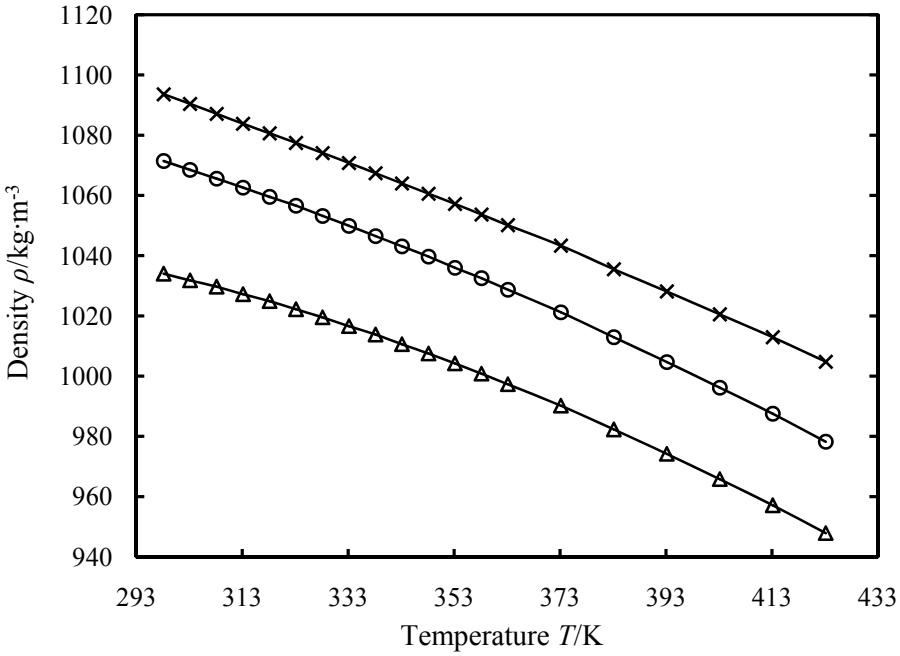

Figure 3-12. Densities of H_2O (1) + DEA (2) solutions at selected mass fractions of DEA: △, 0.3; ○, 0.6; ×, 1.0.

The comparison to the data from the literature is shown in Figure 3-13. The agreement between the measured densities of unloaded aqueous DEA solutions and the results from Maham et al.[8] is good. The maximum deviation between them is 1.7 $kg \cdot m^{-3}$, which is within the experimental uncertainty.

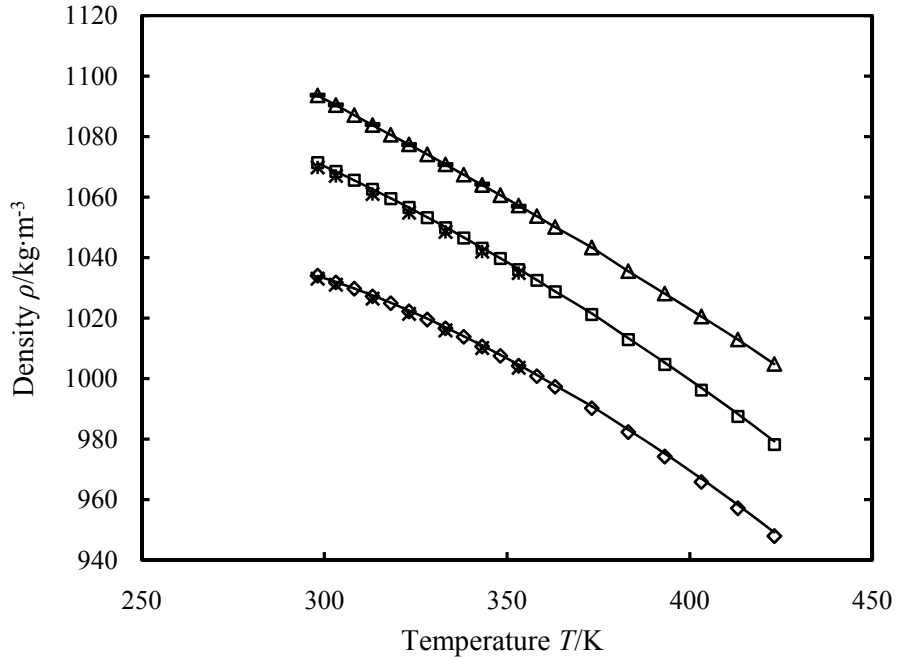

Figure 3-13. Comparison of measured and literature densities of H_2O (1) + DEA (2) solutions for three mass fractions of DEA: This work ◇, 0.3; □, 0.6; △, 1.0; and values from Maham et al.[8] ×, 0.3; *, 0.6; —, 1.0. Lines are calculated by the Redlich-Kister equation with parameters from Table 3-17.

All the densities and the deduced excess molar volumes of water (1) + MDEA (2) solutions at temperatures from (298.15 to 423.15) K and mass fractions of MDEA from 0 to 1 are given in Table 3-7.

Figure 3-14 indicates the trend of densities of unloaded aqueous MDEA solutions as a function of concentration at various temperatures. Densities of unloaded aqueous MDEA solutions increase at first and then decrease when the MDEA concentration increases. The maximum value occurs at $w_2 = 0.7$ for the whole temperature range. Pure MDEA densities are higher than that of water. Figure 3-15 displays densities of unloaded aqueous MDEA solutions in various concentrations as a function of temperature. The trend in Figure 3-15 is the same as Figure 3-9 because the tendency of density changes with mass fraction of MDEA is also parabolic.

Table 3-7. Mass Fraction w, Liquid Densities ρ/kg·m^{-3}, and Deduced Excess Molar Volume V_m^E/m^3·mol^{-1} for [Water (1) + MDEA (2)] Mixture.[a, b, c]

		298.15 K		303.15 K		308.15 K		313.15 K		318.15 K		323.15 K		328.15 K	
w_2	x_2	ρ	$10^6 V_m^E$	ρ	$10^6 V_m^E$	ρ	$10^6 V_m^E$	ρ	$10^6 V_m^E$	ρ	$10^6 V_m^E$	ρ	$10^6 V_m^E$	ρ	$10^6 V_m^E$
0	0	997.0	0	995.6	0	994.0	0	992.2	0	990.2	0	988.0	0	985.7	0
0.3	0.0609	1025.2	-0.222	1022.8	-0.216	1020.3	-0.216	1017.7	-0.211	1014.9	-0.211	1012.0	-0.370	1009.0	-0.367
0.4	0.0916	1035.6	-0.340	1032.8	-0.332	1029.9	-0.329	1026.9	-0.320	1023.8	-0.318	1020.6	-0.563	1017.2	-0.557
0.5	0.1313	1043.3	-0.457	1040.9	-0.447	1037.6	-0.441	1034.3	-0.432	1030.8	-0.426	1027.3	-0.758	1023.7	-0.748
0.6	0.1848	1049.7	-0.590	1046.1	-0.578	1042.5	-0.568	1038.8	-0.559	1034.7	-0.551	1031.1	-0.914	1027.3	-0.898
0.7	0.2608	1053.6	-0.680	1049.9	-0.668	1046.2	-0.659	1042.4	-0.650	1038.5	-0.640	1034.6	-1.121	1030.6	-1.105
0.8	0.3768	1052.3	-0.693	1048.6	-0.687	1044.8	-0.679	1040.9	-0.674	1037.0	-0.668	1033.1	-1.174	1029.1	-1.159
0.9	0.5764	1046.0	-0.541	1042.3	-0.531	1038.4	-0.530	1034.6	-0.532	1030.8	-0.530	1026.9	-0.927	1022.9	-0.920
1.0	1	1036.0	0	1032.4	0	1028.6	0	1024.8	0	1021.0	0	1017.2	0	1013.3	0
		333.15 K		338.15 K		343.15 K		348.15 K		353.15 K		358.15 K		363.15 K	
w_2	x_2	ρ	$10^6 V_m^E$	ρ	$10^6 V_m^E$	ρ	$10^6 V_m^E$	ρ	$10^6 V_m^E$	ρ	$10^6 V_m^E$	ρ	$10^6 V_m^E$	ρ	$10^6 V_m^E$
0	0	983.2	0	980.5	0	977.7	0	974.8	0	971.8	0	968.6	0	965.3	0
0.3	0.0609	1005.9	-0.364	1002.7	-0.359	999.3	-0.356	995.9	-0.353	992.3	-0.349	988.7	-0.345	984.9	-0.341
0.4	0.0916	1013.8	-0.550	1010.3	-0.543	1006.7	-0.536	1003.0	-0.529	999.2	-0.521	995.3	-0.513	991.3	-0.505
0.5	0.1313	1020.1	-0.738	1016.3	-0.725	1012.5	-0.714	1008.5	-0.705	1004.6	-0.694	1000.4	-0.680	996.3	-0.669
0.6	0.1848	1023.6	-0.893	1019.8	-0.883	1015.9	-0.873	1011.9	-0.860	1007.7	-0.845	1003.5	-0.828	999.2	-0.813
0.7	0.2608	1026.6	-1.089	1022.5	-1.070	1018.4	-1.051	1014.2	-1.036	1009.9	-1.017	1005.2	-0.978	1000.9	-0.961
0.8	0.3768	1025.0	-1.144	1020.9	-1.122	1016.8	-1.107	1012.6	-1.092	1008.4	-1.071	1004.1	-1.051	999.8	-1.032
0.9	0.5764	1019.0	-0.911	1015.0	-0.894	1010.9	-0.881	1006.9	-0.875	1002.7	-0.859	998.6	-0.842	994.4	-0.830
1.0	1	1009.4	0	1005.6	0	1001.7	0	997.7	0	993.8	0	989.9	0	985.9	0
		373.15 K		383.15 K		393.15 K		403.15 K		413.15 K		423.15 K			
w_2	x_2	ρ	$10^6 V_m^E$	ρ	$10^6 V_m^E$	ρ	$10^6 V_m^E$	ρ	$10^6 V_m^E$	ρ	$10^6 V_m^E$	ρ	$10^6 V_m^E$		
0	0	958.6	0	951.2	0	943.4	0	935.1	0	926.3	0	917.1	0		
0.3	0.0609	977.2	-0.325	968.8	-0.312	960.2	-0.298	951.2	-0.285	941.9	-0.271	931.9	-0.249		
0.4	0.0916	982.9	-0.470	974.1	-0.449	965.2	-0.427	955.9	-0.406	946.4	-0.384	936.1	-0.351		
0.5	0.1313	987.6	-0.623	978.5	-0.593	969.3	-0.564	959.8	-0.533	950.1	-0.501	939.6	-0.453		
0.6	0.1848	990.7	-0.772	981.4	-0.732	972.1	-0.693	962.5	-0.654	952.7	-0.612	942.3	-0.558		
0.7	0.2608	992.0	-0.895	982.6	-0.849	973.3	-0.803	963.7	-0.756	954.0	-0.707	943.6	-0.641		
0.8	0.3768	990.6	-0.936	981.4	-0.887	972.2	-0.837	962.9	-0.785	953.4	-0.733	943.4	-0.669		
0.9	0.5764	985.7	-0.720	976.9	-0.687	968.1	-0.649	959.3	-0.613	950.4	-0.572	940.9	-0.516		
1.0	1	978.6	0	970.3	0	962.1	0	953.9	0	945.6	0	937.0	0		

[a]: The data were measured under 0.1 MPa from (298.15 to 363.15) K and under 0.7 MPa from (373.15 to 423.15) K.
[b]: Pure water data are from IAPWS.[16]
[c]: Excess molar volumes of aqueous MDEA solutions here are derived data.

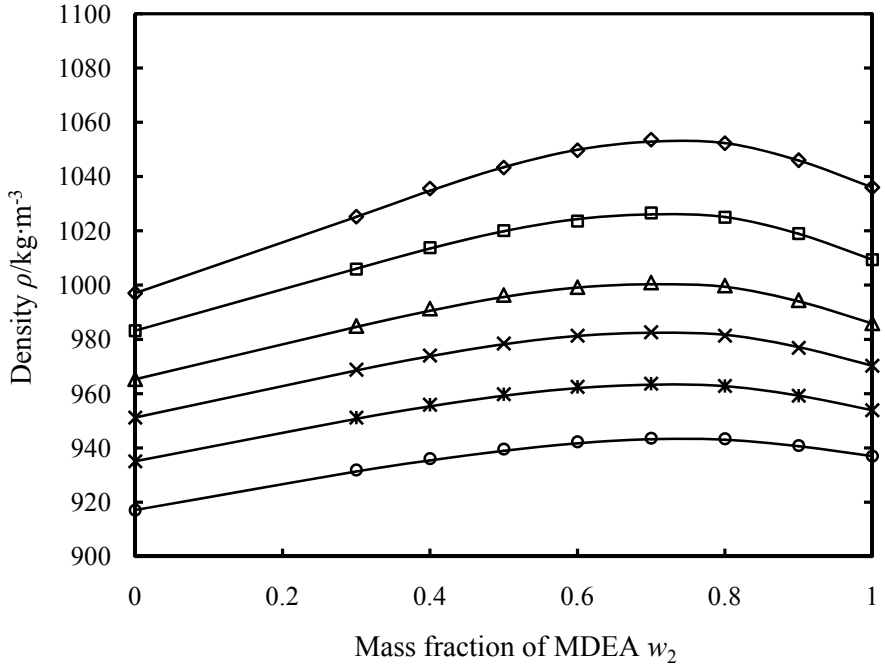

Figure 3-14. Densities of the H_2O (1) + MDEA (2) solutions as a function of mass fraction of MDEA at selected temperatures. Symbols refer to the experimental data: ◇, 298.15 K; □, 333.15 K; △, 363.15 K; ×, 383.15 K; *, 403.15 K; ○, 423.15 K. Lines are calculated by the Redlich-Kister equation with parameters from Table 3-17.

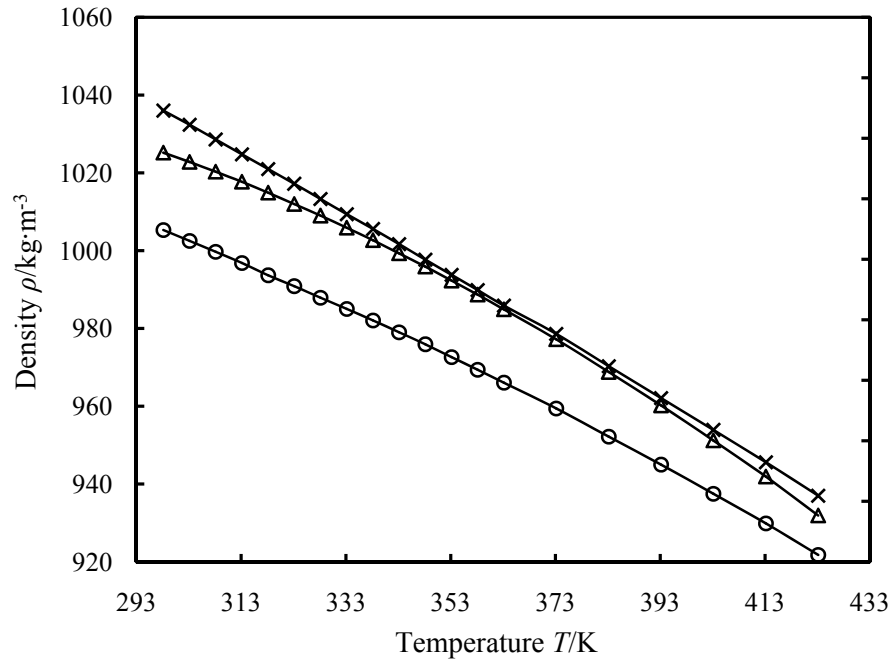

Figure 3-15. Densities of H_2O (1) + MDEA (2) solutions at selected mass fractions of MDEA: △, 0.3; ○, 0.6; ×, 1.0.

Figure 3-16 shows the comparison of measured densities of unloaded aqueous MDEA solutions to the data from the literature. The maximum deviation is 2.4 kg·m^{-3} when compared to the data from Muhammad et al.[15], and 1.2 kg·m^{-3} when compared to the data from Pouryousefi and Idem[13]. The deviations between them are within the experimental uncertainty. It can also be seen from Figure 3-16 that densities of unloaded aqueous MDEA solutions decrease with the rising temperature.

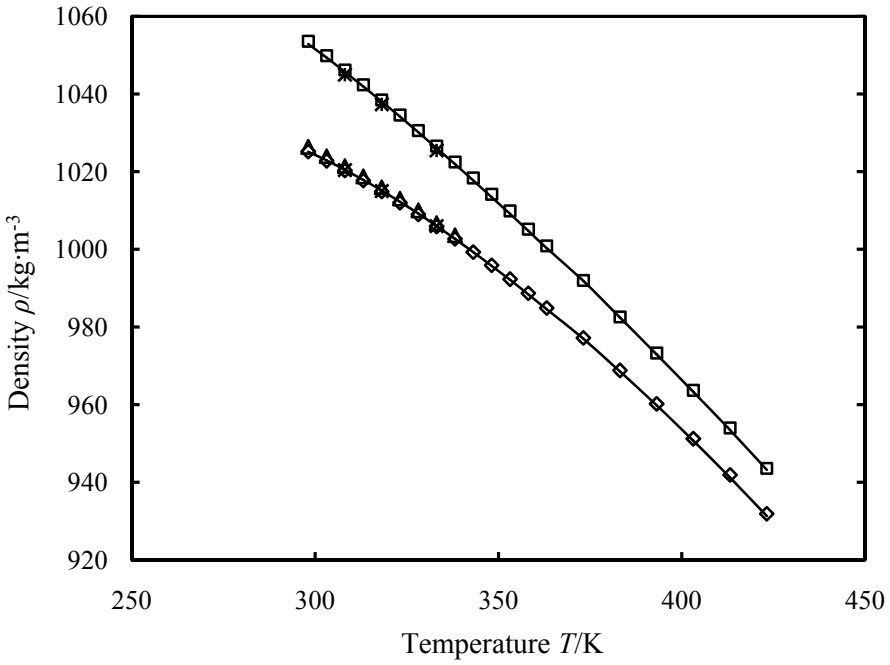

Figure 3-16. Comparison of measured and literature densities of H_2O (1) + MDEA (2) solutions for two mass fractions of MDEA: This work ◇, 0.3; □, 0.7; values from Muhammad et al.[15] △, 0.3; and values from Pouryousefi and Idem[13] ×, 0.3; *, 0.7. Lines are calculated by the Redlich-Kister equation with parameters from Table 3-17.

3.3.2 Density measurements of CO_2 loaded aqueous amine solutions

All the density measurements of CO_2 loaded aqueous MEA solutions at temperatures from (298.15 to 413.15) K are given in Tables 3-8 to 3-11. The mass fractions of MEA in water are 0.3, 0.4, 0.5 and 0.6. The CO_2 loading ranges from α = (0.10 to 0.56) at w_2 = 0.3, α = (0.10 to 0.45) at w_2 = 0.4, α = (0.10 to 0.47) at w_2 = 0.5 and α = (0.10 to 0.48) at w_2 = 0.6. The pressure was atmospheric below 373.15 K and 0.7 MPa from 373.15 K and higher.

Table 3-8. Liquid Densities ρ for Water (1) + MEA (2) + CO_2 (3) from T = (298.15 to 413.15) K and CO_2 Loading from α = (0.10 to 0.56) n_{CO2}/n_{MEA} at w_2 = 0.3.[a]

		α				
***T*/K**	***p*/MPa**	**0.10**	**0.21**	**0.32**	**0.44**	**0.56**
				ρ/kg·m^{-3}		
298.15	0.1	1033.3	1053.4	1075.6	1096.4	1114.2
313.15	0.1	1025.3	1046.4	1066.9	1089.1	1106.8
32315	0.1	1019.6	1041.2	1061.3	1083.8	1101.4
333.15	0.1	1013.8	1035.6	1055.6	1078.2	1095.7
343.15	0.1	1007.6	1029.7	1049.6	1072.3	1088.7
353.15	0.1	1000.2	1023.4	1043.4	1066.0	1081.2
363.15	0.1	993.6	1016.7	1036.7	1059.5	1074.9
373.15	0.7	986.5	1009.2	1030.6	1054.5	1069.1
383.15	0.7	980.1	1002.3	1024.2	1048.2	1063.3
393.15	0.7	973.7	995.7	1018.3	1041.7	1057.6
403.15	0.7	967.4	988.9	1012.9	1036.1	1051.9
413.15	0.7	960.5	982.6	1007.9	1029.5	1045.6

[a]: w_2 is the mass fraction of MEA in the (water + MEA) solutions.

Table 3-9. Liquid Densities ρ for Water (1) + MEA (2) + CO_2 (3) from T = (298.15 to 413.15) K and CO_2 Loading from α = (0.10 to 0.45) n_{CO2}/n_{MEA} at w_2 = 0.4.[a]

		α			
***T*/K**	***p*/MPa**	**0.10**	**0.21**	**0.33**	**0.45**
			ρ/kg·m^{-3}		
298.15	0.1	1037.6	1062.7	1094.5	1129.6
313.15	0.1	1029.5	1054.7	1086.7	1119.9
32315	0.1	1023.7	1049.0	1081.1	1113.8
333.15	0.1	1017.8	1043.0	1075.2	1108.7
343.15	0.1	1011.0	1036.7	1068.6	1103.2
353.15	0.1	1004.8	1029.2	1062.6	1096.3
363.15	0.1	997.0	1023.2	1055.7	1088.8
373.15	0.7	990.5	1016.2	1049.4	1082.4
383.15	0.7	983.1	1009.2	1043.9	1076.6
393.15	0.7	975.7	1002.3	1036.7	1069.9
403.15	0.7	967.8	994.6	1029.8	1063.1
413.15	0.7	960.5	987.6	1023.3	1057.5

[a]: w_2 is the mass fraction of MEA in the (water + MEA) solutions.

Table 3-10. Liquid Densities ρ for Water (1) + MEA (2) + CO_2 (3) from T = (298.15 to 413.15) K and CO_2 Loading from α = (0.10 to 0.47) n_{CO2}/n_{MEA} at w_2 = 0.5.[a]

		α			
***T*/K**	***p*/MPa**	**0.10**	**0.22**	**0.34**	**0.47**
		ρ/kg·m^{-3}			
298.15	0.1	1054.4	1090.5	1130.8	1166.8
313.15	0.1	1044.8	1081.7	1122.5	1158.5
32315	0.1	1038.4	1075.7	1116.8	1152.8
333.15	0.1	1032.0	1069.7	1110.8	1146.9
343.15	0.1	1025.2	1063.2	1104.8	1140.8
353.15	0.1	1018.3	1056.7	1098.5	1134.5
363.15	0.1	1011.0	1049.9	1092.0	1127.3
373.15	0.7	1004.5	1043.0	1085.4	1119.6
383.15	0.7	997.5	1036.9	1079.7	1112.5
393.15	0.7	990.8	1028.8	1073.9	1104.8
403.15	0.7	983.3	1021.0	1067.9	1098.4
413.15	0.7	976.8	1012.8	1061.2	1092.6

[a]: w_2 is the mass fraction of MEA in the (water + MEA) solutions.

Table 3-11. Liquid Densities ρ for Water (1) + MEA (2) + CO_2 (3) from T = (298.15 to 413.15) K and CO_2 Loading from α = (0.10 to 0.48) n_{CO2}/n_{MEA} at w_2 = 0.6.[a]

		α			
***T*/K**	***p*/MPa**	**0.10**	**0.22**	**0.34**	**0.48**
		ρ/kg·m^{-3}			
298.15	0.1	1065.3	1099.3	1153.6	1200.2
313.15	0.1	1055.4	1088.9	1145.0	1191.6
32315	0.1	1048.9	1081.7	1139.1	1185.8
333.15	0.1	1042.1	1074.4	1133.1	1179.8
343.15	0.1	1035.1	1066.6	1127.0	1173.7
353.15	0.1	1028.0	1058.0	1120.7	1167.8
363.15	0.1	1020.6	1049.4	1114.3	1160.6
373.15	0.7	1014.5	1042.3	1107.0	1153.7
383.15	0.7	1007.3	1035.3	1098.3	1147.8
393.15	0.7	1000.7	1028.9	1092.2	1141.3
403.15	0.7	994.9	1022.3	1085.7	1136.3
413.15	0.7	989.6	1017.1	1079.5	1130.4

[a]: w_2 is the mass fraction of MEA in the (water + MEA) solutions.

The variation of densities of CO_2 loaded aqueous MEA solutions with temperature and CO_2 loading at mass fraction of MEA in water equal to 0.3 are shown in Figure 3-17. As can be seen from the figure, densities of CO_2 loaded aqueous MEA solutions decrease with the rising temperature, and increase with CO_2 loading rising. The function of densities of CO_2 loaded aqueous MEA solutions with temperature is approximately linear. Figure 3-18 shows the densities as a function of CO_2 loading at 323.15 K and mass fractions of MEA in water from 0.3 to 0.5. The densities increase faster with CO_2 loading when the concentration of MEA is higher.

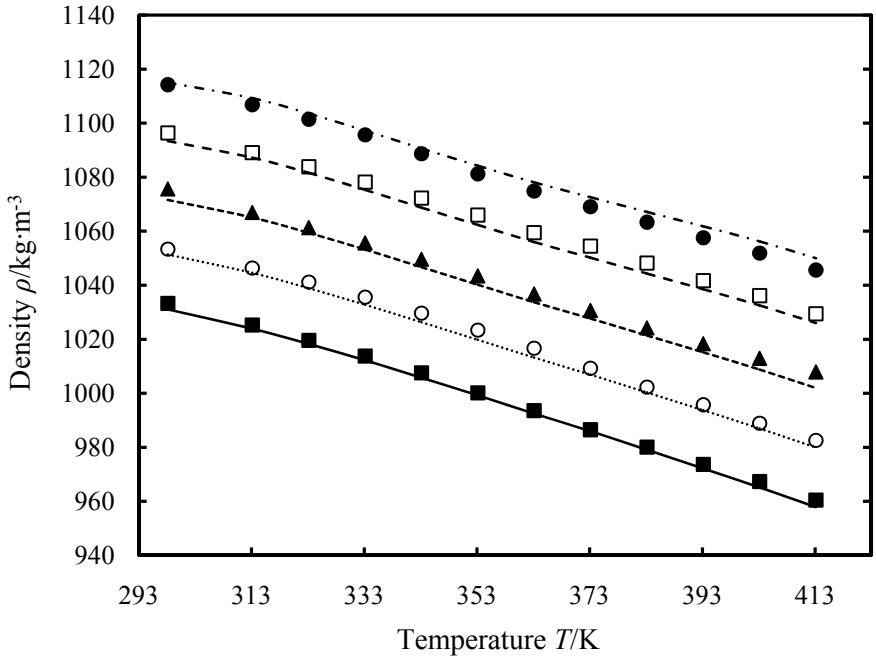

Figure 3-17. Densities of H_2O (1) + MEA (2) + CO_2 (3) solutions as a function of temperature at mass fraction of MEA = 0.3 and different CO_2 loading. Symbols refer to experimental data: ■, α = 0.10; ○, α = 0.21; ▲, α = 0.32; □, α = 0.44; ●, α = 0.56. Lines are correlated data by eqs 3-12 to 3-17 with parameters from Table 3-18: —, α = 0.10; ·····, α = 0.21; ---, α = 0.32; – -, α = 0.44; – · –, α = 0.56.

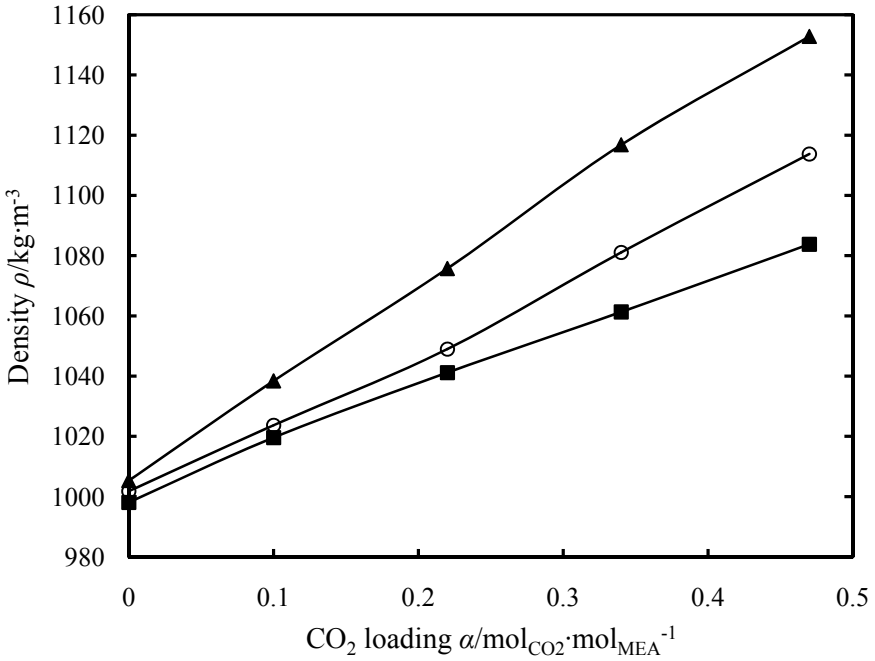

Figure 3-18. Densities of H_2O (1) + MEA (2) + CO_2 (3) solutions as a function of CO_2 loading at 323.15 K and different mass fraction of MEA: ■, 0.3; ○, 0.4; ▲, 0.5.

Measured densities of CO_2 loaded aqueous MEA solutions are compared with literature values from Weiland et al.[11] at 298.15 K in Figure 3-19. As can be seen Figure 3-19, the deviations between this work and Weiland et al.'s data at w_2 = 0.4 is higher than the deviations at w_2 = 0.3. The maximum deviation is 5.3 kg·m^{-3} for w_2 = 0.3 and 11.2 kg·m^{-3} for w_2 = 0.4. These deviations in results are systematic and judged to be within the acceptable error for most purposes (≤ 1%) although it is bigger than the experimental error. No literature results for densities of CO_2 loaded aqueous MEA solutions at w_2 > 0.4 were found.

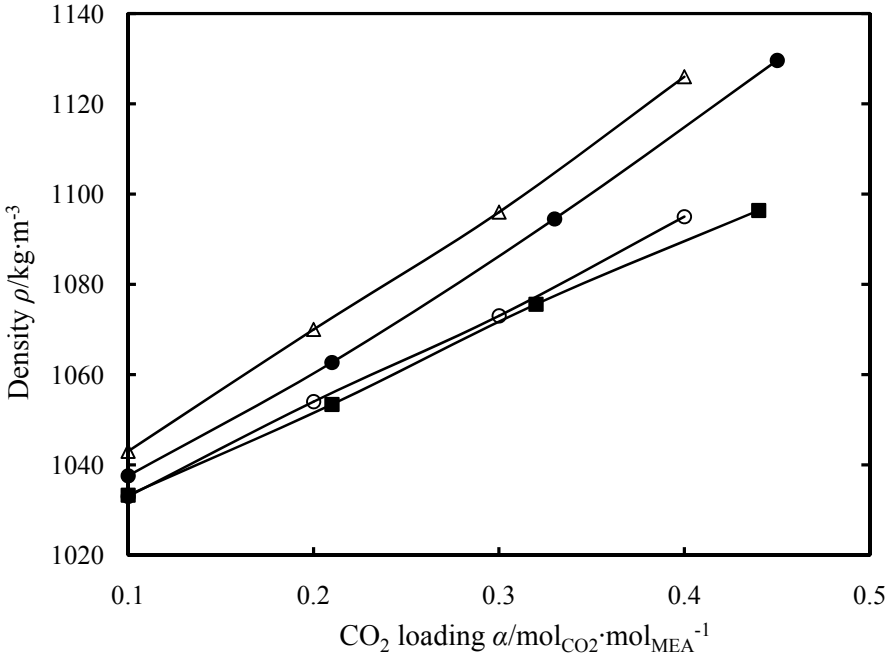

Figure 3-19. Densities of H_2O (1) + MEA (2) + CO_2 (3) solutions as a function for CO_2 loading at 298.15 K and different mass fraction of MEA. Results from this work: ■, w_2 = 0.3; ● w_2 = 0.4; are compared to results from Weiland et al.[11]: ○, w_2 = 0.3; △, w_2 = 0.4.

Density measurements of water (1) + DEA (2) + CO_2 (3) solutions at temperatures from (298.15 to 423.15) K are given in Tables 3-12 and 3-13. The mass fraction of DEA in water was 0.3 and 0.4. The CO_2 loading ranged from 0.1 to 0.5. Figure 3-20 shows densities of CO_2 loaded aqueous DEA solutions as a function of temperature at mass fraction of DEA w_2 = 0.3 and 0.4, and different CO_2 loadings. Densities of CO_2 loaded aqueous DEA solutions decrease with the rising temperature. The densities decrease faster when the temperature is higher. Densities of CO_2 loaded aqueous DEA solutions increase with increased CO_2 loading and mass fraction of DEA. The function of densities of CO_2 loaded aqueous DEA solutions with CO_2 loading is approximately linear. Figure 3-21 illustrates the comparison of the measured densities of CO_2 loaded aqueous DEA solutions to the data from Weiland et al.[11] at 298.15 K.

The agreement is good. The maximum deviation between them is 4.0 kg·m^{-3}, which is within the experimental uncertainty.

Table 3-12. Liquid Densities ρ for Water (1) + DEA (2) + CO_2 (3) from T = (298.15 to 423.15) K and CO_2 Loading from α = (0.1 to 0.5) n_{CO2}/n_{DEA} at w_2 = 0.3.[a]

	α									
	0.1		**0.2**		**0.3**		**0.4**		**0.5**	
***T*/K**	***p*/MPa**	***ρ*/kg·m^{-3}**	***p*/MPa**	***ρ*/kg·m^{-3}**	***p*/MPa**	***ρ*/kg·m^{-3}**	***p*/MPa**	***ρ*/kg·m^{-3}**	***p*/MPa**	***ρ*/kg·m^{-3}**
298.15	0.101	1046.2	0.101	1058.9	0.101	1071.8	0.101	1083.4	0.101	1093.1
303.15	0.101	1044.1	0.101	1056.6	0.101	1069.0	0.101	1080.6	0.101	1090.7
313.15	0.101	1039.4	0.101	1051.8	0.101	1063.8	0.101	1075.4	0.101	1085.5
323.15	0.101	1034.2	0.101	1046.6	0.101	1058.5	0.101	1070.0	0.101	1080.0
333.15	0.101	1028.7	0.101	1041.0	0.101	1052.8	0.101	1064.2	0.101	1074.1
343.15	0.101	1022.6	0.101	1034.9	0.101	1046.7	0.101	1058.0	0.101	1067.9
353.15	0.101	1016.2	0.101	1028.5	0.101	1040.2	0.101	1051.5	0.808	1061.1
363.15	0.101	1009.4	0.808	1022.0	0.808	1033.9	0.808	1045.0	0.808	1054.6
373.15	0.808	1002.4	0.808	1014.9	0.808	1026.6	0.808	1037.6	0.808	1047.2
383.15	0.808	994.8	0.808	1007.3	0.808	1019.0	0.808	1030.0	0.808	1038.9
393.15	0.808	986.8	0.808	999.1	0.808	1011.3	0.808	1021.6		
403.15	0.808	978.4	0.808	990.7	0.808	1002.2				
413.15	0.808	969.6	0.808	981.5						
423.15	0.808	958.4								

[a]: w_2 is the mass fraction of DEA in the (water + DEA) solutions.

Table 3-13. Liquid Densities ρ for Water (1) + DEA (2) + CO_2 (3) from T = (298.15 to 423.15) K and CO_2 Loading from α = (0.1 to 0.5) n_{CO2}/n_{DEA} at w_2 = 0.4.[a]

	α									
	0.1		**0.2**		**0.3**		**0.4**		**0.5**	
***T*/K**	***p*/MPa**	***ρ*/kg·m^{-3}**	***p*/MPa**	***ρ*/kg·m^{-3}**	***p*/MPa**	***ρ*/kg·m^{-3}**	***p*/MPa**	***ρ*/kg·m^{-3}**	***p*/MPa**	***ρ*/kg·m^{-3}**
298.15	0.101	1062.8	0.101	1079.6	0.101	1094.6	0.101	1109.0	0.101	1123.0
303.15	0.101	1060.3	0.101	1076.8	0.101	1091.6	0.101	1106.4	0.101	1120.3
313.15	0.101	1055.1	0.101	1071.2	0.101	1086.0	0.101	1101.0	0.101	1114.8
323.15	0.101	1049.6	0.101	1065.6	0.101	1080.4	0.101	1095.3	0.101	1108.9
333.15	0.101	1043.7	0.101	1059.8	0.101	1074.5	0.101	1089.3	0.101	1102.9
343.15	0.101	1037.5	0.101	1053.5	0.101	1068.2	0.101	1082.9	0.101	1096.4
353.15	0.101	1030.9	0.101	1047.0	0.101	1061.6	0.101	1076.3	0.808	1090.3
363.15	0.101	1023.9	0.808	1040.1	0.808	1054.7	0.808	1069.9	0.808	1083.1
373.15	0.808	1016.7	0.808	1033.1	0.808	1047.9	0.808	1062.4	0.808	1075.7
383.15	0.808	1009.0	0.808	1025.6	0.808	1040.3	0.808	1054.8	0.808	1067.7
393.15	0.808	1000.9	0.808	1017.4	0.808	1032.1	0.808	1046.4		
403.15	0.808	992.5	0.808	1008.9	0.808	1023.4				
413.15	0.808	984.1	0.808	1000.5						
423.15	0.808	973.4								

[a]: w_2 is the mass fraction of DEA in the (water + DEA) solutions.

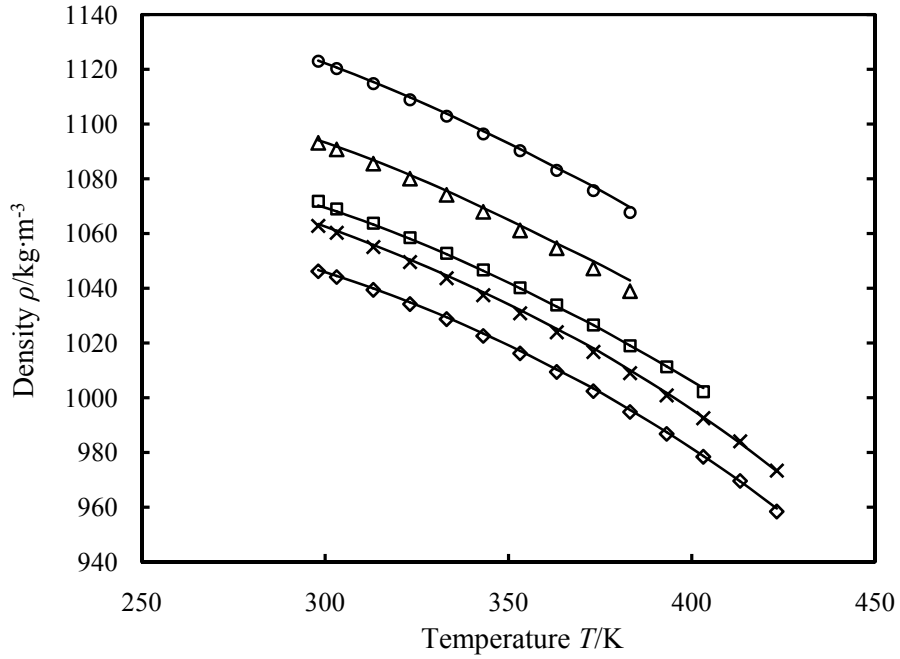

Figure 3-20. Densities of the H_2O (1) + DEA (2) + CO_2 (3) solutions as a function of temperature at different mass fractions of DEA and CO_2 loadings. Symbols refer to the experimental data: ◇, $w_2 = 0.3$, α = 0.1; □, $w_2 = 0.3$, α = 0.3; △, $w_2 = 0.3$, α = 0.5; ×, $w_2 = 0.4$, α = 0.1; ○, $w_2 = 0.4$, α = 0.5. Lines are the correlated data by eqs 3-12 to 3-17 with parameters from Table 3-18.

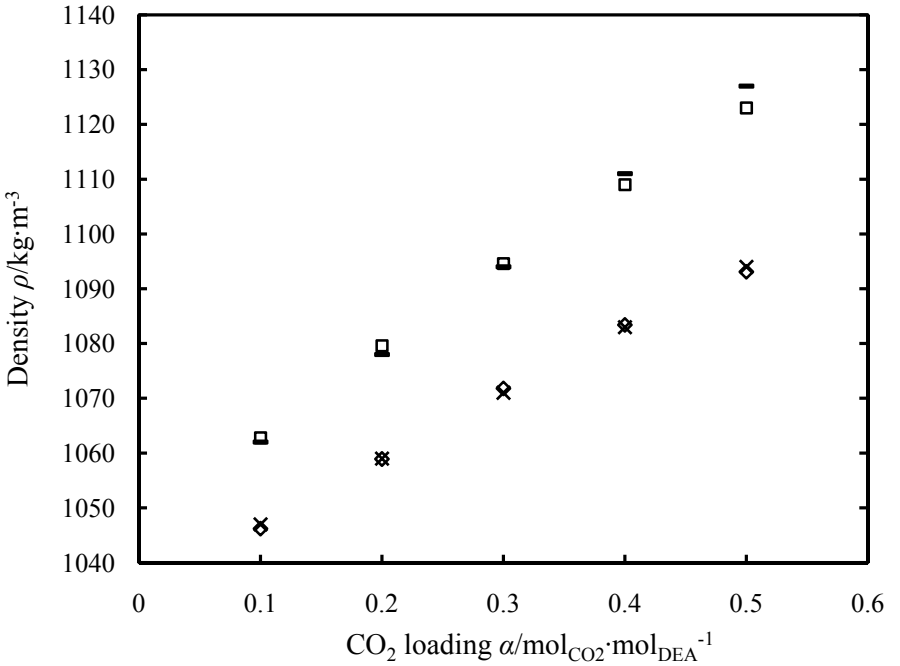

Figure 3-21. Comparison of measured and literature densities of H_2O (1) + DEA (2) + CO_2 (3) solutions as a function of CO_2 loading at 298.15 K. This work: ◇, $w_2 = 0.3$; □, $w_2 = 0.4$; and values from Weiland et al.[11]: ×, $w_2 = 0.3$; —, $w_2 = 0.4$.

Density measurements of water (1) + MDEA (2) + CO_2 (3) solutions at temperatures from (298.15 to 423.15) K are given in Tables 3-14 and 3-15. The mass fraction of MDEA in water

was 0.3 and 0.4. The CO_2 loading ranged from 0.1 to 0.5. Figure 3-22 displays densities of CO_2 loaded MDEA solutions as a function of temperature at different compositions. The trend is the same as for CO_2 loaded aqueous DEA solutions. The measured densities of CO_2 loaded aqueous MDEA solutions are very close to the data from Weiland et al.[11] as evidenced shown in Figure 3-23. The maximum deviation between this work and the literature is 3.3 $kg \cdot m^{-3}$, which is within the experimental uncertainty.

Table 3-14. Liquid Densities ρ for Water (1) + MDEA (2) + CO_2 (3) from T = (298.15 to 423.15) K and CO_2 Loading from α = (0.1 to 0.5) n_{CO2}/n_{MDEA} at w_2 = 0.3.[a]

	α									
	0.1		**0.2**		**0.3**		**0.4**		**0.5**	
***T*/K**	***p*/MPa**	***ρ*/kg·m^{-3}**	***p*/MPa**	***ρ*/kg·m^{-3}**	***p*/MPa**	***ρ*/kg·m^{-3}**	***p*/MPa**	***ρ*/kg·m^{-3}**	***p*/MPa**	***ρ*/kg·m^{-3}**
298.15	0.101	1036.1	0.101	1046.6	0.101	1056.5	0.101	1064.5	0.101	1074.7
303.15	0.101	1033.6	0.101	1044.1	0.101	1053.9	0.101	1061.9	0.101	1072.0
313.15	0.101	1028.3	0.101	1038.6	0.101	1048.3	0.101	1056.2	0.101	1066.3
323.15	0.101	1022.5	0.101	1032.7	0.101	1042.4	0.101	1050.3	0.101	1060.4
333.15	0.101	1016.3	0.101	1026.5	0.101	1036.1	0.101	1044.1	0.101	1054.2
343.15	0.101	1009.7	0.101	1019.9	0.101	1029.5	0.101	1037.5	0.101	1047.6
353.15	0.101	1002.7	0.101	1012.9	0.101	1022.5	0.808	1030.8	0.808	1040.9
363.15	0.808	995.6	0.808	1005.8	0.808	1015.0	0.808	1023.4	0.808	1033.0
373.15	0.808	988.1	0.808	998.1	0.808	1007.2	0.808	1015.6	0.808	1025.2
383.15	0.808	979.9	0.808	990.2	0.808	998.8	0.808	1007.5		
393.15	0.808	970.9	0.808	981.5	0.808	987.3				
403.15	0.808	961.8	0.808	971.3						
413.15	0.808	951.9	0.808	959.9						
423.15	0.808	944.1								

[a]: w_2 is the mass fraction of MDEA in the (water + MDEA) solutions.

Table 3-15. Liquid Densities ρ for Water (1) + MDEA (2) + CO_2 (3) from T = (298.15 to 423.15) K and CO_2 Loading from α = (0.1 to 0.5) n_{CO2}/n_{MDEA} at w_2 = 0.4.[a]

	α									
	0.1		**0.2**		**0.3**		**0.4**		**0.5**	
***T*/K**	***p*/MPa**	***ρ*/kg·m^{-3}**	***p*/MPa**	***ρ*/kg·m^{-3}**	***p*/MPa**	***ρ*/kg·m^{-3}**	***p*/MPa**	***ρ*/kg·m^{-3}**	***p*/MPa**	***ρ*/kg·m^{-3}**
298.15	0.101	1049.4	0.101	1063.3	0.101	1076.9	0.101	1089.8	0.101	1102.6
303.15	0.101	1046.5	0.101	1060.4	0.101	1073.9	0.101	1086.8	0.101	1099.5
313.15	0.101	1040.5	0.101	1054.2	0.101	1067.7	0.101	1080.6	0.101	1093.3
323.15	0.101	1034.1	0.101	1047.8	0.101	1061.3	0.101	1074.1	0.101	1086.9
333.15	0.101	1027.4	0.101	1041.1	0.101	1054.6	0.101	1067.4	0.101	1080.2
343.15	0.101	1020.4	0.101	1034.1	0.101	1047.5	0.808	1060.8	0.808	1072.9
353.15	0.101	1012.9	0.101	1026.7	0.808	1040.5	0.808	1053.5	0.808	1066.3
363.15	0.808	1005.2	0.808	1019.4	0.808	1032.5	0.808	1045.7	0.808	1057.8
373.15	0.808	997.3	0.808	1011.1	0.808	1024.6	0.808	1037.5		
383.15	0.808	988.8	0.808	1002.5	0.808	1015.7				
393.15	0.808	979.7	0.808	993.3						
403.15	0.808	970.4								
413.15	0.808	960.1								
423.15										

[a]: w_2 is the mass fraction of MDEA in the (water + MDEA) solutions.

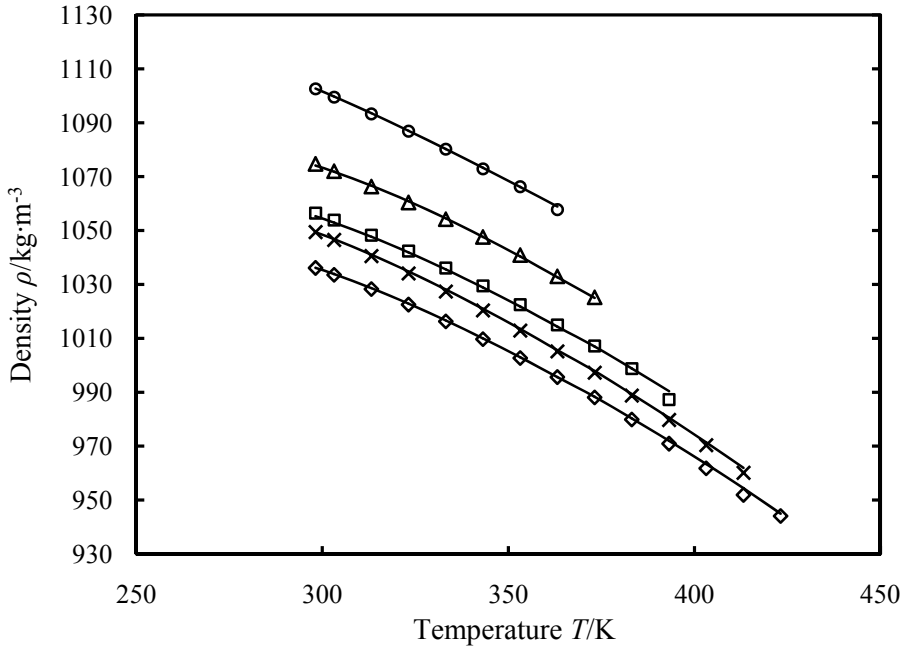

Figure 3-22. Densities of the H_2O (1) + MDEA (2) + CO_2 (3) solutions as a function of temperature at different mass fractions of MDEA and CO_2 loadings. Symbols refer to the experimental data: ◇, $w_2 = 0.3$, $\alpha = 0.1$; □, $w_2 = 0.3$, $\alpha = 0.3$; △, $w_2 = 0.3$, $\alpha = 0.5$; ×, $w_2 = 0.4$, $\alpha = 0.1$; ○, $w_2 = 0.4$, $\alpha = 0.5$. Lines are the correlated data by eqs 3-12 to 3-17 with parameters from Table 3-18.

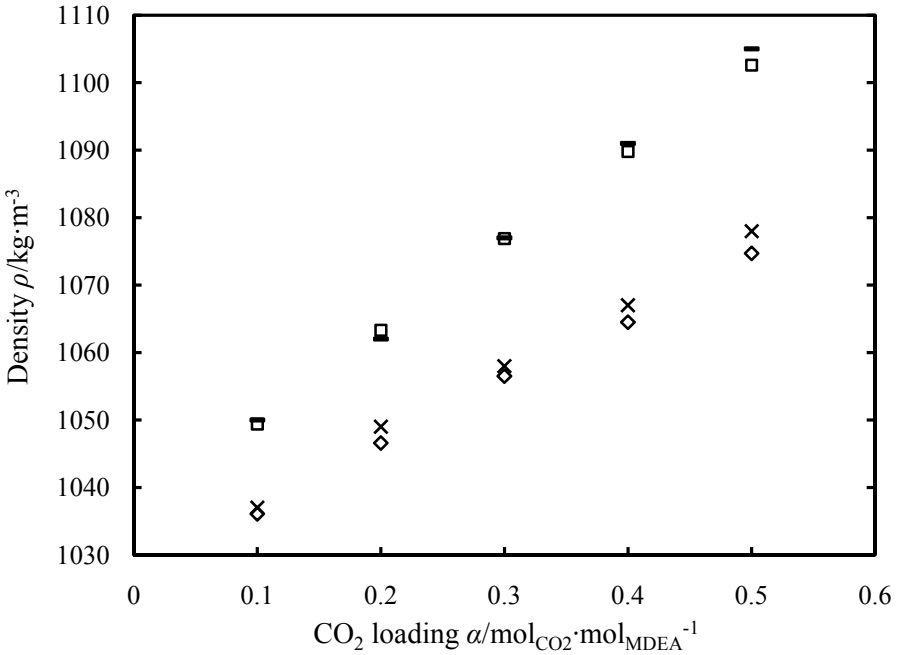

Figure 3-23. Comparison of measured and literature densities of H_2O (1) + MDEA (2) + CO_2 (3) solutions as a function of CO_2 loading at 298.15 K: This work ◇, $w_2 = 0.3$; □, $w_2 = 0.4$; and values from Weiland et al.[11] ×, $w_2 = 0.3$; —, $w_2 = 0.4$.

Some densities of CO_2 loaded aqueous amine solutions at high temperatures could not be measured because bubbles formed inside the external measuring cell. The pressure needed to prevent CO_2 desorption is obviously higher than that in our gas supply system which was limited to 8 bar.

3.4 Model for Data Representation

3.4.1 Density correlation for unloaded aqueous amine solutions

Densities of unloaded aqueous amine solutions from this work have been analysed by calculating the excess molar volumes. These are in turn correlated by the Redlich-Kister[17] equation with parameters being fitted by nonlinear regression analysis. The excess molar volumes are defined by:

$$V_m^{\,E} / \mathrm{m^3 \cdot mol^{-1}} = V_m / \mathrm{m^3 \cdot mol^{-1}} - ((V_1^{\,o} / \mathrm{m^3 \cdot mol^{-1}})x_1 + (V_2^{\,o} / \mathrm{m^3 \cdot mol^{-1}})x_2) \qquad (3\text{-}7)$$

where V_m represents the molar volume of the mixture. Furthermore V_j and x_j are molar volume and mole fraction respectively for component j. j = 1 refers to water, and 2 to amine. Superscript ^{o} refers to the pure component data.

The excess molar volumes are correlated with the polynomial equation due to Redlich-Kister by least-squares fitting of the parameters A_j.

$$V_m^{\,E} / \mathrm{m^3 \cdot mol^{-1}} = x_2(1-x_2)\sum_{j=0}^{i} A_j(1-2x_2)^j \times 10^{-6} \qquad (3\text{-}8)$$

Here A_j are adjustable parameters, and i represent an integer varying from 1 to a number that is justified by the measuring results. The excess molar volumes derived from the density data and used as basis for the correlation work are tabulated in Tables 3-5 to 3-7. i was chosen as 3 for unloaded aqueous MEA solutions and 4 for unloaded aqueous DEA and MDEA solutions. The fourth or fifth parameter reduces the average relative deviation (ARD) by roughly 75%. The correlated A_j values at each temperature were given in Appendix 3-5 to 3-7.

The parameters of the Redlich-Kister equation may in turn be fitted to an empirical function of temperature as suggested by Mandal et al.[12]. In their case a second order polynomial in temperature was used. As in their work the parameters and their temperature relationship was regressed in one go using nonlinear regression analysis. However, in this work it was found that a linear temperature relationship of the type:

$$A_j = a_{j0} + a_{j1}(T/\mathrm{K} - 273.15) \tag{3-9}$$

represented the data well for unloaded aqueous MEA solutions. And also a second order polynomial function of temperature:

$$A_j = a_{j0} + a_{j1}(T/\mathrm{K} - 273.15) + a_{j2}(T/\mathrm{K} - 273.15)^2 \tag{3-10}$$

represented the data well for unloaded aqueous DEA and MDEA solutions. The regression data were inspected and no systematic error related to temperature was seen. The fitted coefficients of the Redlich-Kister equation for excess molar volumes of unloaded aqueous MEA, DEA and MDEA solutions from (298.15 to 423.15) K are presented in Tables 3-16 and 3-17.

Table 3-16. Coefficients for Density Correlations of Unloaded Aqueous MEA Solutions.

Redlich-Kister parameter	R-K temperature coefficient	MEA
A_0	a_{00}	-2.643
	a_{01}	0.00260
A_1	a_{10}	-0.690
	a_{11}	0.00189
A_2	a_{20}	0.440
	a_{21}	-0.0000318
A_3	a_{30}	1.870
	a_{31}	-0.00123

Table 3-17. Coefficients for Density Correlations of Unloaded Aqueous DEA Solutions and Unloaded Aqueous MDEA Solutions.

Redlich-Kister parameter	R-K temperature coefficient	DEA	MDEA
A_0	a_{00}	-2.671	-4.952
	a_{01}	0.0032	0.0029
	a_{02}	0.000002	0.0001
A_1	a_{10}	-1.4185	-3.3629
	a_{11}	0.002	0.0096
	a_{12}	0.00004	0.000006
A_2	a_{20}	0.1593	7.3229
	a_{21}	-0.0062	0.0677
	a_{22}	0.0001	-0.0008
A_3	a_{30}	-6.6007	-24.645
	a_{31}	0.1139	-0.0891
	a_{32}	-0.0008	0.0017
A_4	a_{40}	7.9739	20.089
	a_{41}	-0.1226	0.0009
	a_{42}	0.0007	-0.0009

The maximum deviation between the measured densities of unloaded aqueous MEA solutions and the correlated data is 2.9 kg·m^{-3} and the average absolute deviation is 0.8 kg·m^{-3}. The maximum deviation for unloaded aqueous DEA solutions is 1.6 kg·m^{-3} and the average absolute deviation is 0.2 kg·m^{-3}. The maximum deviation for unloaded aqueous MDEA solutions is 1.2 kg·m^{-3} and the average absolute deviation is 0.3 kg·m^{-3}. These deviations are within the experimental error and negligible for engineering estimates. The good agreement between the measured densities of unloaded aqueous amine solutions and the correlated data by eqs 3-7 to 3-10 can also be seen from Figures 3-7, 3-11 and 3-14.

3.4.2 Density correlation for CO_2 loaded aqueous amine solutions

Densities of CO_2 loaded aqueous amine solutions from this work have been analysed by calculating the molar volumes of the mixture. These are in turn correlated by the equations from the literature with parameters being fitted by nonlinear regression analysis. The molar volumes are defined by:

$$V / \mathrm{m}^3 \cdot \mathrm{mol}^{-1} = \frac{x_1(M_1 / \mathrm{kg} \cdot \mathrm{mol}^{-1}) + x_2(M_2 / \mathrm{kg} \cdot \mathrm{mol}^{-1}) + x_3(M_3 / \mathrm{kg} \cdot \mathrm{mol}^{-1})}{\rho / \mathrm{kg} \cdot \mathrm{m}^{-3}} \qquad (3\text{-}11)$$

The molar volumes of CO_2 loaded aqueous amine solutions are correlated by eqs 3-12 and 3-13 as suggested by Weiland et al.[11].

$$V / \mathrm{m}^3 \cdot \mathrm{mol}^{-1} = x_1(V_1 / \mathrm{m}^3 \cdot \mathrm{mol}^{-1}) + x_2(V_2 / \mathrm{m}^3 \cdot \mathrm{mol}^{-1}) + (x_3 V_{CO_2} + x_1 x_2 V^* + x_2 x_3 V^{**}) \times 10^{-6} \qquad (3\text{-}12)$$

$$V^{**} = c + d x_2 \qquad (3\text{-}13)$$

Here V_j, x_j, M_j and ρ_j are mole volume, mole fraction, molar mass and density respectively for component j. No subscript refers to the mixture, j = 1 refers to water, 2 to amine, and 3 to CO_2. The molar volumes derived from the density data and used as basis for the correlation work were enclosed in Appendix 3-8. V_1 and V_2 were calculated from the density data of pure water and pure amine respectively and tabulated in Appendix 3-9. V_{CO2}, V^*, c and d are free parameters which were attained by nonlinear regression analysis with two independent variables. These correlated free parameters V_{CO2}, V^*, c and d at each temperature were given in Appendix 3-10.

The parameters V_{CO2}, V^*, c and d are in turn fitted to the polynomial function of temperature as shown in eqs 3-14 to 3-17.

$$V_{CO_2} = \sum_{k=0}^{n} a_k (T / \mathrm{K} - 273.15)^k \qquad (3\text{-}14)$$

$$V^* = \sum_{k=0}^{n} b_k (T/\mathrm{K} - 273.15)^k \quad (3\text{-}15)$$

$$c = \sum_{k=0}^{n} c_k (T/\mathrm{K} - 273.15)^k \quad (3\text{-}16)$$

$$d = \sum_{k=0}^{n} d_k (T/\mathrm{K} - 273.15)^k \quad (3\text{-}17)$$

With respect to CO_2 loaded aqueous MEA solutions, n equals to 4 for V_{CO2} and n equals to 3 for V^*, c and d. Moreover, a third order polynomial relationship to temperature (n = 3) was used for CO_2 loaded aqueous DEA solutions, while a second order polynomial equation (n = 2) was used for CO_2 loaded aqueous MDEA solutions. The values of the fitted coefficients in eqs 3-14 to 3-17 are presented in Table 3-18.

Table 3-18. Parameters for Density Correlations of CO_2 Loaded Aqueous MEA, DEA and MDEA Solutions.

Parameter	**Temperature coefficient**	MEA	DEA	MDEA
V_{CO_2}	a_0	12.6520	-99.03	150.76
	a_1	-0.4065	1.5623	-6.6205
	a_2	0.0096	-0.003	0.0638
	a_3	-0.000077	-0.00006	0
	a_4	0.00000017	0	0
V^*	b_0	-2.6676	-4.4968	-7.8996
	b_1	0.0016	0.0391	0.02
	b_2	0.00013	-0.0006	-0.00005
	b_3	-0.0000015	0.000003	0
c	c_0	-25.3952	2569.2	-4014.7
	c_1	1.2716	-40.791	185.57
	c_2	-0.03845	0.117	-1.7894
	c_3	0.00023	0.0012	0
d	d_0	73.6487	-15362	26682
	d_1	-3.9579	251.53	-1250.2
	d_2	0.1029	-0.8198	12.047
	d_3	-0.00059	-0.0065	0

The maximum deviation between the measured densities of CO_2 loaded aqueous MEA solutions and the correlated data is 16 $kg \cdot m^{-3}$ and the average absolute deviation is 3.8 $kg \cdot m^{-3}$. The maximum deviation between the measured densities of CO_2 loaded aqueous DEA solutions and the correlated data is 3.9 $kg \cdot m^{-3}$ and the average absolute deviation is 0.6 $kg \cdot m^{-3}$. The maximum deviation between the measured CO_2 loaded aqueous MDEA solutions and the correlated data is 3.8 $kg \cdot m^{-3}$ and the average absolute deviation is 0.5 $kg \cdot m^{-3}$. The agreement between the correlated and experimental densities is satisfactory. These deviations are within the experimental error. The good consistency between the measured densities of CO_2 loaded

aqueous amine solutions and the correlated results can also be seen from Figures 3-17, 3-20 and 3-22.

3.5 Assessment of Experimental Uncertainties

The assessment of the measured densities of unloaded and CO_2 loaded aqueous amine solutions are presented in this section.

3.5.1 The assessment method for uncertainties of density measurements

Uncertainties of the density measurements in this work have been analysed with the international recommendations for reporting uncertainties in mind (NIST TN 1297; ISO guide "GUM"; also adopted by ANSI). The reported densities should be broken down to analyse the effect of variables in our measurement program. This could be written as:

$$\rho = f(T, w_2, \alpha, \rho_{\text{instrument}}) \tag{3-18}$$

where the variables are temperature, mass fraction of amine, CO_2 loading and the instrument error. The combined standard uncertainty can be calculated by:

$$u_c^2(\rho) = \sum_{i=1}^{N} \left(\frac{\partial \rho}{\partial x_i}\right)^2 u_i^2(x_i) \tag{3-19}$$

The combined expanded uncertainty can be calculated by:

$$U_c(\rho) = k u_c(\rho) \text{ (level of confidence = 0.95, } k = 2) \tag{3-20}$$

3.5.2 Uncertainties of density measurements of unloaded amine solutions

The uncertainty of density measurements of unloaded aqueous amine solutions arises from several sources involved in the temperature rise measurement, the error from mass fraction of amine and instrument error. Take unloaded aqueous MEA solutions as an example, the uncertainty calculations are shown as follows:

(1) The uncertainty caused by the temperature rise measurement.

The temperature accuracy is specified as ± 0.03 K for DMA 4500 used at $T < 373.15$ K, and ± 0.05 K for DMA HP used at $T \geq 373.15$ K. Based on our measurement results, the change of density is 0.8 kg·m^{-3} when the change of temperature is 1 K. So the uncertainty that is caused by the temperature rise measurement is:

$$\frac{0.8\ \mathrm{kg\cdot m^{-3}}}{1\ \mathrm{K}} \times 0.03\ \mathrm{K} = 0.024\ \mathrm{kg\cdot m^{-3}}, \quad \text{at } T < 373.15\ \mathrm{K}$$

$$\frac{0.8\ \mathrm{kg\cdot m^{-3}}}{1\ \mathrm{K}} \times 0.05\ \mathrm{K} = 0.04\ \mathrm{kg\cdot m^{-3}}, \quad \text{at } T \geq 373.15\ \mathrm{K}$$

(2) The uncertainty caused by the error from mass fraction of MEA.

The accuracy of mass fraction of MEA is estimated as ± 0.005 based on the purity of MEA (0.995). Based on our measurement results, the maximum change of density is 6.6 $\mathrm{kg\cdot m^{-3}}$ when the change of mass fraction is 0.1. So the uncertainty the caused by the error from mass fraction of MEA is:

$$\frac{6.6\ \mathrm{kg\cdot m^{-3}}}{0.1} \times 0.005 = 0.33\ \mathrm{kg\cdot m^{-3}}$$

(3) The uncertainty caused by instrument accuracy.

Instrument accuracy for DMA 4500 used at $T < 373.15$ K is given as 0.05 $\mathrm{kg\cdot m^{-3}}$ by the manufacturer, while for DMA HP used at $T \geq 373.15$ K is given as 0.1 $\mathrm{kg\cdot m^{-3}}$.

Then the combined standard uncertainty of density measurements of unloaded aqueous MEA solutions can be calculated by combining the various sources of uncertainty using a root-sum-of-squares formula.

$$u_c(\rho) = \sqrt{(0.024\ \mathrm{kg\cdot m^{-3}})^2 + (0.33\ \mathrm{kg\cdot m^{-3}})^2 + (0.05\ \mathrm{kg\cdot m^{-3}})^2} = 0.335\ \mathrm{kg\cdot m^{-3}}, \text{ at } T < 373.15\ \mathrm{K}$$

$$u_c(\rho) = \sqrt{(0.04\ \mathrm{kg\cdot m^{-3}})^2 + (0.33\ \mathrm{kg\cdot m^{-3}})^2 + (0.1\ \mathrm{kg\cdot m^{-3}})^2} = 0.347\ \mathrm{kg\cdot m^{-3}}, \text{ at } T \geq 373.15\ \mathrm{K}$$

So the combined expanded uncertainty of density measurements of unloaded aqueous MEA solutions is $U_c(\rho) = ku_c(\rho) = 0.68\ \mathrm{kg\cdot m^{-3}}$ at $T < 373.15$ K and $U_c(\rho) = ku_c(\rho) = 0.70\ \mathrm{kg\cdot m^{-3}}$ at $T \geq 373.15$ K (level of confidence = 0.95, $k = 2$). The uncertainties of density measurements of unloaded aqueous amine solutions are shown in Table 3-19.

Table 3-19. Uncertainties of Density Measurements of Unloaded Aqueous Amine Solutions.

Uncertainties	Amine type		
	MEA	**DEA**	**MDEA**
$u(T)$	0.03 K at $T < 373.15$ K 0.05 K at $T \geq 373.15$ K	0.03 K at $T < 373.15$ K 0.05 K at $T \geq 373.15$ K	0.03 K at $T < 373.15$ K 0.05 K at $T \geq 373.15$ K
$u(w_2)$	0.005	0.02	0.02
Instrument accuracy	0.05 kg·m^{-3} at $T < 373.15$ K 0.1 kg·m^{-3} at $T \geq 373.15$ K	0.05 kg·m^{-3} at $T < 373.15$ K 0.1 kg·m^{-3} at $T \geq 373.15$ K	0.05 kg·m^{-3} at $T < 373.15$ K 0.1 kg·m^{-3} at $T \geq 373.15$ K
$u_c(\rho)$	0.335 kg·m^{-3} at $T < 373.15$ K 0.347 kg·m^{-3} at $T \geq 373.15$ K	1.755 kg·m^{-3} at $T < 373.15$ K 1.757 kg·m^{-3} at $T \geq 373.15$ K	1.501 kg·m^{-3} at $T < 373.15$ K 1.504 kg·m^{-3} at $T \geq 373.15$ K
$U_c(\rho)$	0.67 kg·m^{-3} at $T < 373.15$ K 0.69 kg·m^{-3} at $T \geq 373.15$ K	3.51 kg·m^{-3}	3.00 kg·m^{-3} at $T < 373.15$ K 3.01 kg·m^{-3} at $T \geq 373.15$ K

3.5.3 Uncertainties of density measurements of CO_2 loaded amine solutions

The uncertainty of density measurements of CO_2 loaded aqueous amine solutions arises from several sources involved in the temperature rise measurement, the error from mass fraction of amine, the error from CO_2 loading amount and instrument error. Take CO_2 loaded aqueous DEA solutions as an example, the uncertainty calculations are shown as follows:

(1) The uncertainty caused by the temperature rise measurement.

The temperature accuracy is specified as ± 0.03 K for DMA 4500 used at $T < 373.15$ K, and ± 0.05 K for DMA HP used at $T \geq 373.15$ K. Based on our measurement results, the change of density is 0.7 kg·m^{-3} when the change of temperature is 1 K. So the uncertainty that caused by the temperature rise measurement is:

$$\frac{0.7\ \text{kg}\cdot\text{m}^{-3}}{1\ \text{K}} \times 0.03\ \text{K} = 0.021\ \text{kg}\cdot\text{m}^{-3}, \quad \text{at } T < 373.15\ \text{K}$$

$$\frac{0.7\ \text{kg}\cdot\text{m}^{-3}}{1\ \text{K}} \times 0.05\ \text{K} = 0.035\ \text{kg}\cdot\text{m}^{-3}, \quad \text{at } T \geq 373.15\ \text{K}$$

(2) The uncertainty caused by the error from mass fraction of DEA.

Because the purity of DEA is 0.98, the accuracy of mass fraction of DEA is estimated as ± 0.02. This accuracy is a conservative error since part of the 0.02 unknown with respect to fraction is likely to be water. Based on our measurement results, the maximum change of density is 29.9 kg·m^{-3} when the change of mass fraction is 0.1. So the uncertainty that is caused by the error from mass fraction of DEA is:

$$\frac{29.9\ \mathrm{kg\cdot m^{-3}}}{0.1}\times 0.02 = 5.98\ \mathrm{kg\cdot m^{-3}}$$

(3) The uncertainty caused by the error from CO_2 loading.

The way to titrate CO_2 loaded amine solution is to do two parallel experiments and then to make an average if there is no big difference between them. So the accuracy of CO_2 loading can be calculated based on it, which is estimated as ± 0.003. Based on our measurement results, the maximum change of density is 16.4 $\mathrm{kg\cdot m^{-3}}$ when the change of CO_2 loading is 0.1. So the uncertainty that is caused by the error from CO_2 loading is:

$$\frac{16.4\ \mathrm{kg\cdot m^{-3}}}{0.1}\times 0.003 = 0.492\ \mathrm{kg\cdot m^{-3}}$$

(4) The uncertainty caused by instrument accuracy.

Instrument accuracy for DMA 4500 used at $T < 373.15$ K is given as 0.05 $\mathrm{kg\cdot m^{-3}}$ by the manufacturer, while for DMA HP used at $T \geq 373.15$ K is given as 0.1 $\mathrm{kg\cdot m^{-3}}$.

Then the combined standard uncertainty of density measurements of CO_2 loaded aqueous DEA solutions can be calculated by combining the various sources of uncertainty using a root-sum-of-squares formula.

$$u_c(\rho) = \sqrt{0.021^2 + 5.98^2 + 0.492^2 + 0.05^2}\ \mathrm{kg\cdot m^{-3}} = 6.0\ \mathrm{kg\cdot m^{-3}}, \text{ at } T < 373.15\ \mathrm{K}$$

$$u_c(\rho) = \sqrt{0.035^2 + 5.98^2 + 0.492^2 + 0.1^2}\ \mathrm{kg\cdot m^{-3}} = 6.0\ \mathrm{kg\cdot m^{-3}}, \text{ at } T \geq 373.15\ \mathrm{K}$$

So the combined expanded uncertainty of density measurements of CO_2 loaded aqueous DEA solutions is $U_c(\rho) = ku_c(\rho) = 12\ \mathrm{kg\cdot m^{-3}}$ (level of confidence = 0.95, k = 2). The uncertainties of density measurements of CO_2 loaded aqueous amine solutions are shown in Table 3-20.

Table 3-20. Uncertainties of Density Measurements of CO_2 loaded Aqueous Amine Solutions.

Uncertainties	Amine type		
	MEA	**DEA**	**MDEA**
$u(T)$	0.03 K at $T < 373.15$ K 0.05 K at $T \geq 373.15$ K	0.03 K at $T < 373.15$ K 0.05 K at $T \geq 373.15$ K	0.03 K at $T < 373.15$ K 0.05 K at $T \geq 373.15$ K
$u(w_2)$	0.005	0.02	0.02
$u(\alpha)$	0.003	0.003	0.003
Instrument accuracy	0.05 kg·m^{-3} at $T < 373.15$ K 0.1 kg·m^{-3} at $T \geq 373.15$ K	0.05 kg·m^{-3} at $T < 373.15$ K 0.1 kg·m^{-3} at $T \geq 373.15$ K	0.05 kg·m^{-3} at $T < 373.15$ K 0.1 kg·m^{-3} at $T \geq 373.15$ K
$u_c(\rho)$	2.163 kg·m^{-3} at $T < 373.15$ K 2.165 kg·m^{-3} at $T \geq 373.15$ K	6.0 kg·m^{-3}	5.6 kg·m^{-3}
$U_c(\rho)$	4.33 kg·m^{-3}	12 kg·m^{-3}	11.2 kg·m^{-3}

The uncertainty that is caused by the error from mass fraction of amine dominates in the uncertainties of unloaded and CO_2 loaded aqueous amine solutions density measurements.

3.6 Conclusions

In this study, density data for the systems water + MEA, water + DEA and water + MDEA at amine mass fractions from 0.3 to 1.0 at temperatures from (298.15 to 423.15) K have been measured. The data are correlated using excess molar volumes to represent the deviations from ideal mixtures. Derived excess molar volumes of the binary system were correlated by the Redlich-Kister equation. The parameters of the Redlich-Kister equation were in turn fitted to a linear function of temperature for unloaded aqueous MEA solutions, and a second order polynomial function of temperature for unloaded aqueous DEA and MDEA solutions. The average absolute deviation between the measured densities and the correlated data is 0.8 kg·m^{-3} for unloaded aqueous MEA solutions, 0.2 kg·m^{-3} for unloaded aqueous DEA solutions, and 0.3 kg·m^{-3} for unloaded aqueous MDEA solutions. These deviations between the measured results and the correlated data by the regressed models are less than the experimental error.

Densities of CO_2 loaded aqueous MEA solutions have been measured at temperatures from (298.15 to 413.15) K with the mass fraction of MEA of 0.3, 0.4, 0.5, and 0.6. Density

data for the systems water + DEA + CO_2 and water + MDEA + CO_2 at different amine mass fractions (0.3, 0.4) and different CO_2 loadings (0.1, 0.2, 0.3, 0.4, 0.5) at temperatures from (298.15 to 423.15) K have also been measured. Derived molar volumes of the ternary system were fitted by the equations from Weiland et al.[11] The parameters V_{CO2}, V^*, c and d were in turn fitted to the polynomial function of temperature. The average absolute deviation between the measured densities and the correlated data is 3.8 kg·m^{-3} for CO_2 loaded aqueous MEA solutions, 0.6 kg·m^{-3} for CO_2 loaded aqueous DEA solutions and 0.5 kg·m^{-3} for CO_2 loaded aqueous MDEA solutions. These deviations between the measured results and the correlated data by the regressed models are negligible for engineering estimates.

Notation

c	concentration, mol/L
m	mass, g
M	molar mass, kg/mol
n	mole number, mol
T	temperature, K
u	standard uncertainty
U	expanded standard uncertainty
V	molar volume, m^3/mol
V^E	excess molar volume, m^3/mol
V_{HCl}	volume of titrimetric HCl solution, ml or L
V_{NaOH}	volume of titrimetric NaOH solution, ml or L
w	mass fraction
x	mole fraction

Greek letters

α	CO_2 loading, moles of CO_2/moles of amine
ρ	density, kg/m^3

Subscripts

1	water
2	amine
3	CO_2
BS	blank sample
c	combined
m	mixture

Superscripts

o	pure component

References

(1) Leibush, A. G.; Shorina, E. G. Physico-Chemical Properties of Ethanolamine. *Zh. Prikl. Khim*. **1947**, *20*, 69-76.

(2) Touhara, H.; Okazaki, S.; Okino, F.; Tanaka, H.; Ikari, K.; Nakanishi, K. Thermodynamic properties of aqueous mixtures of hydrophilic compounds 2. Aminoethanol and its methyl derivatives. *J. Chem. Thermodyn.* **1982**, *14*, 145-156.

(3) Murrieta-Guevara, F.; Rodriguez, A. T. Liquid Density as a Function of Temperature of Five Organic Solvents. *J. Chem. Eng. Data* **1984**, *29*, 204-206.

(4) Wang, Y. W.; Xu, S.; Otto, F. D.; Mather, A. E. Solubility of N_2O in alkanolamines and in mixed solvents. *The Chem. Eng. J*. **1992**, *48*, 31-40.

(5) Li, M. H.; Shen, K. P. Densities and Solubilities of Solutions of Carbon Dioxide in Water + Monoethanolamine + *N*-Methyldiethanolamine. *J. Chem. Eng. Data* **1992**, *37*, 288-290.

(6) DiGullio, R. M.; Lee, R. J.; Schaeffer, S. T.; Brasher, L. L.; Teja, A. S. Densities and Viscosities of the Ethanolamines. *J. Chem. Eng. Data* **1992**, *37*, 239-242.

(7) Pagé, M.; Huot, J.; Jolicoeur, C. A comprehensive thermodynamic investigation of water-ethanolamine mixtures at 10, 25, and 40°C. *Can. J. Chem*. **1993**, *71*, 1064-1072.

(8) Maham, Y.; Teng, T. T.; Hepler, L. G.; Mather, A. E. Densities, Excess Molar Volumes, and Partial Molar Volumes for Binary Mixtures of Water with Monoethanolamine, Diethanolamine, and Triethanolamine from 25 to 80°C. *J. Solution Chem.* **1994**, *23*, 195-205.

(9) Li, M.; Lie, Y. Densities and Viscosities of Solutions Monoethanolamine + N-Methyldiethanolamine + Water and Monoethanolamine + 2-Amino-2-methyl-1-propanol + Water. *J. Chem. Eng. Data* **1994**, *39*, 444-447.

(10) Lee, M.; Lin, T. Density and Viscosity for Monoethanolamine + Water, + Ethanol, and + 2-Propanol. *J. Chem. Eng. Data* **1995**, *40*, 336-339.

(11) Weiland, R. H.; Dingman, J. C.; Cronin, D. B.; Browning, G. J. Density and Viscosity of Some Partially Carbonated Aqueous Alkanolamine Solutions and Their Blends. *J. Chem. Eng. Data* **1998**, *43*, 378-382.

(12) Mandal, B. P.; Kundu, M.; Bandyopadhyay, S. S. Density and Viscosity of Aqueous Solutions of (N-Methyldiethanolamine + Monoethanolamine), (N-Methyldiethanolamine + Diethanolamine), (2-Amino-2-methyl-1-propanol + Monoethanolamine), (2-Amino-2-methyl-1-propanol + Diethanolamine). *J. Chem. Eng. Data* **2003**, *48*, 703-707.

(13) Pouryosefi, F.; Idem, R. O. New Analytical Technique for Carbon Dioxide Absorption Solvents. *Ind. Eng. Chem. Res.* **2008**, *47*, 1268-1276.

(14) Amundsen, T. G.; Øi, L. E.; Eimer, D. A. Density and Viscosity of Monoethanolamine + Water + Carbon Dioxide from (25 to 80) °C. *J. Chem. Eng. Data* **2009**, *54*, 3096-3100.
(15) Rinker, E. B.; Oelschlager, D. W.; Colussi, A. T.; Henry, K. R.; Sandall, O. C. Viscosity, Density, and Surface Tension of Binary Mixtures of Water and *N*-Methyldiethanolamine and Water and Diethanolamine and Tertiary Mixtures of These Amines with Water over the Temperature Range 20-100 °C. *J. Chem. Eng. Data* **1994**, *39*, 392-395.
(16) Spasojević, V. D.; Šerbanović, S. P.; Djordjević, B. D.; Kijevčanin, M. L. Densities, Viscosities, and Refractive Indices of Aqueous Alkanolamine Solutions as Potential Carbon Dioxide Removal Reagents. *J. Chem. Eng. Data* **2013**, *58*, 84-92.
(17) Muhammad, A.; Mutalib, M. A.; Murugesan, T.; Shafeeq, A. Density and Excess properties of Aqueous *N*-Methyldiethanolamine Solutions from (298.15 to 338.15) K. *J. Chem. Eng. Data* **2008**, *53*, 2217-2221.
(18) Harvey, A. H. *Thermodynamic Properties of Water*; NIST: Boulder, Colorado, 1998.
(19) Redlich, O.; Kister, A. T. Algebraic representation of thermodynamic properties and the classification of solutions. *Ind. Eng. Chem.* **1948**, *40*, 345-348.

4. Surface tension measurements of aqueous MEA solutions

Abstract

Surface tensions of aqueous MEA solutions were measured at temperatures from (303.15 to 333.15) K by the sessile bubble method. The mass fraction of MEA ranged from 0 to 1.0. Surface tensions of aqueous MEA solutions decrease significantly as temperature increases. The temperature dependency of surface tension of aqueous MEA solutions is approximately linear in the temperature range considered. Moreover, surface tensions of aqueous MEA solution decrease as mole fraction of MEA increases. Measured surface tensions of aqueous MEA solutions in this work were compared with Vázquez et al.'s data. The experimental surface tensions were correlated with temperature by a linear relationship. The correlated surface tensions by the linear equation and the experimental data have very good agreement. The surface tensions of aqueous MEA solutions were correlated with mole fraction of MEA by both an empirical model and a chemical model. The chemical model shows better agreement with the experimental surface tension data than the empirical model.

4.1 Introduction

Monoethanolamine (MEA) has been used for absorption of acid gases since 1930. Mass fraction of MEA was generally increased from 0.15 to 0.30 by 1970, and this has been standard since then although higher compositions have been explored on a research basis. Recent attention given to CO_2 capture from exhaust gases in order to avoid global warming has caused increased interest in MEA due to its high affinity for CO_2. Very large absorbent flows would need to be circulated. A further increase in mass fraction of MEA would help to reduce these flows. Surface tensions of these solutions are needed to perform a variety of engineering calculations. Surface tension (γ) is defined as force per unit length; the unit is N/m.

Surface tension data for aqueous amine solutions have previously been reported by a number of authors. These are summarized in Table 4-1 including the range of concentration and temperature, the number of points measured and also the method used by all authors. Different measuring methods of surface tension had been used by the authors, such as the

Wilhelmy plate method, the capillary-rise technique and pendant drop method. The Wilhelmy plate method measures the force due to wetting for a plate which is perpendicular to the liquid surface.[5] In the capillary-rise technique, the end of a capillary is immersed into the solution.[6] The height of the solution inside the capillary is measured. Pendant drop method measures the geometry of a drop which is hanging from a tip or a clinging bubble.[5]

In the present work the surface tensions of aqueous MEA solutions were measured with mass fractions of MEA from 0 to 1.0 at (303.15 to 333.15) K using the sessile drop method. Surface tension measurements of unloaded aqueous DEA and MDEA solutions and CO_2 loaded aqueous amine solutions were performed by another Ph.D student at Telemark University College.

Table 4-1. Reported Surface Tension Measurements of Water (1) + Amines (2).

Source	Components	w_2	T/K	Number of measurements	Method*
Vázquez et al.[1] (1997)	water + MEA	0 to 1	298.15 to 323.15	78	WP
	water + AMP	0 to 1	298.15 to 323.15	84	
	water + MEA + AMP	MEA/AMP 0/0.5 to 0.5/0	298.15 to 323.15	36	
Alvarez et al.[2] (1998)	water + MDEA	0 to 1	298.15 to 323.15	84	WP
	water + MDEA + MEA	MDEA/MEA 0/0.5 to 0.5/0	298.15 to 323.15	36	
	water + MDEA + DEA	MDEA/DEA 0/0.5 to 0.5/0	298.15 to 323.15	36	
	water + MDEA + AMP	MDEA/AMP 0/0.5 to 0.5/0	298.15 to 323.15	36	
Maham and Mather[3] (2001)	water + MDEA	0 to 1	298.15 to 328.15	48	CR
	water + DMEA	0 to 1	298.15 to 328.15	48	
Aguila-Hernández et al.[4] (2001)	water + DEA	0.1 to 0.3	293.15 to 363.15	21	DCR PD
	water + MDEA	0.1 to 0.5	323.15	5	
	water + MDEA + DEA	MDEA/DEA 0/0.5 to 0.5/0	313.15 to 333.15	27	

*WP: The Wilhelmy plate principle / CR: The capillary-rise technique / DCR: Differential capillary-rise method. / PD: Pendant drop method

4.2 Experimental Section

4.2.1 Preparing aqueous MEA solutions

This part has been introduced in detail in Section 3.2.1. Pure MEA and Milli-Q water (18.2 MΩ-cm) were degassed and then mixed together. The purity of MEA is 0.995. Aqueous MEA solutions were prepared by an analytical balance with an accuracy of ± 0.1 mg. Nitrogen was blown to the conical flask for protection after the mixed solution was made.

4.2.2 Measuring instrument and procedure

Surface tension was measured at 10 K intervals, from (303.15 to 333.15) K using a Rame-Hart Model 500 Advanced Goniometer with DROPimage Advanced v2.4, which employs the pendant or sessile drop method. The picture of this instrument is shown in Figure 4-1.

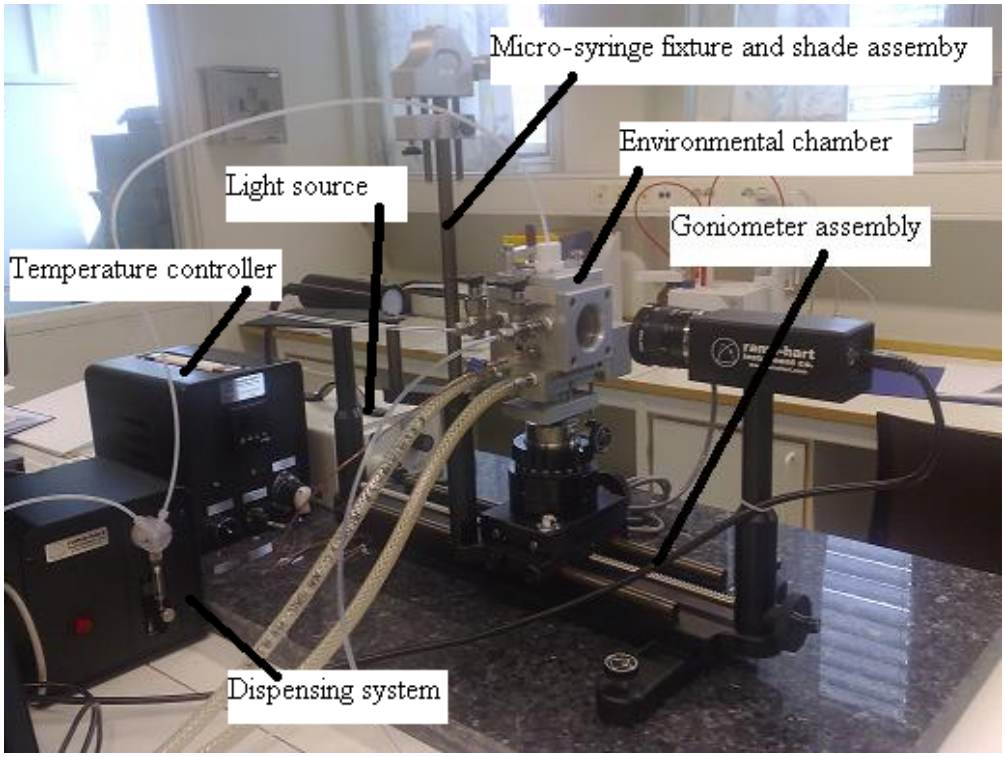

Figure 4-1. Rame-Hart Model 500 Advanced Goniometer

The Rame-Hart Model 500 Advanced Goniometer consists of Goniometer assembly (The components of it were illustrated in Figure 4-2), light source with country-specific cordset, the connected PC and LCD with DROPimage program installed, automated dispensing system, an environmental chamber and the temperature controller. A micro-syringe fixture and shade assembly (shade excluded with wafer support) will be needed when the environmental

chamber is absent. The surface tension is calculated by use of the drop or bubble geometry size which is obtained by digitizing the image from the camera.

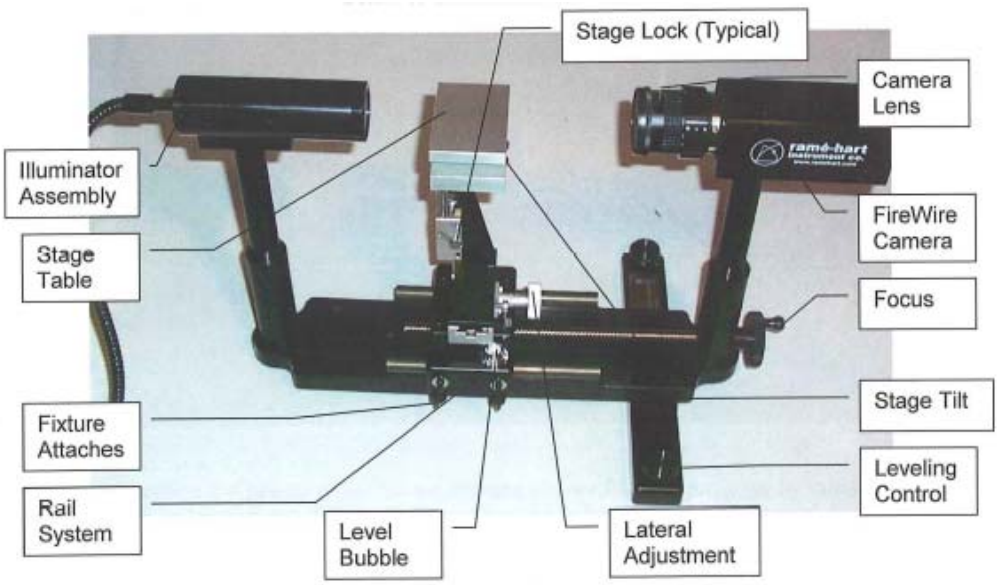

Figure 4-2. The primary components of the Goniometer assembly.[7]

This surface tension measurement is based on the measurement of the static shape of an axisymmetric drop or bubble.[8] The types of drop or bubble are divided into pendant and sessile according to their shape. The pendant drop or bubble is long and narrow. The sessile drop or bubble is short and wide. A pendant drop is one which hang down from a tip. A sessile drop is a sitting drop that rests on a surface. Moreover, a bubble supported from below is called a pendant bubble, and a bubble supported from above is called a sessile bubble.[8] The illustration of these four types of drops and bubbles will be shown later (See Figure 4-9).

The pendant drop method that measures a liquid drop which hangs down from a tip has not been adopted because the concentration of component in the drop changes due to evaporation when the temperature is rising. In addition, the temperature of small drop is not easy to monitor and control. A bubble which hangs down from a tip was measured instead. The sessile bubble method was used in this work. The sketch of the experimental set-up is shown in Figure 4-3. A cuvette was used to contain liquid and make sure the light did not change directions. The way to generate the bubble is by first sucking the liquid from the cuvette to the needle by the dispenser, and then sucking the gas into the needle, and finally pushing the liquid and gas in the needle which are sucked earlier to the cuvette. The picture of the bubble is shown in Figure 4-4.

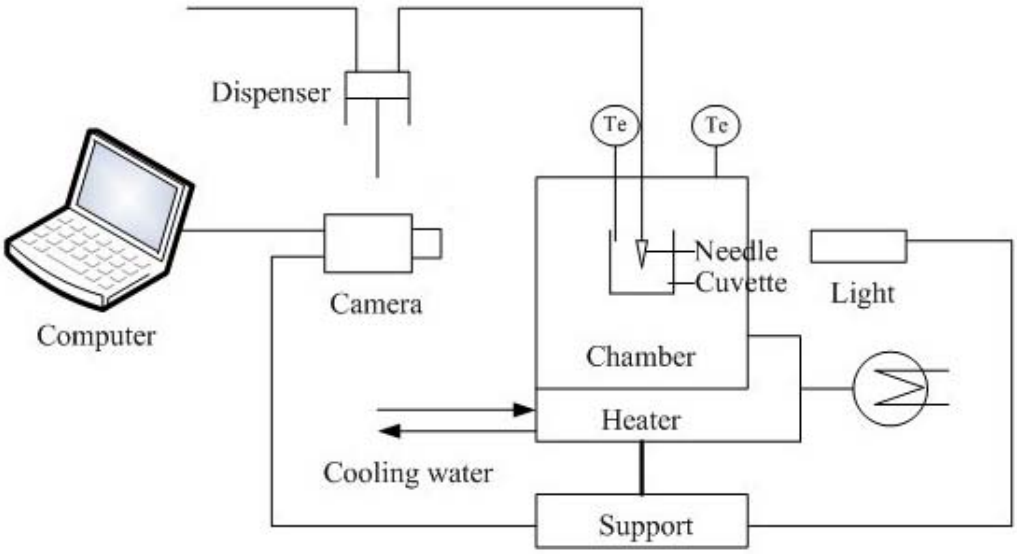

Figure 4-3. The sketch of the experimental set-up of surface tension measurements.

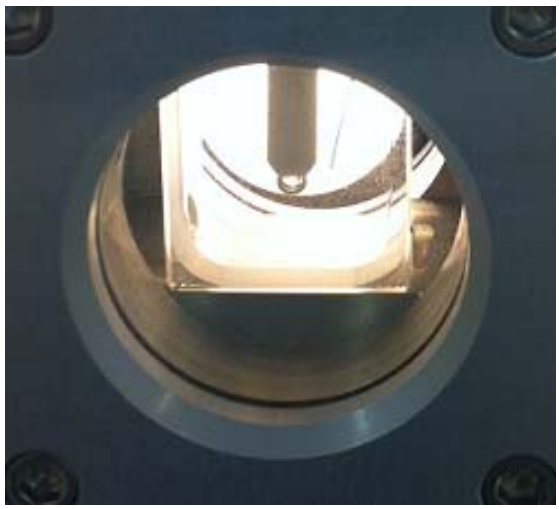

Figure 4-4. The picture of the generated bubble.

There are four main parts in the procedure of surface tension measurements by Rame-Hart Model 500 Advanced Goniometer; calibrating the system, starting a new experiment and setting the parameters, using the dispenser to generate the bubble, and setting the crosshair cursor position to perform the measurement.

a) Calibrating the system

Calibration should be performed when the magnification of the optical system is changed. Because the ratio of image size to real size will be measured during calibration. Once focal distance has been changed, the ratio should be measured again. An object with known size can be used for calibration (see Figure 4-5). Three types of methods e.g. Horizontal, Vertical and Sphere can be used in the calibration procedure.

Figure 4-5. A known object. The diameter of the sphere is 4 mm. The diameter and height of the cylinder are 4 mm and 13 mm, respectively.

b) Starting a new experiment and setting the parameters

A new experiment can be started through "**New Experiment Wizard**" in the DROPimage program. There are three types of experiments which are Surface Tension-Pendant, Surface Tension-Sessile, and Contact Angle. "Surface Tension-Pendant" is used to measure the surface tension of pendant drop or bubble. "Surface Tension-Sessile" is used to measure the surface tension of sessile drop or bubble. "Contact Angle" is used to measure the contact angle between two phases. In this work, the type of "Surface Tension-Sessile" was selected.

Since a bubble was measured, air and aqueous MEA solutions were chosen as bubble phase and external phase respectively in the program. Because a Teflon needle was used to generate the bubble, Teflon was chosen as solid phase. Aqueous MEA solutions at different mass fractions and temperatures as the new materials should be added in the "**Phase Editor**". The densities are required data of a new material that the program uses to determine the measurement geometry and to make the calculations. Equidistant time interval between each measurement was chosen in this work. The total number of measurements was set to 10 which means the program will measure the same bubble 10 times at the same time interval and then give the average surface tension value. "**No volume step**" which produces a constant volume measurement was selected in the dialog box "**Volume control parameters**".

c) Using the dispenser to generate the bubble

The program supports a dispenser to control the volume of drop or bubble. The steps of generating a bubble in detail by the dispenser were given in Appendix 4-2.

d) Setting the crosshair cursor position and performing the measurement

The program takes the position of the crosshair cursor as a reference to detect the edge of drop or bubble. The horizontal line should be at the extreme top for this sessile bubble, while the vertical line should be close to the centerline of the image as shown in Figure 4-6. After setting the crosshair cursor position, the "**Measure**" button can be pressed to perform the measurement. Then the surface tension results will be given automatically. The difficulty and key point of this measurement is to get the bubble to be symmetric to its vertical axis. The head of the needle needs to be completely flat and horizontal during measurements.

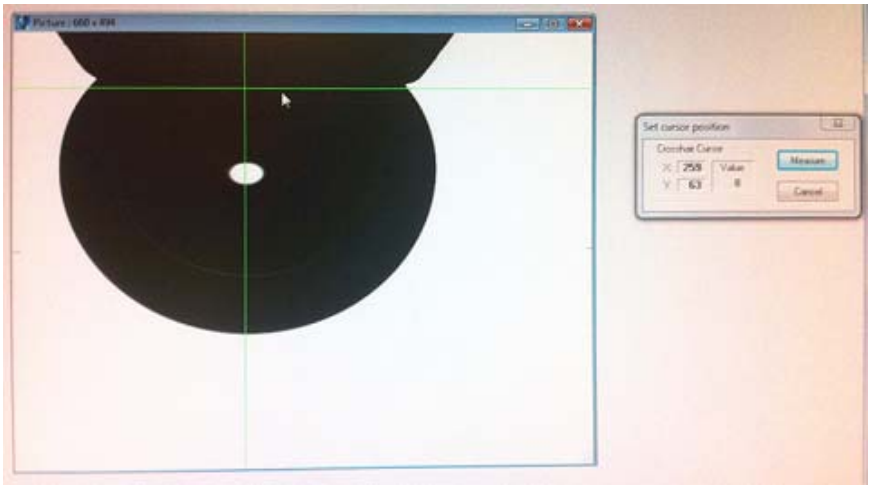

Figure 4-6. The main window with the selection crosshair.

The values of the mole fractions of MEA, x_2, correspond to the mass fractions from 0 to 1.0, at 0.1 intervals as shown in Table 4-2. For each temperature and mass fraction of MEA, 10 different bubbles were generated. Based on the previous setting, each bubble will be measured 10 times and the average surface tension value of that bubble is given. The average of surface tensions of 10 different bubbles was calculated, and the surface tension at certain temperature and mass fraction of MEA is obtained by that. The maximum deviations from the average surface tension value were less than 0.0004 $N \cdot m^{-1}$.

4.2.3 Principle of the surface tension measurements

Sessile bubble method was used in our surface tension measurements by Rame-Hart Model 500 Advanced Goniometer. Surface tension is calculated from the following equation which is derived from the Young-Laplace equation[7]:

$$\gamma = \Delta\rho g R_0^{\,2} / \beta \tag{4-1}$$

Here $\Delta\rho$ is the mass density difference between the bubble and the surrounding medium, R_0 is the radius of curvature at the bubble apex and β is the shape factor. The geometry of a bubble is shown in Figure 4-7. The camera captures the image of the bubble which is hanging from a tip. Then the program analyses the geometry of the bubble image to get R_0 and β. The calculation of β for a sessile bubble is introduced in the manual of the Rame-Hart Model 500 Advanced Goniometer and given in the following equations[7]:

$$\beta = \frac{R_0^{\,2}}{H^2} \times f(\xi),\ \xi = \frac{2H}{D_E} \tag{4-2}$$

$$\begin{cases} \xi<1:\ f(\xi) = -4.1788(\xi-1) + 1.9086(\xi-1)^2 + 4.5738(\xi-1)^3 \\ \xi>1:\ f(\xi) = -4.3626(\xi-1) + 1.1961(\xi-1)^2 \end{cases} \tag{4-3}$$

Here D_E is the maximum diameter of the bubble, and H is the distance from bubble apex to the points where maximum diameter is. D_E and H are also illustrated in Figure 4-8. Since the densities of different phases have already been input when starting a new experiment in the program, the surface tension can be calculated automatically.

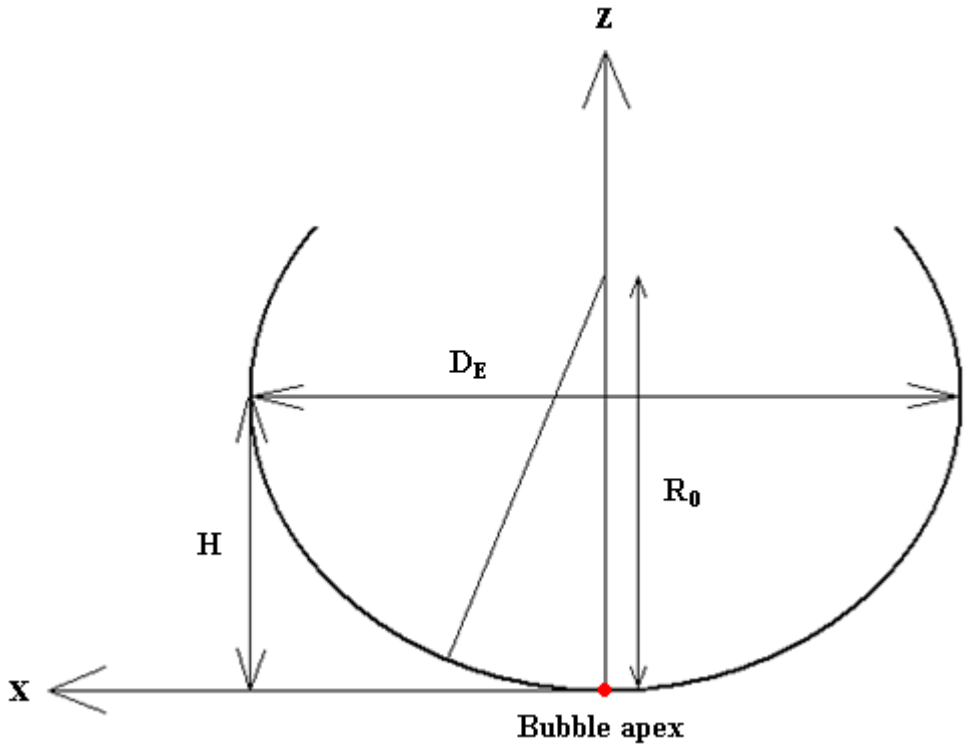

Figure 4-7. The geometry of a bubble. R_0 is the radius of curvature at the bubble apex. D_E is the maximum diameter. H is the distance from apex to the points where maximum diameter is.

Figure 4-8 shows four types of drops and bubbles along with the corresponding plusminus sign of β. A drop hanging from a tip (a) or a clinging bubble (c) will form a pendant type which is long and narrow. While, a bubble hanging from a tip (d) or a clinging drop (b) will form a sessile type which is short and wide. When DROPimage program was used to measure the surface tension, the type of the shape (pendant or sessile) needs to be chosen in the beginning. Since the density difference is defined as the density of the phase inside the drop or bubble subtracting the density of the phase outside, $\Delta\rho$ is smaller than 0 for the bubble and larger than 0 for the drop. The direction of gravity acceleration g is negative for the hanging drop or bubble and positive for the clinging drop or bubble. In conclusion, the shape factor β is negative for pendant types, and positive for sessile types.

$$\gamma = \Delta\rho g R_0^2 / \beta$$

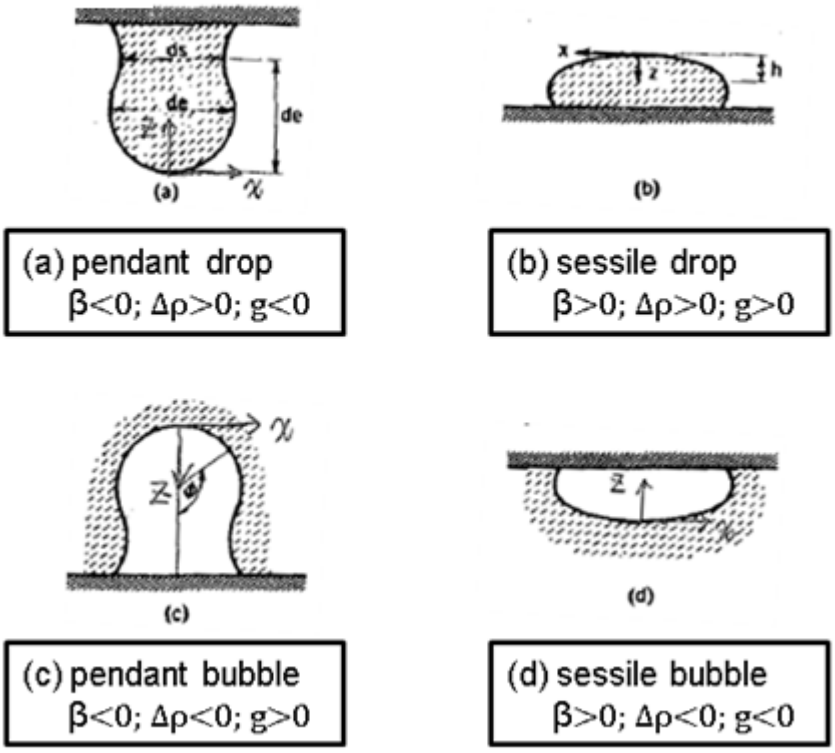

Figure 4-8. Shapes of sessile and pendant drops and bubbles.[9]

4.2.3.1 Young-Laplace equation

Young–Laplace equation and its application to a revolved surface are key points of the theory of this surface tension measurement, because they are the basis of the instrument's computer program. Young–Laplace equation describes the pressure difference across the interface between two static fluids due to surface tension.[10] For the case that a capillary put into a container of water as shown in Figure 4-9, it has $P_A = P_B = P_D = P_{air}$, $P_C = P_B - \rho gh$. The two sides on liquid surface have a pressure difference ($P_C < P_D$). Liquid surface in the capillary is concave according to the observation. Young explained this phenomenon that liquid goes up through capillary because of surface tension, and goes down because of gravity. This results in a concave liquid surface. There exists a pressure difference between two sides on a curved surface. Then Laplace calculated how much this pressure difference is by mathematical method. The Young-Laplace equation can be expressed as:

$$\Delta P = \gamma\left(\frac{1}{R_1} + \frac{1}{R_2}\right) \tag{4-4}$$

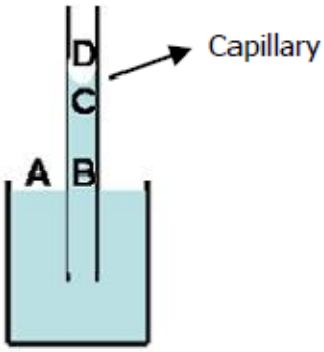

Figure 4-9. Capillary phenomenon.

4.2.3.2 Applying the Young-Laplace equation to a revolved surface

Figure 4-10 illustrates the principal radii of curvature for a revolved surface. Here O is the apex of the revolved surface. R_1 is the radius of curvature of the meridian line at point K. O' is the centre of a circle of the cross section at point K. Make a surface through point K which is perpendicular to tangent of meridian line at point K. The radius of curvature of intersecting line between that surface and our revolved surface is R_2. Included angle between R_2 and rotation axis is θ. r is the radius of the cross section at point K. s is the length of the arc of the meridian section, measured from the origin to the point under consideration.

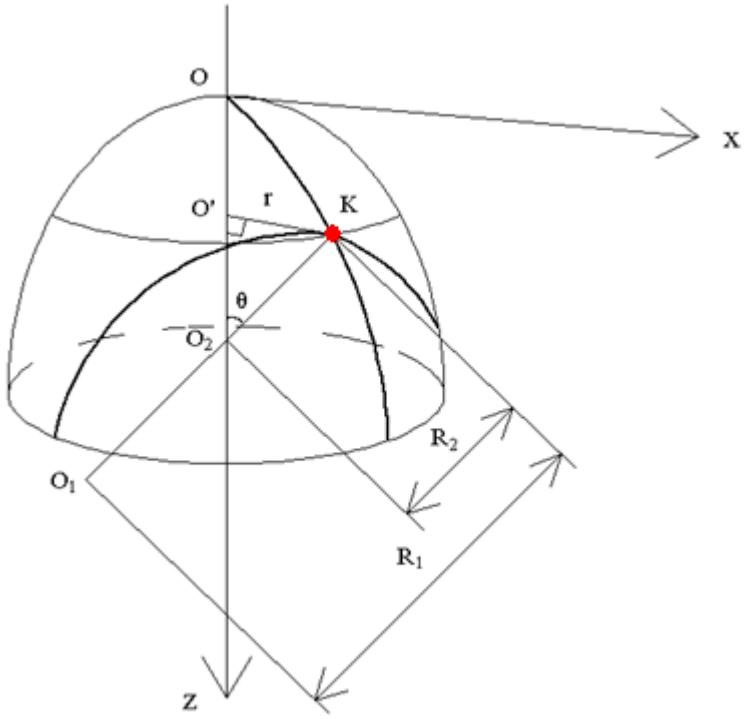

Figure 4-10: The principal radii of curvature of revolved surface.

So it has[10]:

$$R_1 = \frac{\mathrm{d}s}{\mathrm{d}\theta} \tag{4-5}$$

$$R_2 = \frac{r}{\sin\theta} = \frac{x}{\sin\theta} \tag{4-6}$$

$$\frac{\mathrm{d}x}{\mathrm{d}s} = \cos\theta, \frac{\mathrm{d}z}{\mathrm{d}s} = \sin\theta \tag{4-7}$$

If K is the original point O, $R_1 = R_2 = R_0$.

The pressure difference at point K is:

$$\Delta P = \Delta\rho g z + C \tag{4-8}$$

C is a constant. When $z = 0$, it has $\Delta P = C = \gamma(\frac{1}{R_1} + \frac{1}{R_2})_{z=0} = \frac{2\gamma}{R_0}$.

Substituting eqs 4-5, 4-6 and 4-8 into eq 4-4 and it has:

$$\frac{\Delta\rho g z + C}{\gamma} = \frac{\mathrm{d}\theta}{\mathrm{d}s} + \frac{\sin\theta}{x} \tag{4-9}$$

$$\frac{\Delta\rho g z}{\gamma} + \frac{2}{R_0} = \frac{\mathrm{d}\theta}{\mathrm{d}s} + \frac{\sin\theta}{x} \tag{4-10}$$

$$\frac{\Delta\rho g R_0^{\,2}(z/R_0)}{\gamma} + 2 = \frac{\mathrm{d}\theta}{\mathrm{d}(s/R_0)} + \frac{\sin\theta}{x/R_0} \tag{4-11}$$

Let $\beta = \Delta\rho g R_0^{\,2}/\gamma$ and non-dimensionalization $X = x/R_0$, $Z = z/R_0$, $S = s/R_0$, the equation becomes:

$$\beta Z + 2 = \frac{\mathrm{d}\theta}{\mathrm{d}S} + \frac{\sin\theta}{X} \tag{4-12}$$

So there have the following equations for a bubble or drop:

$$\begin{cases} \gamma = \Delta\rho g R_0^{\,2}/\beta \\ \dfrac{\mathrm{d}\theta}{\mathrm{d}S} + \dfrac{\sin\theta}{X} = \beta Z + 2 \\ \dfrac{\mathrm{d}x}{\mathrm{d}s} = \cos\theta \\ \dfrac{\mathrm{d}z}{\mathrm{d}s} = \sin\theta \end{cases} \tag{4-13}$$

4.2.3.3 Solution of bubble and drop equation

MATLAB was used to solve eq 4-13 with the initial condition for $S = 0$ it has $X = 0$, $Z = 0$, $\theta = 0$. The equation becomes $d\theta/ds = 1$ when $S = 0$. The profile $Z = f(X)$ is given by a specified β. Figure 4-11 shows the sessile bubble profile when $\beta = 1$. The relationship between geometric size of a bubble (or drop) and β will be known through the foregoing calculation. As long as a lot of profiles correspond to various values of β were got, approximate solution of β will in turn be available through polynomial fitting. The solution of β was available in the manual of the Rame-hart Model 500 Advanced Goniometer.[7]

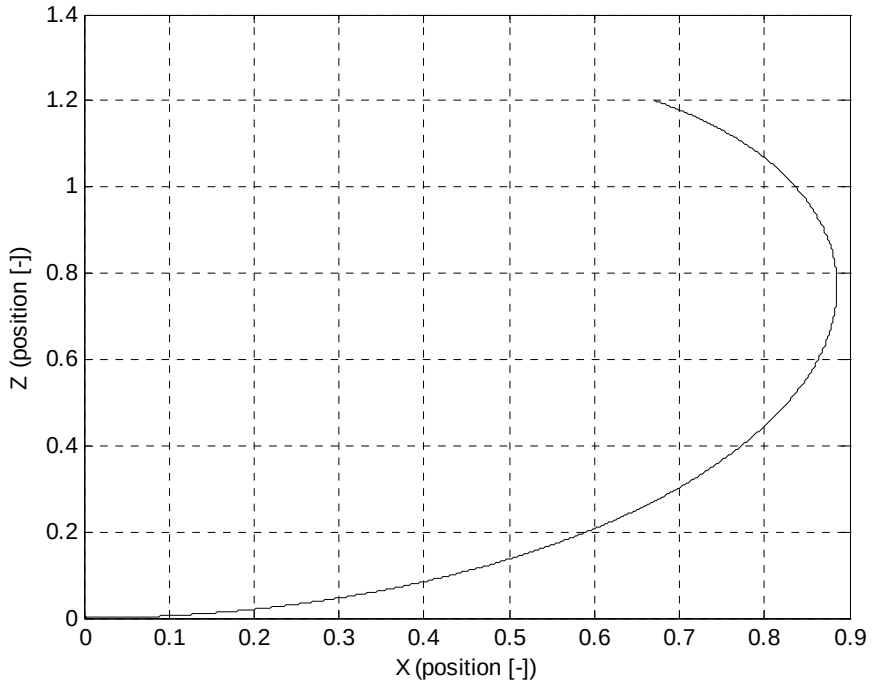

Figure 4-11. The drop profile $Z = f(X)$ when $\beta = 1$.

4.3 Results and Discussion

The measured surface tensions of aqueous MEA solutions are tabulated in Table 4-2. The temperature ranges from (303.15 to 333.15) K, and the composition ranges from $w_2 = 0$ to 1.0. The surface tension varies with the temperature and the mole fraction of MEA as shown in Figures 4-12 and 4-13. It was observed that as the temperature increases the surface tension of aqueous MEA solutions decreases. This is because when the temperature increases, thermal motion of molecules increases, molecules at the surface stretch more, inter-molecular attraction decreases, and then the surface tension decreases. The function of surface tension of

aqueous MEA solutions with temperature is approximately linear. Moreover, surface tension decreases as mole fraction of MEA increases. The reason is that the organic solute in aqueous MEA solutions tends to concentrate at the solution-air interface because of the hydrophobic part in the molecule of MEA. According to the fundamental thermodynamic theory which was developed by Gibbs, the effect of the solute concentration on surface tension depends on whether the solute prefers to concentrate at the interface or in the bulk.[11] When the mole fraction of MEA increases, more solutes concentrate at the interface, and then the surface tension of aqueous MEA solution decreases due to the smaller surface tension of MEA comparing to water. The decrease in surface tensions of aqueous MEA solutions is steeper at lower mole fraction of MEA and shallower at higher mole fraction of MEA. Measured surface tensions of aqueous MEA solutions in this work are compared with Vázquez et al.[1]'s data. The maximum deviation between the measured surface tensions and the literature data is 0.0048 $N \cdot m^{-1}$ and the average deviation is 0.0022 $N \cdot m^{-1}$. The comparison between this work and the literature at 303.15 K is shown in Figure 4-14. It can be seen that the maximum deviation occurs at w_2 = 0.3. Since Vázquez et al.'s data is the only literature source for surface tensions of aqueous MEA solutions, the reason for the deviation is difficult to explain. However, similar deviations between the data from Vázquez et al.'s group and other literature were found for surface tensions of aqueous MDEA solutions as shown in Figure 4-15.[2, 3]

Table 4-2. Surface Tension $\gamma/N \cdot m^{-1}$ for Water (1) + MEA (2) from T = (303.15 to 333.15) K and Mass Fraction of MEA from 0 to 1.0.

w_2	x_2	$\gamma/N \cdot m^{-1}$			
		T = 303.15 K	T = 313.15 K	T = 323.15 K	T = 333.15 K
0	0	0.0713	0.0696	0.0680	0.0662
0.1	0.032	0.0668	0.0655	0.0643	0.0625
0.2	0.069	0.0647	0.0633	0.0617	0.0601
0.3	0.112	0.0636	0.0626	0.0612	0.0594
0.4	0.164	0.0617	0.0603	0.0588	0.0573
0.5	0.228	0.0593	0.0582	0.0569	0.0554
0.6	0.307	0.0574	0.0564	0.0552	0.0536
0.7	0.407	0.0558	0.0548	0.0534	0.0518
0.8	0.541	0.0534	0.0524	0.0511	0.0496
0.9	0.726	0.0506	0.0496	0.0484	0.0470
1.0	1	0.0481	0.0467	0.0456	0.0446

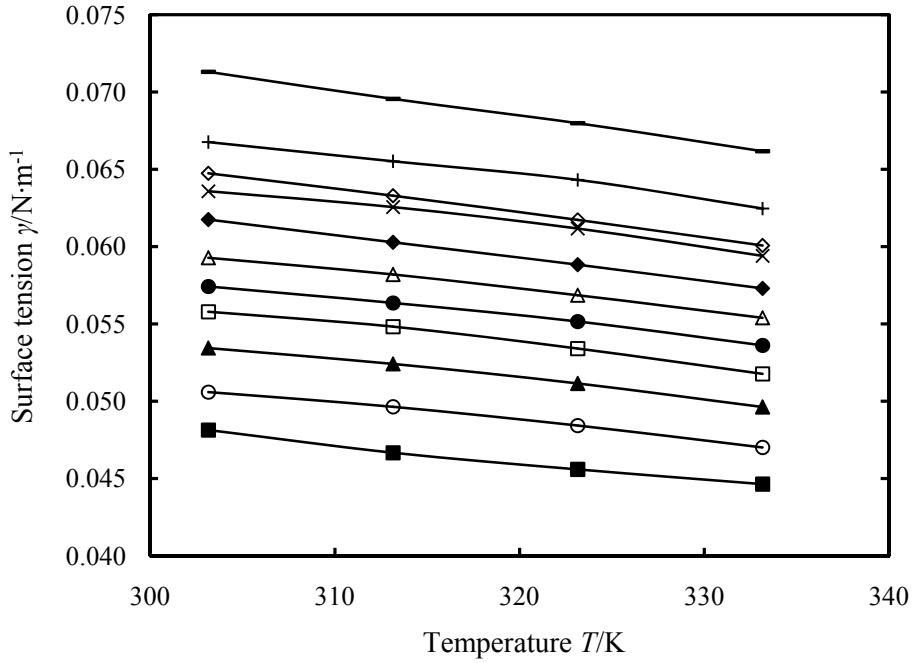

Figure 4-12. Surface tensions of H_2O (1) + MEA (2) solutions as a function of temperature at different mass fractions of MEA: ■, MEA; ○, 0.9; ▲, 0.8; □, 0.7; ●, 0.6; △, 0.5; ♦, 0.4; ×, 0.3; ◊, 0.2; +, 0.1; —, water.

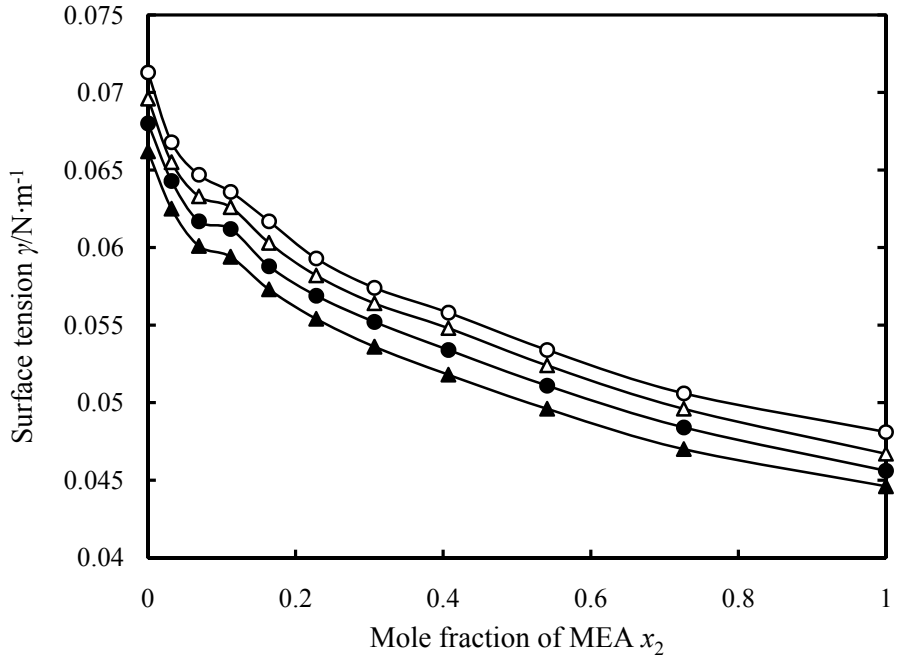

Figure 4-13. Surface tensions of H_2O (1) + MEA (2) solutions as a function of mole fraction of MEA: ○, 303.15 K; △, 313.15 K; ●, 323.15 K; ▲, 333.15 K.

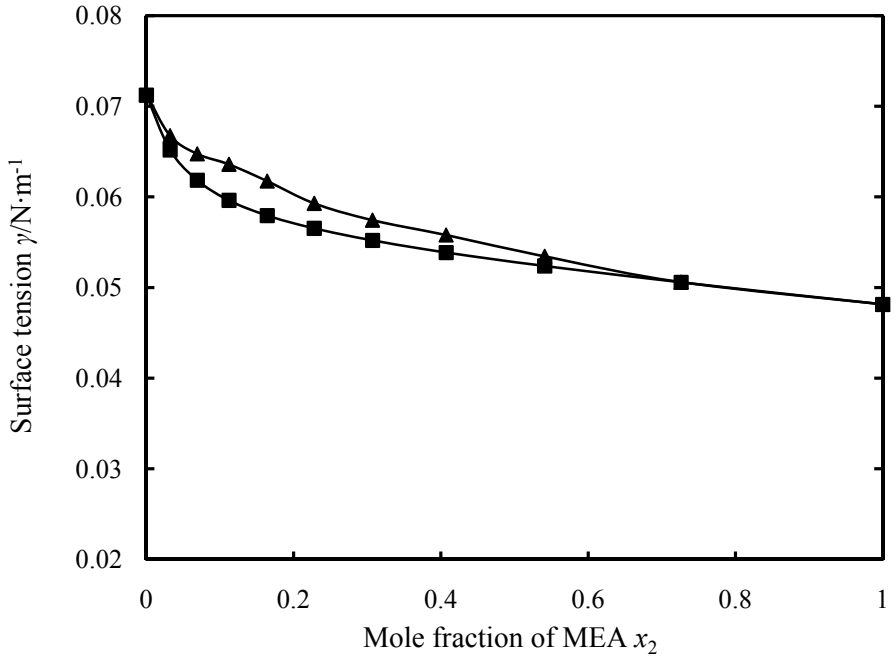

Figure 4-14. A comparison with literature of the H_2O (1) + MEA (2) surface tension data as a function of mole fraction at 303.15 K. ▲, our results; ■, results from Vázquez et al.[1].

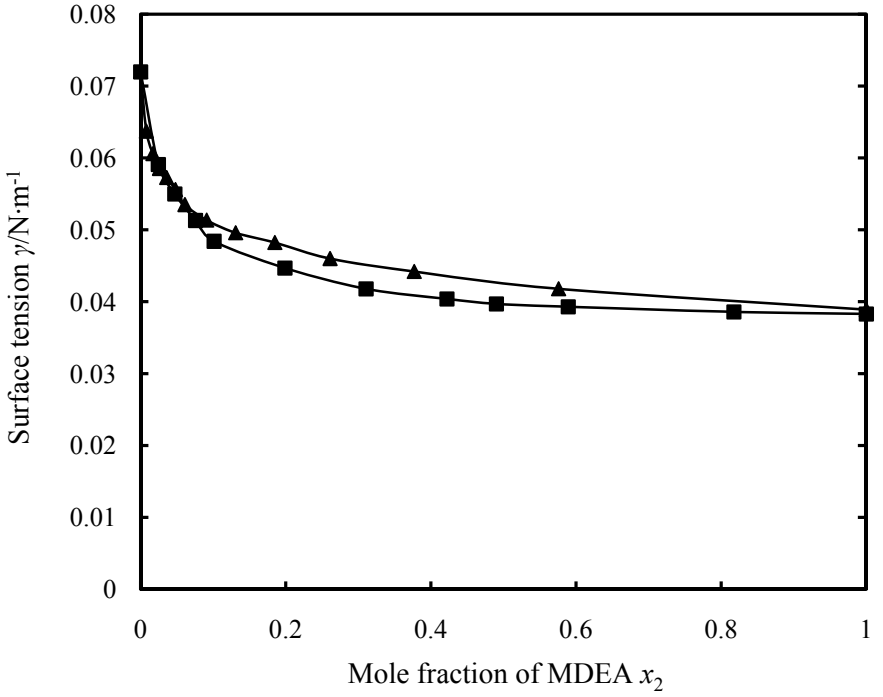

Figure 4-15. A literature comparison of the H_2O (1) + MDEA (2) surface tension data as a function of mole fraction at 298.15 K. ▲, results from Alvarez et al.[2]; ■, results from Maham and Mather[3].

4.4 Model for Data Representation

The experimental surface tensions of aqueous MEA solutions were correlated with temperature and mole fraction of MEA respectively.

4.4.1 The correlation of surface tension with temperature

The surface tensions of binary mixtures were correlated with temperature by a linear relationship.

$$\gamma_m / \mathrm{N \cdot m^{-1}} = K_1 - K_2 (T / \mathrm{K} - 273.15) \tag{4-14}$$

The parameters K_1 and K_2 are listed in Table 4-3. The average absolute deviation is 0.0001 $\mathrm{N \cdot m^{-1}}$ and the maximum deviation is 0.0002 $\mathrm{N \cdot m^{-1}}$. The correlated surface tensions by eq 4-14 and the experimental data have good agreement. The deviations are within experimental error.

Table 4-3. Surface Tension Fitting Parameters K_1 and K_2 for Water (1) + MEA (2) Solutions.

x_2	K_1	K_2	x_2	K_1	K_2	x_2	K_1	K_2
0.000	0.07639	0.0001699	0.164	0.06619	0.0001480	0.541	0.05737	0.0001270
0.032	0.07109	0.0001407	0.228	0.06327	0.0001298	0.726	0.05430	0.0001198
0.069	0.06947	0.0001558	0.307	0.06132	0.0001263	1.000	0.05146	0.0001158
0.112	0.06795	0.0001396	0.407	0.05999	0.0001345			

4.4.2 The correlation of surface tension with mole fraction of MEA

The surface tensions of aqueous amine blends were correlated with mole fraction by both an empirical model and the chemical model.

An empirical correlation model for estimating surface tension of aqueous amine blends is suggested by Norbert Asprion[12].

$$\gamma_m / \mathrm{N \cdot m^{-1}} = \gamma_1 / \mathrm{N \cdot m^{-1}} + \sum_{i \geq 2} \frac{S_i x_i}{1 + \sum_{j \geq 2}^{i} (S_j - 1) x_j} (\gamma_i / \mathrm{N \cdot m^{-1}} - \gamma_1 / \mathrm{N \cdot m^{-1}}) \tag{4-15}$$

Here only one adjustable parameter S_2 is needed for binary mixtures.

The chemical model for correlating surface tension of aqueous amine blends is suggested by Connors and Wright.[13]

$$\gamma_m / \mathrm{N \cdot m^{-1}} = \gamma_1 / \mathrm{N \cdot m^{-1}} + \sum_{i \geq 2} \left(1 + \frac{a_i x_1}{(1-b_i)\left(1 + \sum_{j \geq 2}^{i} \frac{b_j}{(1-b_j)} x_j\right)}\right) x_i \left((\gamma_i / \mathrm{N \cdot m^{-1}}) - (\gamma_1 / \mathrm{N \cdot m^{-1}})\right)$$

(4-16)

This model includes two adjustable parameters a_2 and b_2 for a system with two components.

The fitted parameters S_2, a_2 and b_2 of the empirical correlation model and chemical model were presented in Table 4-4. The average absolute deviation between the experimental data and the correlated results from the empirical correlation model is 0.0006 $\mathrm{N \cdot m^{-1}}$ and the maximum deviation is 0.0020 $\mathrm{N \cdot m^{-1}}$. While, the average absolute deviation between the measured data and the correlated results from the chemical model is 0.0004 $\mathrm{N \cdot m^{-1}}$ and the maximum deviation is 0.0013 $\mathrm{N \cdot m^{-1}}$. The agreement is satisfactory. The average absolute deviation is within the experimental error (± 0.0004 $\mathrm{N \cdot m^{-1}}$). The correlation results were compared in Figure 4-16. The chemical model shows better agreement with the experimental surface tension data than the empirical model.

Table 4-4. Surface Tension Fitting Parameters S_2, a_2 and b_2 of the Empirical Correlation Model and Chemical Model for Water (1) + MEA (2) Solutions.

	Empirical correlation model	**Chemical model**	
***T*/K**	$\boldsymbol{S_2}$	$\boldsymbol{a_2}$	$\boldsymbol{b_2}$
303.15	3.6783	0.5127	0.8964
313.15	3.3038	0.4632	0.9017
323.15	3.3243	0.4754	0.8942
333.15	3.4910	0.5106	0.8827

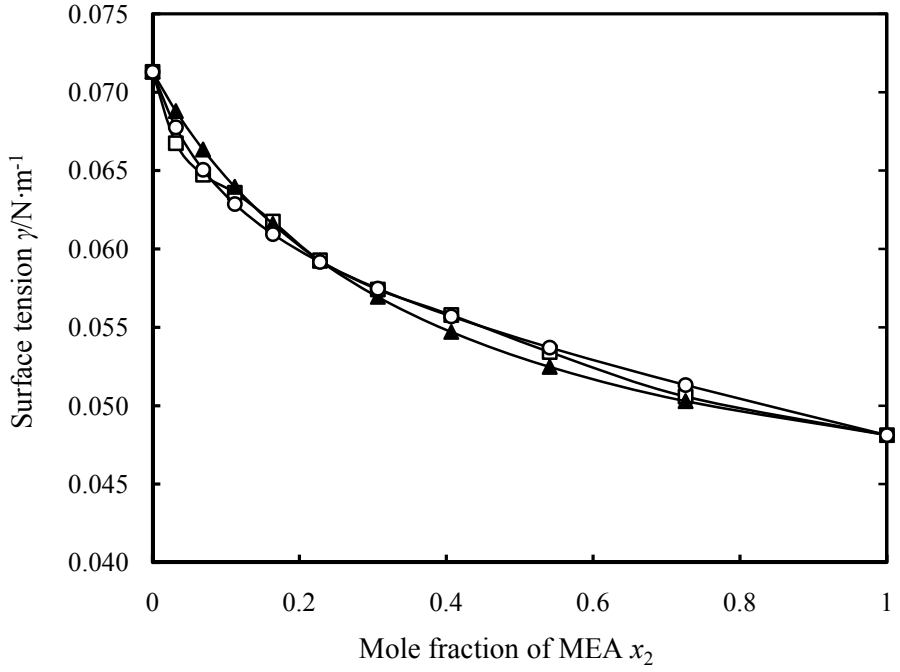

Figure 4-16. Surface tension of H_2O (1) + MEA (2) solutions as a function of mole fraction at 303.15 K. □, Our experimental results; ▲, Empirical correlation model results; ○, Chemical model results.

4.5 Assessment of Experimental Uncertainties

The uncertainty analysis method has been introduced in Section 3.5. The uncertainty of surface tension measurements of unloaded aqueous MEA solutions arises from several sources involved in the temperature rise measurement, the error from mass fraction of MEA and instrument error. The temperature accuracy is estimated as ± 0.2 K by the calibration results of the thermocouples. Based on our measurement results, the change of surface tension is 0.0002 $N \cdot m^{-1}$ when the change of temperature is 1K. The accuracy of weight fraction of MEA is estimated as ± 0.005. The maximum change of surface tension is 0.0045 $N \cdot m^{-1}$ when the change of mass fraction of MEA is 0.1. Instrument accuracy is given as 0.00003 $N \cdot m^{-1}$ by the manufacturer.[14] The combined standard uncertainty of surface tension measurements is 0.0002 $N \cdot m^{-1}$ which is determined by combining the error from temperature measurement, mass fraction of MEA and instrument error. The combined expanded uncertainty of surface tension measurements of aqueous MEA solutions is $U_c(\gamma) = ku_c(\gamma) = 0.0004\ \mathrm{N \cdot m^{-1}}$ (level of confidence = 0.95).

The uncertainty that is caused by the error from mass fraction of MEA dominates in the uncertainties of surface tension measurements of unloaded aqueous MEA solutions.

4.6 Conclusions

Surface tensions of H_2O (1) + MEA (2) mixtures have been measured at temperatures from (303.15 to 333.15) K. The mole fraction of MEA ranges from 0 to 1.0. As the temperature increased, surface tension of aqueous MEA solutions decreased. Moreover, surface tension of aqueous MEA solutions decreased as the mole fraction of MEA increased for a given temperature. The surface tension data were correlated with temperature and mole fraction. The absolute average deviation between the correlated and experimental surface tensions is 0.0001 $N \cdot m^{-1}$ when correlating with temperature. The absolute average deviations between the correlated and experimental surface tensions are 0.0006 $N \cdot m^{-1}$ and 0.0004 $N \cdot m^{-1}$ when correlating with mole fraction by the empirical correlation model and chemical model, respectively. Measurement uncertainty has been estimated as ± 0.0004 $N \cdot m^{-1}$ for comparison. The models fitted to the surface tension data constitute a satisfactory representation with errors that would be negligible for engineering calculations.

Notation

C	constant, Pa
g	gravity acceleration, N/kg
h	height, m
P	pressure, Pa
ΔP	pressure difference between two sides on a curved surface, Pa
r	radius of the cross section at certain point, m
R_0	radius of curvature at the apex of the bubble, m
R_1, R_2	principal radius of curvature, m
s	length of the arc of the meridian section, m
T	temperature, K
u	standard uncertainty
U	expanded standard uncertainty
w	mass fraction
x	mole fraction or distance on the x axis, m
z	distance on the z axis, m

Greek letters

β	the shape factor, also called Bond number
γ	surface tension, N/m
θ	included angle between R_2 and rotation axis, degree

$\Delta\rho$	density difference between the bubble and the surrounding medium, kg/m^3

Subscripts

1	water
2	amine
A, B, C, D	position
c	combined
m	mixture

References

(1) Vázquez, G.; Alvarez, E.; Navaza, J. M.; Rendo, R.; Romero, E. Surface Tension of Binary Mixtures of Water + Monoethanolamine and Water + 2-Amino-2-methyl-1-propanol and Tertiary Mixtures of These Amines with Water from 25 °C to 50 °C. *J. Chem. Eng. Data* **1997**, *42*, 57-59.

(2) Alvarez, E.; Rendo, R.; Sanjurjo, B.; Sánchez-Vilas, M..; Navaza, J. M. Surface Tension of Binary Mixtures of Water + N-Methyldiethanolamine and Ternary Mixtures of This Amine and Water with Monoethanolamine, Diethanolamine, and 2-Amino-2-methyl-1-propanol from 25 to 50 °C. *J. Chem. Eng. Data* **1998**, *43*, 1027-1029.

(3) Maham, Y.; Mather, A. E. Surface Thermodynamics of Aqueous Solutions of Alkylethanolamines. *Fluid Phase Equilib.* **2001**, *182*, 325-336.

(4) Aguila-Hernández, J.; Trejo, A.; Gracia-Fadrique, J. Surface Tension of Aqueous Solutions of Alkanolamines: Singe Amines, Blended Amines and Systems with Nonionic Surfactants. *Fluid Phase Equilib.* **2001**, *185*, 165-175.

(5) "Surface and Interfacial Tension". Langmuir-Blodgett Instruments. Retrieved 2007-09-08.

(6) Calvert, James B. "Surface Tension (physics lecture notes)". University of Denver. Retrieved 2007-09-08.

(7) Manual of the Rame-Hart Model 500 Advanced Goniometer.

(8) Webster, J. G. *The Measurement, Instrumentation, and Sensors: Handbook*; CRC Press LLC: Boca Raton, FL, 1999.

(9) Adamson, A. W.; Gast, A. P. *Physical Chemistry of Surfaces*; Wiley: New York, 1997.

(10) Ghosh, P. *Colloid and Interface Science*; PHI Learning Pvt. Ltd: New Delhi, 2009.

(11) Tropea, C.; Yarin, A.; Foss, J. F. *Springer Handbook of Experimental Fluid Mechanics*; Springer-Verlag: Berlin, Heidelberg, 2007.

(12) Asprion, N. Surface Tension Models for Aqueous Amine Blends. *Ind. Eng. Chem. Res.* **2005**, *44*, 7270-7278.
(13) Connors, K. A.; Wright, J. L. Dependence of Surface Tension on Composition of Binary Aqueous-Organic Solutions. *Anal. Chem.* **1989**, *61*, 194-198.
(14) Hansen F. K. Surface Tension by Image Analysis: Fast and Automatic Measurements of Pendant and Sessile Drops and Bubbles. *J. Colloid Interface Sci*. **1993**, *160*, 209-217.

5. Liquid Phase Mass Transfer Coefficient Measurements of CO_2 Absorption into Individual Liquid Droplets

Abstract

A novel experimental set-up was constructed to study the mass transfer characteristics between CO_2 and liquid droplets. The liquid phase mass transfer coefficients of CO_2 absorption into water droplets during droplet life-time (formation and fall together) were measured at temperatures T = 303.65 K and 323.15 K, droplet falling heights h = 0.41 m and 0.59 m, and droplet formation times t_1 = (0.352 to 2.315) s. The absorption rates of CO_2 into water droplets during droplet formation were measured at different droplet formation times and temperatures T = 297.15 K and 323.15 K. The correlation between the Sherwood number and the Reynolds number of CO_2 absorption by water droplets during droplet fall at 323.15 K was obtained.

The absorption rates of CO_2 into droplets of 30% MEA solutions during droplet formation were measured at 323.15 K and different droplet formation times. The absorption rate of CO_2 into droplets of 30% (wt) aqueous MEA solutions is almost unchanged as the droplet formation time changes. The liquid phase mass transfer coefficients of CO_2 absorption into droplets of 30% MEA solutions during droplet life-time (formation and fall together) were measured at temperatures T = 303.65 K and 323.15 K, and droplet falling heights h = (0.07 to 0.53) m. The correlation between the Sherwood number and the Reynolds number of CO_2 absorption by droplets of 30% MEA solutions during droplet fall at 323.15 K was obtained.

5.1 Introduction

Spray columns have been widely used in industry in many ways. Gas absorption is one of the main applications of the spray column due to its high removal efficiency and low costs.[1] The spray column provides a very large contact surface area between gas-liquid phases. Currently, it is a new process concept for bulk removal of CO_2 from a gaseous stream. A deep understanding of the mass transfer characteristics in the spray column is very important for the optimization of column design and the selection of absorbent.

In recent years, several researchers studied gas absorption in the whole spray or scrubbing systems.[1-3] Turpin et al.[1] studied the characteristics of the mass transfer parameters and H_2S removal efficiency in a laboratory-scale spray tower. Bandyopadhyay and Biswas[2] reported the performance of SO_2 absorption by water and dilute NaOH in a spray tower in which a critical flow atomizer is assembled and obtained the critical design parameters. Kuntz and Aroonwilas[3] measured the overall mass transfer coefficient of CO_2 absorption by aqueous MEA solutions in a spray column and studied the influence of different parameters. They compared the mass transfer feature of the spray column to that of the conventional packed column and concluded that the spray column is promising to be applied to capture CO_2.

The study on gas absorption by individual droplets in sprays is also important for better understanding the mass transfer in the spray column in microscopic view. However, it has been paid very little attention. In this chapter, mass transfer between CO_2 and the unit part of a spray — individual droplets was investigated.

It has generally been accepted that there are three distinct periods in the life-time of drops: drop formation period, fall (or rise) through a surrounding continuous phase period and coalescence period. Mass transfer during the drop formation and the coalescence period have been treated as the end effects and studied separately in order to measure mass transfer during the drop fall period, since mass transfer during drop fall is more interesting in industrial processes.[4-11] Usually, the significance of coalescence can be eliminated in the total mass transfer in many ways because of the possibility of restricting contact area.[10] However, mass transfer during formation is different and has been testified to represent a significant fraction of the total mass transfer by several researchers.[6, 9]

Early researchers studied mass transfer between liquid drops and a surrounding continuous phase during the three stages separately by making extrapolations. Whitman et al.[4] established an absorption apparatus by forming water drops from a capillary, letting them fall through a small column of constant height (60 cm) which was filled with CO_2, and then collecting the drops under a layer of kerosene to analyze the content of CO_2 absorbed as shown in Figure 5-1. The drop formation time was varied and the absorption during fall was calculated by extrapolation to zero formation time. The absorption during formation was attained by assuming the absorption during fall to be constant and subtracting it from total absorption. The absorption of CO_2 into water droplets in their experiments was regarded as

controlled by diffusion of CO_2 through a thin liquid film at the interface. The conclusion was made that the coefficient k_L during fall is much greater than that during formation. The absorption during drop formation can be neglected. Furthermore, the coefficient k_L during formation and during fall were both regarded as independent of drop formation time. There are similarities between absorption and liquid-liquid extraction in spray columns, since they are both mass transfer processes between liquid drops and a continuous surrounding phase. Licht and Conway[5] studied the extraction of acetic acid from water drops by different organic solvents. The columns were designed to perform the extraction experiments at varying column heights. The extraction during drop formation was measured by extrapolation of a plot of results versus column height to zero. The amount of extraction occurring during drop fall was obtained by subtracting the extraction during formation from the total mass transfer amount. These workers found that the over-all transfer coefficient during formation increases as droplet diameter decreases, while the coefficient during fall was only slightly affected by drop size. In addition, the column height does not affect the over-all coefficient essentially. The drop formation time does not affect the amount of solute extracted in a given column height. Sherwood et al.[6] studied the extraction of acetic acid from the drops of organic solvents with water as the continuous phase. The organic solvent drops were formed at a nozzle at the bottom of the column and then rose through the surrounding water phase. The same extrapolation method as used in Licht and Conway's work was used to determine the amount of extracted solute during drop formation. Both Licht and Conway and Sherwood et al. claimed that within the drop there existed a convection current which was an important factor influencing mass transfer rates. However, some of their conclusions are contradictory. Sherwood et al. found out that the transfer coefficient during the whole drop lifetime increases as drop size becomes larger. Moreover, the amount of solute extracted was found to increase as the drop formation time increases. West et al.[7] investigated the extraction of acetic acid from benzene drops by water using similar apparatus and extrapolation method as used in the work of Sherwood et al. Nevertheless, both the extracted amount during drop formation and the total extraction were found to be much less than given by the data of Sherwood et al. This inconsistency was interpreted by West et al. as probably due to different purities of benzene. The unsteady-state diffusion equation for a stagnant sphere, i.e. no internal current, correlated their results well under the assumption that the extracted amount was always 14% during drop formation. Licht and Pansing[8] performed a further investigation of solute transfer from single drops for liquid-liquid extraction based on the work of Licht and Conway. Six types of solute transfer mechanisms for drop movement through column were discussed. The properties

associated with the vibration in the drop during its fall were found to be one of the most significant factors for the solute transfer mechanism. In addition, they concluded that the extrapolation method proposed by previous authors[5-7] was incorrect by comparing the extrapolated data to the predicted results.

In summary, the extrapolation method to determine the mass transfer during drop formation was found to be imprecise because inappropriate assumptions have been made during these calculations, for instance, absorption during fall is assumed to be constant for different droplet formation time.

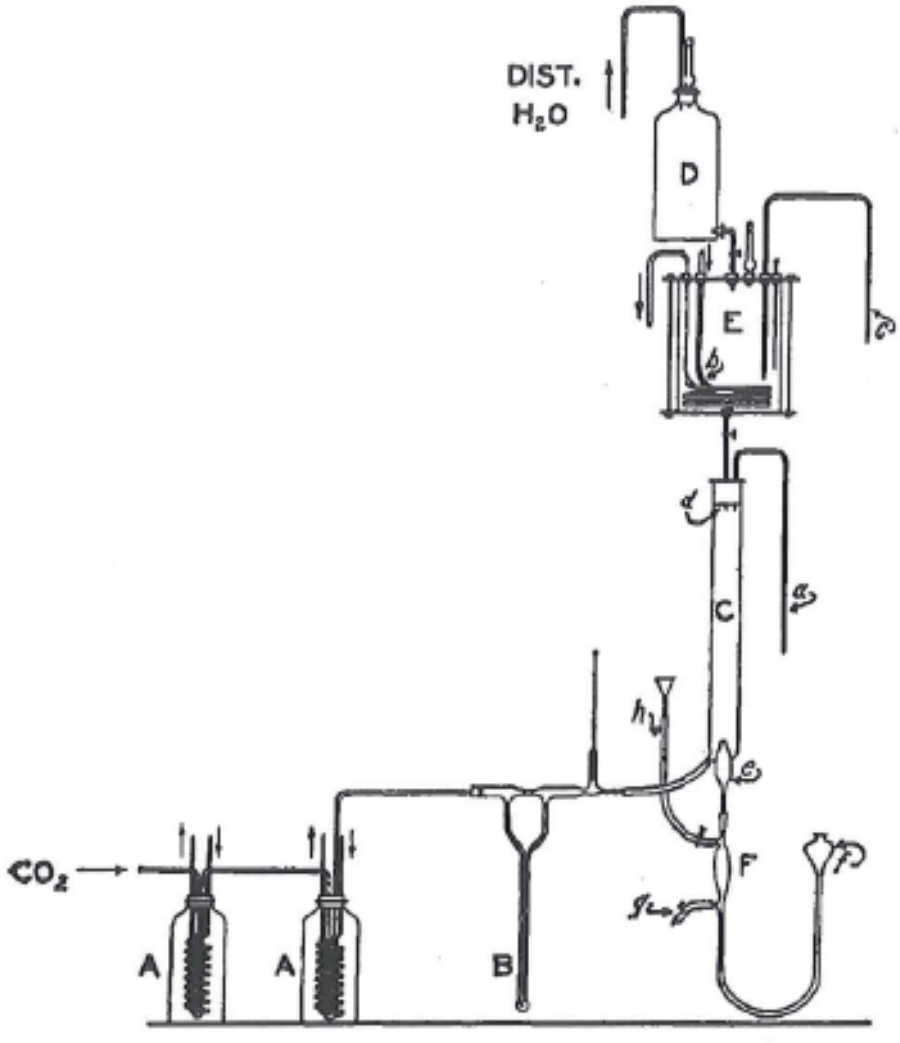

Figure 5-1. Apparatus for CO_2 absorption into water drops by Whitman et al.[4]. A: water saturator; B: thermometer; C: absorption chamber; D: water container; E: feed tank; F: discharge tube; a: CO_2 outlet; b: heating or cooling coil; c: sampling tube for feed water; d: capillary tip; e: kerosene layer; f: mercury leveling device; g: sampling tube for CO_2 absorbed water; h: introducing tube for kerosene.[4]

Therefore, some researchers attempted to directly measure the mass transfer during drop formation by experiments. Dixon and Russell[9] studied the absorption of CO_2 into water drops by using a similar apparatus as employed by Whitman et al. except that the absorption chamber was replaceable as shown in Figure 5-2. A short tube was used as the chamber to determine the absorption during formation since the drops will fall into kerosene as soon as they detached from the capillary tip in Fig. 5-2 (a), while a long tube was used instead to measure the absorption during formation and fall in Fig. 5-2 (b). They found out that both the absorption rate of CO_2 into water drops during formation and during fall decrease as the drop formation time increases, first rapidly and then gradually. The absorption during formation cannot be neglected because the amount of CO_2 absorbed during formation is larger than that during fall over the range covered by these experiments. The explanation was that the turbulence inside the drop produced by the injection of the supply jet enhances the mass transfer coefficient significantly. The magnitude of turbulence depends on the velocity of the jet and the needle size. In other words, the turbulence intensifies as the decrease in drop formation time and drop diameter. The absorption coefficient were correlated by the following equation[9]:

$$K_L = \frac{2.32(\Delta + 12.5)}{t_1^{0.8}} \tag{5-1}$$

Here K_L is the over-all transfer coefficient, Δ is the defined "degree of turbulence" which is inversely proportional to the capillary internal radius, and t_1 is the drop formation time. The work and results from Dixon and Russell seems more convincing. Rajan and Heideger[10] directly investigated the mass transfer between a slightly soluble organic drop and the surrounding water during drop formation by experiments. The instantaneous mass transfer coefficient was found to decrease sharply with time early in the formation period and remain constant after a while because the convection within the drop is greatest when the drop size is smallest. The time average mass transfer coefficient during drop formation increases as the decrease in drop formation time and also increases with the nozzle diameter. Heideger and Wright[11] further studied the liquid-liquid extraction between water drops and the surrounding immiscible organic solute during drop formation by experiments over a wide range of drop formation time in order to obtain a better understanding of the circulation inside the drop. They found that the circulation decays as the drop grows, and the turbulence within the drop after detachment reduces as drop formation time increases. It was observed that there exist two distinct regions — the average transfer coefficient decreases sharply as formation time increases in the rapid formation region where the convection dominates the mass transfer,

while it decreases slowly in the slow formation region because the circulation ceases and the molecular diffusion becomes significant. A circulation number proposed by Humphrey et al.[12] was used to evaluate the transition from circulating to stagnant drops. It was suggested that the drop will have experienced this transition before detachment from the nozzle when the circulation number is less than 1.0.

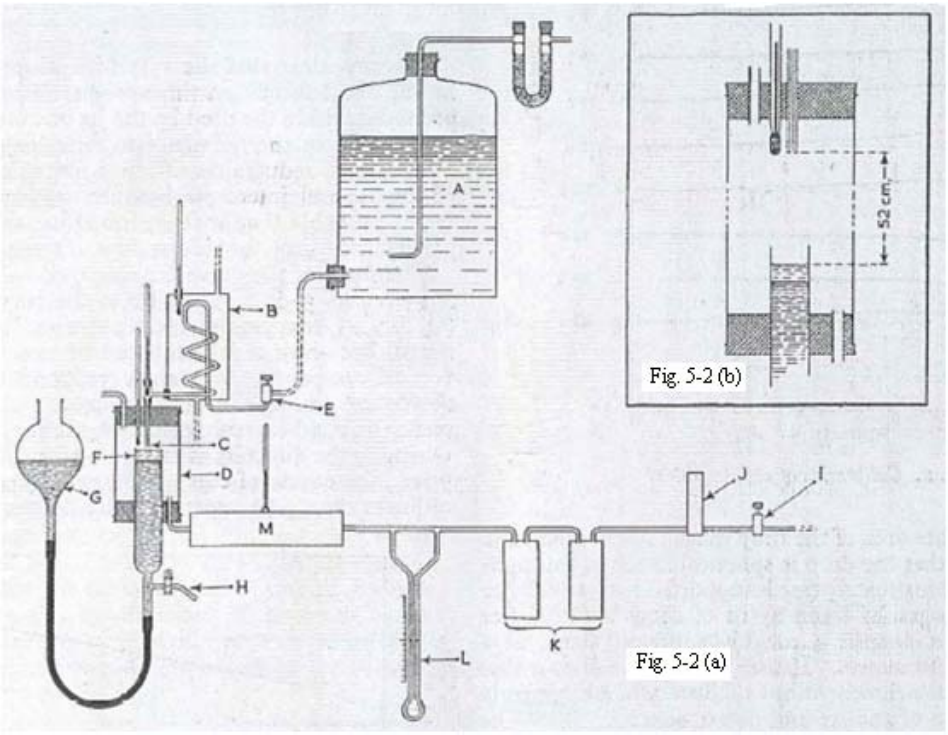

Figure 5-2. Apparatus for CO_2 absorption into water drops by Dixon and Russell[9]. A: water container; B and M: thermostat; C: capillary tip; D: absorption chamber; E and I: needle valve; F: kerosene layer; G: mercury-leveling tube; H: sampling tube for CO_2 absorbed water; J: gas governor; K: humidifiers; L: flowmeter.[9]

Two widely accepted mathematical models which describe the mass transfer during drop formation were developed by several researchers. Ilkovic[13] and Angelo et al.[14] proposed the surface stretch model under the condition that there is no additional fresh material of dispersed phase on the interface when the drop grows. Groothuis and Karmers[15] came up with the fresh surface model based on the assumption that there is no fluid element distortion in the interface area when the drop grows. Both of the two mathematical models were established based on the penetration theory. Popovich et al.[16] summarized that these models can all be represented by the following equation if the drop is spherical and grows at a uniform volumetric rate:

$$N_A = \text{const}(C_s - C_0)(D\pi)^{1/2} d_f^{\,2} t_f^{\,-2/3} t^{1/6} \qquad (5\text{-}2)$$

Here N_A is the mass transfer rate of solute A, C_s is the saturated concentration of the diffusing substance in the liquid drop, C_0 is the initial concentration of the diffusing substance in the liquid drop which varies for different models, D is the diffusion coefficient, d_f is the drop diameter at the end of the formation period, and t_f is the drop formation time.[16] Noteworthy, all of the descriptive models just mentioned for mass transfer during drop formation are limited to the drops without any circulation inside. However, droplet internal convection is only insignificant for the drops which have a very long formation time according to the conclusion of previous researchers. Therefore, the descriptive mass transfer model for the drops stating that their internal convection affects the mass transfer between the droplet and the surrounding continuous phase is very worthy of an in-depth study.

Srinivasan and Aiken[17] measured the liquid phase mass transfer coefficient of CO_2 absorption into a stream of water droplets. Levich's theory[18] of eddies at free liquid surface which summarized by Davies[19] and used to analyze the experimental results from Srinivasan and Aiken. The following correlation was acquired:

$$Sh_d = 0.14(Sc_d)^{1/2}(We_d)^{1/2}(Re_d)^{5/16} \tag{5-3}$$

Hoh et al.[20] re-examined Srinivasan and Aiken's data and concluded that the jet of water droplets in their case is in the laminar flow regime. A modified correlation was obtained by using the laminar flow equation due to Blasius:

$$Sh = 5.89(Sc)^{1/2}(Oh)(Re)^{3/4} \tag{5-4}$$

Here Oh is the Ohnesorge number which has no velocity terms and relates the viscous forces to inertial and surface tension forces ($Oh = \frac{\sqrt{We}}{Re} = \frac{\mu}{\rho\sigma d}$).

Chen et al.[21] simulated CO_2 absorption into single droplets of alkaline solutions by the software ANSYS FLUENT v12. They found that the CO_2 absorbed amount in the droplet increases as the pH value of the absorbent increases. Chen et al.[22] also theoretically analyzed CO_2 absorption by a stationary single Selexol, Rectisol, and water droplet. They found that the absorption rates of CO_2 into droplets increases as the temperature increases. In addition, their analysis shows that Rectisol droplet has the highest CO_2 capture capacity compared to water and Selexol droplet.

The studies of the mass transfer between liquid droplets and the surrounding continuous phase without chemical reaction in the literature were summarized in Table 5-1. No literature data for mass transfer involving chemical reaction between liquid droplets and a continuous phase has been found.

Table 5-1. Literature Study on Mass Transfer between Liquid Droplets and the Surrounding Continuous Phase.

Source	Phases		*T* [ºC]		*d* [mm]		t_1 [s]		*h* [m]	
	Dispersed (drops)	Continuous	low	high	low	high	low	high	low	high
Whitman et al.[4] (1926)	water	CO_2	22.6	24.8	5.42	5.56	0.5	5.4	0.6	
Licht and Conway[5] (1950)	acetic acid + water	organic solvent	-		3.42	4.51	0.8	4.5	0.08	0.76
Sherwood et al.[6] (1939)	acetic acid + organics	water	22	28	1.89	5.61	-		0.05	1.46
West et al.[7] (1951)	acetic acid + benzene	water	25		2.90	6.48	0.2	1.5	0.09	1.49
Licht and Pansing[8] (1953)	acetic acid + water	organic solvent	25		2.94	4.19	0.4	10.0	0.01	2.00
	acetic acid + organic	water			2.09	4.23				
Dixon and Russell[9] (1950)	water	CO_2	21		-		0.5	8.4	0.52	
Rajan and Heideger[10] (1971)	Ethyl Acetoacetate	water	24		-		0.629	6.048	0	
Heideger and Wright[11] (1986)	water	2-ethoxyethyl acetate	24		3.441	3.868	2.52	32.43	0	
Srinivasan and Aiken[17] (1988)	water	CO_2	25		0.0824		-		-	

As can be seen from the preceding discussion, Whitman et al.[4] and Dixon and Russell[9] established the absorption apparatus to study the mass transfer between CO_2 and single water droplet in early years as shown in Figures 5-1 and 5-2. In order to further accurately measure the mass transfer coefficient of CO_2 absorption into liquid droplets and better understand the mass transfer characteristics, a modified experimental set-up was constructed. The details of the new apparatus were introduced in Section 5.4. Mass transfer between CO_2 and liquid droplets with and without chemical reaction were both studied.

5.2 Theory

In this work, liquid phase mass transfer coefficients of CO_2 into liquid droplets were measured for both physical absorption and chemical absorption. In addition, diffusion coefficient of CO_2 absorption into water droplets was calculated for comparing with the reported reference data to explain the mass transfer mechanism. Therefore, the derivations of calculation formulas for these properties were introduced below.

5.2.1 Derivation of diffusion coefficient for the non-steady state diffusion of gas into liquid droplets

In this section, the derivation of unsteady-state diffusion coefficient of gas into liquid droplets was presented.

The concentration distribution for the non-steady state diffusion in a sphere is given by[23]:

$$\frac{C-C_0}{C_1-C_0}=1+\frac{2a}{\pi r}\sum_{n=1}^{\infty}\frac{(-1)^n}{n}\sin\frac{n\pi r}{a}\exp(-Dn^2\pi^2t/a^2) \tag{5-5}$$

where C_1 is the constant concentration at the surface of the droplet, C_0 is the initially uniform concentration of the droplet, n is the natural number, and a is the radius of the droplet.

The concentration gradient can be calculated by differentiation of eq 5-5:

$$\begin{aligned}&\frac{\partial C}{\partial r}=(C_1-C_0)\cdot\frac{\partial}{\partial r}[\frac{2a}{\pi r}\sum_{n=1}^{\infty}\frac{(-1)^n}{n}\sin\frac{n\pi r}{a}\exp(-Dn^2\pi^2t/a^2)]=(C_1-C_0)\cdot\\&[-\frac{2a}{\pi r^2}\sum_{n=1}^{\infty}\frac{(-1)^n}{n}\sin\frac{n\pi r}{a}\exp(-Dn^2\pi^2t/a^2)+\frac{2a}{\pi r}\sum_{n=1}^{\infty}\frac{(-1)^n}{n}\cdot\frac{n\pi}{a}\cos\frac{n\pi r}{a}\exp(-Dn^2\pi^2t/a^2)]\end{aligned} \tag{5-6}$$

It has $r = a$, $\sin n\pi = 0$, $\cos n\pi = (-1)^n$ at the surface, so:

$$(\frac{\partial C}{\partial r})_{r=a}=(C_1-C_0)\cdot\frac{2}{a}\sum_{n=1}^{\infty}\exp(-Dn^2\pi^2t/a^2) \tag{5-7}$$

Mass transfer rate Q at the surface can be calculated by:

$$\begin{aligned}Q&=AD(\frac{\partial C}{\partial r})_{r=a}=4\pi a^2D(C_1-C_0)\cdot\frac{2}{a}\sum_{n=1}^{\infty}\exp(-Dn^2\pi^2t/a^2)\\&=8\pi aD(C_1-C_0)\sum_{n=1}^{\infty}\exp(-Dn^2\pi^2t/a^2)\end{aligned} \tag{5-8}$$

The total amount of diffusion substance for time t is:

$$
\begin{aligned}
M_t &= \int_0^t Q dt = 8\pi aD(C_1 - C_0)\int_0^t \sum_{n=1}^{\infty} \exp(-Dn^2\pi^2 t/a^2)dt \\
&= 8\pi aD(C_1 - C_0)\sum_{n=1}^{\infty}\int_0^t \exp(-Dn^2\pi^2 t/a^2)dt \\
&= 8\pi aD(C_1 - C_0)\sum_{n=1}^{\infty}[\frac{1}{-Dn^2\pi^2/a^2}\exp(-Dn^2\pi^2 t/a^2)]_0^t \\
&= 8\pi aD(C_1 - C_0)\sum_{n=1}^{\infty}\frac{1}{Dn^2\pi^2/a^2}[1-\exp(-Dn^2\pi^2 t/a^2)] \\
&= 8\pi a^3(C_1 - C_0)\sum_{n=1}^{\infty}\frac{1}{n^2\pi^2}[1-\exp(-Dn^2\pi^2 t/a^2)] \\
&= 8\pi a^3(C_1 - C_0)[\sum_{n=1}^{\infty}\frac{1}{n^2\pi^2} - \sum_{n=1}^{\infty}\frac{1}{n^2\pi^2}\exp(-Dn^2\pi^2 t/a^2)]
\end{aligned}
\tag{5-9}
$$

Substituting the equation $\sum_{n=1}^{\infty}\frac{1}{n^2} = \frac{\pi^2}{6}$ into eqs 5-9:[24]

$$
M_t = \frac{4}{3}\pi a^3(C_1 - C_0)[1 - \frac{6}{\pi^2}\sum_{n=1}^{\infty}\frac{1}{n^2}\exp(-Dn^2\pi^2 t/a^2)] \tag{5-10}
$$

Normally M_t can be obtained by experimental measurements. Therefore, diffusion coefficient for the non-steady state diffusion of gas into liquid droplets can by calculated from eq 5-10.

5.2.2 Derivation of liquid phase mass transfer coefficient of gas absorption into liquid droplets without chemical reaction

In this section, the derivation of liquid phase mass transfer coefficient of gas into liquid droplets for physical absorption is presented.

Due to the fact that the molecular diffusion coefficients of solutes are several orders of magnitude greater in gases than in liquids, the gas phase mass transfer coefficient is much greater than liquid phase coefficient in most instances which causes that the absorption process is controlled by the liquid phase resistance unless the solubility is very high.[17] The liquid phase mass transfer coefficient between liquid droplets and gas without chemical reaction was derived on the following assumptions:

(1) The droplet keeps spherical during formation and fall.

(2) The droplet grows at a uniform volumetric rate during formation.
(3) The droplet diameter and droplet formation time keep constant during each measurement.
(4) The absorption is in equilibrium at the gas-liquid interface and in accordance with Henry's law.

The mass balance equation of gas absorption into liquid droplets without chemical reaction is given by:

$$V_d \frac{dC}{dt} = k_L A_d (C_e - C) \tag{5-11}$$

Integrating eq 5-11 with boundary conditions (at $t = 0$, $C = 0$; at $t = t$, the concentration is C) and it has:

$$C_e - C = C_e e^{-6k_L t/d} \tag{5-12}$$

The mass transfer amount of gas absorption into a liquid droplet during its lifetime τ is:

$$M_\tau = \int_0^\tau k_L A_d (C_e - C) dt = \int_0^\tau k_L A_d C_e e^{-6k_L t/d} dt = \frac{A_d C_e d}{6}(1 - e^{-6k_L \tau/d}) \tag{5-13}$$

The mass transfer amount of gas absorption into a liquid droplet during infinite time is:

$$M_\infty = \int_0^\infty k_L A_d (C_e - C) dt = \int_0^\infty k_L A_d C_e e^{-6k_L t/d} dt = \frac{A_d C_e d}{6} \tag{5-14}$$

The fractional approach to equilibrium is defined by:

$$F = \frac{M_\tau}{M_\infty} = 1 - e^{-6k_L \tau/d} \tag{5-15}$$

Rearranging yields:

$$k_L = \frac{d}{6\tau} \ln(\frac{1}{1-F}) \tag{5-16}$$

F can be calculated by:

$$M_\tau = \frac{-\mathrm{d}n / \mathrm{d}t}{\varphi} \tag{5-17}$$

$$M_\infty = V_2 C_e = V_2 \cdot \frac{P}{H} \tag{5-18}$$

$$F = \frac{M_\tau}{M_\infty} = \frac{(-\mathrm{d}n / \mathrm{d}t) \cdot H}{V_2 P \varphi} \tag{5-19}$$

Here $-\mathrm{d}n/\mathrm{d}t$ is the absorption rate, φ is the droplet formation rate, V_2 is the volume of the droplet, P is the pressure of CO_2 in the gas chamber, and H is Henry's coefficient.

Therefore, liquid phase mass transfer coefficient of gas absorption into liquid droplets without chemical reaction can be calculated from eqs 5-16 and 5-19.

5.2.3 Derivation of liquid phase mass transfer coefficient of gas absorption into liquid droplets with chemical reaction

In this section, the derivation of liquid phase mass transfer coefficient of gas into liquid droplets for chemical absorption was presented.

According to the two-film theory, the total absorption rate equation of the gas-liquid reaction is as follows:

$$N_A = k_L{}^0 E A_d (C_i - C) = k_G A_d (P - P_i) \tag{5-20}$$

For a irreversible chemical reaction, the concentration of gas in the liquid bulk can be considered as zero ($C = 0$).[25] Therefore, the rate equation can be written as:

$$N_A = k_L{}^0 E A_d C_i \tag{5-21}$$

Hence, the liquid phase mass transfer coefficient for gas absorption into single liquid droplet with chemical reaction can be calculated by:

$$k_L = k_L{}^0 E = \frac{N_A}{A_d C_i} = \frac{N_A}{A_d (P_i / H)} = \frac{(-\mathrm{d}n / \mathrm{d}t) \cdot H}{\varphi \cdot \tau \cdot A_d \cdot P_i} \tag{5-22}$$

5.3 Experimental Section

A novel experimental set-up (droplet chamber) for mass transfer studies between individual droplets and the surrounding CO_2 gas was constructed in this work as shown in Figure 5-3.

The experimental equipment consists of a gas supply and saturation system, a droplet generation device, a gas chamber, a temperature control box, a pressure measuring device, an overflow section, a soap film flow meter for measuring gas make-up, and a photography system. A schematic diagram of this new experimental set-up is shown in Figure 5-4.

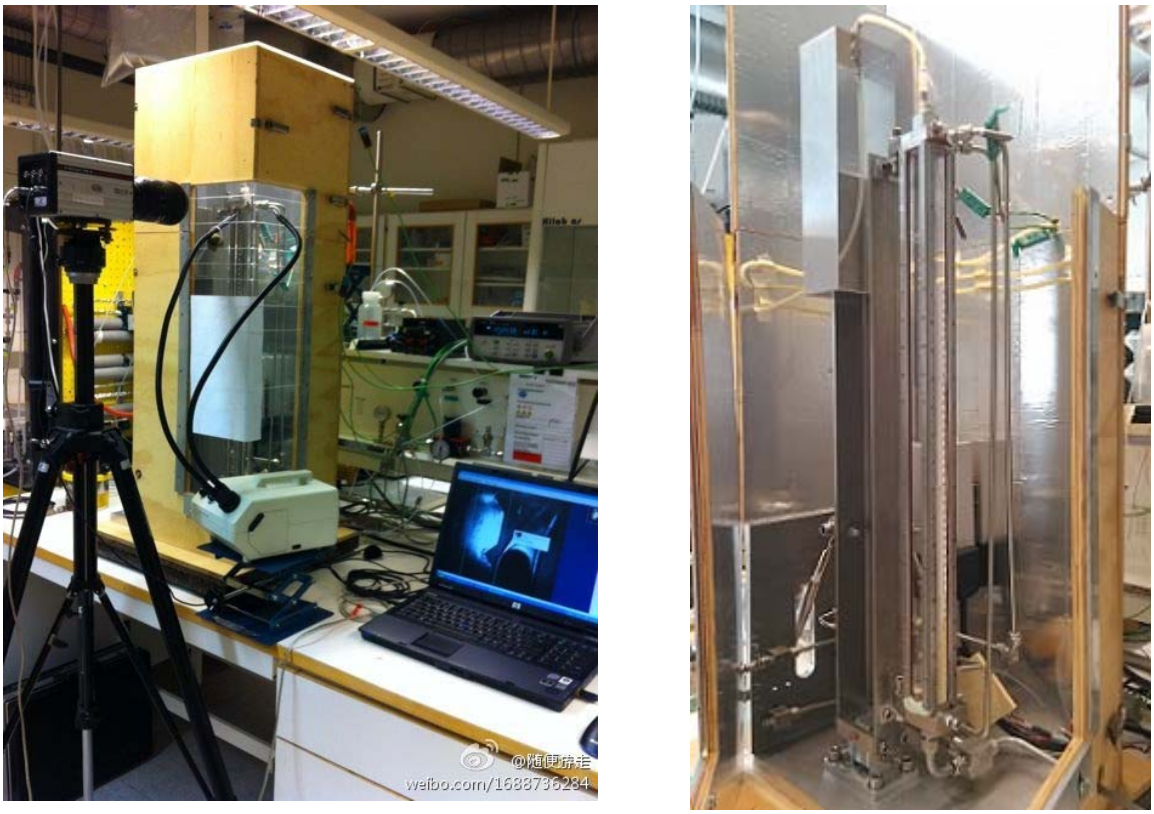

Figure 5-3. The picture of the novel experimental apparatus for studying gas absorption into liquid droplets.

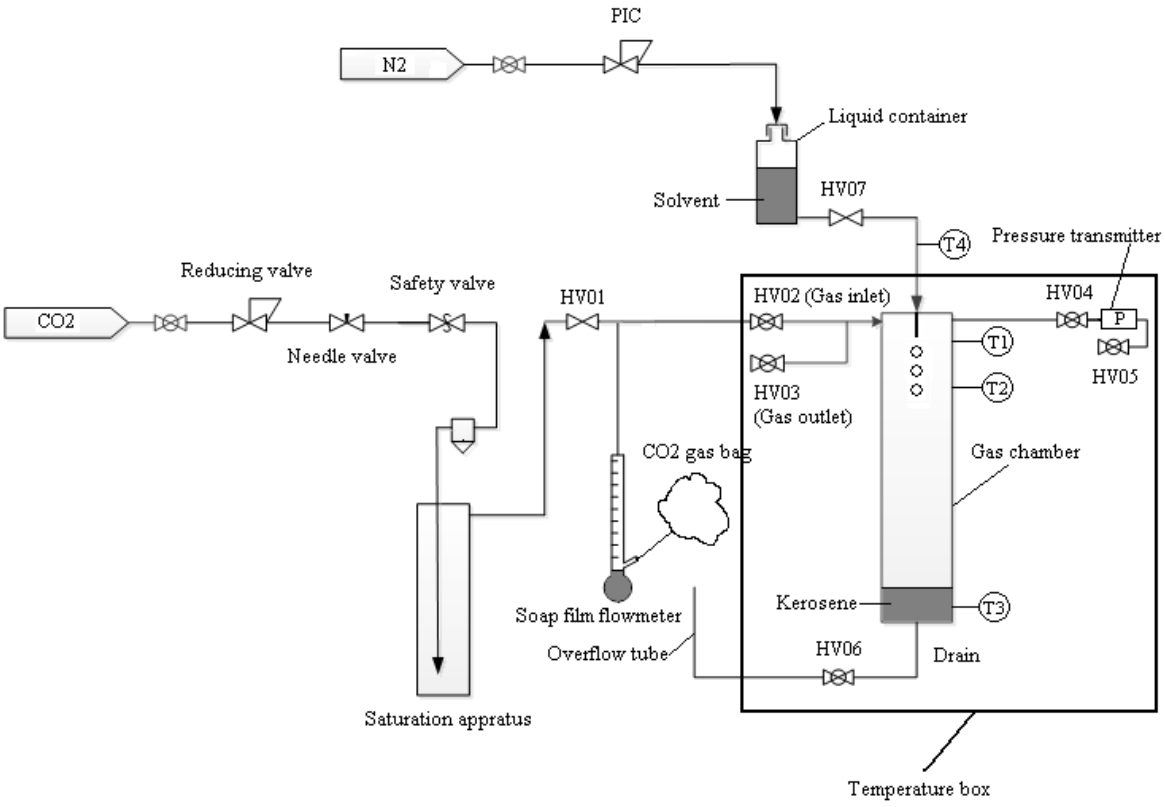

Figure 5-4. The sketch of a novel experimental apparatus for studying CO_2 absorption by liquid droplets.

Carbon dioxide (purchased from AGA with purity 99.99%) was fed through a pressure regulator (0 to 4 bar) and a needle valve into the saturation apparatus. The simple schematic diagram of the saturation apparatus is shown in Figure 5-4. Details of the saturation apparatus is shown in Figure 5-5. CO_2 passes through a surge flask, flows through a small hole on the bottom of the inner tube and then bubbles through the water. The humidified CO_2 enters the gas chamber through valve HV01.

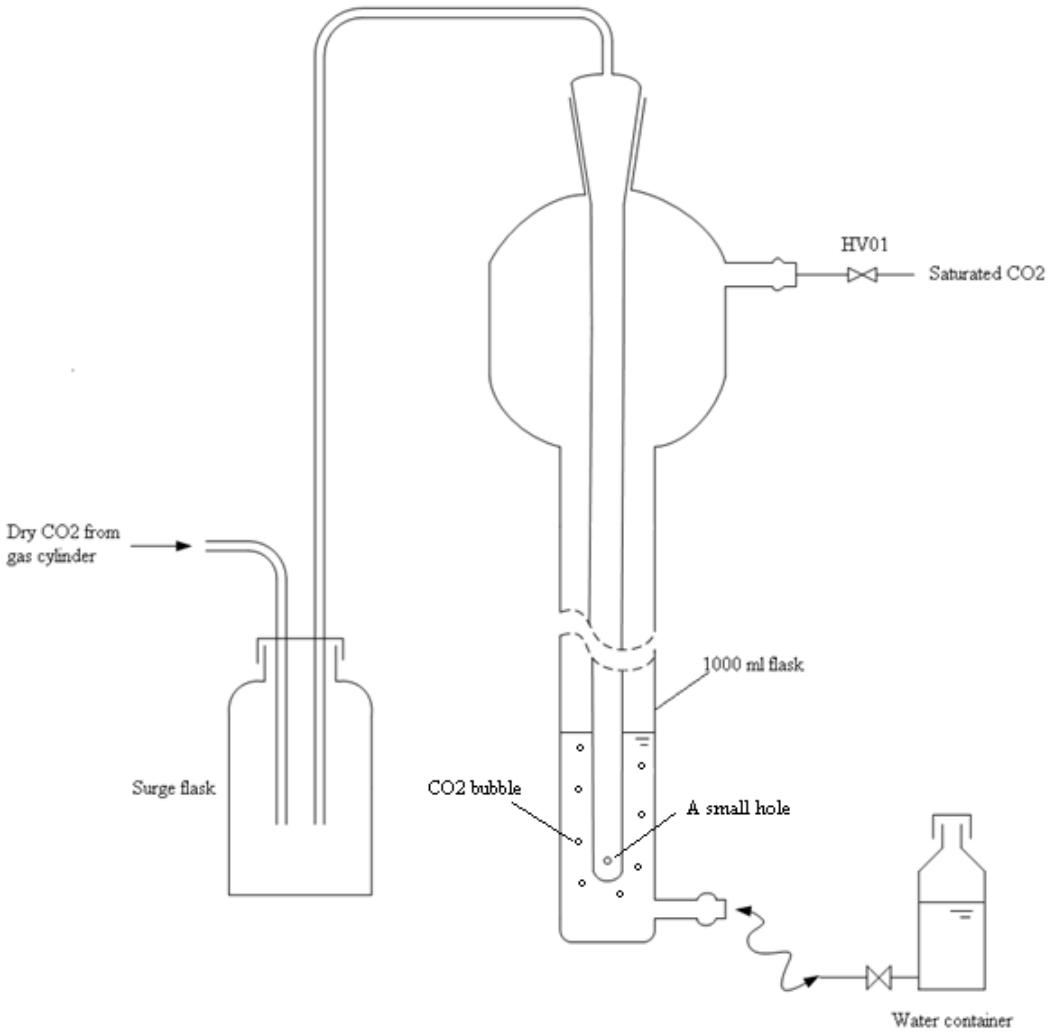

Figure 5-5. The sketch of the saturation apparatus.

A humidity and temperature transmitter MI-63113 from VAISALA was used to test the water saturation of CO_2 that was humidified by this apparatus as shown in Figure 5-6. The measured relative humidity of CO_2 under different CO_2 flow rates and different heights of water were tabulated in Table 5-2. The results show that the flow rate of CO_2 over the range

covered by these experiments and the height of water does not affect the saturation very much. The relative humidity of the saturated CO_2 was always around 80% when the temperature is about 23 °C. This lack of saturation only brings an error of 0.54% for the results, and therefore affects very little to our experiments.

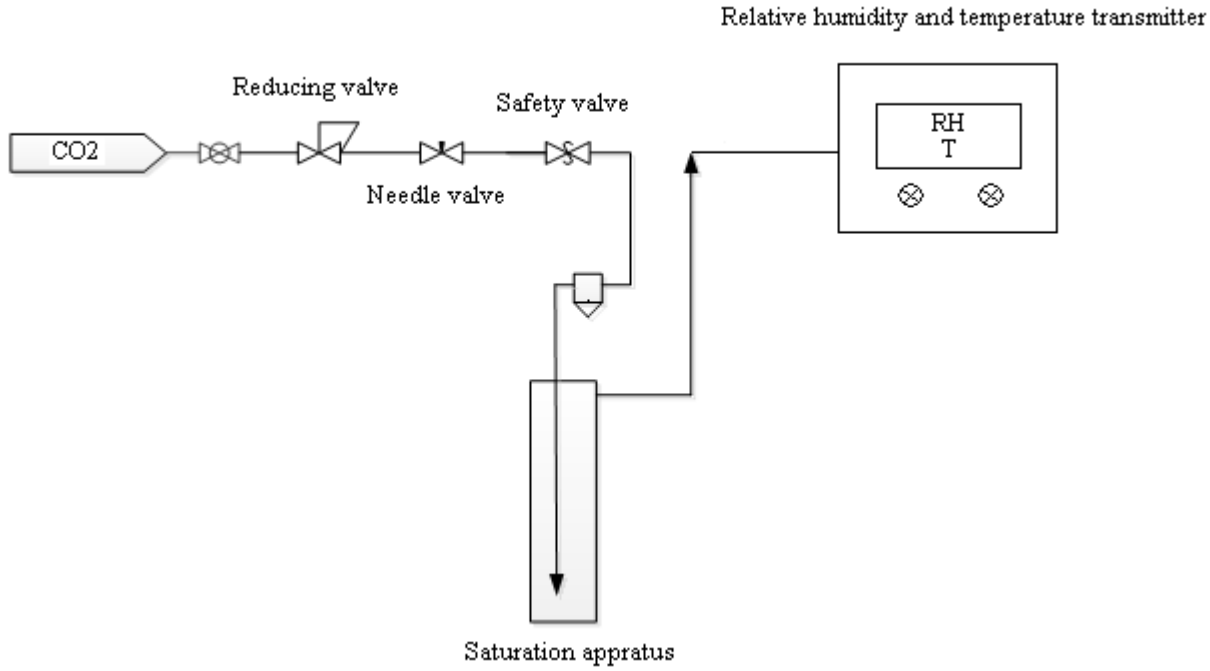

Figure 5-6. The sketch of the saturation testing set-up.

Table 5-2. The Relative Humidity of the Saturated CO_2 under different conditions.

The height of water [cm]	Pressure regulator [bar]	Needle valve[a]	T [°C]	Relative humidity (RH)[b]	Water vapor pressure [hPa]	$P_{H2O(g)}/P_{CO2}$
20.2	0.2	7	23.4	80.2	23.12	0.023
20.2	0.4	7	23.2	81.4	23.19	0.023
20.2	0.6	7	23.0	80.3	22.61	0.023
20.2	0.4	4	23.6	80.6	23.50	0.024
27.0	0.4	4	23.6	81.0	23.62	0.024

[a]: The degree of opening of the needle valve was divided into eight levels.
[b]: RH means the ratio of the actual vapor pressure of water to the saturated vapor pressure of water.

Kerosene was injected into the gas chamber through drain valve HV06 to prevent CO_2 from being absorbed by sedimentary liquid on the bottom as shown in Figure 5-4. The droplets sink below the kerosene very fast because the density of kerosene is significantly lower than water or aqueous MEA solutions. Therefore the coalescence effect during droplet

lifetime is negligible in this work. The kerosene was kept at a constant level by an overflow section which is equivalent to a U-tube (Figure 5-4). Dripping droplets were spilled out through the overflow tube. The absorption experiments can be performed under different droplet falling heights by changing the length of the overflow tube thus altering the kerosene level. The rate of CO_2 make-up was measured by a soap film flow meter when CO_2 in the gas chamber was being absorbed by the liquid droplets. The picture of the soap film flow meter is shown in Figure 5-7. The gas bag which is full of saturated CO_2 was made by a thin plastic bag. The valve HV02 is kept open when the experiment is in progress, hence the pressure in the gas chamber is always consistent with the pressure in the gas bag, which is the same as the pressure in the laboratory. A barometer was available to read this.

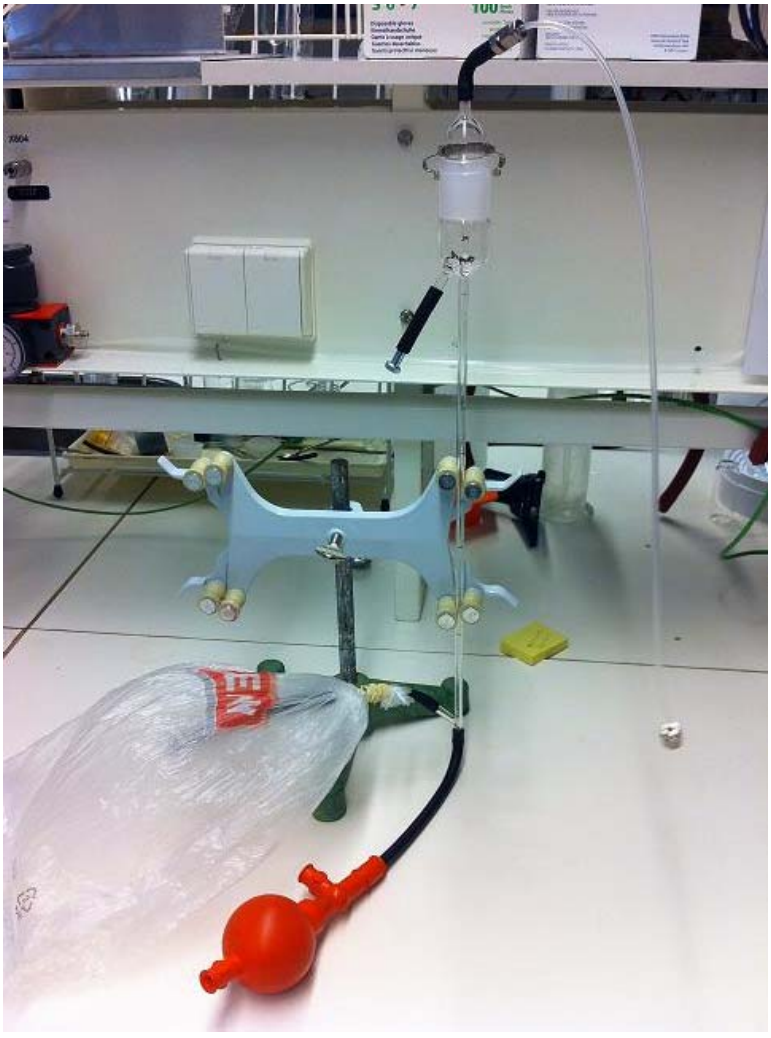

Figure 5-7. The picture of the soap film flow meter.

A pressure transmitter (Model 154N-015G-R) was mounted for monitoring the pressure change in the gas chamber. The pressure transmitter was connected to Agilent BenchLink

Data Logger 34972A to record the data online. The pressure calibrator (Druck DPI620 Advanced Modular Calibrator from GE Measurement & Control) was used to calibrate the pressure sensor to obtain the transformational relation between electric potential and pressure. The calibration curve is shown in Figure 5-8.

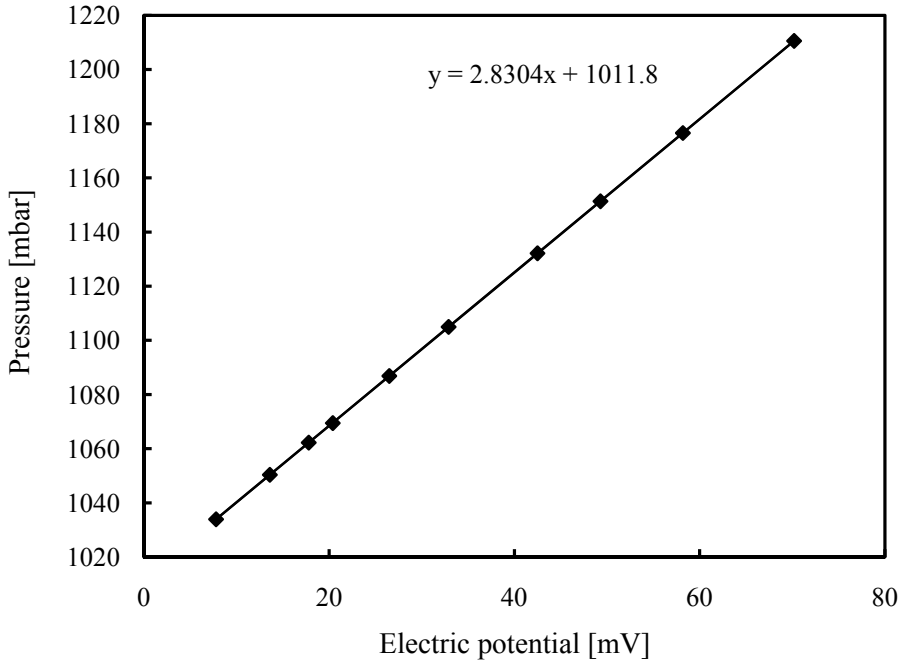

Figure 5-8. Calibration curve for the pressure transmitter (Model 154N-015G-R).

The gas chamber (3×3×60 cm) was manufactured by CMR Prototech based on a design agreed up front. The design drawing of the gas chamber was provided by CMR Prototech and shown in Figure 5-9. Four sides of the chamber were made of glass in order to enable taking pictures of the droplets. Side edges were fixed with M3 screws and special glue. The verticality of the gas chamber can be adjusted. The internal structure of the top of the chamber for fixing the needle is illustrated in Figure 5-10. A ruler with the set length was fixed inside the chamber to assist in determining the size of the droplets.

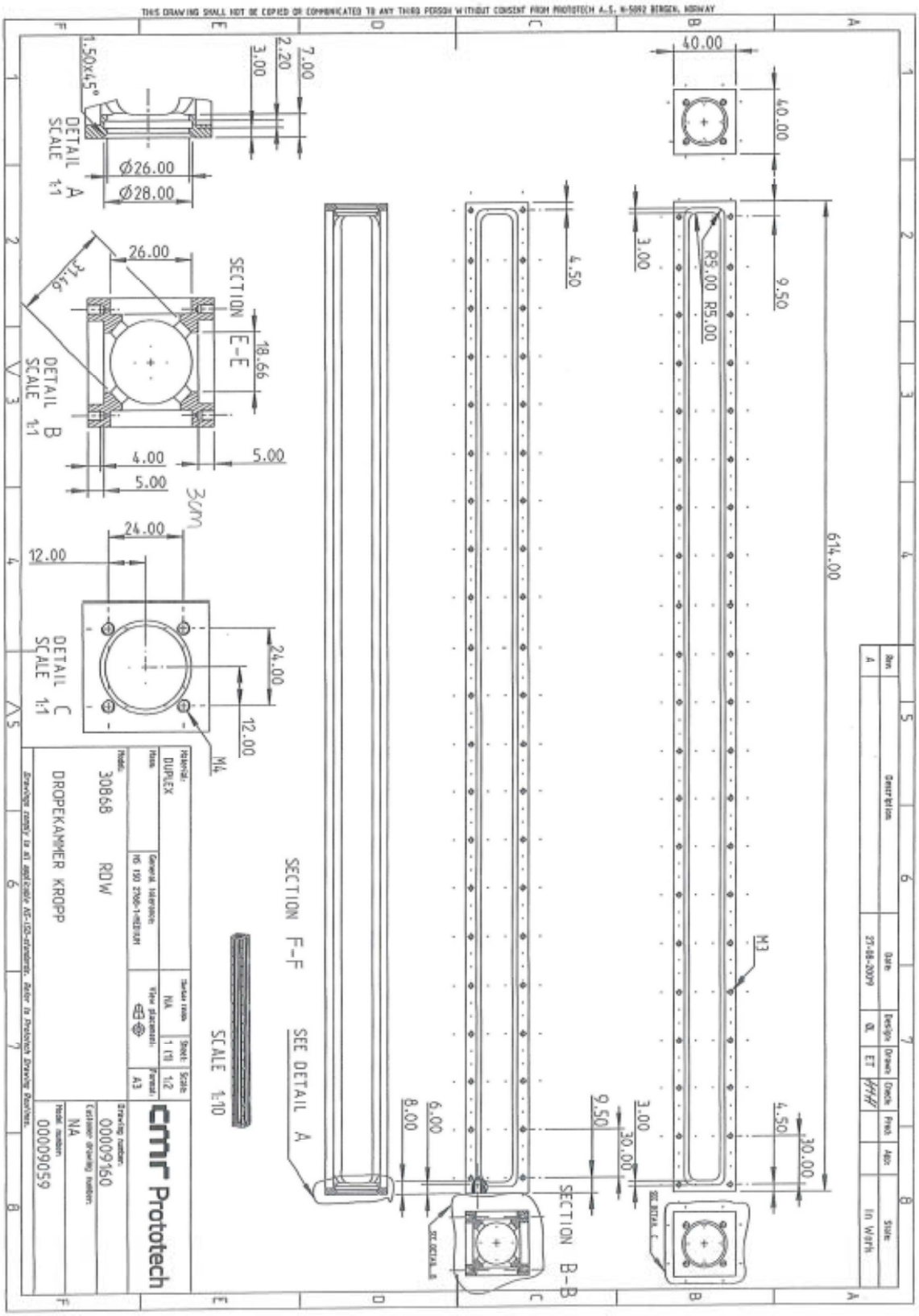

Figure 5-9. The design drawing of the gas chamber from CMR Prototech.

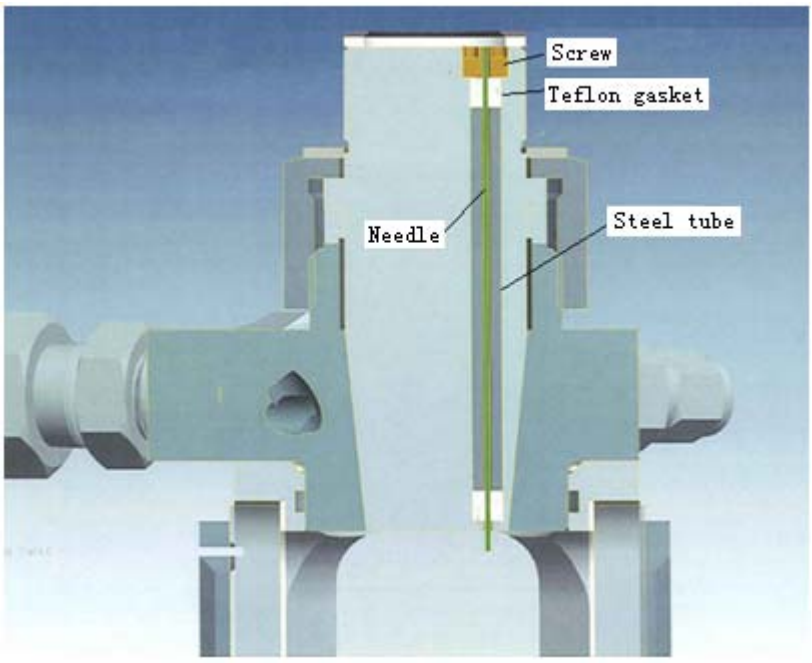

Figure 5-10. The internal structure of the top of the chamber.

A temperature control box was built around the chamber. The box was made of wood which has low thermal conductivity. The front corner was made up of several pieces of plastic sheets so that the pictures can be taken from different vertical positions. A fan heater (HGL 046 400W) from STEGO and an associated temperature control device were used in this work. Four K-thermocouples were used to measure the temperatures of gas phase at different heights in the chamber, the kerosene and the liquid phase. The temperature results were also recorded by Agilent BenchLink Data Logger 34972A. The thermocouples were calibrated by a temperature calibrator from AMETEK (Type: CTC-140 A RS232). The gas temperature on the upper part of the chamber was a little higher than the lower part. The temperature difference over the whole chamber was less than 0.5 K. An average temperature over the chamber can be used for the k_L calculation because the decrease in solubility is approximately balanced with the increase in absorption rate when the temperature rises over the range that these experiments covered.[4] The absorption experiments were carried out at different temperatures.

This apparatus produces individual droplets by pushing the liquid through a needle with the help of pressurized nitrogen. Nitrogen passes through a pressure regulator (0 to 1.6 bar) and then enters into a 1000 ml flask. The experiments can be performed under different droplet formation rates by changing the pressure of N_2 and the setting of valve HV07. The liquid flows through a long hose in the temperature control chamber to make sure that the

temperature of the droplets are consistent with the temperature in the chamber. A needle (gauge 25) with a blunt tip was used in this work. The outer diameter of the needle is 0.51 mm and the inner diameter is 0.26 mm. Two different lengths of the needle (100 mm and 283 mm) were chosen for our experiments. In order to study the absorption during only droplet formation, the long needle was used to let the droplets deposit under kerosene as soon as they detached from the needle.

A high speed video camera X-Stream XS-3 with a macro lens (Nikon AF-S Micro Nikkor 105 mm f/2.8G ED) was used to take photographs to determine the size of droplets and the droplet formation time. The frame speed is 400 fps and the exposure time is 2497 μs here. The videos were analyzed by the software MotionPro X Studio. A SCHOTT KL 1500 electronic halogen light source was used. The procedure of the absorption experiments between liquid droplets and gas was presented in Appendix 5-3.

In our experiments, pure CO_2 is filled in the gas chamber to eliminate the gas side mass transfer resistance. Therefore, the overall mass transfer coefficient of the gas phase and liquid phase in this work are respectively:

$$K_G = \frac{1}{\frac{1}{k_G} + \frac{H}{k_L}} \approx \frac{k_L}{H} \tag{5-23}$$

$$K_L = \frac{1}{\frac{1}{k_L} + \frac{1}{Hk_G}} \approx k_L \tag{5-24}$$

The measurement accuracy of liquid phase mass transfer coefficients of CO_2 absorption by liquid droplets mainly depends on the deviations of determinations of the droplet diameter and the absorption rate. The deviation of the droplet diameter is about ± 0.05 mm. The deviation of the absorption rate is about ± 1×10^{-9} mol/s. As a result, the measurement accuracy of liquid phase mass transfer coefficients is around ± 8%.

5.4 The determination of experimental parameters

In this section, the determination of experimental parameters, such as droplet diameters (d_1, d_2 and d), droplet formation rate φ, droplet formation time t_1, droplet falling time t_2, and

droplet life time τ, were introduced. Here, the subscript 1 means the condition during droplet formation, 2 means during droplet fall, and no subscript means during droplet life time (formation and fall together).

5.4.1 The droplet diameters

a) The average droplet diameter during formation d_1

The average droplet diameter during formation was determined by the assumption that the droplet stays spherical during formation and grows at a uniform volumetric rate. For a spherical particle growing at a constant volumetric rate, the droplet surface area has an exponential relationship with time[16]:

$$A_d = \pi d^2 = \pi d_f^{\,2} t_f^{\,-2/3} t^{2/3} \tag{5-25}$$

Here A_d is the surface area of droplet, d is the droplet diameter at time t, and t is the droplet growing time. The subscript f means the condition at the end of formation period. Therefore, d_f is the droplet diameter when the droplet detaches from the needle, and t_f is the time that the droplet needs to complete growing. t_f is equal to the droplet formation time t_1.

Rearranging yields:

$$\frac{d}{d_f} = \left(\frac{t}{t_f}\right)^{1/3} \tag{5-26}$$

The time average droplet diameter during formation d_1 can be calculated by integrating eq 5-26 with time and given:

$$d_1 = \frac{3}{4} d_f \tag{5-27}$$

where d_1 is the average droplet diameter during formation and d_f is the droplet diameter when the droplet detaches from the needle. It is assumed that the droplet diameter does not change during fall, hence $d_f = d_2$.

Figure 5-11 shows how the droplet diameter increases with time during formation and verifies that the assumption of a spherical drop with constant volumetric growth rate is reasonable by comparing the experimental droplet sizes which were obtained from the high speed camera to the value that is calculated from eq 5-26.

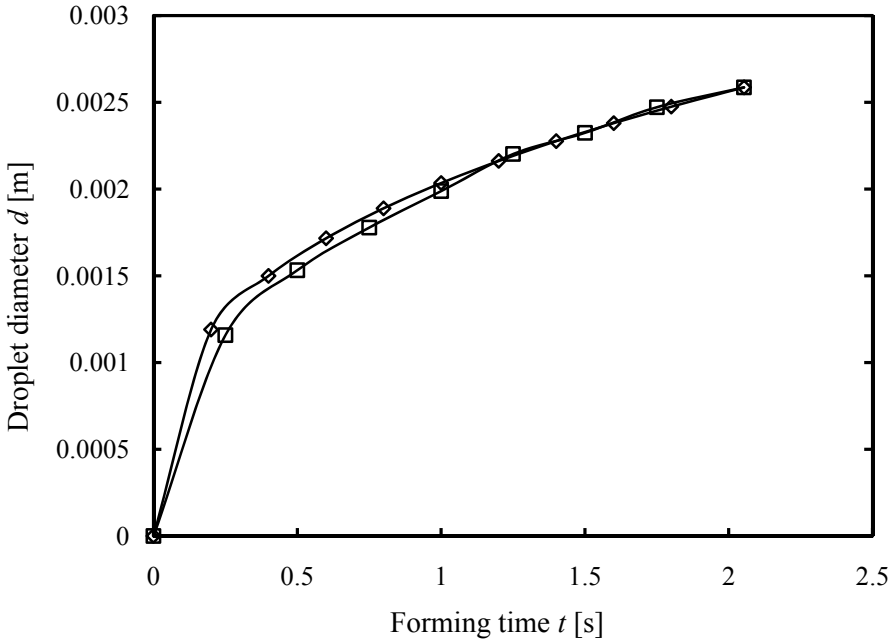

Figure 5-11. The droplet diameter as a function of time during formation. □, the experimental data from the high speed camera; ◇, the calculated data from eq 5-26.

b) The droplet diameter during fall d_2

The droplet diameter during fall can be calculated from the high speed camera as shown in the example in Figure 5-12. The length unit L on the actual scale is 0.01 m. So the droplet diameter during fall is:

$$d_2 = \frac{12.46}{51.33} \times 0.01\,\text{m} = 0.00243\,\text{m} \tag{5-28}$$

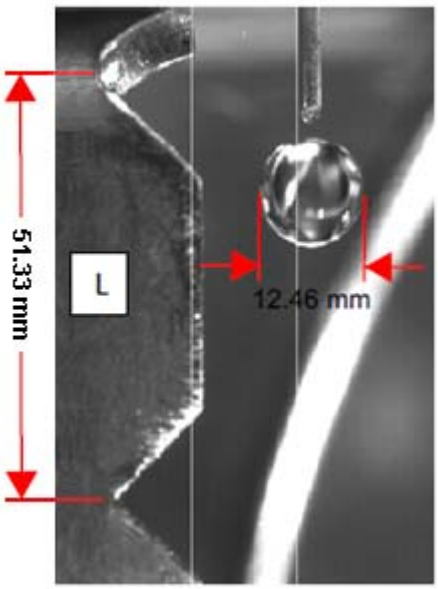

Figure 5-12. The calculation of droplet diameter during fall by the high speed camera.

c) The average droplet diameter during formation and fall *d*

The time average droplet diameter during formation and fall can be calculated by:

$$d = \frac{d_1 t_1 + d_2 t_2}{t_1 + t_2} = \frac{d_1 t_1 + d_2 t_2}{\tau} \tag{5-29}$$

Here d_1 and d_2 are the droplet diameter during formation and during fall respectively, t_1 and t_2 are the droplet formation time and droplet falling time, respectively. τ is the droplet lifetime during formation and fall.

5.4.2 The droplet formation rate φ

The droplet formation rate can also be calculated by analyzing a video obtained with a high speed camera as shown in Figure 5-13.

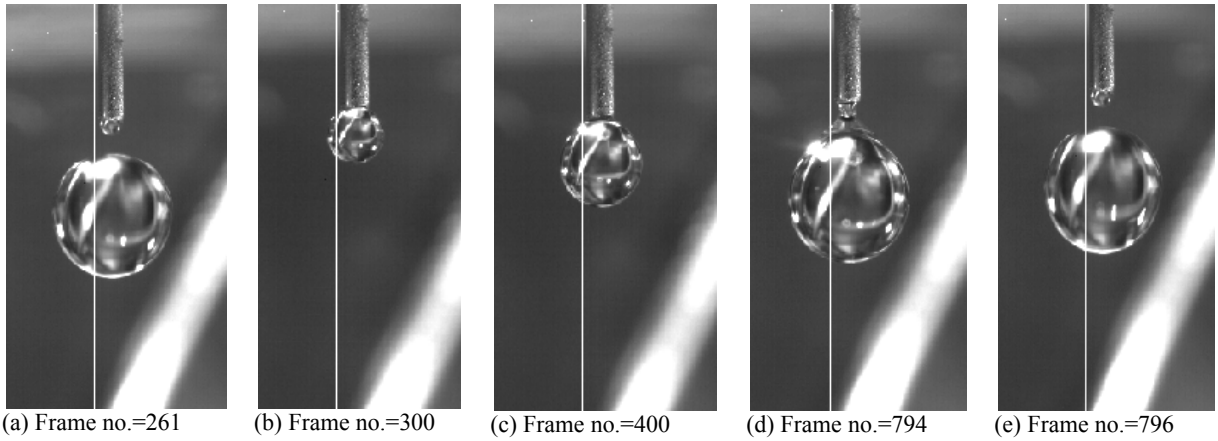

(a) Frame no.=261 (b) Frame no.=300 (c) Frame no.=400 (d) Frame no.=794 (e) Frame no.=796

Figure 5-13. The formation process of a droplet.

The camera frame speed is 400 fps (frames per second). The frame numbers for one droplet to form is 796-261+1 = 536. Then the time for one droplet to form is t_1 = 536/400 s = 1.34 s. The droplet formation rate is:

$$\varphi = \frac{1}{1.34}\,\mathrm{s}^{-1} = 0.746\,\mathrm{s}^{-1} \tag{5-30}$$

5.4.3 The droplet formation time t_1, droplet falling time t_2 and droplet lifetime τ

a) The droplet formation time t_1

The droplet formation time t_1 can be obtained by analyzing the video from the high speed camera as shown in Section 5.4.2.

b) The droplet falling time t_2

Since the gas chamber is too tall to take a photograph of the whole droplet falling process, the droplet falling time was indirectly calculated by eq 5-31 which is derived from the force balance equation of a falling droplet.

$$\begin{cases} \dfrac{\mathrm{d}s}{\mathrm{d}t} = u \\ \dfrac{\mathrm{d}u}{\mathrm{d}t} = g - \varepsilon_d \dfrac{3u^2}{4d} \dfrac{\rho_g}{\rho_d} \end{cases} \tag{5-31}$$

Here s is the droplet falling distance, t is the droplet falling time, u is the droplet velocity, ds/dt is the differential of s, du/dt is the differential of u, g is the acceleration of gravity, ε_d is the drag coefficient of droplet, d is the droplet diameter, ρ_g is the density of gas, and ρ_d is the density of droplet. The drag coefficient of droplet ε_d was calculated by the correlations from Morsi and Alexander[26].

A Matlab program was used to solve eq 5-31 and calculate the droplet falling time when the droplet falling distance is given. The Matlab program is shown in Appendix 5-4. Figures 5-14 and 5-15 illustrate the good agreement between the experimental results from the high speed camera and the Matlab simulated results during the early stage of droplet free fall. The calculations of the experimental droplet velocity are presented in Appendix 5-5.

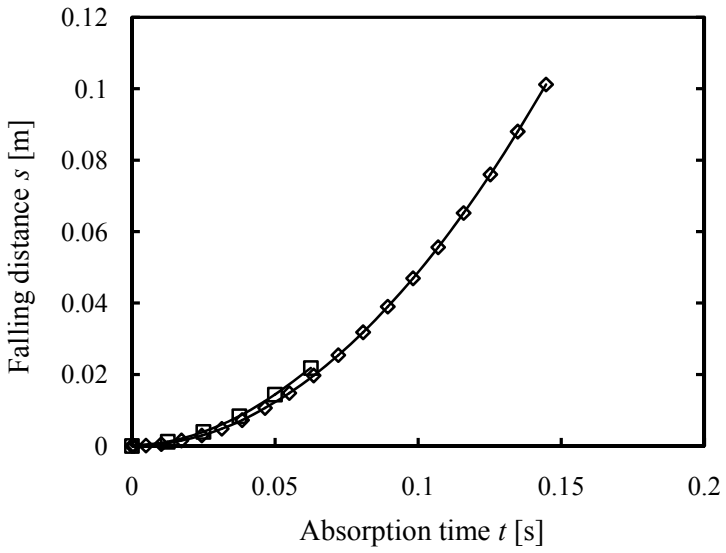

Figure 5-14. The droplet falling distance varies along with time. □, the experimental data from the high speed camera; ◇, the Matlab simulated results.

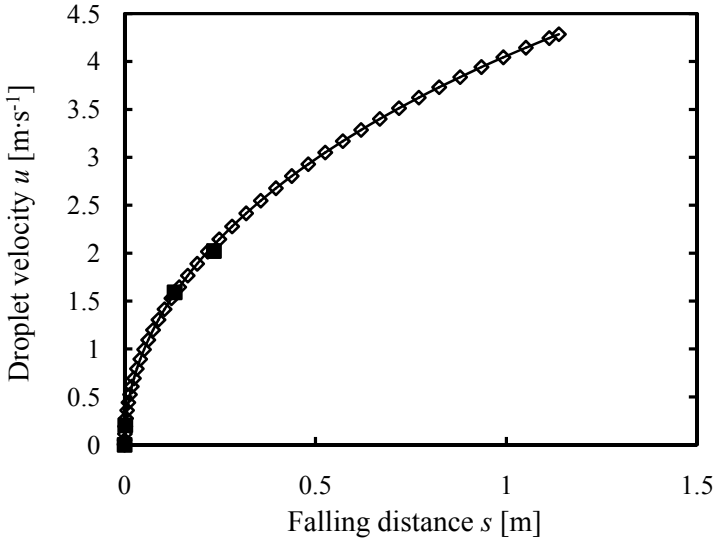

Figure 5-15. The droplet velocity varies along with the droplet falling distance. ■, the experimental data from the high speed camera; ◇, the Matlab simulated results.

c) The droplet lifetime τ

The droplet lifetime during formation and fall can be calculated by:

$$\tau = t_1 + t_2 \tag{5-32}$$

5.5 CFD Simulation of a Droplet Chamber

In this work, a novel experimental set-up called "a droplet chamber" was built to obtain the mass transfer information of CO_2 absorption by liquid droplets. A droplet chamber apparatus is essentially a gas chamber through which droplets flow. The droplets should be monosized and the size of droplet is known. During the process of choice of droplet generator in the droplet chamber, it is important to know the information of a falling droplet by CFD simulations. The model Volume of Fluid (VOF) was used to calculate a single droplet falling, and the software used is FLUENT.

5.5.1 The VOF model

The VOF model is one of the Euler-Euler multiphase models available in FLUENT. Different phases are treated mathematically as interpenetrating continua. A surface-tracking technique is applied to a fixed Eulerian grid which is designed for two or more immiscible fluids where the position of the interface between the fluids is of interest and calculated by the

VOF model.[27] The transient tracking of any liquid-gas interface can be done by computing a time-dependent solution. Hence, the shape and motion of the droplet in a gas chamber can be predicted by the VOF model. The formulation of time-dependent simulation with the geometric reconstruction interpolation scheme is recommended.[28] The non-iterative solver can be used to increase the speed and efficiency of the calculations when using the pressure-based segregated algorithm for time-dependent flow calculations.[28] The effects of surface tension along the interface is also considered in this work. The continuum surface force (CSF) model which is proposed by Brackbill et al.[27] is available in FLUENT.

5.5.2 Problem description

This work considers the transient tracking of a liquid-gas interface in the geometry as shown in Figure 5-16. Due to difficulties with a diverging pressure correction, the calculation area was minimized to be able to increase the number of cells to solve the details. The axial symmetry of the problem allows a 2D geometry to be used. The domain consists of two regions: a liquid chamber and a gas chamber. The dimensions are summarized in Table 5-3. At time zero, the nozzle is filled with liquid, while the rest of the domain is filled with gas. This is done by patching liquid in the nozzle region. Both fluids are assumed to be at rest. To initiate the injection, the velocity of liquid phase at the inlet boundary is given as velocity-inlet condition. A constant velocity inlet is used in this simulation.

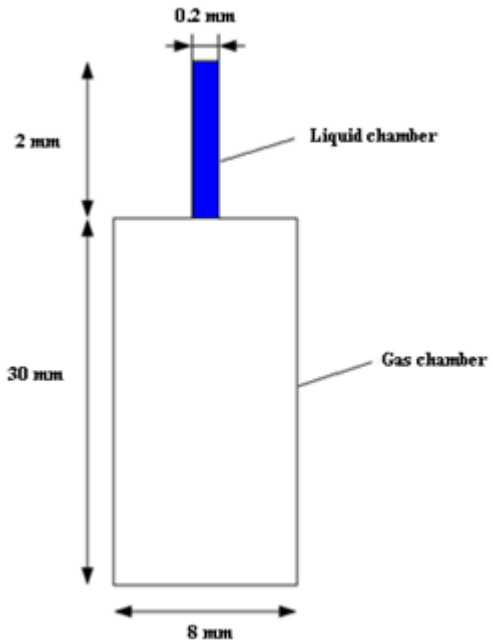

Figure 5-16. Schematic of the calculation area in this work.

Table 5-3. Droplet Chamber Dimensions – Calculation Area for Simulation.

	Radius (mm)	Length (mm)
Liquid chamber	0.1	2
Gas chamber	4	30

The properties of the two phases involved in the simulation are given in Table 5-4. For the sake of simplicity, air has been used as the gas, and water as the liquid. In general, it is possible to specify the primary and secondary phases whichever way preferred. Since an initial volume fraction of 1 for the liquid phase will be patched in the liquid chamber, it is more convenient to choose the liquid phase as a secondary phase.

Table 5-4. Properties of the Two Phases Involved in the Simulation.

	Primary phase (Gas)	Secondary phase (Liquid)
Density [kg/m^3]	1.225	998.2
Viscosity [kg/(m·s)]	1.7894E-05	0.001003
Surface tension [dyn/cm^2]	-	73.5

[a]: Gas = Air; Liquid = Water

For VOF calculations, the operating density should be defined as the density of the lightest phase which excludes the build-up of hydrostatic pressure within the lightest phase and improves the round-off accuracy for the momentum balance.[27] Hence, the operating density is given as the density of the gas phase. For the interphase interaction, wall adhesion is enabled, so that contact angles between the fluid and the wall can be prescribed in order to adjust the normal and curvature of the surface near the wall.

5.5.3 Grid generation

The grid in this work is generated in Gambit 2.4.6. It requires too much computer capacity to generate a very fine mesh in the entire geometry. Therefore, the geometry has been divided into several areas with different type of meshing. The mesh was refined more in the upper part of the geometry, especially in regards to the area where the liquid enters into the gas chamber. The edge representing the liquid's entrance to the gas chamber is meshed with small intervals. The "neighbor" edge, that together with the liquid's entrance edge represents the "roof" of the gas chamber, is meshed in such a way that the cell density increases towards the liquid's

entrance. Downstream the gas chamber, the cell density develops towards an uniform cell density across the chamber. The interior of the model which is composed of a fine grid of quadrilateral cells can be seen by zooming after the import of grid into FLUENT as shown in Figure 5-17.

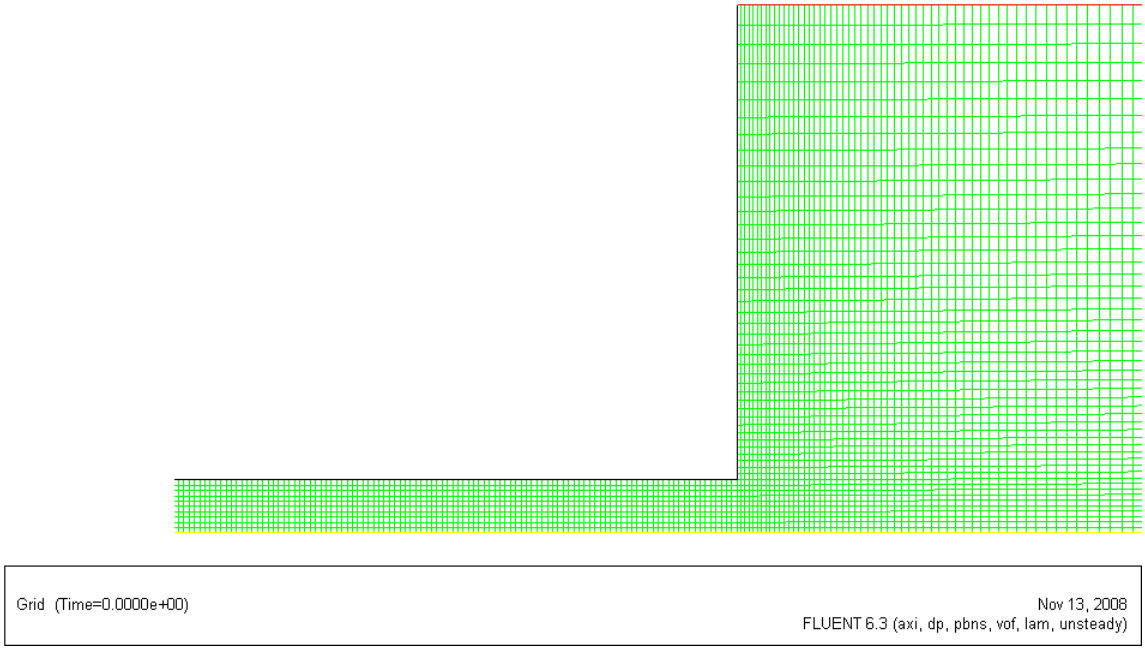

Figure 5-17. The quadrilateral grid that is zoomed in on the area of the liquid's entrance into the gas chamber in FLUENT. (The grid was drawn together with Marit Kleven.)

The boundary specifications for each edge of the grid are given in Figure 5-18. The purple edge (top of the liquid chamber) is named "Inflow". The green edge (side of the liquid chamber) is named "Inlet-wall". The yellow edge (top of the gas chamber) is named "Top-wall". The red edge (side of the gas chamber) is named "Vertical-wall". The blue edge (bottom of the gas chamber) is named "Outlet". The black line represents the symmetry axis. The boundary types for each edge of the grid are given in Table 5-5.

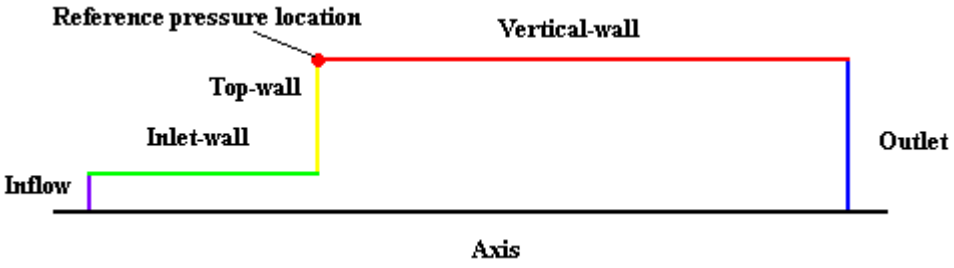

Figure 5-18. Boudary specifications for each edge of the grid.

Table 5-5. Boundary Types for Each Edge of the Grid.

Name	Boundary type	Comment
Inflow	VELOCITY_INLET	Top of the liquid chamber
Outlet	PRESSURE_OUTLET	Bottom of the gas chamber
Axis	AXIS	-
Inlet-wall	WALL	Side of the liquid chamber
Top-wall	WALL	Top of the gas chamber
Vertical-wall	WALL	Side of the gas chamber

5.5.4 FLUENT Simulation Set-up

The 2D simulations are performed in Fluent 6.3.26. Because the dimensions are small, the double-precision version of FLUENT will be used. The simulation set-up, i.e. FLUENT models, is given in Table 5-6. The 1st order implicit formulation is assumed sufficient for this case. For a time-dependent VOF calculation, FLUENT will refine the time step for the volume fraction calculation automatically based on the input maximum Courant number allowed near the free surface.[27] In this work, the default value of 0.25 is kept, i.e. the time step will be chosen to be at most one-fourth the minimum transit time for any cell near interface.

Table 5-6. FLUENT Models.

Solver	Pressure-based
Time	Unsteady state, non-iterative time advancement
Formulation	Implicit, 1st order
Space	Axisymmetric
Multiphase model	VOF, Explicit scheme, Courant number=0.25 Click on "Implicit Body Force"
Viscous model	Laminar
Energy equation	Not activated
Operating Conditions	Click on "Gravity" (X: 9.81 m/s^2, Y: 0 m/s^2) Click on Specified Operating Density"

The solution controls, e.g. discretization schemes, are given in Table 5-7. For the Pressure-Velocity Coupling, the Fractional Step scheme is chosen. It is worth to notice that the PRESTO! pressure discretization scheme, which is used in this work, is less stable when

using the non-iterative time-advancement solver. As a consequence, smaller time steps may be required. Since the Explicit scheme has been used for the multiphase model in this work, the relaxation factor for volume fraction does not need to be given in the control panel. On the contrary, the relaxation factor for volume fraction has to be set if the Implict scheme is chosen. The reason is probably that with respect to the Implicit scheme, the iterative solution of volume fraction for the transport equation has to be given in every time step.

Table 5-7. Solution Controls.

	Discretization Schemes	**Non-iterative Solver Controls Relaxation Factor**			
		Max. corrections	Correction tolerance	Residual tolerance	Relaxation factor
Volume Fraction	Geo-Reconstruct	-	-	-	-
Pressure	PRESTO!	10	0.25	0.0001	1
Momentum	QUICK	5	0.05	0.0001	1

The boundary conditions are given in Table 5-8. The operating pressure in the simulations is 1 atm, and the reference pressure location is set to a point where it is likely to believe that the fluid will always be 100% gas as shown in Figure 5-18. The velocity-inlet condition and the pressure-outlet condition are given for the secondary phase, i.e. water. Hence for the liquid phase, the volume fraction is equal to 1 at the inlet and the backflow volume fraction is equal to 0. The material of the walls are assumed to be stainless steel. Therefore, the contact angle for WALL is set to 70 deg.

Table 5-8. Boundary Conditions.

VELOCITY_INLET	0.194 m/s; 0.5 m/s
PRESSURE_OUTLET	0 Pa
Contact angle for WALL	70 deg

5.5.5 Simulation Results

The process of formation and fall of the droplet can be simulated by the VOF model. Two velocity-inlet conditions were considered.

5.5.5.1 Case 1, the inlet velocity is constant and equal to 0.194 m/s

In order to compare the simulated results with the experimental data, the inlet velocity was set to 0.194 m/s which is the same as the experimental condition. In our experimental process, the droplets were produced by pushing the liquid through a needle with the help of pressurized nitrogen. Hence, the experimental velocity of the fluid leaving the nozzle can be estimated by $u = \frac{V_d / t_1}{A}$. Here V_d is the volume of the droplet, t_1 is the droplet formation time, and A is the cross area of the needle. A set of experimental data (the droplet diameter is 1.84 mm, the droplet formation time is 0.5248 s, and the the size of the needle is 0.2 mm) was used. The simulated results are given below.

a) The droplet diameter and the droplet formation time

Figure 5-19 shows a droplet which just detached from the liquid chamber in the CFD simulation. Since the real dimensions of the liquid chamber are already known as given in Table 5-3, the droplet diameter can be calculated. The droplet diameter in the CFD simulation is calculated to be 1.83 mm. Since the start time is zero, the simulated droplet formation time is 0.4832 s in this case. As can be seen from the results, the deviations between the experimental data and the simulated results are good. In this case, the accuracy of the droplet diameter is 0.5 %, which is very low. The accuracy of the droplet formation time is 7.9 %.

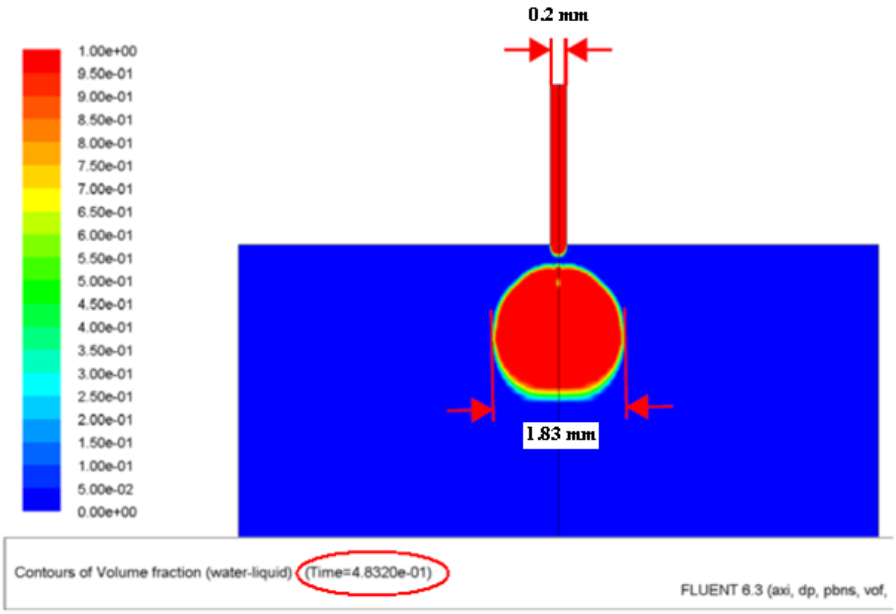

Figure 5-19. The contours of volume fraction of water phase at t = 0.4832 s (inlet velocity 0.194 m/s).

b) The droplet falling distance vs. the droplet falling time

The process of the droplet free fall can also be simulated by CFD. The droplet falling distance at each time can be calculated by the contours of volume fraction of water phase. The curve of the simulated droplet falling distance changing with the droplet falling time is shown in Figure 5-20. As mentioned earlier, the droplet falling time at certain droplet falling distance in this work was calculated from eq 5-31 by Matlab. The comparisons between the CFD simulation, the Matlab calculated results and the data which were directly got by experiments for the curve of droplet falling distance vs. droplet falling time are also given in Figure 5-20. The agreement between them is good.

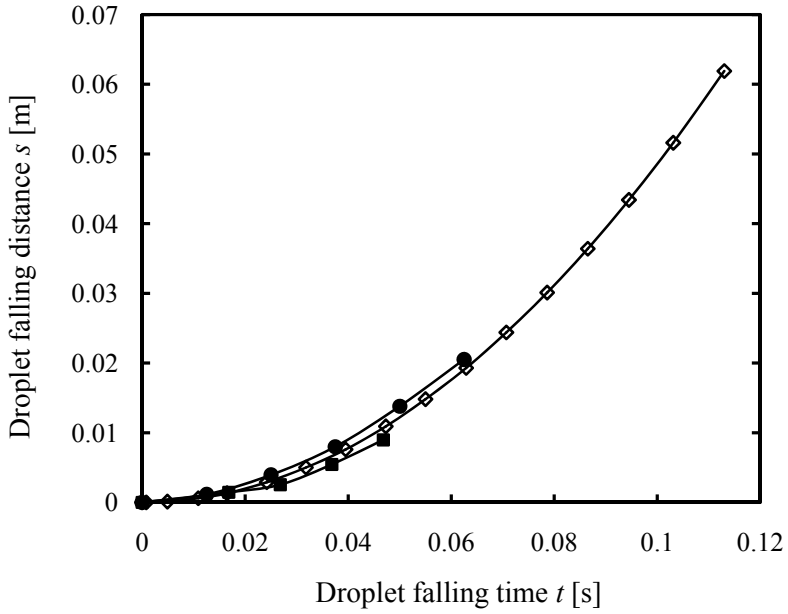

Figure 5-20. The droplet falling distance varies along with time. ■, CFD simulated results by the VOF model; ◇, Matlab calculated results; ●, the experimental data from the high speed camera.

5.5.5.2 Case 2, the inlet velocity is constant and equal to 0.5 m/s

In this case, a higher inlet velocity (0.5 m/s) is used, and the simulated droplet diameter is around 1.05 mm as shown in Figure 5-21 (a). The droplet in Figure 5-21 (a) is smeared out due to not high enough numerical accuracy. The maximum velocity in the center of the fluid leaving the nozzle is around 1 m/s as shown in Figure 5-21 (b), which is much larger than the experimental value (0.194 m/s). In our experimental system, the droplets are generated by pushing the liquid through a needle with the help of pressurized nitrogen. The liquid was contained in a 1000 ml flask. It can be expected from the simulated results that in order to generate the droplets which have the diameter smaller than 1 mm, the required pressure of

nitrogen will be much larger than the pressure that the flask can sustain in our system. As a matter of fact, several needles were tested for our apparatus. The droplet diameters were always 3.2 mm, 2.5 mm and 1.8 mm for the needles which have the inside diameter 0.51 mm, 0.26 mm and 0.2 mm respectively.

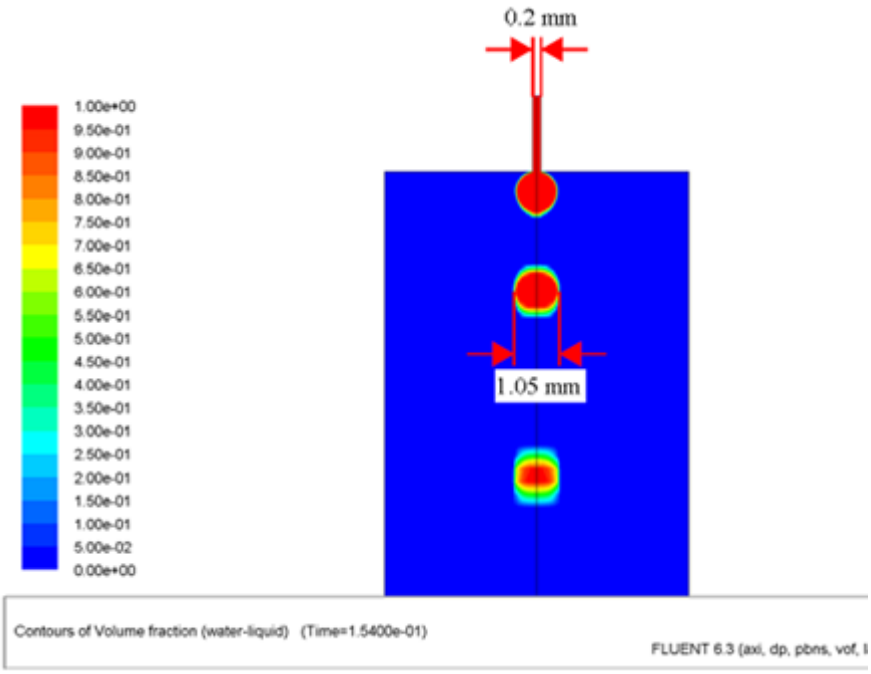

(a) The contours of volume fraction of water phase at t = 0.154 s.

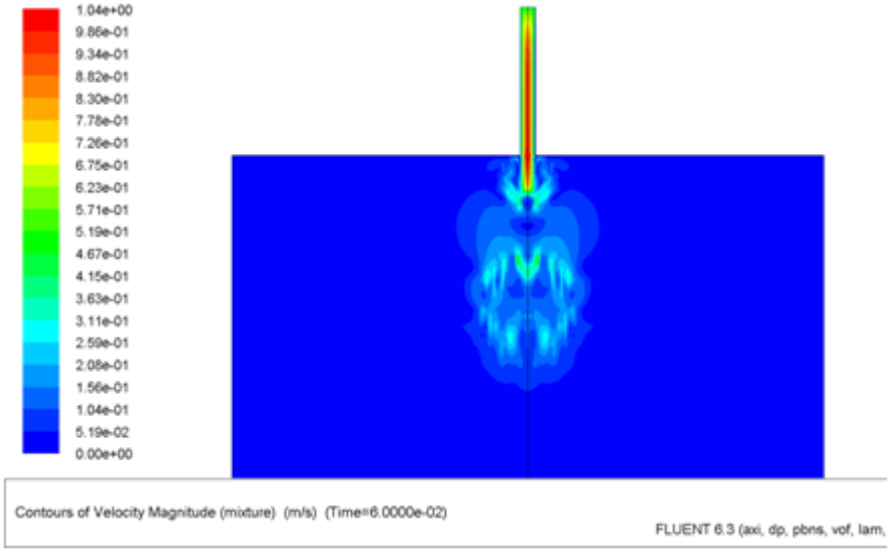

(b) The contours of velocity at t = 0.06 s.

Figure 5-21. Simulation of a falling droplet in a gas chamber (inlet velocity 0.5 m/s).

In conclusion, the droplet diameter and the droplet formation time can be estimated by the CFD simulation. The agreement between the experimental droplet size and the CFD simulated

result is very good, as the deviation is only 0.5 %. The deviation of droplet formation time between the experimental data and the CFD simulated result is OK. However, the exact data still needs to be obtained by the high speed camera for accurately calculating the liquid phase mass transfer coefficient. The curve of droplet falling distance varying with droplet falling time given by the CFD simulation agrees well with the Matlab calculated results and the experimental data from the high speed camera. It can be found by the CFD simulation that the diameter of the droplet which is generated by the present system cannot be as small as 1 mm. The liquid chamber needs to be modified if the droplet diameter is required to be close to the real size in industry (≤ 0.5 mm). The material and the structure of the liquid chamber should be designed to withstand the pressure. Vibration on the droplet generation system may be necessary if small droplets need to be produced.

5.6 Results and discussion

5.6.1 Mass transfer without chemical reaction

The absorption experiments of CO_2 into water droplets were performed to study mass transfer between gas and liquid droplets without chemical reaction.

5.6.1.1 Mass transfer mechanism to droplets formed by sending pressurized liquid through a needle — physical absorption

Mass transfer between gas and liquid phases without chemical reaction can be controlled by diffusion and convection. The mass transfer mechanism without chemical reaction of gas absorption into liquid droplets formed by sending pressurized liquid through a needle will be discussed in this section. If it is assumed that mass transfer between CO_2 and water droplets in this work was controlled by diffusion, the calculation of the total amount of diffusion substance for time t in our experiment can be derived from eq 5-10 and given:

$$M = \varphi t \cdot \frac{4}{3}\pi a^3 C_1 \cdot [1 - \frac{6}{\pi^2}\sum_{n=1}^{\infty}\frac{1}{n^2}\exp(-Dn^2\pi^2\tau/a^2)] \quad (5\text{-}33)$$

Here φ is the droplet formation rate, and φt is the number of droplets if the experiment is run for time t. The residence time for each droplet is τ. C_0 is assumed to be zero in this work since there is little CO_2 in the liquid initially.

Based on the assumption that the absorption is in equilibrium at the gas-liquid interface and the validity of Henry's law ($C_1 = \frac{P}{H}$):

$$M = \varphi t \cdot \frac{4}{3}\pi a^3 \cdot \frac{P}{H} \cdot [1 - \frac{6}{\pi^2}\sum_{n=1}^{\infty}\frac{1}{n^2}\exp(-Dn^2\pi^2\tau/a^2)] \tag{5-34}$$

The total amount of mass transfer can also be calculated by the reduction of moles of the gas phase. It is assumed that the average absorption rate –dn/dt is constant.

$$M = \int_0^t (-\frac{\mathrm{d}n}{\mathrm{d}t})\mathrm{d}t = -\frac{\mathrm{d}n}{\mathrm{d}t}t \tag{5-35}$$

So:

$$M = \varphi t \cdot \frac{4}{3}\pi a^3 \cdot \frac{P}{H} \cdot [1 - \frac{6}{\pi^2}\sum_{n=1}^{\infty}\frac{1}{n^2}\exp(-Dn^2\pi^2\tau/a^2)] = -\frac{\mathrm{d}n}{\mathrm{d}t}t \tag{5-36}$$

Rearranging yields:

$$\sum_{n=1}^{\infty}\frac{1}{n^2}\exp(-Dn^2\pi^2\tau/a^2) = \frac{\pi^2}{6}[1 - \frac{3(\mathrm{d}n/\mathrm{d}t)H}{4\pi a^3 P\varphi}] \tag{5-37}$$

Based on eq 5-37, the diffusion coefficient of CO_2 absorption into water droplets in this work can be calculated. The experimental results of CO_2 absorption into water droplets at 303.5 K were tabulated in Table 5-9. Henry's coefficient of CO_2 in water refers to the data from Versteeg and van Swaaij[29].

Table 5-9. The Experimental Results of CO_2 Absorption into Water Droplets at 303.5 K.

water droplets + CO_2							
***T* [K]**	***P* [Pa]**	***h* [m]**	***a* [m]**	***τ* [s]**	**d*n*/d*t* [mol/s]**	***H* [Pa·m^3/mol]**	***φ* [s^{-1}]**
303.5	100060	0.59	0.00102	0.928	-1.538E-07	3526	1.747

The calculated diffusion coefficient equals to 10.7×10^{-9} m^2/s which is 4.7 times larger than the value (D = 2.29×10^{-9} m^2/s) from Davidson and Cullen[30]. This indicates that the assumption that the mass transfer between CO_2 and water droplets in this work was controlled by diffusion is unreasonable. There exists convection inside the droplets. The convection significantly enhances the mass transfer between gas and liquid phases. Srinivasan and Aiken[17] found the same by comparing the experimental F (fractional approach to equilibrium, $F = M_\tau/M_\infty$) with absorption into stagnant droplet as shown in Figure 5-22. This convection

was produced by the velocity of the liquid leaving the needle. Conceivably, the convection within the droplets could increase when the velocity of the liquid leaving the needle is larger, and therefore the mass transfer rate would increase.

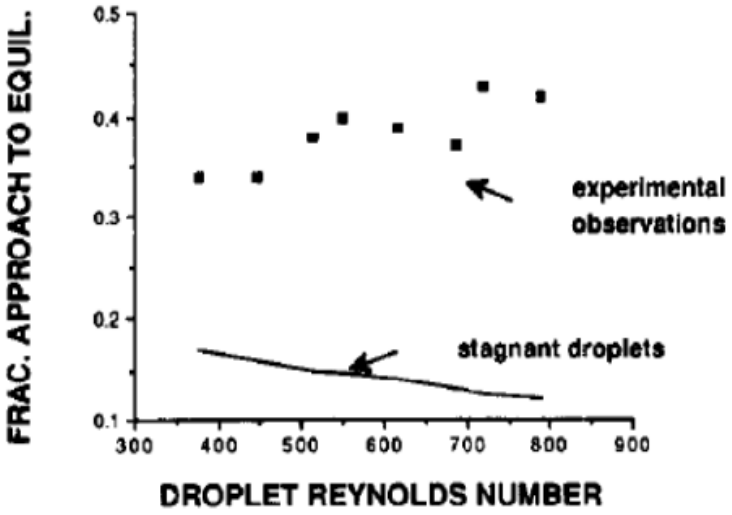

Figure 5-22. Comparison of experimental results from literature with absorption into stagnant droplets.[17]

5.6.1.2 Mass transfer during formation and fall ($h \neq 0$ m)

The average liquid phase mass transfer coefficients of CO_2 absorption into water droplets during formation and fall at different temperatures, droplet formation times and droplet falling heights were found by experiments. A short needle (100 mm) was used. The measured liquid phase mass transfer coefficients and the uncertainties are given in Table 5-10. The variations of liquid phase mass transfer coefficients of CO_2 into water droplets during formation and a fall of 0.59 m as a function of droplet formation time at 303.65 K and 323.15 K were shown in Figure 5-23. The liquid phase mass transfer coefficient of CO_2 absorption into water droplets during formation and fall increases as the temperature rises and decreases as the droplet formation time increases. When the droplet formation time increases, the convection inside the water droplet is reduced, and therefore the mass transfer coefficient decreases. When the temperature increases, even though the solubility of CO_2 in water decreases, the diffusivity of CO_2 in water increases and the convection inside the water droplet increases, and therefore the liquid phase mass transfer coefficient increases. The changes of liquid phase mass transfer coefficients of CO_2 absorption into water droplets during formation and a falling height of 0.41 m and 0.59 m respectively as a function of droplet formation time at 323.15 K were displayed in Figure 5-24. The average liquid phase mass transfer coefficient increases as the droplet falling height increases. This is because the instantaneous mass transfer coefficient

increases as the droplet velocity increases during droplet fall. The increase in this relative velocity between the gas and liquid phase will give more convection inside the droplet.

Table 5-10. The Measured Liquid Phase Mass Transfer Coefficients of CO_2 Absorption into Water Droplets during Droplet Formation and Fall.[a, b, c]

T [K]	P [Pa]	h [m]	-dn/dt [mol/s]	φ [s^{-1}]	t_1 [s]	t_2 [s]	d_2 [m]	H [Pa·m^3/mol]	k_L [cm/s]
303.65	100000	0.59	2.631E-07	2.837	0.352	0.3557	0.00253	3526	0.0253
303.65	100060	0.59	1.538E-07	1.747	0.572	0.3559	0.00240	3526	0.0203
303.65	99810	0.59	0.497E-07	0.759	1.318	0.3560	0.00254	3526	0.0064
303.65	99980	0.59	0.404E-07	0.487	2.053	0.3552	0.00259	3526	0.0055
303.65	100550	0.41	1.704E-07	2.424	0.413	0.2941	0.00254	3526	0.0173
303.65	100610	0.41	0.925E-07	1.556	0.643	0.2955	0.00243	3526	0.0116
323.15	100710	0.59	2.378E-07	2.878	0.347	0.3552	0.00245	5219	0.0405
323.15	102420	0.59	1.626E-07	1.732	0.577	0.3556	0.00246	5219	0.0355
323.15	102380	0.59	0.678E-07	0.718	1.393	0.3561	0.00245	5219	0.0183
323.15	100740	0.59	0.606E-07	0.468	2.137	0.3550	0.00260	5219	0.0177
323.15	99760	0.41	1.866E-07	2.532	0.395	0.2950	0.00252	5219	0.0321
323.15	99810	0.41	1.217E-07	1.660	0.602	0.2983	0.00243	5219	0.0267
323.15	100680	0.41	0.553E-07	0.656	1.524	0.2951	0.00256	5219	0.0127
323.15	100430	0.41	0.464E-07	0.432	2.315	0.2957	0.00257	5219	0.0126

[a]: k_L was calculated from eqs 5-16 and 5-19.
[b]: Henry's coefficients of CO_2 in water refer to the data from Versteeg and Swaaij[29].
[c]: Standard uncertainties u are $u(T)$ = 0.2 K, $u(h)$ = 0.01 m, $u(t_1)$= 0.001 s, and the combined expanded uncertainty is $U_c(k_L)$ = 0.0009 cm/s (level of confidence = 0.95). The relative uncertainty of k_L is 4.34%.

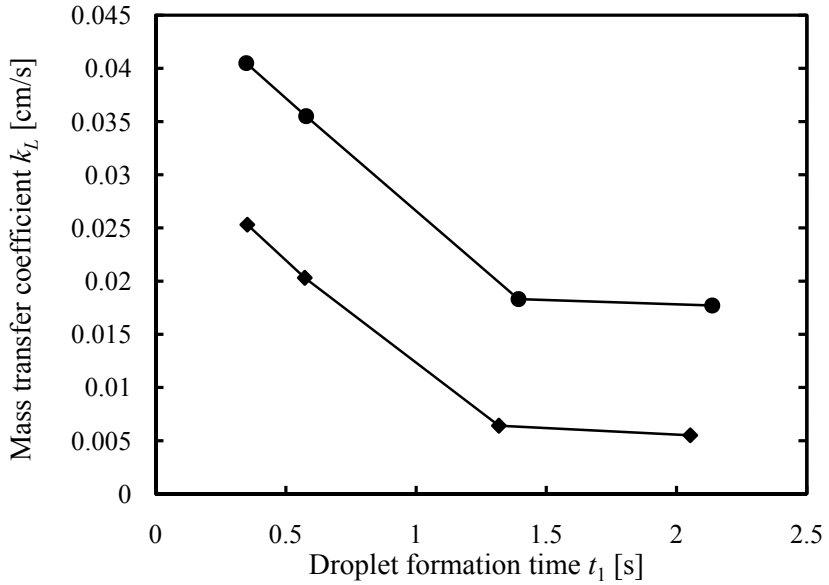

Figure 5-23. The variation of liquid phase mass transfer coefficients k_L of CO_2 into water droplets during formation and a fall of 0.59 m as a function of droplet formation time t_1 at different temperatures. ♦, 303.65 K; ●, 323.15 K.

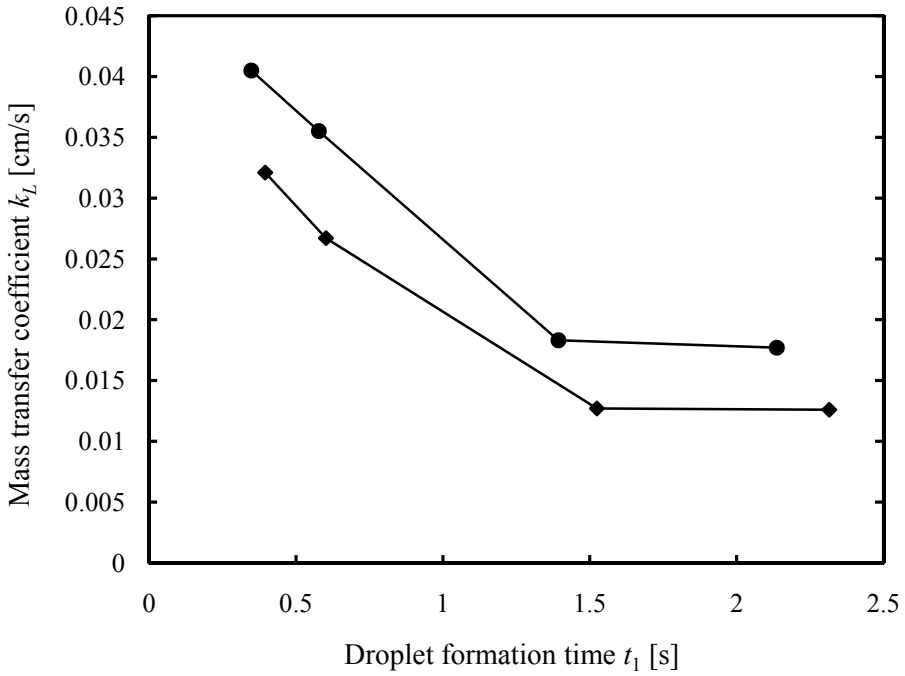

Figure 5-24. The change of liquid phase mass transfer coefficient k_L of CO_2 into water droplets during formation and fall as a function of droplet formation time t_1 at 323.15 K. ♦, droplets fall through a height of 0.41 m; ●, droplets fall through a height of 0.59 m.

5.6.1.3 Mass transfer during only droplet formation ($h \approx 0$ m)

The absorption rates of CO_2 into water droplets during only formation ($h \approx 0$ m) were directly measured by increasing the height of overflow tube and letting the droplets deposit under kerosene as soon as they detached from the needle in this work. A long needle (283 mm) was used. The results are given in Table 5-11.

Table 5-11. The Absorption Rate of CO_2 into Water Droplets during Droplet Formation.

T [K]	Droplet formation time t_1 [s]	Absorption rate $(-dn/dt)_1$ [mol/s]
297.15	0.660	4.80E-08
297.15	1.532	3.02E-08
323.15	0.332	8.31E-08
323.15	0.518	5.64E-08
323.15	1.302	4.18E-08
323.15	2.325	3.93E-08

Throughout the literature, only Dixon and Russell[9] directly measured the absorptive amount of CO_2 into water droplets during droplet formation at 294.15 K by experiments. The

comparison between the results from Dixon and Russell[9] and our data is shown in Figure 5-25. The agreement between the measured results and the literature is good.

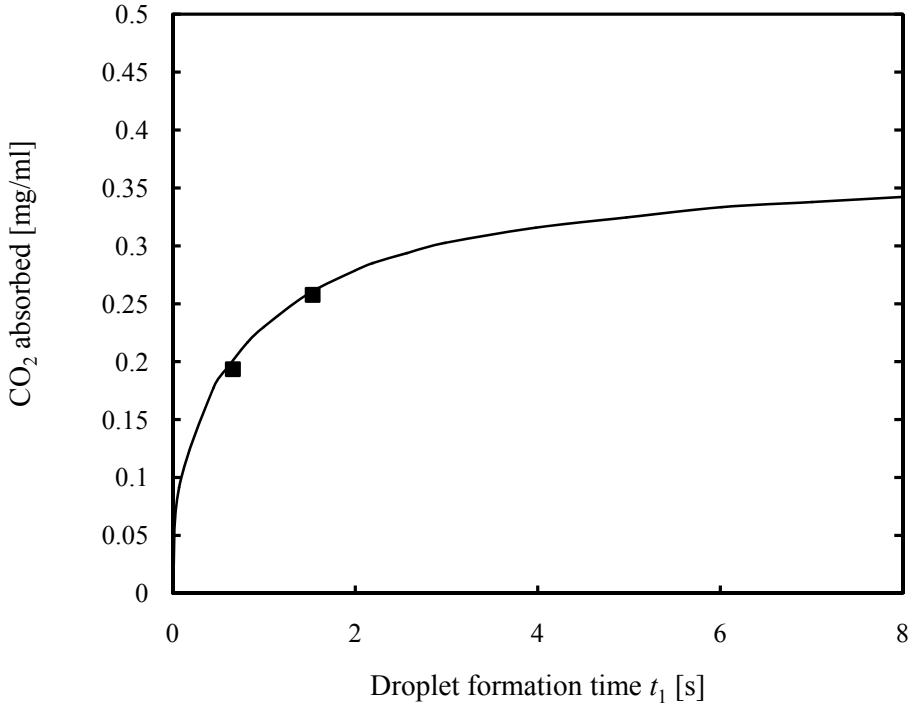

Figure 5-25. The comparison of the absorptive amount of CO_2 into unit volume of water droplets during droplet formation. ■, the experimental data of this work at 297.15 K. Line refer to the data from Dixon and Russell[6] at 294.15 K.

Figure 5-26 shows the variation of the absorption rate of CO_2 into water droplets during only formation with droplet formation time in this work. As can be seen from Figure 5-26, the experimental average absorption rate of CO_2 into water droplets during only formation decreases as the droplet formation time increases, first very quickly when the formation time is smaller than 0.5 s and then only slowly. The absorption rate decreases very slowly as the droplet formation time increases when the formation time is larger than 1.5 s. Rajan and Heideger[10] studied the mass transfer between a slightly soluble organic drop and the surrounding liquid phase, and found a similar tendency as shown in Figure 5-27 even though the mass transfer is controlled by the continuous phase in their experiments. For the droplets with similar volumes, the convection inside the droplet intensifies when the droplet formation time is smaller because the velocity of the liquid leaving the needle is larger. The more convection inside the droplet, the more mass transfer during certain time between CO_2 and water droplets. Therefore the mass transfer rate increases when the droplet formation time decreases. The convection inside the droplet has a very significant influence on the mass

transfer if the droplet formation time is very small. Therefore for the droplets which have very small formation time, the mass transfer rate declines sharply as the droplet formation time increases. On the other hand, convection becomes less important compared to diffusion in the total mass transfer for the droplets which have large formation time. Hence the mass transfer rate decreases slowly as the droplet formation time increases for the droplets which have large formation time. When the droplet formation time is large enough, the droplet is basically stagnant, mass transfer between CO_2 and water droplets will be controlled by diffusion only and the droplet formation time will not affect the mass transfer rate anymore. Most of the literature presented the results and discussed the descriptive models over the range of large droplet formation time. It was mainly focused on the droplets with the formation time less than 2.5 s in this work.

When studying mass transfer during only formation, the droplets will deposit under kerosene as soon as they detached from the needle and their falling height is about 0 m, which results in the splashing of kerosene on the glass at the position where the droplet detaches. As a result, the high speed camera cannot capture clear image of the droplet and then the droplet diameter cannot be measured accurately when doing experiments during only formation. Hence, liquid phase mass transfer coefficients during only droplet formation are not given.

The absorption rate of CO_2 into water droplets during droplet formation at 323.15 K was correlated with droplet formation time by:

$$-\frac{\mathrm{d}n}{\mathrm{d}t}/\mathrm{mol}\cdot\mathrm{s}^{-1} = a - b\ln\left(t_1/\mathrm{s} - c\right) \tag{5-38}$$

The correlated parameters were tabulated in Table 5-12. The correlated results were compared to the experimental data in Figure 5-26. The average relative deviation between the experimental absorption rate and the fitted data is 2.04%.

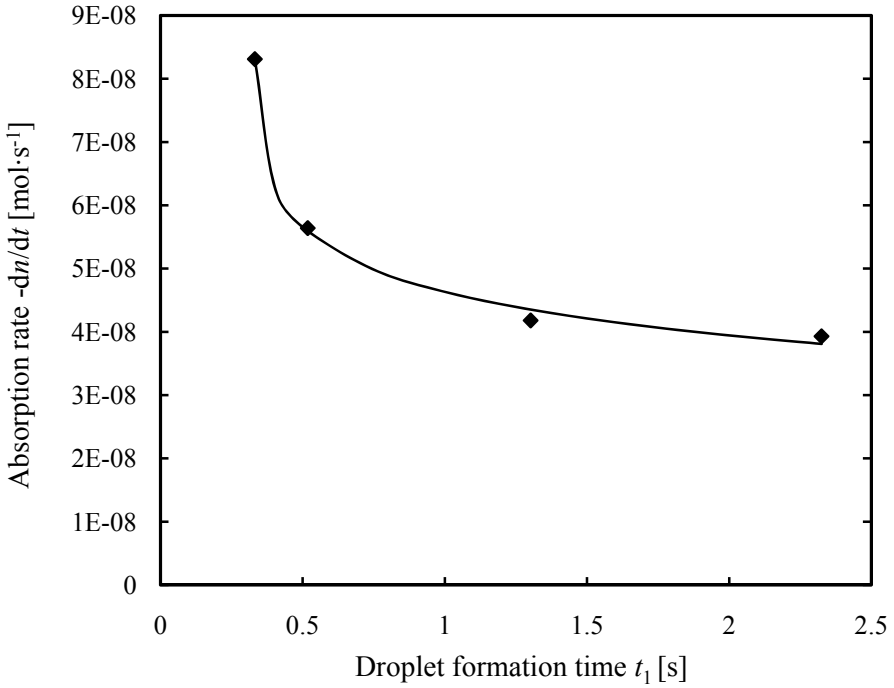

Figure 5-26. The absorption rate of CO_2 into water droplets during only formation varies with droplet formation time at 323.15 K. Symbols refer to our experimental data. The curve is calculated by eq 5-38.

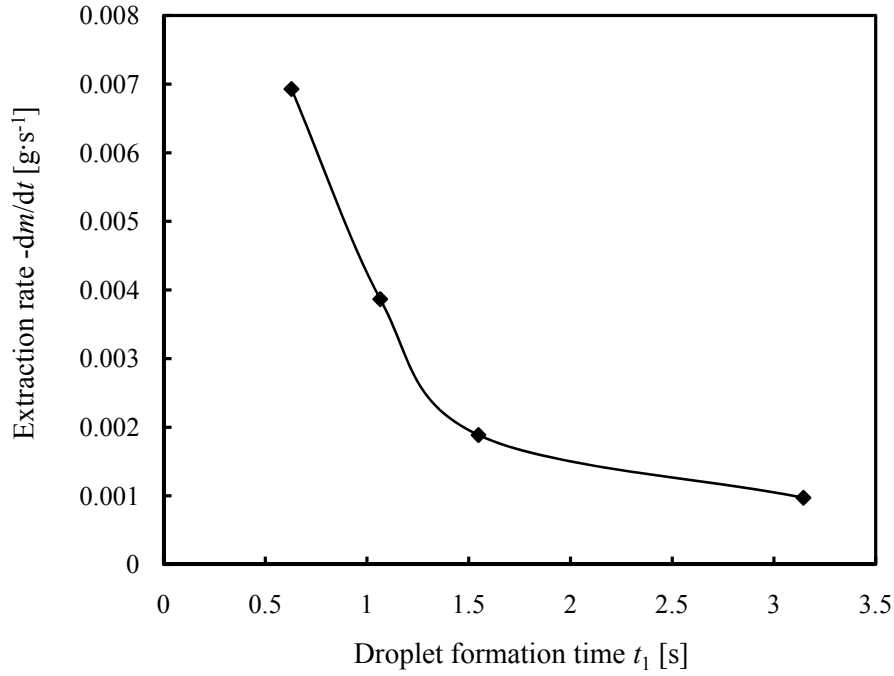

Figure 5-27. The literature data of experimental mass transfer rate between a slightly soluble organic drop and the surrouding water varies with droplet formation time (20 gauge needle). These data are from Rajan and Heideger[10].

Table 5-12. Correlated Parameters for the Absorption Rate of CO_2 into Water Droplets during Droplet Formation at 323.15 K.

a [mol/s]	b [mol/s^2]	c [s]
4.33×10^{-8}	7.56×10^{-9}	0.3268

5.6.1.4 Mass transfer during only droplet fall

The absorption rate of CO_2 into water droplets during only droplet fall was calculated by subtracting the absorption during formation from the total mass transfer during drop life-time. Thus the liquid phase mass transfer coefficient during only droplet fall can be derived.

The moles of CO_2 that was absorbed by every single droplet during its forming process can be calculated by:

$$\Delta n_1 = \frac{(-\mathrm{d}n/\mathrm{d}t)_1}{\varphi} \tag{5-39}$$

The moles of CO_2 that was absorbed by every single droplet during the period that it forms and then falls a certain distance can be calculated by:

$$\Delta n = \frac{-\mathrm{d}n/\mathrm{d}t}{\varphi} \tag{5-40}$$

Therefore the moles of CO_2 that was absorbed by each droplet during only droplet fall can be calculated by:

$$\Delta n_2 = \Delta n - \Delta n_1 \tag{5-41}$$

That is:

$$\Delta n_2 = \frac{(-\mathrm{d}n/\mathrm{d}t)_2}{\varphi} = \frac{-\mathrm{d}n/\mathrm{d}t}{\varphi} - \frac{(-\mathrm{d}n/\mathrm{d}t)_1}{\varphi} \tag{5-42}$$

Hence the absorption rate of CO_2 into water droplets during droplet free fall can be calculated by:

$$(-\mathrm{d}n/\mathrm{d}t)_2 = (-\mathrm{d}n/\mathrm{d}t) - (-\mathrm{d}n/\mathrm{d}t)_1 \tag{5-43}$$

Here Δn is the moles of CO_2 absorption into each water droplet. The subscript 1 means only formation stage, 2 means only falling stage and no subscript refers to the whole process (formation and fall). The derived liquid phase mass transfer coefficients of CO_2 absorption into water droplets during droplet free fall at different droplet formation times and droplet falling heights at 323.15 K are given in Table 5-13.

Table 5-13. The Derived Liquid Phase Mass Transfer Coefficient of CO_2 Absorption into Water Droplets during Droplet Free Fall at 323.15 K.[a, b]

T [K]	P [Pa]	h [m]	$-dn/dt$ [mol/s]	$(-dn/dt)_1$ [mol/s]	$(-dn/dt)_2$ [mol/s]	φ [s^{-1}]	t_1 [s]	t_2 [s]	d_2 [m]	$(k_L)_2$ [cm/s]
323.15	99760	0.41	1.866E-07	0.636E-07	1.230E-07	2.532	0.395	0.2950	0.00252	0.0513
323.15	99810	0.41	1.217E-07	0.531E-07	0.686E-07	1.660	0.602	0.2983	0.00243	0.0460
323.15	100680	0.41	0.553E-07	0.420E-07	0.133E-07	0.656	1.524	0.2951	0.00256	0.0184
323.15	100430	0.41	0.464E-07	0.381E-07	0.083E-07	0.432	2.315	0.2957	0.00257	0.0173
323.15	102420	0.59	1.626E-07	0.538E-07	1.088E-07	1.732	0.577	0.3556	0.00246	0.0612
323.15	102380	0.59	0.678E-08	0.429E-08	0.249E-07	0.718	1.393	0.3561	0.00245	0.0298

[a]: The subscript 1 means only forming period, and 2 means only falling period. No subscript refers to the whole formation and falling period together.
[b]: The absorption rates during droplet formation and fall ($-dn/dt$) were found by experiments. The absorption rates during droplet formation here ($(-dn/dt)_1$) were correlated by eq 5-38.

A comparison of the absorption rate of CO_2 into water droplets during the droplet free fall to the absorption rate during the droplet formation is illustrated in Figure 5-28. The vertical intercepts between two curves were the absorption rate of CO_2 into water droplets during droplet free fall. As can be seen from Figure 5-28, the quantity of CO_2 absorbed by each water droplet during a fall of 0.41 m was larger than that absorbed during formation when the droplet formation time is smaller than 0.75 s, and gradually smaller than that absorbed during formation when the droplet formation time is larger than 0.75 s. The critical point (0.75 s) maybe varies for different experimental conditions. But what is certain, is that the absorption rate of CO_2 into water droplet during droplet fall is larger than that during droplet formation for the quickly formed droplets and is much smaller than that during formation for the slowly formed droplets. This is because the contact time between water droplets and CO_2 during formation is much larger than during fall when the droplet formation time is large. In addition, the absorption rate of CO_2 into water droplets during fall decreases as the droplet formation time increases, at first sharply and then slowly. Dixon and Russell[9] found the same trends that the quantity of CO_2 absorbed during a fall of fixed length decreases as the formation time increases, and is less than that absorbed during formation over the range of formation time measured as shown in Figure 5-29.

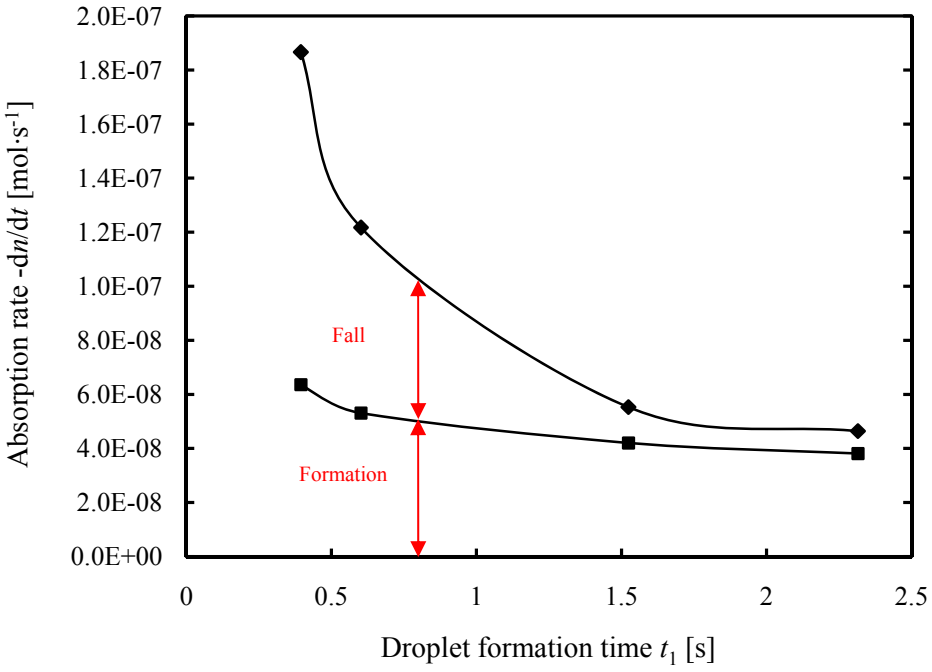

Figure 5-28. The absorption rate of CO_2 into water droplets varies with droplet formation time at 323.15 K. ■, during formation; ♦, during formation and falling through 0.41 m height.

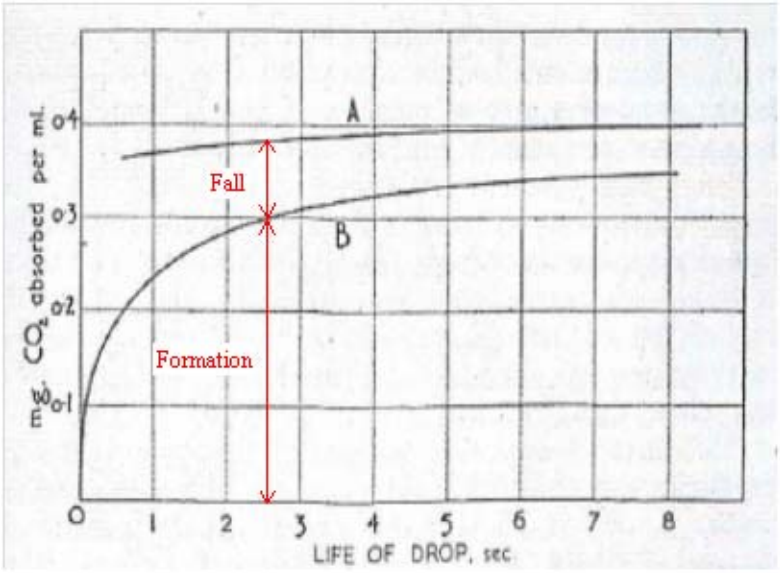

Figure 5-29. Absorption of carbon dioxide during formation (curve B) and during formation and fall (curve A) — Tip No. 6 from Dixon and Russell[6].

Since the liquid phase mass transfer coefficient of CO_2 absorption by water droplets during droplet falling varies with droplet formation time, a useful dimensionless parameter characterizing the magnitude of droplet formation time is defined as:

$$\zeta = \frac{t_1}{\tau} \tag{5-44}$$

A fitted formula between the Sherwood number, the Reynolds number and ζ of CO_2 absorption by water droplets during droplet falling was obtained by the Nonlinear Curve Fitting Tool of OriginPro:

$$Sh = 2.3\times10^{10}\cdot(\zeta + 4.546)^{-20.137}\, Re^{1.733} \tag{5-45}$$

The correlated results were compared to the experimental data in Figure 5-30. The average relative deviation between the experimental liquid phase mass transfer coefficient of CO_2 absorption by water droplets and the correlated data is 4.23%. This deviation is within the experimental uncertainty which is 4.34% (see Table 5-10). However, the parameter 1.733 is uncertain because the range of the Reynolds number is small (*Re* = 6141 to 6971).

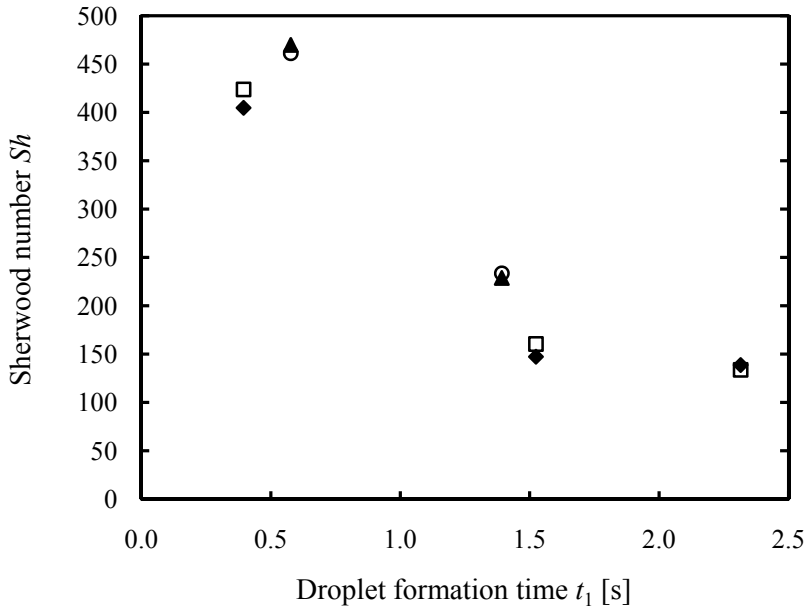

Figure 5-30. The Sherwood number of CO_2 absorption into water droplets during droplet free fall. ♦, experimental data, *Re* = 6141; □, correlated data from eq 5-45, *Re* = 6141; ▲, experimental data, *Re* = 6971; ○, correlated data from eq 5-45, *Re* = 6971.

5.6.2 Mass transfer with chemical reaction

Absorption experiments of CO_2 into droplets of 30% MEA solution were performed to study mass transfer between gas and liquid droplets with chemical reaction.

5.6.2.1 Mass transfer during only droplet formation ($h \approx 0$ m)

The measuring method of CO_2 absorption by droplets of 30% MEA solution during only droplet formation ($h \approx 0$ m) is the same as for CO_2 absorption by water droplets which has been described earlier. The measured absorption rates are given in Table 5-14.

Table 5-14. The Absorption Rate of CO_2 into Droplets of 30% MEA Solution during Droplet Formation at 323.15 K.

T [K]	P [Pa]	Droplet formation time t_1 [s]	Absorption rate $(-dn/dt)_1$ [mol/s]
323.15	101380	0.708	8.535E-07
323.15	101190	0.940	8.555E-07
323.15	101710	1.435	8.566E-07

As can be seen from Table 5-14, the absorption rate of CO_2 into droplets of 30% MEA solution does almost not vary as the droplet formation time changes. This is probably because the convection inside the droplets of 30% MEA solution is small due to the higher viscosity of aqueous MEA solutions, and the intensity of convection does not change very much over the range that these measurements covered. The average absorption rate of CO_2 by droplets of 30% MEA solution during formation is calculated as 8.552×10^{-7} mol/s. The relative standard deviation is 0.18%.

5.6.2.2 Mass transfer during formation and fall ($h \neq 0$ m)

According to previous analysis of CO_2 absorption by water droplets, the internal flow state of droplets is affected by the droplet formation time, and further affects the mass transfer. However, the internal state of droplets of 30% MEA solution does not change very much over the range that these measurements covered. Hence, only two variables, droplet falling height and temperature, were considered when studying CO_2 absorption by droplets of 30% MEA during droplet formation and fall.

The measuring method of CO_2 absorption by droplets of 30% MEA solution during droplet formation and fall is the same as CO_2 absorption by water droplets which has been introduced earlier. The liquid phase mass transfer coefficient is calculated by eq 5-22 which includes the effect of chemical reaction. The measured liquid phase mass transfer coefficients of CO_2 absorption by droplets of 30% MEA solution during droplet formation and fall at different droplet falling heights and different temperatures and the measurement uncertainties are given in Table 5-15. The results are much greater than k_L of CO_2 into water droplets as expected. The variations of liquid phase mass transfer coefficient of CO_2 into droplets of 30% MEA solution during formation and fall as a function of temperature and droplet falling height are shown in Figure 5-31. The liquid phase mass transfer coefficient of CO_2 into droplets of 30% MEA solution increases as the temperature rises, because the chemical

reaction rate between CO_2 and aqueous MEA solutions increases as the temperature rises. Besides, the liquid phase mass transfer coefficient of CO_2 into droplets of 30% MEA solution increases as the droplet falling height rises. This shows that the instantaneous liquid phase mass transfer coefficient of CO_2 absorption by droplets of 30% MEA solution increases as the relative velocity becomes larger due to more convection inside the droplet.

Table 5-15. The Measured Liquid Phase Mass Transfer Coefficients of CO_2 Absorption into Droplets of 30% MEA Solution during Droplet Formation and Fall.[a, b, c]

T [K]	P [Pa]	h [m]	-dn/dt [mol/s]	φ [s^{-1}]	t_1 [s]	t_2 [s]	d_2 [m]	H [Pa·m^3/mol]	k_L [cm/s]
303.15	101750	0.14	0.610E-06	0.684	1.462	0.1705	0.00262	3675	0.1523
303.15	100860	0.25	1.153E-06	0.840	1.190	0.2293	0.00269	3675	0.2482
303.15	100590	0.53	2.194E-06	0.768	1.302	0.3364	0.00255	3675	0.4847
323.15	100520	0.07	1.010E-06	1.156	0.865	0.1219	0.00273	5242	0.3242
323.15	101380	0.17	1.515E-06	1.266	0.790	0.1899	0.00286	5242	0.3843
323.15	101380	0.33	1.940E-06	1.216	0.822	0.2641	0.00260	5242	0.5425
323.15	100940	0.52	2.892E-06	1.878	0.532	0.3336	0.00232	5242	0.7609

[a]: k_L (i.e. $k_L{}^0E$) was calculated from eq 5-22.
[b]: Henry's coefficients of CO_2 in 30% MEA solutions refer to the data from Jiru et al.[31].
[c]: Standard uncertainties u are $u(T)$ = 0.2 K, $u(h)$ = 0.01 m, $u(t_1)$= 0.001 s, and the combined expanded uncertainty is $U_c(k_L)$ = 0.0191 cm/s (level of confidence = 0.95). The relative uncertainty of k_L is 4.61%.

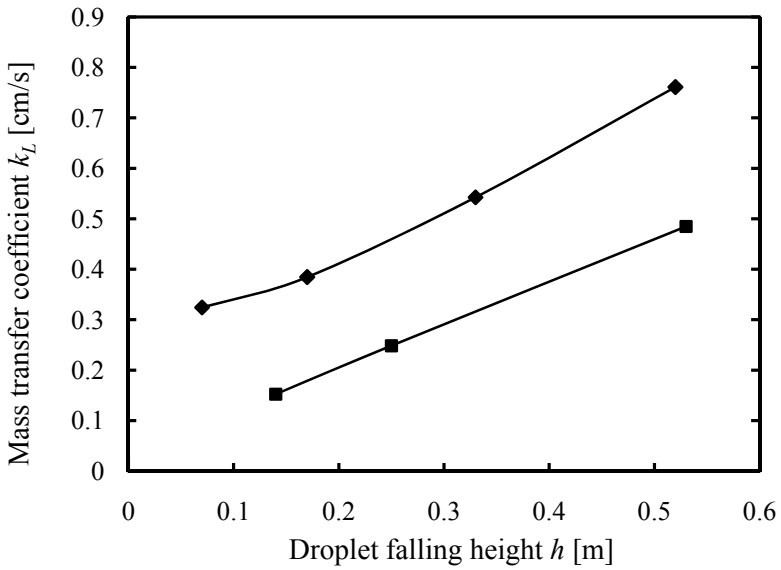

Figure 5-31. The variation of liquid phase mass transfer coefficients k_L of CO_2 absorption into droplets of 30% MEA solution during formation and fall as a function of droplet falling height h at different temperatures. ■, 303.65 K; ♦, 323.15 K.

5.6.2.3 Mass transfer during only droplet fall

The calculation of the absorption rate during only droplet fall has been described earlier and given by eq 5-43. The liquid phase mass transfer coefficients of CO_2 absorption by

droplets of 30% MEA solution at different droplet falling heights at 323.15 K were then derived and given in Table 5-16. As can be seen from Figure 5-32, the liquid phase mass transfer coefficient of CO_2 absorption by droplets of 30% MEA solution during droplet fall increases smoothly as the droplet falling height increases. As a droplet is accelerated all the way during its fall, this shows that the liquid phase mass transfer coefficient of CO_2 absorption by droplets of 30% MEA solution during the droplet fall increases as the droplet velocity increases. The possible reason is that the gas surrounding the liquid droplet is not stationary and higher relative velocity between gas and liquid gives more convection inside the droplet. The gas flow surrounding the liquid droplet intensifies as the droplet fall velocity increases, and thus results in an increase in the mass transfer rate between CO_2 and aqueous MEA solutions.

Table 5-16. The Derived Liquid Phase Mass Transfer Coefficient of CO_2 Absorption into Droplets of 30% MEA Solution during Droplet Free Fall at 323.15 K.[a]

T	P	h	$-dn/dt$	$(-dn/dt)_1$	$(-dn/dt)_2$	φ	t_1	t_2	d_2	$(k_L)_2$
[K]	[Pa]	[m]	[mol/s]	[mol/s]	[mol/s]	[s^{-1}]	[s]	[s]	[m]	[cm/s]
323.15	100520	0.07	1.010E-06	8.552E-07	0.155E-06	1.156	0.865	0.1219	0.00273	0.2453
323.15	101380	0.17	1.515E-06	8.552E-07	0.660E-06	1.266	0.790	0.1899	0.00286	0.5506
323.15	101380	0.33	1.940E-06	8.552E-07	1.085E-06	1.216	0.822	0.2641	0.00260	0.8203
323.15	100940	0.52	2.892E-06	8.552E-07	2.037E-06	1.878	0.532	0.3336	0.00232	0.9965

[a]: The subscript 1 means only forming period, and 2 means only falling period. No subscript refers to the whole formation and falling period together.

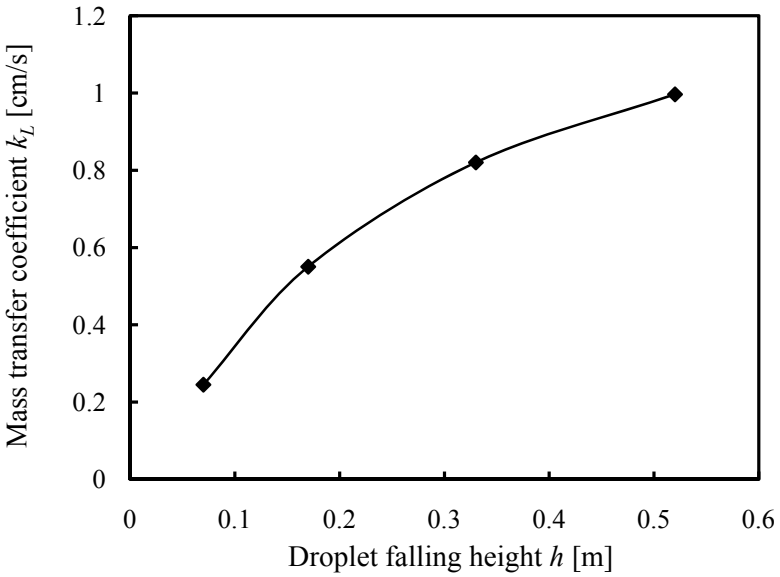

Figure 5-32. The variation of liquid phase mass transfer coefficients k_L of CO_2 absorption into droplets of 30% MEA solution during only droplet fall as a function of droplet falling height h at 323.15 K.

The Sherwood number and the Reynolds number were calculated for the experiments and given in Table 5-17. The following correlation for CO_2 absorption by droplets of 30% MEA solution during droplet fall at 323.15 K was obtained by the Nonlinear Curve Fitting Tool of OriginPro:

$$Sh = 2.378 Re^{1.654} \tag{5-46}$$

The correlated results are compared to the experimental data in Figure 5-33. The average relative deviation between the experimental liquid phase mass transfer coefficient of CO_2 absorption by droplets of 30% MEA solution and the correlated data is 2.94%. This deviation is within the experimental uncertainty which is 4.61% (see Table 5-15).

Table 5-17. The Derived Sherwood Number and Reynolds Number of CO_2 Absorption into Droplets of 30% MEA Solution during Droplet Falling.

***T* [K]**	***Sh***	***Re***
323.15	281101	1181
323.15	662777	1905
323.15	897522	2340
323.15	972629	2533

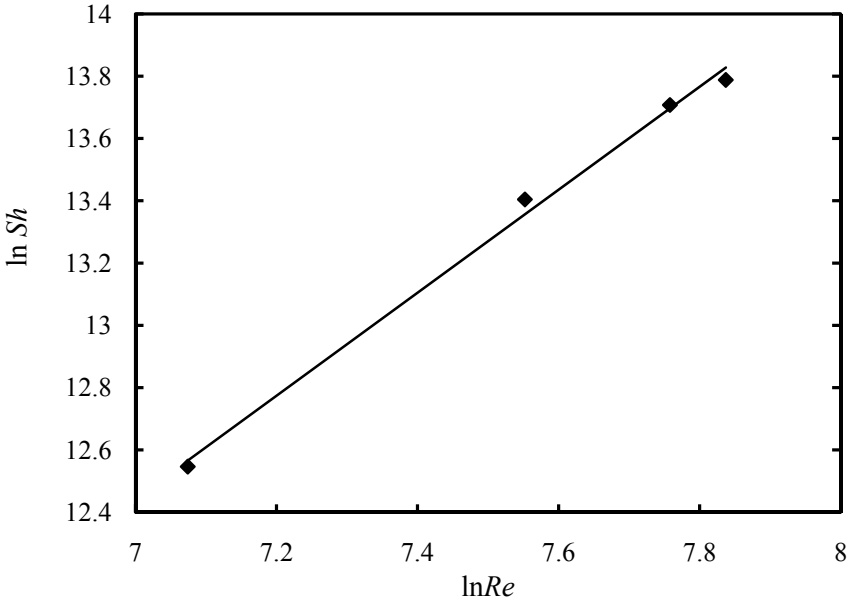

Figure 5-33. Correlation for the average Sherwood number of CO_2 absorption by droplets of 30% MEA solution during droplet falling at 323.15 K. Symbol refers to the experimental results. Line refers to the calculated data from eq 5-46.

5.6.2.4 The enhancement factor estimate

According to the conclusion from Levenspiel[32], the enhancement factor E for fluid-fluid reaction is dependent on two quantities which are the instantaneous enhancement factor E_i and the Hatta modulus M_H. Therefore, the enhancement factors for CO_2 absorption by droplets of 30% MEA solution in this work are estimated by the curve of relationship between E, Ei and M_H as shown in Figure 5-34. The calculations of Ei and M_H are given as follows:

$$E_i = 1 + \frac{D_{\mathrm{MEA}} C_{\mathrm{MEA}} H_{\mathrm{CO_2}}}{2 D_{\mathrm{CO_2}} P_{\mathrm{CO_2}}{}^{i}} \tag{5-47}$$

$$M_H = \frac{\sqrt{D_{\mathrm{CO_2}} k_2 C_{\mathrm{MEA}}}}{k_L{}^{0}} \tag{5-48}$$

Here C_{MEA} is the concentration of MEA, D_{MEA} is the diffusion coefficient of MEA in aqueous MEA solution, D_{CO2} is the diffusion coefficient of CO_2 in aqueous MEA solution, H_{CO2} is the Henry's coefficient of CO_2 in aqueous MEA solution, $P_{\mathrm{CO2}}{}^{i}$ is the pressure of CO_2 at the interface, k_2 is the reaction rate constant, and $k_L{}^{0}$ is the liquid phase mass transfer coefficient of physical absorption.

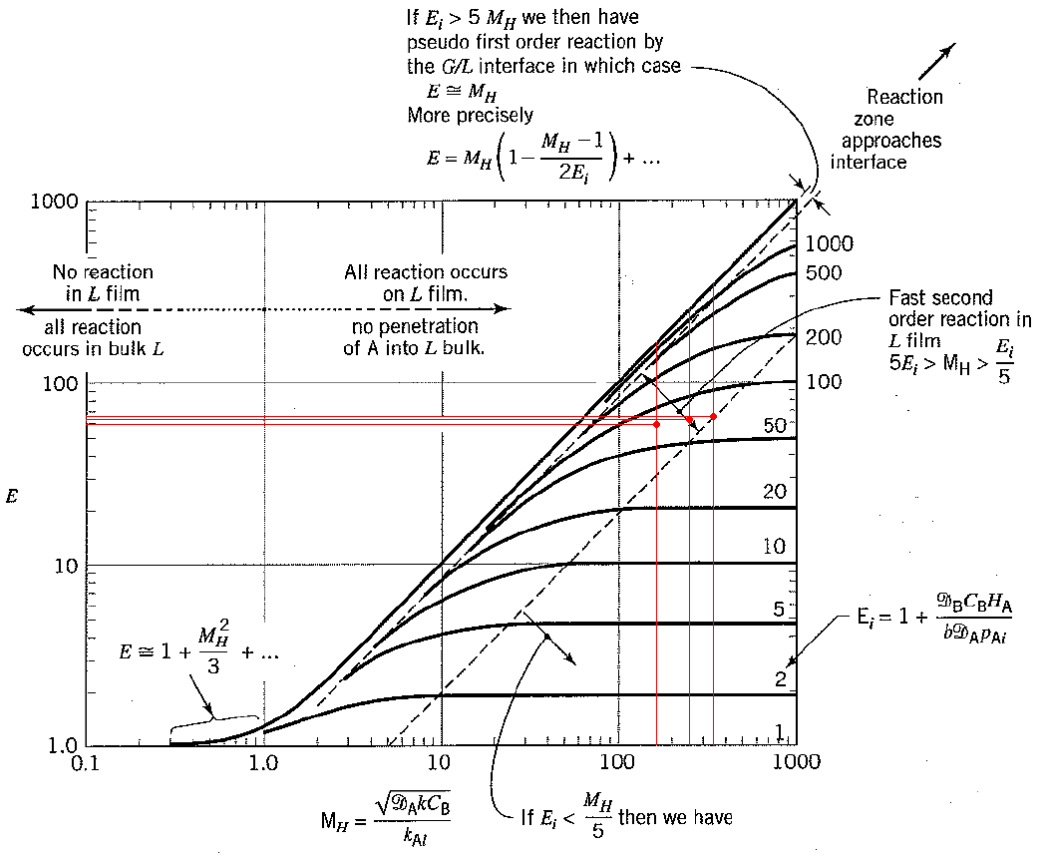

Figure 5-34. The enhancement factor for fluid-fluid reactions as a function of M_H and E_i.[32]

The measured k_L^0 for CO_2 absorption by water droplets is adjusted via knowledge of diffusion coefficients by the N_2O analogy. This modified k_L^0 is used to estimate M_H. The calculated E_i and M_H for CO_2 absorption by droplets of 30% MEA solution during formation and fall at 323.15 K are given in Table 5-18. Thus, the enhancement factor can be obtained from Figure 5-34, which ranges from 60 to 66. The results are in the fast second order reaction region. The measured k_L/k_L^0 from experiments and the estimated E from Figure 5-34 are also compared as shown in Table 5-18. The agreement between them is good, and this verifies the accuracy of our measurements.

Table 5-18. The Estimated Enhancement Factor for CO_2 Absorption by Droplets of 30% MEA Solution at 323.15 K.[a]

h [m]	P [Pa]	D_{MEA} [m^2/s]	D_{CO2} [m^2/s]	H_{CO2} [$Pa \cdot m^3/mol$]	k_2 [$l/(mol \cdot s)$]	k_L^0 [cm/s]	E_i	M_H	E	k_L [cm/s]	$\frac{k_L}{k_L^0}$
0.17	101380	1.32E-09	2.38E-09	5242	33095	0.0058	71	338	**66**	0.3843	**66**
0.33	101380	1.32E-09	2.38E-09	5242	33095	0.0077	71	256	**64**	0.5245	**68**
0.52	100940	1.32E-09	2.38E-09	5242	33095	0.0117	72	168	**60**	0.7609	**65**

[a]: D_{MEA} refer to the data from Snijder et al.[33]. D_{CO2} and k_2 refer to the data from Jiru and Eimer[34, 35].

Through the estimated enhancement factors, the liquid phase mass transfer coefficients of CO_2 into droplets of 30% MEA solution without chemical reaction are further calculated. The results are compared with the measured liquid phase mass transfer coefficients between CO_2 and water droplets under the same conditions and given in Table 5-19. k_L^0 for CO_2-water droplets system is always larger than k_L^0 for CO_2-30% MEA solution droplets system. As discussed earlier, convection does not affect the mass transfer between CO_2 and droplets of 30% MEA solution very much over the range of our measurements. Diffusion is the main driving force of mass transfer in this case. Therefore, the results in Table 5-19 are reasonable because the diffusion coefficient of CO_2 in water is larger than that in 30% MEA solutions.

Table 5-19. The Comparison of k_L^0 for CO_2 absorption into water droplets to k_L^0 for CO_2 absorption into droplets of 30% MEA solution.

T [K]	h [m]	k_L^0 for CO_2-water droplets [cm/s]	k_L^0 for CO_2-30% MEA solution droplets [cm/s]
323.15	0.17	0.0078	0.0058
323.15	0.33	0.0103	0.0082
323.15	0.52	0.0157	0.0127

5.7 Conclusion

A new experimental set-up was established to study CO_2 absorption by liquid droplet with and without chemical reaction. The liquid phase mass transfer coefficient of CO_2 absorption into water droplets during formation and fall increases as the temperature and droplet falling height rise, and decreases as the droplet formation time increases. It was found that there exists convection inside the droplets which were formed by sending pressurized liquid through a needle. The convection significantly enhances the mass transfer between CO_2 and water droplets. The measured absorption rates of CO_2 absorption into water droplets during only formation at 297.15 K agree well with Dixon and Russell's data. The correlation of the absorption rate of CO_2 into water droplets during only formation with droplet formation time at 323.15 K was obtained. The average relative deviation between the experimental absorption rate and the fitted data is 2.04%. The liquid phase mass transfer coefficients of CO_2 into water droplets during only droplet fall at 323.15 K, droplet falling heights h = 0.41 m and 0.59 m, and different droplet formation times were derived. The absorption rate of CO_2 into water droplet during fall is larger than that during formation for the quickly formed droplets, and is much smaller than that during formation for the slowly formed droplets. The correlation between the Sherwood number and the Reynolds number of CO_2 into water droplets during droplet fall at 323.15 K was obtained. The average relative deviation between the experimental liquid phase mass transfer coefficient of CO_2 into water droplets durnig fall and the correlated data is 4.32%. The combined expanded uncertainty of k_L for CO_2 absorption by water droplets is 0.0009 cm/s, and the relative uncertainty is 4.34%.

The absorption rates of CO_2 into droplets of 30% MEA solution during only droplet formation were measured at 323.15 K and different droplet formation times. The absorption rate of CO_2 into droplets of 30% MEA solution almost does not vary as the droplet formation time changes. The liquid phase mass transfer coefficient of CO_2 into droplets of 30% MEA solution during formation and fall increases as the temperature and droplet falling height rise. The liquid phase mass transfer coefficients of CO_2 into droplets of 30% MEA solution during only droplet fall at 323.15 K, and droplet falling heights h = (0.07 to 0.53) m were derived. The correlation between the Sherwood number and the Reynolds number of CO_2 into droplets of 30% MEA solution during droplet fall at 323.15 K was obtained. The average relative deviation between the experimental liquid phase mass transfer coefficient of CO_2 into droplets of 30% MEA solution during fall and the correlated data is 2.94%. The combined expanded

uncertainty of k_L for CO_2 absorption by droplets of 30% MEA solution is 0.0191 cm/s, and the relative uncertainty is 4.61%. The agreement between the estimated enhancement factor and the measured k_L/k_L^0 of CO_2 into droplets of 30% MEA solution is good.

Notation

a	radius of the droplet, m
A	droplet surface area, m^2
C	concentration of solute in the liquid droplet, mol/m^3
C_0	initially uniform concentration of the droplet, mol/m^3
C_1	constant concentration at the surface of the droplet, mol/m^3
d	droplet diameter, m or mm
D	diffusion coefficient, m^2/s
E	chemical reaction enhancement factor
F	fractional approach to equilibrium
h	droplet falling height, m
H	henry's coefficient, $Pa \cdot m^3/mol$
k_2	reaction rate constant, $l/(mol \cdot s)$
k_G	gas phase mass transfer coefficient, $mol/(m^2 \cdot s \cdot Pa)$
k_L	liquid phase mass transfer coefficient, m/s or cm/s
K	overall mass transfer coefficient, cm/h
M	mass transfer amount of gas absorption into a liquid droplet, mol
n	moles of gas in the gas chamber, mol
Δn	moles of gas absorption into every single droplet, mol
$-dn/dt$	absorption rate of gas in the liquid droplet, mol/s
N_A	mass transfer rate of solute A, mol/s
Oh	Ohnesorge number, $We^{1/2}/Re$
P	pressure of CO_2, Pa
Q	mass transfer rate of gas absorption into a liquid droplet, mol/s
r	distance on the radius coordinate of the droplet, m
Re	Reynolds number, $\rho ud/\mu$
s	droplet falling distance, m
Sc	Schmidt number, $\mu/(\rho D)$
Sh	Sherwood number, $k_L d/D$
t	absorption time or droplet growing time, s
u	droplet velocity, m/s
V	droplet volume, m^3
We	Weber number, $u^2\rho d/\sigma$

Greek letters

ε	drag coefficient
ζ	dimensionless parameter, t_1/τ
μ	viscosity, $kg/(m \cdot s)$
ρ	density, kg/m^3
σ	surface tension, N/m
τ	droplet lifetime during formation and fall, s

φ	droplet formation rate, s^{-1}
Δ	"degree of turbulence", cm^{-1}

Subscripts

0	initial value
1	condition for the droplet formation
2	condition for the droplet fall
d	droplet
e	equilibrium
f	condition at the end of formation period
g	gas
G	gas phase
i	interface
L	liquid phase
s	saturation value
∞	infinite time

Superscripts

0	physical absorption

References

(1) Turpin, A.; Couvert, A.; Laplanche, A.; Paillier, A. Experimental Study of Mass Transfer and H_2S Removal Efficiency in a Spray Tower. *Chem. Eng. Process* **2008**, *47*, 886-892.

(2) Bandyopadhyay, A.; Biswas, M. N. Critical Flow Atomizer in SO_2 spray scrubbing. *Chem. Eng. J.* **2008**, *139*, 29-41.

(3) Kuntz, J.; Aroonwilas, A. Performance of Spray Column for CO_2 Capture Application. *Ind. Eng. Chem. Res.* **2008**, *57*, 145-153.

(4) Whitman, W. G.; Long, L.; Wang, H. Y. Absorption of Gases by a Liquid Drop. *Ind. Eng. Chem.* **1926**, *18*, 363-367.

(5) Licht, W.; Conway, J. B. Mechanism of Solute Transfer in Spray Towers. *Ind. Eng. Chem.* **1950**, *42*, 1151-1157.

(6) Sherwood, T. K.; Evans, J. E.; Longor, J. V. A. Extraction in Spray and Packed Columns. *Trans. Amer. Inst. Chem. Engnrs.* **1939**, *35*, 597-622.

(7) West, F. B.; Robinson, P. A.; Morganthaler, A. C.; Beck, T. R.; Mcgregor, D. K. Liquid-Liquid Extraction from Single Drops. *Ind. Eng. Chem.* **1951**, *43*, 234-238.

(8) Licht, W.; Pansing, W. F. Solute Transfer from Single Drops in Liquid-Liquid Extraction. *Ind. Eng. Chem.* **1953**, *45*, 1885-1896.

(9) Dixon, B. E.; Russell, A. A. W. The Absorption of Carbon Dioxide by Liquid Drops. *J. Soc. Chem. Ind.* **1950**, *69*, 284-288.

(10) Rajan, S. M.; Heideger, W. J. Drop Formation Mass Transfer. *A.I.C.h.E. J.* **1971**, *17*, 202-206.

(11) Heideger, W. J.; Wright, M. W. Liquid Extraction during Drop Formation: Effect of Formation time. *A.I.C.h.E. J.* **1986**, *32*, 1372-1376.

(12) Humphrey, J. A. C.; Hummel, R. L.; Smith, J. W. Note on the Mass Transfer Enhancement Due to Circulation in Growing Drops. *Chem. Eng. Sci.* **1974**, *29*, 1496-1500.

(13) Ilkovic, D. Polarographic Studies with the Dropping Mercury Kathode. ― Part XLIV. ― The Dependence of Limiting Currents on the Diffusion Constant, on the Rate of Dropping and on the Size of Drops. *Collection Czech. Chem. Comm.* **1934**, *6*, 498-513.

(14) Angelo, J. B.; Lightfoot, E. N.; Howard, D. W. Generalization of the Penetration Theory for Surface Stretch: Application to Forming and Oscillating Drops. *A.I.C.h.E. J.* **1966**, *12*, 751-760.

(15) Groothuis, H.; Karmers, H. Gas Absorption by Single Drops during Formation. *Chem. Eng. Sci.* **1955**, *4*, 17-25.

(16) Popovich, A. T.; Jervis, R. E.; Trass, O. Mass Transfer during Single Drop Formation. *Chem. Eng. Sci.* **1964**, *19*, 357-365.

(17) Srinivasan, V.; Aiken, R. C. Mass Transfer to Droplets Formed by The Controlled Breakup of A Cylindrical Jet ― Physical Absorption. *Chem. Eng. Sci.* **1988**, *43*, 3141-3150.

(18) Levich, V. G. *Physicochemical Hydrodynamics*; Prentice-Hall: Englewood Cliffs, NJ, 1962.

(19) Davies, J. T. The Effects of Surface Films in Damping Eddies at a Free Surface of a Turbulent Liquid. *Proc. R. Soc.* **1966**, *A290*, 515-526.

(20) Hoh, S. T.; Farid, M. M.; Chen, J.J.J. Mass Transfer to Droplets Formed by the Controlled Breakup of a Cylindrical Jet ― Physical Absorption. *Chem. Eng. Sci.* **2012**, *73*, 329-333.

(21) Chen, W.; Tsai, M.; Hung, C. Numerical Prediction of CO_2 Capture Process by a Single Droplet in Alkaline Spray. *Applied Energy* **2013**, *109*, 125-134.

(22) Chen, W.; Chen, S.; Hung, C. Carbon Dioxide Capture by Single Droplet using Selexol, Rectisol and Water as Absorbents: A Theoretical Approach. *Applied Energy* **2013**, *111*, 731-741.

(23) Crank, J. *The Mathematics of Diffusion*; Clarendon Press: Oxford, 1975.

(24) Knopp, K. *Theory and Application of Infinite Series*; Blackie & Son Ltd: London and Glasgow, 1954.

(25) deMontigny, D.; Tontiwachwuthikul, P.; Chakma, A. Comparing the Absorption Performance of Packed Columns and Membrane Contactors. *Ind. Eng. Chem. Res.* **2005**, *44*, 5726-5732.

(26) Morsi, S. A.; Alexander, A. J. An Investigation of Particle Trajectories in Two-phase Flow Systems. *J. Fluid Mech.* **1972**, *55* (2), 193-208.

(27) Brackbill, J. U.; Kothe, D. B.; Zemach, C. A continuum method for modelling surface tension, *J. Comput. Phys.* **1992**, *100*, 335-354.

(28) Fluent 6.3 Documentation, User's Guide, Chapter 23.

(29) Versteeg, G. F.; van Swaaij, W. P. M. Solubility and Diffusivity of Acid Gases (CO_2, N_2O) in Aqueous Alkanolamine Solutions. *J. Chem. Eng. Data* **1988**, *33*, 29-34.

(30) Davidson, J. F.; Cullen, E. J. The Determination of Diffusion Coefficient for Sparingly Soluble Gases in Liquids. *Trans. Inst. Chem. Eng.* **1957**, *35*, 51-60.

(31) Jiru, Y.; Eimer, D. A.; Wenjuan, Y. Measurements and Correlation of Physical Solubility of Carbon Dioxide in (Monoethanolamine + Water) by a Modified Technique. *Ind. Eng. Chem. Res.* **2012**, *51* (19), 6958-6966.

(32) Levenspiel, O. *Chemical Reaction Engineering*; John Wiley & Sons: New York, 1999.

(33) Snijder, E. D.; Riele, M. J. M.; Versteeg, G. F.; van Swaaij, W. P. M. Diffusion Coefficients of Several Aqueous Alkanolamine Solutions. *J. Chem. Eng. Data* **1993**, *38*, 475-480.

(34) Jiru, Y.; Eimer, D. A. Measurements and Correlations of Diffusivities of Nitrous Oxide and Carbon Dioxide in Moneethanolamine + Water by Laminar Liquid Jet. *Ind. Eng. Chem. Res.* **2012**, *51* (50), 16517-16524.

(35) Jiru, Y.; Eimer, D. A. Determination and Measurements of Mass Transfer Kinetics of CO_2 in Concentrated Aqueous Monoethanolamine Solutions by a Stirred Cell. *Ind. Eng. Chem. Res.* **2013**, *52* (7), 2548-2559.

6. Conclusions and Recommendation for Future Work

6.1 Conclusions

In this work, density data for the systems water + MEA, water + DEA and water + MDEA at amine mass fractions from 0.3 to 1.0 at temperatures from (298.15 to 423.15) K have been measured by Anton Paar density meters DMA 4500 and DMA HP. The maximum density value of unloaded aqueous MEA solutions as a function of composition at a given temperature always occurs at w_2 = 0.5 to 0.7. The densities become lower when the temperature increases for all the compositions. Pure MEA densities may be higher or lower than that of water depending on the temperature. The maximum deviation between the measured densities of unloaded aqueous MEA solutions and Pouryosefi and Idem's data is 0.33 kg·m^{-3}. Densities of unloaded aqueous DEA solutions decrease with the temperature increasing, and increase with the DEA concentration becoming greater. The maximum deviation between the measured densities of unloaded aqueous DEA solutions and Maham et al.'s data is 1.7 kg·m^{-3}. Densities of unloaded aqueous MDEA solutions increase at first and then decrease when the MDEA concentration increases. The maximum value occurs at w_2 = 0.7 for the whole temperature range. Pure MDEA densities are higher than that of water. Densities of unloaded aqueous MDEA solutions decrease with the rising temperature. The maximum deviation for densities of unloaded aqueous MDEA solutions between this work and Muhammad et al.'s data is 2.4 kg·m^{-3}, while between this work and Pouryousefi and Idem's data is 1.2 kg·m^{-3}. The density data of unloaded aqueous amine solutions are correlated using excess molar volumes to represent the deviations from ideal mixtures. Derived excess molar volumes of the binary system were correlated by the Redlich-Kister equation. The parameters of the Redlich-Kister equation were in turn fitted to an empirical function of temperature. The deviations between the measured densities of unloaded aqueous amine solutions and the correlated results are within the experimental error and negligible for engineering estimates.

Densities of CO_2 loaded aqueous MEA solutions have been measured at temperatures from (298.15 to 413.15) K with the mass fraction of MEA of 0.3, 0.4, 0.5, and 0.6. Density data for the systems water + DEA + CO_2 and water + MDEA + CO_2 at different amine mass fractions (0.3, 0.4) and different CO_2 loadings (0.1, 0.2, 0.3, 0.4, 0.5) at temperatures from (298.15 to 423.15) K have also been measured. Anton Paar density meters DMA 4500 and DMA HP were used for the measurements. Densities of CO_2 loaded aqueous amine solutions

decrease with the rising temperature, and increase with CO_2 loading rising. The maximum deviations between the measured densities of CO_2 loaded MEA, DEA and MDEA solutions and Weiland et al.'s data are 12 $kg \cdot m^{-3}$, 4.0 $kg \cdot m^{-3}$, and 3.3 $kg \cdot m^{-3}$ respectively. Derived molar volumes of the ternary system were fitted by the equations from Weiland et al. The parameters were in turn fitted to the polynomial function of temperature. The deviations between the measured results and the correlated data by the regressed models are less than the experimental error.

Surface tensions in water + MEA mixtures have been measured at temperatures from (303.15 to 333.15) K by using a Rame-Hart Model 500 Advanced Goniometer with DROPimage Advanced v2.4, which employs the pendant or sessile drop method. The concentration range was from 0 to 1.0. As the temperature increased, surface tension of aqueous MEA solutions decreased. Moreover, surface tension of aqueous MEA solutions decreased as the mole fraction of MEA increased for a given temperature. The surface tension data were correlated with temperature and mole fraction. The absolute average deviation between the correlated and experimental surface tensions is 0.0001 $N \cdot m^{-1}$ when correlating with temperature. The absolute average deviations between the correlated and experimental surface tensions are 0.0006 $N \cdot m^{-1}$ and 0.0004 $N \cdot m^{-1}$ when correlating with mole fraction by the empirical correlation model and chemical model, respectively. The models fitted to the surface tension data constitute a satisfactory representation with errors that would be negligible for engineering estimates.

A new experimental apparatus was built to study mass transfer between CO_2 and liquid droplets. The individual liquid droplet, which is generated by pushing the liquid through a needle with the help of pressurized nitrogen, falls through a gas chamber one by one and finally deposit under kerosene.

The experiments of CO_2 absorption by water droplets were performed to study mass transfer between CO_2 and liquid droplets without chemical reaction. The diffusion coefficient of CO_2 absorption by water droplet was calculated to prove that there exists convection inside the water droplet and the convection significantly enhances the mass transfer. The liquid phase mass transfer coefficient of CO_2 absorption into water droplets during formation and fall increases as the temperature rises and decreases as the droplet formation time increases. Also, the average liquid phase mass transfer coefficient of CO_2 absorption into water droplets

during formation and fall increases as the droplet falling height increases. The absorption rates of CO_2 into water droplets during only formation at different temperatures were directly measured by increasing the height of overflow tube and letting the droplets deposit under kerosene as soon as they detached from the needle. The experimental absorption rate of CO_2 into water droplets during formation decreases as the droplet formation time increases, first very quickly and then only gradually. The correlation of the absorption rate of CO_2 into water droplets during droplet formation at 323.15 K with droplet formation time was obtained. The average relative deviation between the experimental absorption rate and the fitted data is 2.04%. The absorption rate of CO_2 into water droplets during falling was calculated by subtracting the absorption during formation from the total mass transfer during drop life-time. Thus the liquid phase mass transfer coefficient during droplet falling can be derived. The liquid phase mass transfer coefficient of CO_2 absorption into water droplets during fall decreases as the droplet formation time increases, and increases as the droplet falling heights increases. The correlation between the Sherwood number, the Reynolds number and ζ (a dimensionless parameter characterizing the magnitude of droplet formation time) of CO_2 absorption by water droplets during droplet falling was obtained. The average relative deviation between the experimental Sherwood number and the correlated data is 5.64%.

The experiments of CO_2 absorption by droplets of 30% MEA solutions were performed to study mass transfer between CO_2 and liquid droplets with chemical reaction. The absorption rates of CO_2 into droplets of 30% MEA solutions during droplet formation at 323.15 K were measured. The absorption rate of CO_2 into droplets of 30% MEA solution almost does not vary as the droplet formation time changes. The liquid phase mass transfer coefficient of CO_2 into droplets of 30% MEA solution during droplet formation and fall increases as the temperature and droplet falling height rises. The correlation between the Sherwood number and the Reynolds number of CO_2 absorption by droplets of 30% MEA solution during droplet falling at 323.15 K was obtained. The average relative deviation between the experimental liquid phase mass transfer coefficient and the correlated data is 2.94%. The enhancement factors of CO_2 absorption into droplets of 30% MEA solution during formation and fall at 323.15 K are estimated, which range from 60 to 66.

6.2 Future work

The suggestions for the future work are as follows:

1. In the surface tension measurements, the bubbles are formed downwards which seems not to be reproducible enough. It is suggested that a new bubble nozzle with the whole upwards should be made to test the repeatability.
2. As has been mentioned earlier, the droplet diameter cannot be measured accurately when studying mass transfer during formation because the high speed camera cannot capture clear image of the droplet due to the splash. In the future, a magnet device which is adhered to the inner wall of the glass can be used to clean the wall. Another piece of magnet which is adhered to the outer wall of the glass will be used to adjust the place that needs to be cleaned.
3. In this work, the droplet diameter is always around 2.5 mm. A lot of attempts were made to generate smaller droplets and make the droplet diameter change within a larger range. A smaller needle was tried in this system, but the droplet diameter does not change very much. The vibration were added in the droplet generation system, but it is still a problem to produce the droplets which have the same size and fall vertically. It is suggested to continue working on generating smaller droplets.
4. A new experimental set-up (droplet chamber) was built and used to measure liquid phase mass transfer coefficient of CO_2 absorption by water droplets and droplets of 30% MEA solutions. This apparatus can be used for many other aspects, such as studying reaction kinetics in the spray column, measuring the enhancement factor and studying the selection of absorbent for the spray column.
5. At present, the droplet formation time cannot be controlled as required. In the future, a flowmeter and the corresponding control loop can be included in the droplet generation system to make sure the droplet formation time is known in advance.
6. At this stage, mass transfer between CO_2 and the unit part of a spray, the individual liquid droplet, was studied. More experiments in a pilot-scale setup need to be performed for further understanding the mass transfer in the spray column. In addition, the simulation work need to be done for establishing the mass transfer model.

Appendix

Appendix 3-1. The literature results of density measurements of unloaded and CO_2 loaded aqueous amine solutions.

Table 1. Densities of Water + MEA Mixtures at (298.15 to 353.15) K and Different Mole Fractions from Maham et al.[8].

x_2	ρ/kg·m^{-3}				
	T = 298.15 K	T = 303.15 K	T = 313.15 K	T = 333.15 K	T = 353.15 K
0	997.04	995.65	992.22	983.20	971.80
0.0054	997.67	996.31	992.80	983.78	972.21
0.0148	998.75	997.31	993.71	984.53	972.96
0.0230	999.74	998.22	994.54	985.19	973.62
0.0313	1000.74	999.13	995.37	985.85	974.12
0.0495	1002.90	1001.21	997.20	987.35	975.40
0.0674	1005.10	1003.25	999.03	988.76	976.60
0.0875	1007.56	1005.54	1001.02	990.33	977.88
0.1102	1010.14	1007.95	1003.18	992.08	979.29
0.1626	1015.63	1013.03	1007.59	995.52	981.99
0.2322	1020.97	1018.03	1011.92	998.73	984.44
0.3032	1024.31	1021.12	1014.47	1000.47	985.56
0.4194	1025.94	1022.45	1015.34	1000.47	984.89
0.4653	1025.65	1022.12	1014.84	999.81	984.10
0.5382	1024.52	1020.87	1013.43	998.14	982.32
0.6620	1022.64	1018.95	1011.38	995.82	979.83
0.7228	1019.89	1016.11	1008.43	992.70	976.68
0.7958	1017.72	1013.94	1006.18	990.33	974.07
0.8446	1016.26	1012.45	1004.60	988.72	972.54
0.9336	1013.68	1009.78	1001.94	986.02	969.77
0.9660	1012.80	1008.95	1001.02	985.02	968.82
1	1011.80	1007.95	1000.01	983.95	967.70

Table 2. Densities of Water + DEA Mixtures at (298.15 to 353.15) K and Different Mole Fractions from Maham et al.[8].

x_2	ρ/kg·m^{-3}						
	T = 298.15 K	T = 303.15 K	T = 313.15 K	T = 323.15 K	T = 333.15 K	T = 343.15 K	T = 353.15 K
0	997.04	995.65	992.22	988.04	983.20	977.77	971.80
0.0090	1002.61	1001.13	997.61	993.35	988.43	982.95	977.10
0.0188	1008.35	1006.79	1003.19	998.75	993.66	988.26	982.16
0.0414	1020.43	1018.17	1014.60	1009.91	1004.68	999.03	992.80
0.0690	1033.05	1031.07	1026.46	1021.42	1015.90	1010.08	1003.58
0.1028	1045.70	1043.39	1038.55	1032.88	1027.06	1020.98	1014.30
0.1469	1058.62	1055.65	1050.10	1044.21	1038.12	1031.83	1024.93
0.2054	1069.85	1067.02	1061.04	1054.88	1048.50	1042.02	1034.91
0.2884	1079.81	1076.81	1070.57	1064.15	1057.58	1051.02	1043.85
0.4026	1083.83	1083.74	1077.32	1070.65	1064.16	1057.47	1050.38
0.4992	1089.64	1086.68	1080.17	1073.58	1066.83	1060.23	1052.12
0.6059	1091.48	1088.40	1081.89	1075.29	1068.63	1061.96	1055.09
0.7764	1092.82	1089.81	1083.30	1076.62	1069.87	1063.22	1056.16
0.8012	1092.95	1089.94	1083.43	1076.75	1069.96	1063.39	1056.29
0.8989	1093.33	1090.28	1083.77	1077.05	1070.29	1063.64	1056.58
0.9438	1093.41	1090.41	1083.90	1077.13	1070.38	1063.73	1056.67
1	1093.70	1090.48	1084.01	1077.32	1070.74	1064.30	1056.99

Table 3. Densities of Water + MDEA Mixtures with Different Mole Fractions at 295.15 K, 308.15 K, 318.15 K, and 333.15 K from Pouryousefi and Idem[13].

x_2	ρ/kg·m^{-3}			
	T = 295.15 K	T = 308.15 K	T = 318.15 K	T = 333.15 K
0	997.78	994.03	990.26	980.85
0.017170	1006.50	1002.43	998.23	990.72
0.027080	1011.34	1006.89	1002.43	994.59
0.037819	1016.22	1011.36	1006.40	998.40
0.049908	1021.29	1015.97	1010.89	1002.28
0.063025	1026.68	1020.43	1015.02	1006.00
0.078004	1031.61	1024.82	1019.07	1009.60
0.095026	1036.50	1029.17	1023.05	1013.13
0.113978	1040.92	1033.07	1026.62	1016.28
0.136037	1044.96	1036.60	1029.89	1019.14
0.160258	1048.40	1039.68	1032.64	1021.52
0.191299	1051.43	1042.32	1035.02	1023.58
0.219337	1053.15	1043.81	1036.35	1024.70
0.265515	1054.57	1044.99	1037.37	1025.51
0.320422	1054.78	1045.03	1037.31	1025.34
0.385541	1053.82	1044.00	1036.24	1024.25
0.472801	1051.62	1041.79	1034.04	1022.11
0.586401	1048.33	1038.52	1030.80	1018.98
0.657570	1046.24	1036.43	1028.74	1016.98
0.747724	1043.86	1034.06	1026.39	1014.71
0.858842	1041.26	1031.46	1023.82	1012.21
0.937638	1039.62	1029.81	1022.17	1010.60
1	1040.00	1030.00	1021.00	1009.29

Table 4. Densities of Water + MDEA Mixtures at (298.15 to 338.15) K and Different Mole Fractions from Muhammad et al.[15].

x_2	ρ/kg·m^{-3}								
	T = 298.15 K	T = 303.15 K	T = 308.15 K	T = 313.15 K	T = 318.15 K	T = 323.15 K	T = 328.15 K	T = 333.15 K	T = 338.15 K
0	997.210	995.805	994.183	992.364	990.359	988.180	985.837	983.338	980.692
0.0128	1004.057	1002.479	1000.698	998.731	996.584	994.273	991.808	989.191	986.433
0.0212	1008.406	1006.702	1004.804	1002.724	1000.480	998.073	995.518	992.820	989.984
0.0498	1020.080	1017.933	1015.632	1013.185	1010.589	1007.874	1005.020	1002.039	998.939
0.0645	1026.392	1023.980	1021.433	1018.768	1015.978	1013.062	1010.027	1006.729	1003.614
0.0799	1030.846	1028.249	1025.530	1022.694	1019.743	1016.683	1013.511	1010.236	1006.853
0.1332	1042.798	1039.647	1036.417	1033.102	1029.709	1026.226	1022.667	1019.024	1015.295
0.1557	1045.445	1042.174	1038.830	1035.413	1031.918	1028.343	1024.692	1020.961	1017.154
0.1944	1049.907	1046.417	1042.857	1039.229	1035.539	1031.783	1027.966	1024.082	1020.126
0.2407	1050.842	1048.106	1044.446	1040.729	1036.948	1033.108	1029.246	1025.291	1021.295
0.2725	1052.408	1048.800	1045.139	1041.409	1037.630	1033.742	1029.769	1025.947	1021.898
0.3660	1052.539	1048.778	1044.967	1041.104	1037.198	1033.245	1029.243	1025.197	1021.103
0.4302	1050.974	1047.201	1043.379	1039.509	1035.603	1031.659	1027.676	1023.664	1019.603
0.5642	1046.854	1043.076	1039.276	1035.454	1031.608	1027.753	1023.830	1019.875	1015.875
0.6687	1041.445	1037.681	1033.894	1030.084	1026.252	1022.397	1018.519	1014.618	1010.695
0.7531	1039.267	1035.872	1031.924	1028.732	1025.017	1020.863	1016.835	1012.829	1008.962
1	1038.224	1034.493	1030.749	1026.993	1023.255	1019.469	1015.645	1011.796	1007.921

Table 5. Densities of Water + Amine + CO_2 Mixtures at 298.15 K and Different Mass Fractions of Amine from Weiland et al.[11].

	ρ/kg·m^{-3}											
α	w_2 (2 = MEA)				w_2 (2 = DEA)				w_2 (2 = MDEA)			
	0.1	**0.2**	**0.3**	**0.4**	**0.1**	**0.2**	**0.3**	**0.4**	**0.3**	**0.4**	**0.5**	**0.6**
0.05	1006	1015	1023	1032	1012	1025	1039	1053	1031	1043	1049	1061
0.10	1011	1022	1033	1043	1014	1030	1047	1062	1037	1050	1059	1071
0.15	1016	1030	1044	1056	1017	1035	1050	1069	1043	1054	1066	1080
0.20	1018	1038	1054	1070	1019	1039	1059	1078	1049	1062	1076	1088
0.25	1021	1046	1065	1082	1021	1043	1064	1086	1052	1070	1084	1100
0.30	1024	1053	1073	1096	1023	1049	1071	1094	1058	1077	1092	1112
0.35	1029	1059	1085	1114	1025	1052	1076	1102	1062	1083	1100	1119
0.40	1034	1066	1095	1126	1027	1057	1083	1111	1067	1091	1108	1128
0.45	1038	1072	1106	1139	1030	1062	1090	1119	1072	1098	1116	1136
0.50	1042	1179	1117	1147	1032	1167	1094	1127	1078	1105	1124	1148

Table 6. Densities of Water + MEA + CO_2 Mixtures at (298.15 to 353.15) K and Different Mass Fractions of MEA from Amundsen et al.[14].

T/K	ρ/kg·m^{-3}														
	α					α					α				
	0.1	0.2	0.3	0.4	0.5	0.1	0.2	0.3	0.4	0.5	0.1	0.2	0.3	0.4	0.5
	w_2 = 0.2					w_2 = 0.3					w_2 = 0.4				
298.15	1018.8	1032.7	1047.6	1064.0	1080.0	1028.0	1048.0	1070.0	1095.7	1121.1	1038.0	1063.0	1093.0	1128.5	1159.7
313.15	1012.5	1026.4	1041.3	1057.9	1073.5	1021.0	1041.0	1062.9	1088.5	1114.0	1030.0	1055.0	1085.0	1121.0	
323.15	1007.6	1021.5	1036.4	1053.0	1068.0	1016.0	1035.5	1058.0	1083.0	1108.0	1024.0	1049.0	1079.7	1115.0	
343.15	996.5	1010.5	1025.4	1041.9	1057.0	1004.0	1024.0	1046.4	1071.9		1012.0	1037.0	1068.0	1104.0	
353.15	990.2	1004.3	1019.2	1036.0		997.0	1017.6	1040.2	1066.0		1005.0	1031.0	1062.0	1097.7	

Appendix 3-2. Spreadsheet of a calculation example to the titration process.

The spread sheet of 30% loaded MDEA solution.

The titration results are shown below:

Titrating CO_2 amount			
	m_{sample} [g]	V_{HCl} [L]	V_{NaOH} [L]
A1	0.409	0.02913	0.01332
B1	0.438	0.03088	0.01409
Blank	0	0.01093	0.01060

Titrating concentration of MDEA		
	m_{sample} [g]	V_{HCl} [L]
A1	1.010	0.002427
B1	1.015	0.002433

The calculation process is shown below:

	m_{sample} [g]	c_{HCl} [mol/L]	V_{HCl} [L]	c_{NaOH} [mol/L]	V_{NaOH} [L]	n_{CO2} [mol]	n_{CO2}/m_{sample}[mol/g]
A1	0.409	0.1	0.02913	0.1	0.01332	0.000791	0.001892
B1	0.438	0.1	0.03088	0.1	0.01409	0.000839	0.001877
Blank		0.1	0.01093	0.1	0.01060	0.000017	

So: n_{CO2}/m_{sample} (average) = 0.0018845 mol/g.

m_{sample} [g]	V_{HCl} [L]	c_{HCl} [mol/L]	n_{MDEA} [mol]	n_{MDEA}/ m_{sample}[mol/g]
1.010	0.002427	1	0.002427	0.002403
1.015	0.002433	1	0.002433	0.002397

So: n_{MDEA}/m_{sample} (average) = 0.0024 mol/g

$\alpha = (n_{CO2}/m_{sample})/ (n_{MDEA}/m_{sample})$ = 0.0018845/0.0024= 0.7852 mole CO_2/ mole MDEA.

Appendix 3-3. Spreadsheet of a calculation example to the dilution process.

The calculation spreadsheet for 0.1 loaded 30% MDEA solution.

Mole CO_2 per g sample [mol/g]	0.0018845
Mole MDEA per g sample [mol/g]	0.002400
α_{CO2} [mol/mol]	0.7852
Select loaded sample [g]	10
Sample contains the mole of CO_2 [mol]	0.018845
Sample contains the mole of MDEA [mol]	0.02400
$\alpha_{CO2\ new}$ [mol/mol]	0.1
n_{MDEA} total needed in the loaded solution [mol]	0.18845
New addition of unloaded n_{MDEA} [mol]	0.16445
New addition of unloaded m_{MDEA} [g]	19.5959
w_{MDEA}	0.3
New unloaded MDEA solution needed [g]	65.3197

The dilution results for specific loaded 30% MDEA solution.

CO_2 loading of new 30% loaded MDEA solution	30% high loaded MDEA solution [g]	30% unloaded MDEA solution [g]
0.1	10	65.3197
0.2	10	27.8934
0.3	10	15.4180
0.4	10	9.1803
0.5	10	5.4377

Appendix 3-4. Densities of nitrogen and pure water under high pressure.

Densities of nitrogen could be calculated by ideal gas function.

PV = nRT → ρ = PM/RT. Densities of pure water are from IAPWS[16].

T **[K]**	***P*** **[bar]**	ρ_{N2} **[g/cm^3]**	ρ_{H2O} **[kg/m^3]**
373.15	7	0.006318	0.958630
383.15	7	0.006216	0.951220
393.15	7	0.005996	0.943360
403.15	7	0.005848	0.935060
413.15	7	0.005706	0.926320
423.15	7	0.005571	0.917140
303.15	8	0.008888	0.995963
313.15	8	0.008604	0.992530
323.15	8	0.008337	0.988351
333.15	8	0.008087	0.983515
343.15	8	0.007852	0.978087
353.15	8	0.007629	0.972115
363.15	8	0.007419	0.965637
373.15	8	0.007220	0.958681
383.15	8	0.007032	0.951267
393.15	8	0.006853	0.943406
403.15	8	0.006683	0.935107
413.15	8	0.006521	0.926370
423.15	8	0.006367	0.917191

Appendix 3-5. Fitting coefficients of the Redlich-Kister equation for unloaded aqueous MEA solutions with the R-square.

T/K	A_0	A_1	A_2	A_3	Adj. R-square
298.15	-2.57815	-0.64275	0.43921	1.83925	0.99260
303.15	-2.56536	-0.63330	0.43905	1.83310	0.99306
308.15	-2.55249	-0.62385	0.43889	1.82695	0.99690
313.15	-2.53908	-0.61440	0.43873	1.82080	0.98726
318.15	-2.52652	-0.60495	0.43857	1.81465	0.97268
323.15	-2.51365	-0.59550	0.43841	1.80850	0.98265
328.15	-2.50084	-0.58605	0.43825	1.80235	0.98820
333.15	-2.48735	-0.57660	0.43809	1.79620	0.99174
338.15	-2.47423	-0.56715	0.43793	1.79005	0.97528
343.15	-2.46114	-0.55770	0.43777	1.78390	0.98474
348.15	-2.44887	-0.54825	0.43762	1.77775	0.97523
353.15	-2.43562	-0.53880	0.43746	1.77160	0.97955
358.15	-2.42275	-0.52935	0.43730	1.76545	0.99220
363.15	-2.40920	-0.51990	0.43714	1.75930	0.98126
373.15	-2.30594	-0.44430	0.43587	1.71010	0.98899
383.15	-2.35762	-0.48210	0.43650	1.73470	0.98875
393.15	-2.33151	-0.46320	0.43618	1.72240	0.98915
403.15	-2.64347	-0.69000	0.44000	1.87000	0.98161
413.15	-2.27936	-0.42540	0.43555	1.69780	0.97570
423.15	-2.25324	-0.40650	0.43523	1.68550	0.94567

Appendix 3-6. Fitting coefficients of the Redlich-Kister equation for unloaded aqueous DEA solutions with the R-square.

T/K	A_0	A_1	A_2	A_3	A_4	Adj. R-square
298.15	-2.59759	-1.34687	-0.09113	-3.99113	5.20506	0.99230
303.15	-2.59001	-1.32765	0.44769	-4.94358	5.71939	0.99080
308.15	-2.56836	-1.28911	0.40569	-4.46741	5.13697	0.99260
313.15	-2.54533	-1.27009	0.10154	-3.29099	4.24877	0.99306
318.15	-2.53049	-1.23672	0.18344	-3.07571	3.80838	0.99120
323.15	-2.48308	-1.20981	-0.08698	-2.65577	3.69426	0.98428
328.15	-2.47949	-1.17567	0.13648	-2.59669	3.25502	0.98743
333.15	-2.44749	-1.16445	0.00222	-2.13354	2.93370	0.98902
338.15	-2.42815	-1.19251	-0.06824	-1.14319	1.84170	0.99097
343.15	-2.42635	-1.08902	0.28275	-2.56832	2.99634	0.98903
348.15	-2.42066	-1.04888	0.42746	-2.85803	3.06081	0.98397
353.15	-2.38262	-1.07718	0.01540	-1.38676	1.95049	0.98869
358.15	-2.38033	-0.96995	0.27140	-2.45515	2.71512	0.98688
363.15	-2.39315	-0.90470	0.94707	-3.87129	3.41189	0.98649
373.15	-2.37545	-0.73447	1.47648	-5.76267	4.82675	0.99690
383.15	-2.31093	-0.68243	1.23026	-5.14767	4.42630	0.99652
393.15	-2.27225	-0.58996	1.38902	-5.59343	4.66088	0.99626
403.15	-2.22175	-0.55410	1.23474	-4.99684	4.13484	0.99611
413.15	-2.19097	-0.46425	1.53331	-5.60325	4.34300	0.99176
423.15	-2.12425	-0.17202	1.95760	-8.39079	6.62595	0.90189

Appendix 3-7. Fitting coefficients of the Redlich-Kister equation for unloaded aqueous MDEA solutions with the R-square.

T/K	A_0	A_1	A_2	A_3	A_4	Adj. R-square
298.15	-4.74742	-3.12206	5.57166	-18.83782	15.15159	0.97697
303.15	-4.78674	-3.04464	9.65509	-29.14808	21.76141	0.97902
308.15	-4.72874	-3.01779	9.48232	-28.09274	20.77365	0.97719
313.15	-4.66868	-2.96769	9.17811	-26.70684	19.52099	0.97445
318.15	-4.63347	-2.97930	9.72475	-26.68964	18.85113	0.95842
323.15	-4.55428	-2.90973	9.14614	-25.34509	17.94932	0.96468
328.15	-4.50696	-2.84330	8.97684	-24.54485	17.16452	0.96172
333.15	-4.43475	-2.75441	8.28326	-23.17018	16.35102	0.97113
338.15	-4.33485	-2.68670	7.65428	-21.90248	15.58860	0.97678
343.15	-4.27312	-2.64600	7.52855	-21.40816	15.13230	0.98162
348.15	-4.21982	-2.56115	7.07911	-20.18850	14.20126	0.98262
353.15	-4.13398	-2.50717	6.80405	-19.47996	13.65584	0.98222
358.15	-4.17708	-2.44998	10.55968	-27.81701	18.41673	0.99079
363.15	-4.09412	-2.38800	9.84697	-25.88267	17.02516	0.99085
373.15	-3.44672	-2.48808	3.34625	-10.58562	7.59588	0.99972
383.15	-3.27520	-2.30274	3.06400	-9.87591	6.99865	0.99958
393.15	-3.08793	-2.16545	2.69235	-8.83197	6.17202	0.99959
403.15	-2.87961	-1.99150	1.67759	-6.34233	4.44170	0.99959
413.15	-2.67614	-1.86916	1.18322	-4.77310	3.17705	0.99957
423.15	-2.41776	-1.78979	0.77123	-2.88652	1.65507	0.99949

Appendix 3-8. Derived molar volumes $V/m^3 \cdot mol^{-1}$ of CO_2 loaded aqueous amine solutions.

MEA															
T/K	w_2	α	10^6 V	T/K	w_2	α	10^6 V	T/K	w_2	α	10^6 V	T/K	w_2	α	10^6 V
298.15	0.3	0.1	22.3193	313.15	0.3	0.1	22.4934	323.15	0.3	0.1	22.6192	333.15	0.3	0.1	22.7486
	0.3	0.21	22.1332		0.3	0.21	22.2813		0.3	0.21	22.3925		0.3	0.21	22.5136
	0.3	0.32	21.9056		0.3	0.32	22.0843		0.3	0.32	22.2008		0.3	0.32	22.3207
	0.3	0.44	21.7294		0.3	0.44	21.8750		0.3	0.44	21.9820		0.3	0.44	22.0962
	0.3	0.56	21.6117		0.3	0.56	21.7562		0.3	0.56	21.8629		0.3	0.56	21.9766
	0.4	0.1	24.4551		0.4	0.1	24.6476		0.4	0.1	24.7872		0.4	0.1	24.9309
	0.4	0.21	24.1839		0.4	0.21	24.3673		0.4	0.21	24.4997		0.4	0.21	24.6407
	0.4	0.33	23.7941		0.4	0.33	23.9649		0.4	0.33	24.0890		0.4	0.33	24.2212
	0.4	0.45	23.3467		0.4	0.45	23.5489		0.4	0.45	23.6779		0.4	0.45	23.7868
	0.5	0.1	26.7056		0.5	0.1	26.9510		0.5	0.1	27.1171		0.5	0.1	27.2853
	0.5	0.22	26.1998		0.5	0.22	26.4129		0.5	0.22	26.5603		0.5	0.22	26.7092
	0.5	0.34	25.6123		0.5	0.34	25.8017		0.5	0.34	25.9334		0.5	0.34	26.0735
	0.5	0.47	25.1669		0.5	0.47	25.3472		0.5	0.47	25.4725		0.5	0.47	25.6036
	0.6	0.1	29.6390		0.6	0.1	29.9170		0.6	0.1	30.1024		0.6	0.1	30.2988
	0.6	0.22	29.1121		0.6	0.22	29.3902		0.6	0.22	29.5858		0.6	0.22	29.7868
	0.6	0.34	28.0886		0.6	0.34	28.2995		0.6	0.34	28.4461		0.6	0.34	28.5967
	0.6	0.48	27.3597		0.6	0.48	27.5572		0.6	0.48	27.6920		0.6	0.48	27.8328
343.15	0.3	0.1	22.8885	353.15	0.3	0.1	23.0579	363.15	0.3	0.1	23.2111	373.15	0.3	0.1	23.3781
	0.3	0.21	22.6426		0.3	0.21	22.7820		0.3	0.21	22.9321		0.3	0.21	23.1026
	0.3	0.32	22.4483		0.3	0.32	22.5816		0.3	0.32	22.7276		0.3	0.32	22.8621
	0.3	0.44	22.2177		0.3	0.44	22.3490		0.3	0.44	22.4861		0.3	0.44	22.5928
	0.3	0.56	22.1179		0.3	0.56	22.2714		0.3	0.56	22.4019		0.3	0.56	22.5234
	0.4	0.1	25.0986		0.4	0.1	25.2534		0.4	0.1	25.4510		0.4	0.1	25.6180
	0.4	0.21	24.7904		0.4	0.21	24.9711		0.4	0.21	25.1175		0.4	0.21	25.2905
	0.4	0.33	24.3708		0.4	0.33	24.5084		0.4	0.33	24.6686		0.4	0.33	24.8167
	0.4	0.45	23.9054		0.4	0.45	24.0559		0.4	0.45	24.2216		0.4	0.45	24.3648
	0.5	0.1	27.4663		0.5	0.1	27.6524		0.5	0.1	27.8520		0.5	0.1	28.0323
	0.5	0.22	26.8725		0.5	0.22	27.0378		0.5	0.22	27.2130		0.5	0.22	27.3930
	0.5	0.34	26.2151		0.5	0.34	26.3654		0.5	0.34	26.5223		0.5	0.34	26.6836
	0.5	0.47	25.7405		0.5	0.47	25.8834		0.5	0.47	26.0487		0.5	0.47	26.2279
	0.6	0.1	30.5037		0.6	0.1	30.7144		0.6	0.1	30.9371		0.6	0.1	31.1231
	0.6	0.22	30.0047		0.6	0.22	30.2486		0.6	0.22	30.4965		0.6	0.22	30.7042
	0.6	0.34	28.7515		0.6	0.34	28.9131		0.6	0.34	29.0792		0.6	0.34	29.2710
	0.6	0.48	27.9775		0.6	0.48	28.1188		0.6	0.48	28.2933		0.6	0.48	28.4625
383.15	0.3	0.1	23.5308	393.15	0.3	0.1	23.6854	403.15	0.3	0.1	23.8397	413.15	0.3	0.1	24.0109
	0.3	0.21	23.2616		0.3	0.21	23.4158		0.3	0.21	23.5768		0.3	0.21	23.7280
	0.3	0.32	23.0050		0.3	0.32	23.1383		0.3	0.32	23.2616		0.3	0.32	23.3770
	0.3	0.44	22.7286		0.3	0.44	22.8704		0.3	0.44	22.9940		0.3	0.44	23.1414
	0.3	0.56	22.6463		0.3	0.56	22.7683		0.3	0.56	22.8917		0.3	0.56	23.0297
	0.4	0.1	25.8109		0.4	0.1	26.0066		0.4	0.1	26.2189		0.4	0.1	26.4182
	0.4	0.21	25.4659		0.4	0.21	25.6412		0.4	0.21	25.8397		0.4	0.21	26.0229
	0.4	0.33	24.9474		0.4	0.33	25.1207		0.4	0.33	25.2890		0.4	0.33	25.4496
	0.4	0.45	24.4961		0.4	0.45	24.6495		0.4	0.45	24.8071		0.4	0.45	24.9385
	0.5	0.1	28.2290		0.5	0.1	28.4199		0.5	0.1	28.6366		0.5	0.1	28.8272
	0.5	0.22	27.5541		0.5	0.22	27.7711		0.5	0.22	27.9832		0.5	0.22	28.2098
	0.5	0.34	26.8245		0.5	0.34	26.9694		0.5	0.34	27.1209		0.5	0.34	27.2921
	0.5	0.47	26.3953		0.5	0.47	26.5792		0.5	0.47	26.7341		0.5	0.47	26.8760
	0.6	0.1	31.3456		0.6	0.1	31.5523		0.6	0.1	31.7363		0.6	0.1	31.9062
	0.6	0.22	30.9118		0.6	0.22	31.1041		0.6	0.22	31.3049		0.6	0.22	31.4649
	0.6	0.34	29.5028		0.6	0.34	29.6676		0.6	0.34	29.8452		0.6	0.34	30.0166
	0.6	0.48	28.6088		0.6	0.48	28.7717		0.6	0.48	28.8983		0.6	0.48	29.0492

T/K	w_2	α	10^6 V		T/K	w_2	α	10^6 V		T/K	w_2	α	10^6 V	
			DEA	MDEA				DEA	MDEA				DEA	MDEA
298.15	0.3	0.1	23.0287	23.4251	303.15	0.3	0.1	23.0750	23.4818	313.15	0.3	0.1	23.1794	23.6028
	0.3	0.2	22.8793	23.3033		0.3	0.2	22.9291	23.3591		0.3	0.2	23.0337	23.4828
	0.3	0.3	22.7275	23.1958		0.3	0.3	22.7870	23.2530		0.3	0.3	22.8984	23.3772
	0.3	0.4	22.6048	23.1302		0.3	0.4	22.6633	23.1868		0.3	0.4	22.7729	23.3119
	0.3	0.5	22.5222	23.0171		0.3	0.5	22.5717	23.0750		0.3	0.5	22.6798	23.1984
	0.4	0.1	25.4986	26.1169		0.4	0.1	25.5587	26.1893		0.4	0.1	25.6847	26.3403
	0.4	0.2	25.2589	25.9157		0.4	0.2	25.3246	25.9866		0.4	0.2	25.4570	26.1394
	0.4	0.3	25.0647	25.7244		0.4	0.3	25.1336	25.7962		0.4	0.3	25.2632	25.9460
	0.4	0.4	24.8862	25.5519		0.4	0.4	24.9447	25.6224		0.4	0.4	25.0670	25.7694
	0.4	0.5	24.7183	25.3834		0.4	0.5	24.7779	25.4550		0.4	0.5	24.9001	25.5993
323.15	0.3	0.1	23.2959	23.7367	333.15	0.3	0.1	23.4205	23.8815	343.15	0.3	0.1	23.5602	24.0376
	0.3	0.2	23.1482	23.6170		0.3	0.2	23.2727	23.7596		0.3	0.2	23.4099	23.9134
	0.3	0.3	23.0131	23.5096		0.3	0.3	23.1377	23.6525		0.3	0.3	23.2725	23.8041
	0.3	0.4	22.8879	23.4429		0.3	0.4	23.0126	23.5821		0.3	0.4	23.1475	23.7321
	0.3	0.5	22.7953	23.3275		0.3	0.5	22.9205	23.4646		0.3	0.5	23.0536	23.6125
	0.4	0.1	25.8192	26.5033		0.4	0.1	25.9652	26.6761		0.4	0.1	26.1204	26.8591
	0.4	0.2	25.5908	26.2991		0.4	0.2	25.7308	26.4683		0.4	0.2	25.8847	26.6475
	0.4	0.3	25.3941	26.1025		0.4	0.3	25.5336	26.2683		0.4	0.3	25.6842	26.4464
	0.4	0.4	25.1975	25.9254		0.4	0.4	25.3363	26.0881		0.4	0.4	25.4860	26.2504
	0.4	0.5	25.0326	25.7501		0.4	0.5	25.1688	25.9098		0.4	0.5	25.3180	26.0861
353.15	0.3	0.1	23.7086	24.2054	363.15	0.3	0.1	23.8683	24.3780	373.15	0.3	0.1	24.0350	24.5630
	0.3	0.2	23.5555	24.0787		0.3	0.2	23.7054	24.2486		0.3	0.2	23.8712	24.4357
	0.3	0.3	23.4179	23.9671		0.3	0.3	23.5606	24.1442		0.3	0.3	23.7282	24.3312
	0.3	0.4	23.2905	23.8864		0.3	0.4	23.4354	24.0591		0.3	0.4	23.6026	24.2439
	0.3	0.5	23.2014	23.7645		0.3	0.5	23.3444	23.9462		0.3	0.5	23.5093	24.1284
	0.4	0.1	26.2876	27.0580		0.4	0.1	26.4673	27.2653		0.4	0.1	26.6547	27.4813
	0.4	0.2	26.0454	26.8395		0.4	0.2	26.2182	27.0317		0.4	0.2	26.3958	27.2536
	0.4	0.3	25.8438	26.6243		0.4	0.3	26.0129	26.8306		0.4	0.3	26.1817	27.0375
	0.4	0.4	25.6423	26.4323		0.4	0.4	25.7957	26.6295		0.4	0.4	25.9778	26.8399
	0.4	0.5	25.4596	26.2475		0.4	0.5	25.6289	26.4585		0.4	0.5	25.8052	
383.15	0.3	0.1	24.2186	24.7686	393.15	0.3	0.1	24.4149	24.9982	403.15	0.3	0.1	24.6245	25.2347
	0.3	0.2	24.0513	24.6306		0.3	0.2	24.2487	24.8490		0.3	0.2	24.4543	25.1099
	0.3	0.3	23.9051	24.5358		0.3	0.3	24.0871	24.8216		0.3	0.3	24.3059	
	0.3	0.4	23.7767	24.4388		0.3	0.4	23.9722			0.3	0.4		
	0.3	0.5	23.6971			0.3	0.5				0.3	0.5		
	0.4	0.1	26.8582	27.7175		0.4	0.1	27.0755	27.9750		0.4	0.1	27.3047	28.2431
	0.4	0.2	26.5889	27.4874		0.4	0.2	26.8032	27.7420		0.4	0.2	27.0290	
	0.4	0.3	26.3730	27.2744		0.4	0.3	26.5825			0.4	0.3	26.8085	
	0.4	0.4	26.1650			0.4	0.4	26.3750			0.4	0.4		
	0.4	0.5	25.9985			0.4	0.5				0.4	0.5		
413.15	0.3	0.1	24.8480	25.4972	423.15	0.3	0.1	25.1384	25.7078					
	0.3	0.2	24.6835	25.4081		0.3	0.2							
	0.3	0.3				0.3	0.3							
	0.3	0.4				0.3	0.4							
	0.3	0.5				0.3	0.5							
	0.4	0.1	27.5377	28.5461		0.4	0.1	27.8404						
	0.4	0.2	27.2559			0.4	0.2							
	0.4	0.3				0.4	0.3							
	0.4	0.4				0.4	0.4							
	0.4	0.5				0.4	0.5							

Appendix 3-9. Calculated values of V_1/m^3·mol^{-1} and V_2/m^3·mol^{-1} (1 refers to water, 2 refers to amine).

T/K	10^6 V_1	10^6 V_2		
		MEA	DEA	MDEA
298.15	18.05	60.36	96.1	115.0
303.15	18.08	60.60	96.4	115.4
313.15	18.14	61.08	97.0	116.3
323.15	18.22	61.57	97.6	117.1
333.15	18.31	62.08	98.2	118.1
343.15	18.41	62.59	98.8	119.0
353.15	18.52	63.13	99.5	119.9
363.15	18.65	63.68	100.1	120.9
373.15	18.78	64.23	100.8	121.8
383.15	18.92	64.82	101.5	122.8
393.15	19.08	65.43	102.3	123.9
403.15	19.25	66.05	103.0	124.9
413.15	19.43	66.70	103.8	126.0
423.15	19.63	67.39	104.6	127.2

Appendix 3-10. Fitted V_{CO2}, V^*, c and d for CO_2 loaded aqueous amine solutions at different temperatures.

T/K	V_{CO2}			V^*		
	MEA	DEA	MDEA	MEA	DEA	MDEA
298.15	7.2362	-69.4596	-3.75093	-2.5831	-3.79717	-7.43662
303.15		-52.4998	0.7804		-3.77826	-7.36031
313.15	7.7237	-35.7093	10.15151	-2.4638	-3.65273	-7.16695
323.15	7.8904	-36.4347	13.76332	-2.4519	-3.63906	-6.94224
333.15	8.0722	-31.6073	13.07715	-2.4728	-3.61911	-6.90802
343.15	8.6906	-38.1049	-0.29794	-2.4538	-3.532	-6.73247
353.15	9.7334	-15.6117	10.0619	-2.4618	-3.56122	-6.45067
363.15	9.2673	-19.0926	10.58309	-2.5395	-3.55259	-6.62092

373.15	7.5645	-34.5348	109.0578	-2.7283	-3.55772	-6.39799
383.15	7.1668	-38.5848	242.6593	-2.9071	-3.5036	-6.1811
393.15	4.4032	-57.0331		-3.2236	-3.23747	
403.15	1.0172			-3.5008		
413.15	-1.9738			-3.9963		
423.15						
T/K	**c**			**d**		
	MEA	**DEA**	**MDEA**	**MEA**	**DEA**	**MDEA**
298.15	-14.8309	1804.50705	310.74274	31.2219	-10666.67754	-2461.688140
303.15		1384.28154	184.14592		-8133.56553	-1594.712440
313.15	-22.4521	970.97891	-69.21034	45.3172	-5657.26846	74.049290
323.15	-27.1153	990.8951	-173.68331	55.5722	-5778.16974	780.816430
333.15	-33.2303	872.76389	-159.00088	70.9712	-5076.56807	677.019710
343.15	-43.7854	1035.58135	212.89791	95.8649	-6067.60572	-1849.866190
353.15	-58.3436	475.33824	-92.98378	129.3204	-2720.95329	200.670340
363.15	-58.5884	541.76688	-101.94668	132.3772	-3054.78294	290.766070
373.15	-44.2176	936.6666	-2866.78558	100.3246	-5484.60919	18908.504210
383.15	-48.5563	1047.30783	-6605.48139	117.7127	-6199.52983	44007.983020
393.15	-24.0499	1441.16857		59.3898	-8432.83299	
403.15	3.5665			-5.8057		
413.15	29.4640			-66.9657		
423.15						

Appendix 4-1. The literature results of surface tension measurements of aqueous amine solutions.

Table 4-1. Surface Tensions of Water + MEA Mixtures at (298.15 to 323.15) K and Different Mole Fractions from Vázquez et al.[1].

	γ/N·m^{-1}					
x_2	T = 298.15 K	T = 303.15 K	T = 308.15 K	T = 313.15 K	T = 318.15 K	T = 323.15 K
0	0.07201	0.07121	0.07042	0.06952	0.06884	0.06792
0.015	0.06845	0.06766	0.06668	0.06599	0.06532	0.06440
0.032	0.06597	0.06517	0.06441	0.06350	0.06283	0.06192
0.049	0.06409	0.06329	0.06251	0.06163	0.06096	0.06005
0.069	0.06263	0.06184	0.05106	0.06017	0.05949	0.05859
0.112	0.06041	0.05961	0.05884	0.05794	0.05727	0.05636
0.164	0.05874	0.05794	0.05715	0.05627	0.05558	0.05467
0.228	0.05731	0.05652	0.05574	0.05484	0.05416	0.05325
0.307	0.05599	0.05520	0.05443	0.05352	0.05284	0.05193
0.407	0.05466	0.05386	0.05307	0.05218	0.05149	0.05058
0.541	0.05318	0.05237	0.05158	0.05069	0.05000	0.04909
0.726	0.05138	0.05057	0.04977	0.04888	0.04818	0.04727
1	0.04895	0.04814	0.04734	0.04643	0.04573	0.04481

Appendix 4-2. The procedure for generating a bubble by the dispenser.

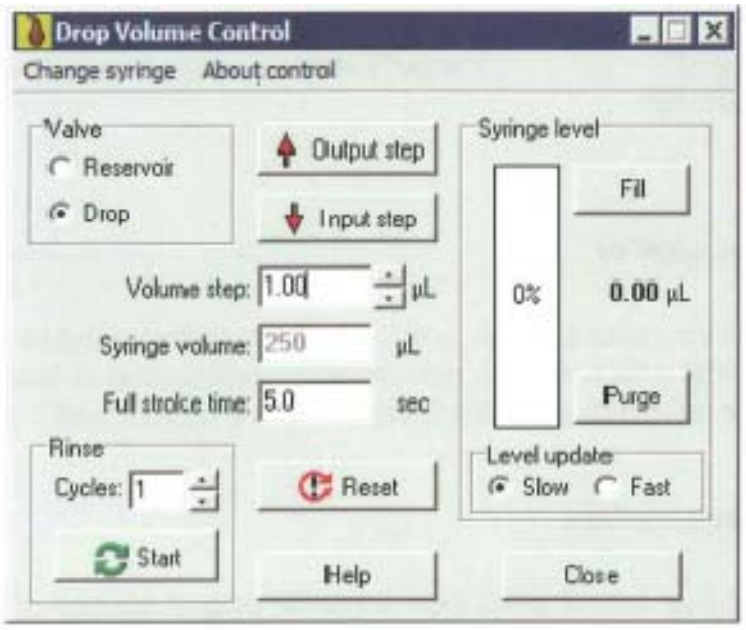

Figure. The volume control window which controls the dispenser.[7]

1. Fill the cuvette with aqueous amine solutions.
2. Put the cuvette in the environmental chamber. Make sure one thermocouple is inside the liquid, and the other is in touch with the gas.
3. Increase the temperature to the needed value by the temperature controller.
4. Put the needle into the cuvette.
5. Chose Valve "**Drop**" and press "**Fill**" in the volume control window.
6. Chose Valve "**Reservoir**" and press "**Purge**" in the volume control window.
7. Repeat steps 5 and 6 for several times to suck the liquid into the needle.
8. Take the needle out of the cuvette. Put it in the environmental chamber.
9. Repeat steps 5 and 6 for several times to suck the gas into the needle until a section of liquid can be seen in the connected hose.
10. Put the needle back into the cuvette.
11. Set the "**Volume step**" and Press "**Output step**" in the volume control window to generate the bubble.

Appendix 4-3. Original data of the surface tension measurements.

$w_2 = 0$												
	$T = 303.15$ K			$T = 313.15$ K			$T = 323.15$ K			$T = 333.15$ K		
	γ [mN/m]	β	volume [mm^3]	γ [mN/m]	β	volume [mm^3]	γ [mN/m]	β	volume [mm^3]	γ [mN/m]	β	volume [mm^3]
	71.33	1.021	42.830	69.80	1.016	40.590	67.68	1.024	38.760	66.05	1.020	37.100
	71.10	1.161	49.480	69.47	1.240	51.210	67.63	1.304	52.070	66.16	1.155	44.290
	71.60	1.061	44.820	69.18	1.273	52.460	67.95	1.175	46.310	65.87	1.221	47.030
	71.42	1.109	47.960	69.78	1.136	46.550	68.28	1.175	46.730	66.27	1.128	42.440
	71.29	1.073	45.130	69.30	1.174	47.860	67.75	1.304	52.180	65.95	1.136	42.640
	71.20	1.086	45.710	69.43	1.175	48.040	68.22	1.198	47.660	66.29	1.142	42.850
	71.51	1.094	46.470	69.65	1.172	48.440	67.68	1.232	48.700	66.18	1.148	43.440
	71.27	1.101	46.600	69.99	1.167	48.500	68.23	1.228	49.220	66.23	1.149	43.610
	71.01	1.104	46.730	69.43	1.191	48.850	68.15	1.598	66.040	66.26	1.155	43.640
	71.25	1.112	47.070	69.46	1.217	50.110	68.26	1.238	50.090	66.38	1.154	43.790
Average	**71.30**			**69.55**			**67.98**			**66.16**		

$w_2 = 0.1$												
	$T = 303.15$ K			$T = 313.15$ K			$T = 323.15$ K			$T = 333.15$ K		
	γ [mN/m]	β	volume [mm^3]	γ [mN/m]	β	volume [mm^3]	γ [mN/m]	β	volume [mm^3]	γ [mN/m]	β	volume [mm^3]
	66.55	1.005	36.91	65.54	1.104	40.89	64.22	0.571	16.84	62.69	0.928	32.00
	66.87	1.072	40.24	65.59	0.979	35.34	64.34	0.642	19.91	62.55	0.919	31.47
	66.68	0.646	20.14	65.49	0.930	33.11	64.51	0.857	29.96	62.32	0.945	32.35
	65.98	0.761	25.14	65.59	1.082	39.98	64.12	0.976	35.08	62.45	1.304	47.53
	66.83	0.980	36.06	65.48	1.261	47.52	64.11	0.636	19.58	62.91	0.761	24.69
	66.63	1.378	53.16	65.62	0.820	28.01	64.13	1.257	47.32	62.45	0.818	26.95
	66.84	1.037	38.64	65.45	0.941	33.47	65.27	0.763	26.16	62.43	0.819	27.00
	66.81	1.260	48.46	65.40	0.823	28.04	64.20	1.089	40.04	62.29	0.891	30.10
	67.27	0.696	22.86	65.34	0.807	27.25	64.09	1.051	38.30	62.27	0.891	30.10
	66.99	0.868	31.20	65.60	0.998	36.21	64.10	1.220	45.77	62.21	0.919	31.28
Average	**66.75**			**65.51**			**64.31**			**62.46**		

w_2 = 0.2												
	T = 303.15 K			T = 313.15 K			T = 323.15 K			T = 333.15 K		
	γ [mN/m]	β	volume [mm^3]	γ [mN/m]	β	volume [mm^3]	γ [mN/m]	β	volume [mm^3]	γ [mN/m]	β	volume [mm^3]
	64.79	0.942	32.48	63.24	1.218	42.77	61.82	0.999	34.15	60.38	0.841	26.03
	64.34	1.176	42.05	63.74	0.860	27.42	62.35	0.639	17.92	60.30	1.000	32.57
	64.14	1.151	40.78	63.31	1.215	42.00	61.31	0.915	30.17	60.03	1.165	38.85
	64.36	1.052	35.88	63.16	1.149	39.15	61.61	0.794	25.26	59.96	1.342	45.56
	64.74	0.927	31.83	63.18	1.066	35.71	61.67	0.969	32.88	59.84	1.542	52.61
	64.74	0.780	25.13	63.29	0.992	32.75	61.59	1.172	41.13	59.61	1.695	57.61
	64.73	1.013	35.55	63.05	1.411	49.35	61.73	0.825	26.72	60.12	0.682	19.23
	65.15	0.935	32.40	63.08	1.304	45.26	61.57	0.850	27.71	59.99	0.758	22.29
	65.25	0.820	27.19	63.74	0.647	18.10	61.71	0.924	31.00	60.30	1.026	33.61
	65.12	0.760	24.26	63.11	1.295	45.10	61.79	0.974	33.17	60.17	1.164	38.94
Average	**64.74**			**63.29**			**61.72**			**60.07**		

w_2 = 0.3												
	T = 303.15 K			T = 313.15 K			T = 323.15 K			T = 333.15 K		
	γ [mN/m]	β	volume [mm^3]	γ [mN/m]	β	volume [mm^3]	γ [mN/m]	β	volume [mm^3]	γ [mN/m]	β	volume [mm^3]
	63.91	0.964	31.85	62.00	1.513	51.87	61.39	1.069	32.24	59.32	0.808	23.53
	63.80	1.053	35.51	62.44	0.801	24.05	61.27	1.221	38.03	59.31	0.953	29.50
	63.56	0.973	31.89	62.54	0.966	31.15	61.26	1.370	43.56	59.28	1.347	44.59
	63.61	0.999	33.06	62.36	1.158	38.82	61.15	1.540	49.44	59.59	1.076	34.65
	63.51	1.042	34.76	62.13	1.368	46.72	61.58	1.172	37.94	59.34	1.751	58.65
	63.41	1.089	36.63	62.47	0.828	25.23	61.15	1.018	30.16	59.62	0.877	26.69
	63.40	1.162	39.57	62.46	1.045	34.35	61.25	1.326	42.01	59.39	1.343	44.62
	63.38	1.193	40.82	62.32	1.252	42.51	61.12	1.645	53.06	59.42	0.997	31.47
	63.26	1.288	44.43	62.07	0.705	19.76	61.68	0.942	27.58	59.49	0.923	28.51
	63.13	1.318	45.47	62.48	0.943	30.13	61.35	1.077	33.98	59.42	0.895	27.29
Average	**63.50**			**62.33**			**61.32**			**59.42**		

w_2 = 0.4												
	T = 303.15 K			T = 313.15 K			T = 323.15 K			T = 333.15 K		
	γ [mN/m]	β	volume [mm^3]	γ [mN/m]	β	volume [mm^3]	γ [mN/m]	β	volume [mm^3]	γ [mN/m]	β	volume [mm^3]
	61.99	1.133	36.93	60.42	1.078	33.73	58.62	1.123	34.36	57.23	1.116	33.32
	61.74	1.249	41.14	60.24	1.206	38.45	58.88	0.887	25.48	57.32	0.938	26.73
	61.75	1.688	56.78	60.15	1.343	43.37	58.70	1.026	30.77	57.17	1.078	31.90

	61.44	0.690	18.50	60.09	1.493	48.61	58.56	1.183	36.52	57.29	1.219	37.09
	61.96	0.880	26.65	60.07	1.324	42.63	58.50	1.334	41.89	57.11	1.376	42.39
	61.82	1.042	33.17	60.47	0.924	27.73	58.49	1.488	47.21	57.18	1.543	48.05
	61.72	1.215	39.80	60.62	1.015	31.49	58.84	1.640	52.70	57.18	1.718	53.62
	61.56	1.412	46.96	60.41	1.151	36.54	59.28	0.866	24.97	57.41	1.101	32.95
	61.84	1.130	36.65	60.15	1.294	41.64	59.48	0.999	30.42	57.34	1.280	39.34
	61.58	1.379	45.77	60.08	1.445	46.92	58.81	1.207	37.69	57.68	0.960	27.93
Average	**61.74**			**60.27**			**58.82**			**57.29**		

w_2 = 0.5												
	***T* = 303.15 K**			***T* = 313.15 K**			***T* = 323.15 K**			***T* = 333.15 K**		
	γ [mN/m]	β	volume [mm^3]	γ [mN/m]	β	volume [mm^3]	γ [mN/m]	β	volume [mm^3]	γ [mN/m]	β	volume [mm^3]
	59.25	1.586	48.29	58.42	1.499	45.10	56.84	1.503	44.13	55.55	0.884	23.53
	58.91	1.139	32.67	58.17	1.069	30.02	56.85	1.655	48.88	55.55	1.326	39.11
	59.44	1.299	38.88	58.26	1.220	35.49	56.62	0.951	25.04	55.57	1.064	30.12
	59.48	1.437	43.65	58.36	1.382	41.14	56.73	1.084	29.90	55.60	1.742	52.41
	59.28	1.306	38.93	57.80	0.885	22.91	56.82	1.213	34.50	55.36	0.885	23.60
	59.32	1.605	48.96	58.02	1.024	28.25	56.91	1.357	39.44	55.13	0.954	25.15
	58.95	1.942	58.76	58.04	1.165	33.34	57.00	1.513	44.59	55.30	0.839	20.59
	59.47	1.431	43.41	58.08	1.311	38.45	56.95	1.670	49.48	55.00	1.411	39.99
	59.14	0.950	25.94	58.45	1.459	43.81	56.85	1.838	54.41	55.57	0.853	21.42
	59.49	1.219	36.09	58.34	1.615	48.74	56.93	0.853	22.38	55.28	1.395	39.93
Average	**59.27**			**58.19**			**56.85**			**55.39**		

w_2 = 0.6												
	***T* = 303.15 K**			***T* = 313.15 K**			***T* = 323.15 K**			***T* = 333.15 K**		
	γ [mN/m]	β	volume [mm^3]	γ [mN/m]	β	volume [mm^3]	γ [mN/m]	β	volume [mm^3]	γ [mN/m]	β	volume [mm^3]
	56.46	1.246	34.17	56.50	1.049	29.23	55.36	1.082	29.91	53.76	0.893	22.48
	56.93	0.934	23.63	56.35	1.370	40.18	55.17	1.447	41.91	53.61	1.249	34.58
	57.03	1.330	37.55	56.49	1.744	52.04	55.16	1.805	52.70	53.70	1.618	46.18
	56.99	1.645	47.46	56.26	0.878	22.82	55.30	1.421	41.21	54.14	1.019	27.28
	57.84	0.873	23.13	56.43	1.194	34.34	55.06	0.894	22.93	53.52	0.894	22.93
	57.88	1.174	34.34	56.40	1.582	47.01	55.13	1.240	35.08	53.65	1.846	52.68
	57.76	1.510	45.64	56.26	0.941	25.01	55.17	1.634	47.67	52.80	1.189	32.67
	57.91	1.245	36.91	56.20	1.171	33.24	55.46	0.823	20.50	53.60	1.591	45.07
	57.66	0.927	25.14	56.48	1.365	40.01	54.58	1.158	31.70	53.80	2.037	57.79
	57.70	1.077	30.68	56.17	0.893	23.20	55.12	1.464	31.70	53.49	1.327	38.27
Average	**57.42**			**56.35**			**55.15**			**53.61**		

w_2 = 0.7												
	T = 303.15 K			T = 313.15 K			T = 323.15 K			T = 333.15 K		
	γ [mN/m]	β	volume [mm^3]	γ [mN/m]	β	volume [mm^3]	γ [mN/m]	β	volume [mm^3]	γ [mN/m]	β	volume [mm^3]
	55.65	1.428	40.43	54.88	1.439	41.05	53.50	1.005	24.82	51.89	0.947	21.68
	55.55	1.938	55.35	54.80	1.672	48.03	53.38	1.401	37.51	51.91	1.453	37.54
	55.54	1.826	52.35	54.83	1.467	41.85	53.28	1.749	47.57	51.65	2.068	53.56
	55.64	0.628	13.70	54.93	1.283	36.14	53.20	1.949	52.86	52.21	1.201	31.40
	55.97	1.394	38.52	54.77	1.623	46.54	53.45	1.409	37.89	51.48	1.068	25.44
	55.73	1.632	46.52	54.79	1.319	37.19	53.52	1.071	27.04	51.50	1.546	39.86
	55.84	1.296	36.22	54.64	1.645	47.05	53.40	1.684	45.70	51.83	1.050	25.27
	55.97	2.009	57.19	54.74	1.491	42.56	53.55	1.290	34.17	51.72	1.532	39.78
	55.97	1.178	31.63	54.98	1.099	30.08	53.42	1.480	39.87	51.86	1.098	26.86
	55.91	1.294	36.76	54.83	1.454	41.42	53.27	1.630	44.08	51.62	1.319	33.71
Average	**55.78**			**54.82**			**53.40**			**51.77**		

w_2 = 0.8												
	T = 303.15 K			T = 313.15 K			T = 323.15 K			T = 333.15 K		
	γ [mN/m]	β	volume [mm^3]	γ [mN/m]	β	volume [mm^3]	γ [mN/m]	β	volume [mm^3]	γ [mN/m]	β	volume [mm^3]
	53.29	0.972	23.50	52.62	0.923	21.81	51.25	1.228	30.83	49.36	1.129	25.59
	53.18	1.068	26.56	52.51	1.137	28.69	51.12	1.421	36.44	49.94	1.028	22.97
	53.22	1.328	34.76	52.50	1.183	30.12	50.99	1.653	42.78	49.52	1.228	28.67
	53.61	1.194	31.30	52.29	1.380	35.92	51.22	0.930	21.44	49.77	1.442	35.02
	53.59	1.387	36.95	52.37	1.502	39.59	51.25	1.054	25.43	49.55	1.705	41.86
	53.67	1.241	32.54	52.35	1.312	33.93	51.05	1.536	39.61	49.57	1.125	25.70
	53.51	1.341	35.50	52.24	1.433	37.38	51.24	1.452	37.43	49.51	1.270	29.90
	53.16	0.632	11.99	52.05	1.378	35.56	51.15	1.638	42.46	49.42	1.242	28.98
	53.58	1.469	39.38	52.48	1.098	27.31	51.11	1.692	43.90	49.69	0.935	19.79
	53.47	1.764	47.68	52.66	1.065	26.59	51.06	1.787	46.28	49.83	1.099	25.06
Average	**53.43**			**52.41**			**51.14**			**49.62**		

w_2 = 0.9												
	T = 303.15 K			T = 313.15 K			T = 323.15 K			T = 333.15 K		
	γ [mN/m]	β	volume [mm^3]	γ [mN/m]	β	volume [mm^3]	γ [mN/m]	β	volume [mm^3]	γ [mN/m]	β	volume [mm^3]
	50.73	1.029	23.46	49.70	1.444	33.89	48.44	1.438	33.98	46.84	1.101	23.64
	50.73	1.000	22.51	49.45	1.562	36.79	48.48	1.945	46.92	47.04	1.720	39.97
	50.86	1.198	28.66	49.47	1.788	42.58	48.43	2.086	50.15	47.02	2.025	47.16
	50.31	1.323	31.75	49.74	1.344	31.21	48.36	1.250	28.76	46.90	1.069	22.58
	50.35	1.579	38.96	49.62	1.586	37.62	48.40	1.361	31.89	47.17	1.553	35.98

	50.72	1.015	22.97	49.59	1.795	42.93	48.43	1.515	36.06	47.23	2.204	51.47
	50.54	1.212	28.77	49.80	1.270	29.15	48.46	1.870	45.10	46.95	1.104	23.67
	50.59	1.514	37.37	49.65	1.522	35.96	48.40	1.148	25.86	47.07	1.233	27.39
	50.44	1.778	44.11	49.67	1.762	42.24	48.39	1.314	30.48	47.09	1.341	30.36
	50.67	1.337	31.02	49.59	2.036	48.73	48.41	1.458	34.41	46.71	1.050	21.76
Average	**50.59**			**49.63**			**48.42**			**47.00**		

w_2 = 1.0												
	***T* = 303.15 K**			***T* = 313.15 K**			***T* = 323.15 K**			***T* = 333.15 K**		
	γ [mN/m]	β	volume [mm^3]	γ [mN/m]	β	volume [mm^3]	γ [mN/m]	β	volume [mm^3]	γ [mN/m]	β	volume [mm^3]
	48.15	0.926	18.86	46.89	1.433	31.89	45.54	1.190	24.88	44.74	1.000	19.30
	48.05	0.940	19.16	46.80	1.907	43.36	45.43	1.192	24.82	44.73	1.368	29.10
	48.10	1.369	31.27	46.49	2.375	52.94	45.56	1.621	35.88	44.76	1.530	33.15
	48.10	1.495	34.63	46.68	2.269	51.12	45.61	1.874	41.87	44.73	1.624	35.40
	48.53	1.079	23.52	46.15	1.751	38.74	45.63	1.165	24.22	44.67	1.781	39.03
	47.86	1.221	26.98	46.68	1.800	40.64	45.56	0.967	17.97	44.83	1.504	32.64
	48.13	1.277	28.78	46.42	2.150	48.14	45.89	1.162	23.54	44.43	1.625	34.90
	47.95	0.882	17.56	46.81	2.118	48.11	45.42	1.411	29.56	44.67	2.339	50.77
	48.26	1.092	23.74	47.03	1.423	31.79	45.64	1.121	22.22	44.22	1.190	23.95
	48.18	1.248	28.06	46.64	1.755	39.59	45.52	1.077	20.85	44.47	1.295	26.82
Average	**48.13**			**46.66**			**45.58**			**44.63**		

Appendix 5-1. The design drawing of the ruler with the unit length of 1 cm in the gas chamber, from CMR Prototech.

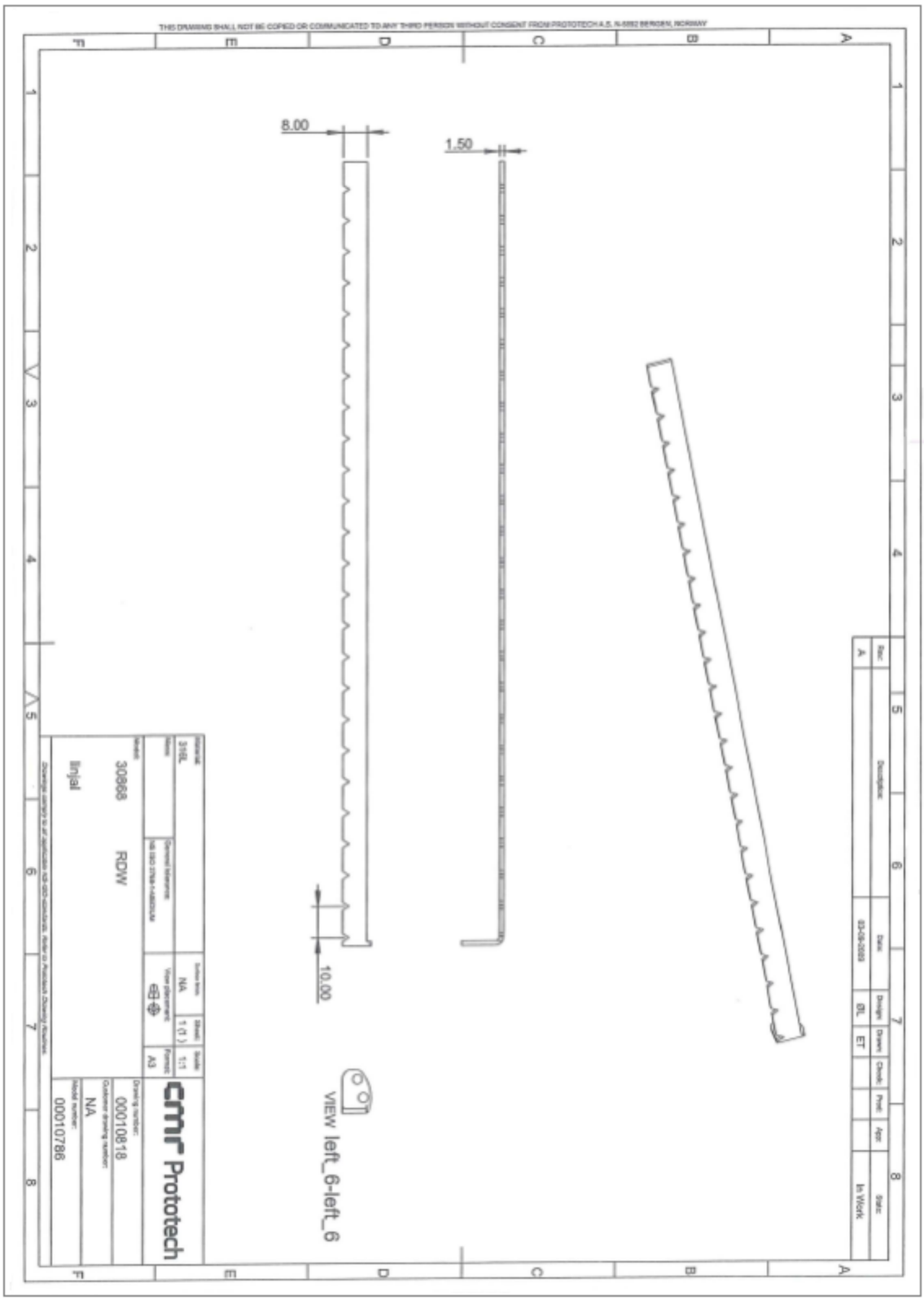

Appendix 5-2. Temperature calibration curves for the thermocouples.

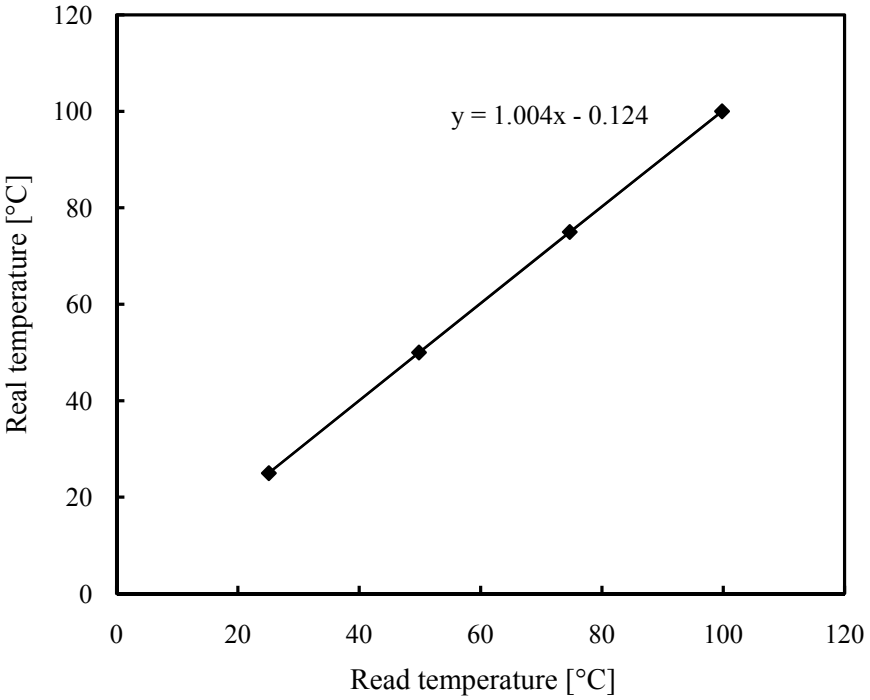

(a) The temperature calibration curve for thermocouple 1

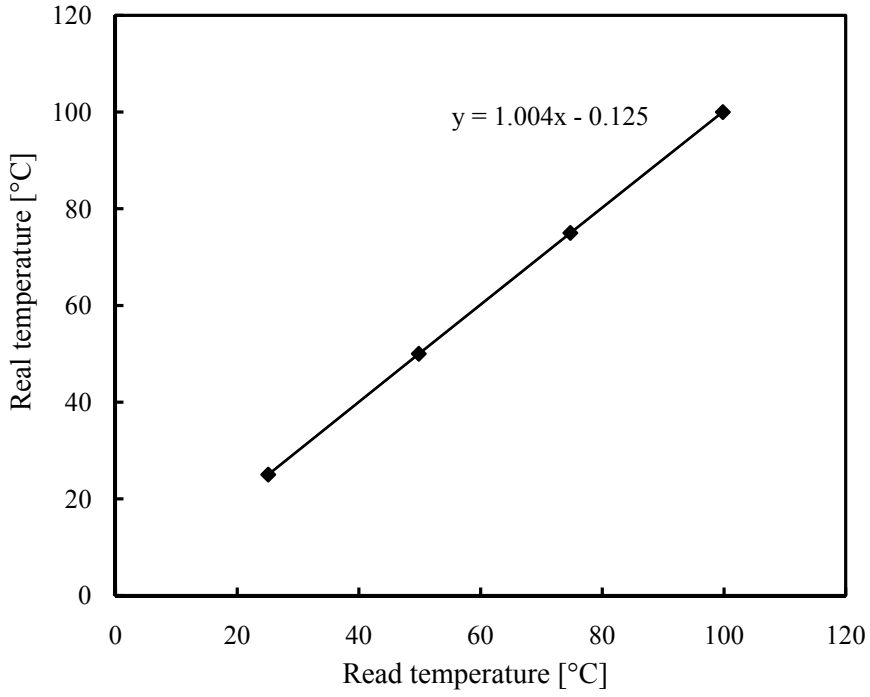

(b) The temperature calibration curve for thermocouple 2

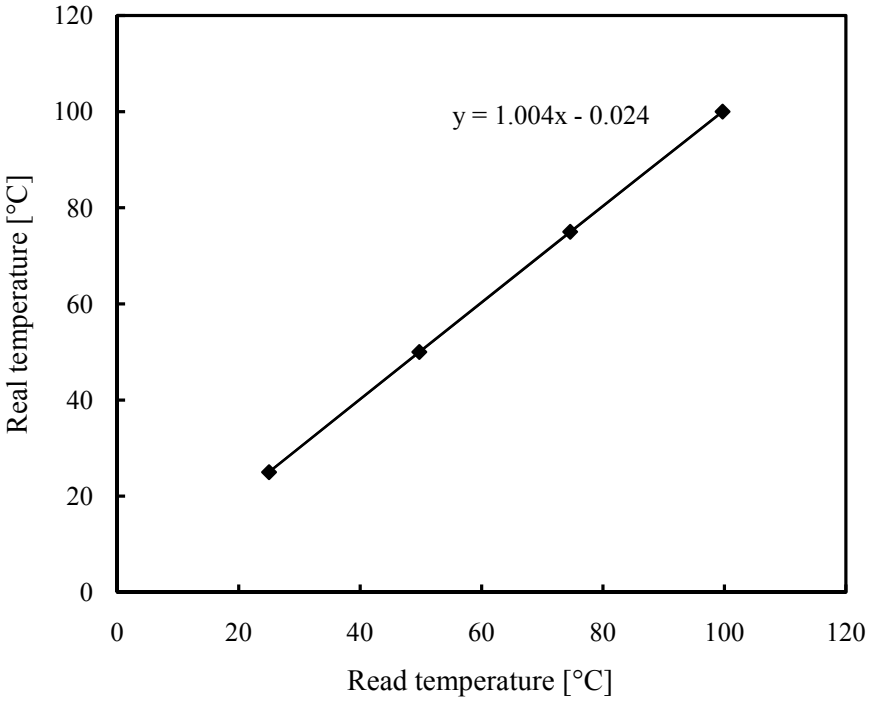

(c) The temperature calibration curve for thermocouple 3

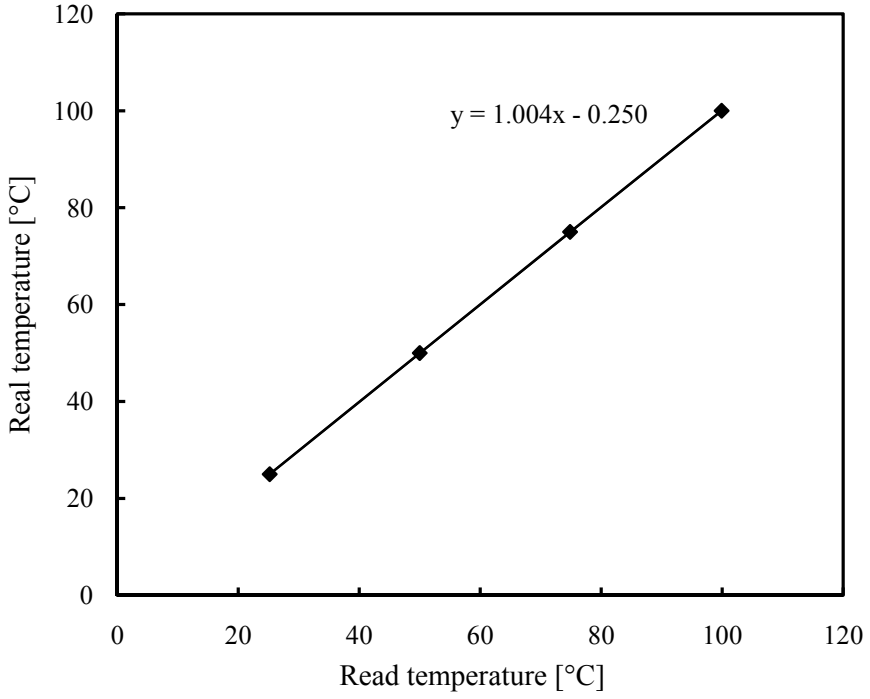

(d) The temperature calibration curve for thermocouple 4

Appendix 5-3. The procedure of absorption experiments for liquid droplets and gas.

1. Open values HV03, HV04, and HV06. Close valves HV01, HV02, HV05 and HV07. Fill ethanol into the chamber through valve HV06 until the chamber is full of ethanol. Air in the chamber was vented through valve HV03.
2. Close valve HV03. Open valves HV01 and HV02. Fill CO_2 into the chamber to drain ethanol out of the chamber through valve HV06.
3. Blow CO_2 for a while until the chamber is totally dry.
4. Close valve HV02, fill the gas bag with CO_2 and then stop CO_2 blowing. Close valve HV01.
5. Set the temperature value as needed on the temperature control device.
6. Connect the data logger to a computer. The temperatures at different positions and the pressure in the chamber were recorder when the experiment is running.
7. Open valve HV03. Fill kerosene into the chamber through drain valve HV06. And then open valve HV02, close valve HV03.
8. Wait until the temperatures of gas phase and kerosene up to the desired value.
9. Fill the liquid container with the solvent. Open the N_2 valve and increase the pressure of N_2.
10. Open valve HV07 to produce the droplets.
11. Let the droplets keep dripping. Wait until the level of kerosene in the chamber being constant.
12. Measure the reduced rate of the volume of CO_2 by the soap film flow meter.
13. Take the video by the high speed camera to obtain the droplet diameter and the droplet formation rate.
14. Close the N_2 valve and valve HV07 to stop droplets dripping.
15. Open valve HV01. Drain the kerosene and the deposit solvent out by blowing CO_2 through valve HV02.
16. Open valve HV03. Fill ethanol into the chamber and then drain the ethanol out.
17. Repeat step 16 several times to rinse the chamber with ethanol until the chamber is clean.
18. Blow CO_2 through the chamber until the inner wall is dry.
19. Close all the valves.

Appendix 5-4. The Matlab program for simulating the droplet free fall and calculating the droplet falling time (written by Morten C. Melaaen).

```
t0=0;
t1=0.5;
tspan=[t0; t1];
x0=[0; 0];     %Initial conditions: first position, next velocity.
options=odeset('RelTol',1e-6,'AbsTol',[1e-6 1e-6]);
global rhofl rhopar dia myfl g Vfl model;
model=1;  % model=1 is model used by Fluent

rhopar=1008.4;    %kg/m^3
dia=0.002618;       %m
rhofl=1.776;        %kg/m^3
myfl=1.526e-5;     %Ns/m^2
g=9.81;           %m/s^2
Vfl=0.0;            %m/s

[t,x]=ode23('part',tspan,x0,options);
figure(1)
plot(t,x(:,1))
t
x(:,1)
x(:,2)
xlabel('t (time [s])')
ylabel('x1(t) (position [m])')
grid on

figure(2)
plot(t,x(:,2))
xlabel('t [sek]')
ylabel('x2(t) (velocity [m/s])')
grid on
```

```
figure(3)
plot(x(:,1),x(:,2))
xlabel('x1(t) (distance [m])')
ylabel('x2(t) (velocity [m/s])')
grid on

function xdot=part(t,x)

xdot=zeros(2,1);
global rhofl rhopar dia myfl g Vfl model;

Vrel=x(2)-Vfl+0.000001;
Rep=abs(rhofl*Vrel*dia/myfl);

if model==1
  if Rep<0.1
    a1=0;
    a2=24;
    a3=0;
  elseif Rep<1
    a1=3.69;
    a2=22.73;
    a3=0.0903;
  elseif Rep<10
    a1=1.222;
    a2=29.1667;
    a3=-3.8889;
  elseif Rep<100
    a1=0.6167;
    a2=46.5;
    a3=-116.67;
  elseif Rep<1000
    a1=0.3644;
    a2=98.33;
```

```
    a3=-2778;
  elseif Rep<5000
    a1=0.357;
    a2=148.62;
    a3=-4.75e4;
  elseif Rep<10000
    a1=0.46;
    a2=-490.546;
    a3=57.87e4;
  elseif Rep<50000
    a1=0.5191;
    a2=-1662.5;
    a3=5.4167e6;
  end %if
  Cd=a1+a2/Rep+a3/Rep^2;
end %if

xdot(1)=x(2);
xdot(2)=-Cd*3./(4.*dia)*rhofl/rhopar*abs(Vrel)*Vrel+g;
```

Appendix 5-5. The calculations of the experimental droplet velocity.

The droplet falling distance and the corresponding droplet velocity were measured at three different points.

Point A:

The position of point A was shown in Fig. 1 (a). Therefore the droplet falling distance at point A is:

$$s_1 = (\frac{30.85 - 10.39}{110.61}) \times 0.01\ \text{m} = 0.0018\ \text{m}$$

The picture of the next frame was shown in Fig. 1 (b). Therefore the droplet falling distance after one frame is:

$$s_1' = (\frac{35.79}{108.53} - \frac{10.39}{110.61}) \times 0.01\ \text{m} = 0.0023\ \text{m}$$

The frame speed is 400 fps. So, the time distance between one frame is:

$$t_1 = \frac{1}{400}\text{s} = 0.0025\ \text{s}$$

Hence the instantaneous velocity at point A is:

$$u_1 = \frac{s_1' - s_1}{t_1} = 0.2\ \text{m/s}$$

The calculations of droplet falling distance and the corresponding droplet velocity at the other two points are the same as that just introduced. The results are given below:

$$s_2 = 0.1314\ \text{m}; u_2 = 1.59\ \text{m/s}$$
$$s_3 = 0.2338\ \text{m}; u_3 = 2.02\ \text{m/s}$$

Table. The experimental droplet falling distance and the corresponding droplet velocity.

Droplet falling distance *s* [m]	**Droplet velocity *u* [m/s]**
0	≈ 0
0.0018	0.20
0.1314	1.59
0.2338	2.02

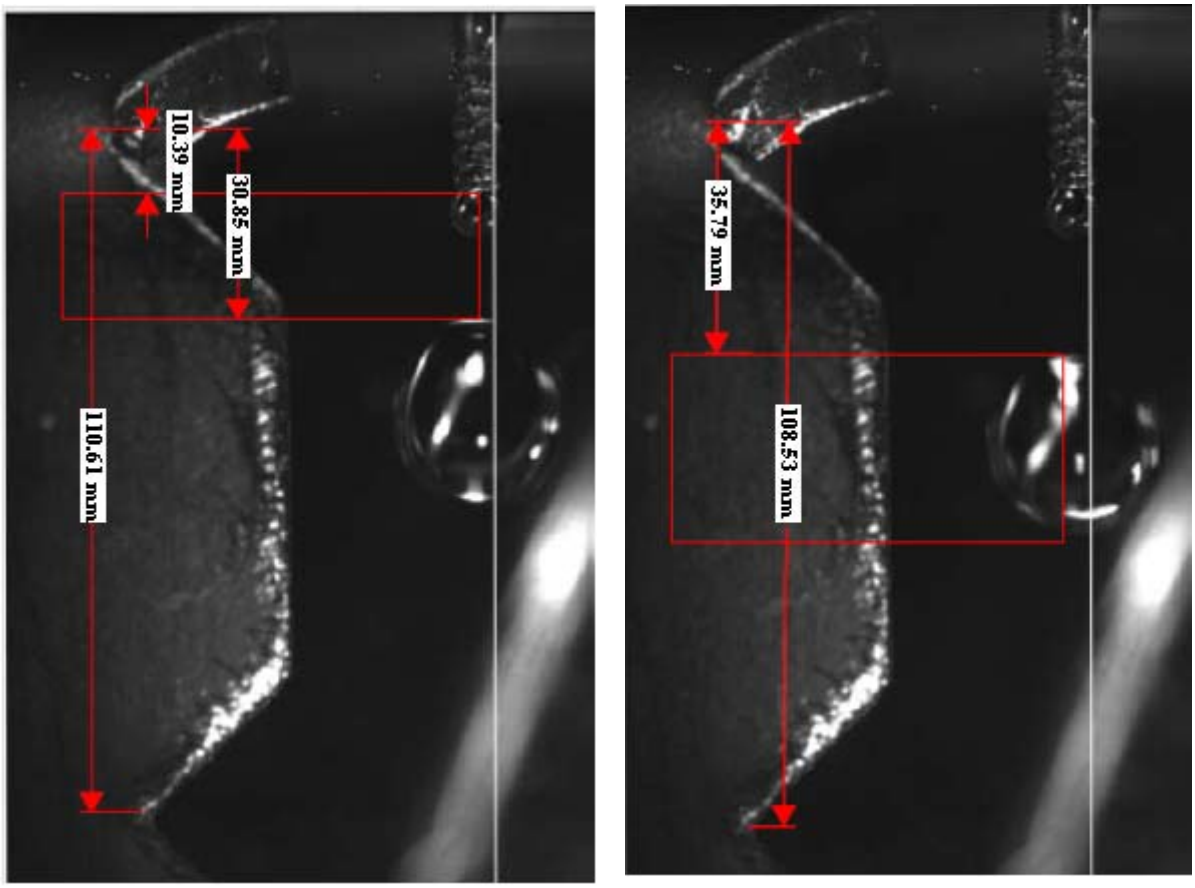

(a) The position of point A (b) The picture after one frame

Figure 1. The calculation of droplet falling distance and droplet velocity at point A.

Appendix 6. List of publications and presentations.

Publications:

1. Han, J.; Jin, J.; Eimer, D. A.; Melaaen, M. C. Density of Water (1) + Monoethanolamine (2) + CO_2 (3) from (298.15 to 413.15) K and Surface Tension of Water (1) + Monoethanolamine (2) from (303.15 to 333.15) K. *J. Chem. Eng. Data*, **2012**, *57* (4), pp 1095–1103.
2. Han, J.; Jin, J.; Eimer, D. A.; Melaaen, M. C. Density of Water (1) + Diethanolamine (2) + CO_2 (3) and Water (1) + N-Methyldiethanolamine (2) + CO_2 (3) from (298.15 to 423.15) K. *J. Chem. Eng. Data*, **2012**, *57* (6), pp 1843–1850.
3. Han, J.; Eimer, D. A.; Melaaen, M. C. Liquid Phase Mass Transfer Coefficient of Carbon Dioxide Absorption by Water Droplet, Accepted by GHGT-11.
4. Han, J.; Eimer, D. A.; Melaaen, M. C. The Mass Transfer Characteristics of CO_2 Absorption by Individual Liquid Droplet. In preparation for submission to Chemical engineering research & design.

Presentations:

1. Han, J.; Eimer, D. A.; Melaaen, M. C. Mass transfer between carbon dioxide and liquid droplets formed by a novel experimental set-up. International Conference on Carbon Reduction Technologies, Poland. 19-22 September 2011.
2. Han, J.; Eimer, D. A.; Melaaen, M. C. Liquid Phase Mass Transfer Coefficient of CO_2 Absorption by Water Droplet. International Conference on Greenhouse Gas Technologies (GHGT), Japan. 18-22 November 2012.

ISBN 978-82-7206-377-0
ISSN 1893-3068

www.hit.no
2014